Functional Two-Dimensional Materials: A Computational Study of Complex Processes at Interfaces

---

Dissertation

zur

Erlangung der naturwissenschaftlichen Doktorwürde
(Dr. sc. nat.)

vorgelegt der

Mathematisch-naturwissenschaftlichen Fakultät

der

Universität Zürich

von

Ralph Oliver Koitz

aus

Österreich

Promotionskomitee

Prof. Dr. Jürg Hutter (Vorsitz und Leitung)

Prof. Dr. Thomas Greber

Dr. Marcella Mauri-Iannuzzi

Zürich, 2015

Abstract

Functional two-dimensional nanomaterials with well-defined properties are of prime importance in science and technology. Especially since the discovery of graphene, interest in large-scale molecular layers of one atom thickness has surged. Adsorbed on transition metals, such monolayer sheets form versatile functional heterostructures. They may be utilized for applications as catalysts for chemical reactions, as substrates that direct and align adsorbed molecules and as insulating layers to decouple adsorbates from the metal.

The first part of this work examines hexagonal boron nitride (*h*-BN) adsorbed on nickel, copper, and cobalt. At the outset, fundamental properties of these heterostructures are studied with methods based on density functional theory. Depending on the nature of the substrate and the lateral position of the sheet, chemi- and physisorptive interactions of varying strength are observed. Guided by images from tunneling microscopy, the apparent corrugation of *h*-BN/Cu is then analyzed. Electronic structure calculations of the non-commensurate surface show that the lattice mismatch of *h*-BN and Cu gives rise to an electronic corrugation while the monolayer remains topographically flat. This corrugation also affects the orbital levels of adsorbed porphine molecules, depending on their lateral position on the surface. Furthermore, metal-supported *h*-BN is examined for use in oxygen activation and catalysis. Particularly *h*-BN/Cu shows promise as a cathode material for O_2 reduction in fuel cells. The predicted overpotential for this reaction is lower than what is currently achieved on platinum.

The second part focuses on two-dimensional metal-organic networks. A *tris*-terpyridine derived model molecule (TTPB) can be polymerized to form a well-defined monolayer on both metal surfaces and an air-water interface. The properties of TTPB on gold and copper substrates are investigated with respect to adsorption energies and electronic properties. The experimentally observed preferential orientation of the molecules on Cu is confirmed. TTPB on liquid water is examined with extensive simulations based on *ab initio* molecular dynamics. The water surface plays a central role in this system, as it mildly stabilizes the molecule and allows metal ions to reach the surface from the solution where they interlink the monomers. The metadynamics method is used to energetically quantify the uptake of Zn ions from the liquid and the binding free energy of the TTPB dimer.

The results from this work provide important details on the structure, properties, and functionality of selected two-dimensional materials. They highlight the importance of detailed simulations for the interpretation of experimental results and for the modeling and prediction of properties.

Zusammenfassung

Funktionale zweidimensionale Nanomaterialien mit wohldefinierten Eigenschaften sind von zentraler Bedeutung für Wissenschaft und Technologie. Insbesondere seit der Entdeckung von Graphen besteht reges Interesse an grossflächigen molekularen Schichten mit der Dicke eines einzelnen Atoms. Werden solche monomolekularen Lagen auf Übergangsmetalle aufgebracht, entstehen vielfältige funktionale Heterostrukturen. Diese finden potentielle Anwendung als Katalysatoren für chemische Reaktionen, als Substrate, welche adsorbierte Moleküle definiert steuern und ausrichten können, und als Isolationsschichten um Adsorbat und Metall zu entkoppeln.

Der erste Teil dieser Arbeit befasst sich mit hexagonalem Bornitrid (*h*-BN), aufgebracht auf Nickel, Kupfer und Cobalt. Zunächst werden grundlegende Eigenschaften dieser Heterostrukturen mit Methoden basierend auf Dichtefunktionaltheorie untersucht. Je nach Typ des Substrates und lateraler Anordnung der Schicht auf der Oberfläche treten unterschiedlich starke chemi- oder physisorptive Wechselwirkungen auf. Angeleitet von Tunnelmikroskopiebildern wird anschliessend die beobachtete Korrugation von *h*-BN/Cu analysiert. Berechnungen der Elektronenstruktur der nicht-kommensurablen Oberfläche zeigen, dass die Fehlanpassung der Gitterkonstanten von *h*-BN und Cu eine elektronische Korrugation hervorruft, während die Schicht topografisch flach bleibt. Diese Korrugation beeinflusst auch die Orbitalniveaus von adsorbiertem Porphin, je nachdem wo sich dieses auf der Oberfläche befindet. Darüber hinaus wird metallgestütztes *h*-BN hinsichtlich seiner Eignung zur Sauerstoffaktivierung und Katalyse untersucht. Insbesondere *h*-BN/Cu zeigt vielversprechende Eigenschaften als Kathodenmaterial zur O_2-Reduktion in Brennstoffzellen. Hierbei ist die vorhergesagte Überspannung niedriger als derzeit auf Platin realisiert werden kann.

Im zweiten Teil werden zweidimensionale metall-organische Netzwerke untersucht. Ein *tris*-Terpyridin-basiertes Modellmolekül (TTPB) kann sowohl auf Metalloberflächen, als auch an Luft-Wasser Grenzflächen mit Hilfe von Metallionen zu einer wohldefinierten Monoschicht polymerisiert werden. TTPB auf Gold- und Kupfersubstraten wird im Hinblick auf Adsorptionsenergien und elektronische Eigenschaften untersucht. Die experimentell beobachtete bevorzugte Ausrichtung der Moleküle auf Cu wird bestätigt. TTPB auf flüssigem Wasser wird mit umfangreichen Simulationen auf basis von *ab initio* Molekulardynamik untersucht. Hierbei kommt der Wasseroberfläche zentrale Bedeutung zu, da sie das Molekül sanft zu stabilisieren vermag und Metallionen aus der Flüssigkeit zur Oberfläche gelangen können, wo sie die Monomere verknüpfen. Mit Hilfe der Metadynamik-Methode werden die Aufnahme von Zn-Ionen aus der Lösung und die freie Bindungsenergie des TTPB-Dimeres quantifiziert.

Die gesammelten Ergebnisse dieser Dissertation liefern wichtige Details zu Struktur, Eigenschaften, und Funktionalität ausgewählter zweidimensionaler Materialien. Sie unterstreichen die Relevanz von detaillierten Simulationen bei der Deutung von experimentellen Ergebnissen, sowie zur Modellierung und Vorhersage von Eigenschaften.

Acknowledgments

This thesis describes my research in four years at the University of Zurich. I am grateful to many people for their help and guidance throughout this time.

First and foremost, I thank my advisor, Prof. Jürg Hutter, for the opportunity to work in his group. I am grateful for his support in academic matters and beyond, and for the freedom he gave me to develop and pursue my own ideas.

I would like to express my sincere gratitude to Dr. Marcella Iannuzzi for her constant support, for tirelessly answering all my questions, and for guiding my work in the right direction. I also thank Dr. Ari Seitsonen for many helpful discussions that taught me about condensed matter physics and other tricky subjects.

I thank my office mate Florian, as well as the entire Hutter group, for the friendly working atmosphere and the mutual support.

I am very grateful to Dr. Felix Studt and Prof. Jens Nørskov for hosting me in their group at Stanford University for the summer of 2014. Working there was a great chance to explore the subtleties of computational electrochemistry and gave me many new impulses for my work.

The research presented here is built on numerous external collaborations. Particularly, I would like to thank Dr. Thomas Dienel at EMPA for fruitful exchange on surface-supported MOFs, and Dr. Willi Auwärter at TUM for the joint work on Cu-supported *h*-BN.

This work has received of support from various organizations. I thank the Swiss National Science Foundation for supporting this project financially and the Swiss National Supercomputing Center for generous computing resources. I am especially grateful to the Japanese High-Performance Computing initiative for awarding me with a "Junior Researcher Promotion" grant for calculation time on the K supercomputer.

Finally, I wholeheartedly thank my wife Irina, my sister Martina, my parents, and my entire family for their unwavering support in all matters. Without them, none of this would have been possible. This thesis is dedicated to them.

Zurich, Switzerland
August 2015

Ralph Koitz

Publications

1. Koitz, R.; Nørskov, J. K.; Studt, F. A Systematic Study of Metal-Supported Boron Nitride Materials for the Oxygen Reduction Reaction. *Phys. Chem. Chem. Phys.* **2015**, *17*, 12722–12727
2. Koitz, R.; Iannuzzi, M.; Hutter, J. Building Blocks for Two-Dimensional Metal-Organic Frameworks Confined at the Air-Water Interface: An Ab Initio Molecular Dynamics Study. *J. Phys. Chem. C* **2015**, *119*, 4023–4030
3. Joshi, S.; Bischoff, F.; Koitz, R.; Ecija, D.; Seufert, K.; Seitsonen, A. P.; Hutter, J.; Diller, K.; Urgel, J. I.; Sachdev, H.; Barth, J. V.; Auwärter, W. Control of Molecular Organization and Energy Level Alignment by an Electronically Nanopatterned Boron Nitride Template. *ACS Nano* **2014**, *8*, 430–442
4. Barman, S.; Khutia, A.; Koitz, R.; Blacque, O.; Furukawa, H.; Iannuzzi, M.; Yaghi, O. M.; Jainak, C.; Hutter, J.; Berke, H. Synthesis and Hydrogen Adsorption Properties of Internally Polarized 2,6-Azulenedicarboxylic Acid Based MOFs. *J. Mat. Chem. A* **2014**, *2*, 18823–18830
5. Koitz, R.; Seitsonen, A. P.; Iannuzzi, M.; Hutter, J. Structural and Electronic Properties of a Large-Scale Moiré Pattern of Hexagonal Boron Nitride on Cu(111) Studied with Density Functional Theory. *Nanoscale* **2013**, *5*, 5589–5595
6. Gómez Díaz, J.; Ding, Y.; Koitz, R.; Seitsonen, A. P.; Iannuzzi, M.; Hutter, J. Hexagonal Boron Nitride on Transition Metal Surfaces. *Theor. Chem. Acc.* **2013**, *132*, 1350
7. Joshi, S.; Ecija, D.; Koitz, R.; Iannuzzi, M.; Seitsonen, A. P.; Hutter, J.; Sachdev, H.; Vijayaraghavan, S.; Bischoff, F.; Seuferd, K.; Barth, J. V.; Auwärter, W. Hexagonal Boron Nitride on Cu(111): An Electronically Corrugated Monolayer. *Nano Lett.* **2012**, *12*, 5821 – 5828

Contents

1

Introduction

Since the discovery of graphene, interest in atomically thin two-dimensional (2D) materials has surged.[1] They find possible applications in electronics,[2,3] optical devices,[4] and catalysts.[5] Alongside experimental investigations, computational studies provide valuable insight into the structure and properties of complex materials. Hexagonal boron nitride (*h*-BN) is a structural analog of graphene, exhibiting both similar and complementary properties.[3,6] A major part of this work is devoted to heterostructures composed of *h*-BN adsorbed on metals. The second, also related, focus area is 2D metal-organic frameworks (MOFs). These structures can be produced and tailored by linking together precursor molecules through metal ions. This gives one very detailed control over the structure and properties of these sheets.

This thesis is subdivided into five chapters. This first chapter outlines the motivation for the presented work and provides an introduction into the investigated materials. The theoretical details underlying Density Functional Theory and Molecular Dynamics are presented in Chapter 2 along with a description of the employed computational set-up. Chapter 3 presents metal-supported *h*-BN, focusing on the electronic corrugation of the material, molecule adsorption and O_2 activation. Chapter 4 describes 2D MOFs prepared by linking precursor molecules on metal surfaces as well as the surface of liquid water, with emphasis on the dynamics of the ligand molecules and the energetics of their aggregation. Finally, Chapter 5 presents conclusions and an outlook to further research.

The rest of this chapter presents the motivation for this work, introduces the state of the art in adsorbed 2D materials, and outlines some concepts and experimental techniques of relevance.

1.1 Motivation

Surfaces and adsorption processes are of prime importance in chemistry, physics, and nanoscience. They can be used to catalyze chemical transformations, align and confine molecules, and can be tuned to influence material properties at the atomic scale. This enables one to design and create versatile nanostructures.[7]

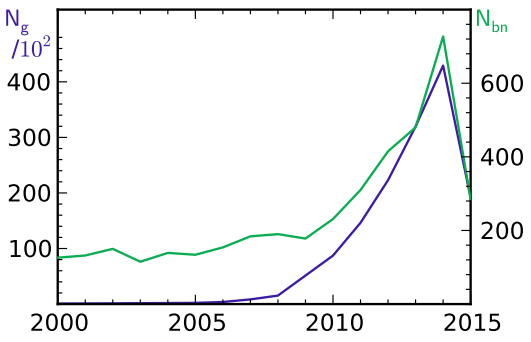

Figure 1.1|Number of articles about graphene (N_g) and *h*-BN (N_{bn}) in Web of Science, 2000 – 2015.

Graphene is a 2D material composed of a single infinite sheet of sp^2-hybridized carbon atoms, essentially a single layer of a graphite lattice. Since the discovery and preparation of free-standing graphene in 2004,[8,9] and the subsequent 2008 Nobel Prize, interest in atomically flat monolayers has risen sharply.[1] Fig. 1.1 shows the number of articles published on graphene per year, between 2000 and 2015. The rapid growth of research activity in this field is remarkable, and new advances are continuously being made. Hexagonal boron nitride (*h*-BN) is isoelectronic and isostructural to graphene, composed of a honeycomb lattice of alter-

nating B and N atoms. Also *h*-BN has experienced a remarkable gain in popularity (Fig. 1.1), although with a lower absolute number of publications than graphene.

A major contribution to the attractiveness of these two materials are their properties and the ease of their fabrication.[10] Graphene is a zero-gap semiconductor with a remarkable electronic structure and extremely high electronic and thermal conductivity.[1,10,11] Furthermore, the material is exceptionally strong, flexible, leightweight and strongly optically absorbant.[10] Producing graphene can be as easy as exfoliating a graphite flake with adhesive tape. *h*-BN is also characterized by a high tensile strength and flexibility, and is additionally chemically inert and electrically non-conductive.[6] In combination with suitable adsorption surfaces, *h*-BN forms diverse heterostructures with useful properties (*vide infra*).

In some instances, however, the properties of these 2D sheets may be unsuitable to a particular application. Another class of sheet-like materials are 2D MOFs, which exhibit an extremely high degree of tunability. They are composed of individual precursor molecules, interlinked by metal ions. Thus, the entire toolbox of organic chemistry can be utilized to fine-tune any properties of the molecule, compounded by the option to choose the linking ions. Furthermore, they can be prepared using chemical methods, at easily accessible temperatures and without the need for complex vacuum equipment.

In order to utilize 2D materials, they need to be designed towards a particular purpose. To control and design them, one needs an in-depth understanding of their formation and properties. Modern characterization techniques such as Scanning Tunneling Microscropy (STM), Atomic Force Microscopy (AFM), spectroscopic methods (angle-resolved photoemission, ARPES, and X-ray absorption, XAS), and diffraction (low-energy electron diffraction, LEED, X-ray diffraction, XRD) can provide valuable high-resolution information on surfaces and 2D structures. While these methods have advanced to considerable maturity, theory and simulations can provide additional crucial insight. Computation offers exquisitely fine control over every aspect of the investigated system. The position of each atom is known and can be modified arbitrarily. Numerous quantities, including spectra and band structures, can be computed and directly compared with experimental data. Thus calculations can serve as a valuable tool for interpreting measurements.

The central theme of this thesis is 2D materials, particularly in combination with adsorption on surfaces. Specifically, the focus is on *h*-BN adsorbed on Cu, in the context of recent experiments that observed a corrugation of the surface using STM, in the absence of topographic buckling.[12] Using very large-scale DFT calculations, we rationalize this result in the presented work.[13] The results also serve to explain the electronic level alignment of adsorbed porphyrin on *h*-BN/Cu.[14] Furthermore, we investigate the catalytic properties of *h*-BN adsorbed on Ni, Co, and Cu, and find that the latter shows promise for use as an oxygen activating catalyst for fuel cell cathodes. Related to 2D MOFs, we study a recent experimental approach to produce extended 2D sheets from monomers confined on a water surface.[15] Using MD simulations, we characterize the dynamic structures of the molecules on the water layer, and investigate the free energy of the formation of monomer-metal complexes and dimers.[16] This knowledge can serve to taylor the properties of monomers and guide the choice of metals in order to optimize the material.

1.2 Two-Dimensional Sheets Adsorbed on Metal Surfaces

Hexagonal Boron Nitride

Replacing all the C atoms in graphene (Fig. 1.2(a)) with alternating B and N yields *h*-BN (Fig. 1.2(b)). In terms of properties, graphene and *h*-BN have both commonalities and contrasts. The in-plane lattice constant of graphene is 2.46 Å and that of *h*-BN is 2.50 Å,[17] giving very similar bond lengths. In both materials all nearest-neighbor distances are the same due to symmetry. In the bulk both materials exhibit layered structures, graphene with an AB stacking and *h*-BN with AA' stacking. Electronically,

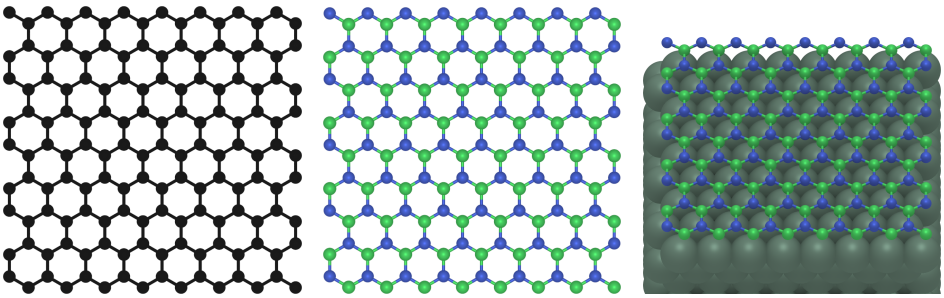

Figure 1.2|Sketch of (a) a single graphene sheet, (b) a single *h*-BN sheet, and (c) an *h*-BN sheet on a metal surface. Atom colors: C, black; B, green; N, blue; metal, grey-green.

graphene is a zero-gap semiconductor, whose band structure is characterized by the peculiar Dirac cone at the K point of the 2D Brillouin zone.[10] In contrast, *h*-BN has a wide band gap of about 6 eV, making it essentially insulating at room temperature.[18,19]

Crystalline *h*-BN has been known and used for a long time, but free-standing single layer sheets have only been fabricated recently.[20] Atomic-resolution characterization of *h*-BN is impeded by the fact that most methods cannot distinguish between B and N atoms, but this limitation could be overcome using high-resolution TEM.[20] Individual layers of *h*-BN are more commonly prepared and characterized on solid supports (Fig. 1.2(c)), especially transition metals (TMs).

Adsorption on Transition Metals

A facile approach to produce atomically thin *h*-BN is through the decomposition of suitable precursor molecules on TMs. Common starting materials are borazine,[21] $(HBNH)_3$ and ammonia borane[22] $H_3N{:}BH_3$, which are brought into contact with a hot substrate (750–1000°C). The molecules then decompose and form an extended sheet. Since the metal catalyzes the reaction the process automatically terminates once the surface is fully covered by a monolayer. Numerous *h*-BN/metal heterostructures have been prepared following this approach, e.g., on Cu(111),[22,23] Ni(111),[24,25] Co(0001),[26] Ir(111),[27] Pt(111),[22] Ru(0001),[28] Fe(110),[29] Ag(111),[30] and Rh(111).[21] By tuning the composition of the substrate it is possible to greatly increase the grain size and thus the crystallinity of the layer.[31]

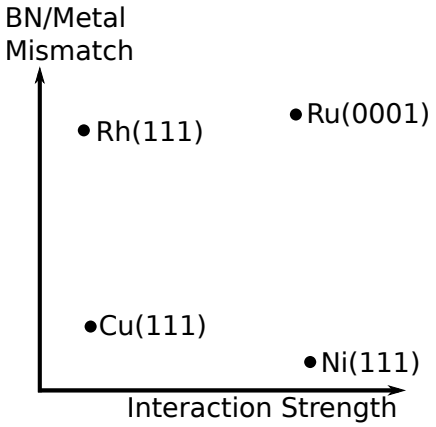

Figure 1.3|Schematic plot of lattice mismatch vs. interaction strength for various metal substrates for *h*-BN.

The choice of the stubstrate profoundly influences the structure of the resulting adsorption system. The properties of the heterostructure are governed by two parameters, the (mis)fit of the *h*-BN and metal lattices, as well as their interaction strength. We define the lattice mismatch between the monolayer and substrate, $\alpha_{s,TM}$, as follows:

$$\alpha_{s,TM} = \frac{a_s - a_{TM}}{a_{TM}}, \tag{1.1}$$

where a refers to the in-plane lattice constant of the sheet and TM, respectively. Metals with low α are, e.g., Ni ($\alpha = 0.78\%$[32]) and Cu ($\alpha = -1.68\%$[32]), while Rh ($\alpha = -6.79\%$[32]) and Ru ($\alpha = -7.4\%$[33]) have high mismatch values. Ni and Ru interact strongly with *h*-BN and Cu and Rh more weakly.[34] This

range of mismatch/interaction strength is visualized schematically in Fig. 1.3, based on *h*-BN adsorption energies from ref. 34 (Section 3.1).

In the case of a large mismatch, the adsorption system has to compensate in order to restore periodicity of the lattice. This results in superstructures with large repeat units. A significant example of this is the *BN nanomesh*, formed by *h*-BN on Rh(111).[21] Due to the strong mismatch, the monolayer is deformed into a periodically corrugated sheet, with 2 nm "pores" of depth 1 Å.[21] After its discovery, numerous further studies examined the nanomesh, both experimentally[35] and computationally.[36–39] Aside from fundamental interest in the properties and formation of the heterostructure, extensive studies of the functionality and applications of the material have also been conducted: The pores of the nanomesh may be used to confine water[40] and catalytic Pd clusters,[41] the surface orients molecules and catalyzes their decomposition,[42] can immobilize atoms under the BN layer[43,44] and can be perforated by ion bombardment to yield circular 2 nm holes.[45]

The substrates examined in this thesis are Ni(111) and Cu(111), with brief consideration also given to Co(0001). Ni(111) is among the most studied supports for *h*-BN. Numerous spectroscopic studies have investigated *h*-BN/Ni(111) to probe its electronic structure and adsorption properties.[23–25,46–51] The relevant results are summarized in Section 3.1. In terms of functionality and chemical activity, recent computational studies suggest significant potential for *h*-BN/Ni(111). Wasey et al. have suggested that the surface favorably adsorbs molecular O_2, with a binding energy of -1.87 eV and a concurrent stretch of the O–O bond by $\sim$0.3 Å.[52] This is sufficient to activate O_2 for the oxidation of gaseous CO.[52] Crucially, free-standing *h*-BN is not active for this reaction. In a related study, Lyalin et al. predict a potential application for *h*-BN/Ni(111) to catalyze the oxygen reduction reaction as it occurs in a fuel cell.[53,54] The surface is found to selectively adsorb particular molecules (O_2, NO_2), but is inactive towards others ($CO_{(2)}$, H_2O, $N_{(2)}O$).[55]

Cu(111) is somewhat less studied as a substrate for *h*-BN adsorption, but has recently received increased attention. From spectroscopy it was conjectured that *h*-BN is much more weakly bound on Cu than on Ni,[23] with almost no change in electronic structure upon adsorption. Extended *h*-BN multi[56]- and monolayers[12,57] can be grown on Cu(111) by chemical vapor deposition. The *h*-BN monolayer on Cu(111) was found to form Moiré patterns of corrugation with long range periodicity, as described in detail in Section 3.2. The material has been shown to be useful for the preparation of large and uniform graphene sheets, which can then be delaminated from Cu along with their BN support and directly used in electronics applications.[58] Furthermore, computational studies indicate the potential of *h*-BN/Cu(111) to activate O_2, similar to Ni(111).[53]

The experimentally and theoretically least characterized heterostructure is *h*-BN/Co(0001). *h*-BN could successfully be grown by decomposition of ammonia borane and characterized with microscopy techniques.[26] The Co(0001) surface has a very similar lattice constant as Ni, and is also chemically comparable. One can thus expect similar activity and properties as shown by *h*-BN/Ni(111).

Adsorption Registries

The *h*-BN layer can be laterally placed in various positions relative to the metal substrate. Most commonly, the monolayer is adsorbed on (111) facets of *fcc*-metals. In that case, the substrate consists of layers that are stacked above one another in an ABC sequence: The second ("*hcp*"-)layer is shifted relative to the first, the third ("*fcc*"-)layer relative to the second, and the fourth layer is at the same lateral position as the first ("*top*"-)layer.

The surface unit cell of the metal has the same periodic structure as the monolayer. Thus, *h*-BN can be placed in various high-symmetry positions laterally. An N atom can be directly above a *top*-layer metal atom, causing the B to reside in a hollow site, either above an atom in the *hcp* or *fcc* layer.

These configurations can be referred to as $N_{top}B_{hcp}$ and $N_{top}B_{fcc}$. Exchanging the atomic species yields the $B_{top}N_{hcp}$ and $B_{top}N_{fcc}$ configurations, analogously. Lastly, N and B may both reside in hollow sites, i.e. $N_{fcc}B_{hcp}$ and $B_{fcc}N_{hcp}$ configurations. To illustrate this concept, the $N_{top}B_{fcc}$ configuration is schematically shown in Fig. 1.4, all others can be deduced by shifting and/or rotating the monolayer.

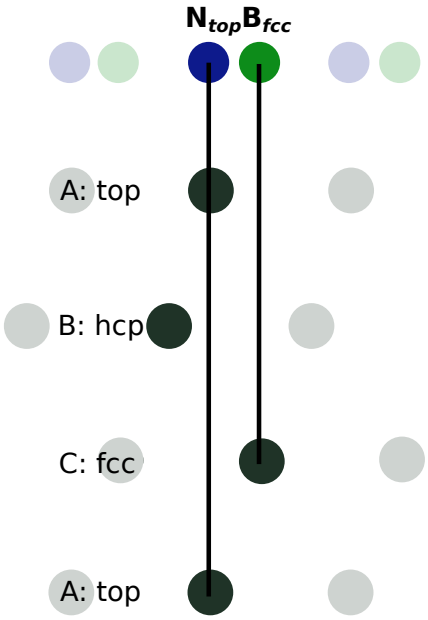

Figure 1.4|Schematic drawing of *h*-BN commensurately adsorbed on a metal surface in the $N_{top}B_{fcc}$ registry. Four metal layers with ABC stacking are shown. Atom colors: B, green; N, blue; metal, grey-green.

Moiré Patterns

Unless the mismatch α of the monolayer and substrate is zero, the two lattices are incommensurate. For small values of α, the BN layer may adapt to the metal and slightly stretch or compress. Larger mismatches need to be compensated by the formation of superlattices. The periodicity of the substrate and of the monolayer combine, or "interfere" to generate a secondary, long range periodicity, leading to the formation of a Moiré pattern.[59] Both the lattice constant mismatch and a possible rotation (by an angle ϕ) of the monolayer affect the properties of this pattern.

Fig. 1.5 shows a series of Moiré patterns generated by placing a monolayer with a particular lattice constant onto a substrate. The commensurate system ($\alpha = \phi = 0$, panel (a)) shows no long range periodicity. Panels (b) and (c) are characterized by different mismatch values, and both exihibit pronounced Moiré patterns. The larger the mismatch, the shorter is the periodicity of the resulting superlattice. The same can be seen in panels (d) and (e), where the monolayer is rotated at different angles. Larger ϕ gives rise to smaller superlattice constants.

A general formula for the lattice constant of the Moiré pattern as a function of mismatch was derived by Hermann:[59]

$$\kappa = \frac{p}{\sqrt{(1-p)^2 + p\phi^2}}, \tag{1.2}$$

where p is the ratio of the surface lattice constants (i.e. $\alpha+1$). κ is termed the Moiré factor, and expresses the lattice constant of the superlattice as a multiple of the substrate lattice constant. Here, the adsorbed monolayer is assumed to remain unmodified by adsorption, i.e. it does not stretch, compress, or buckle.

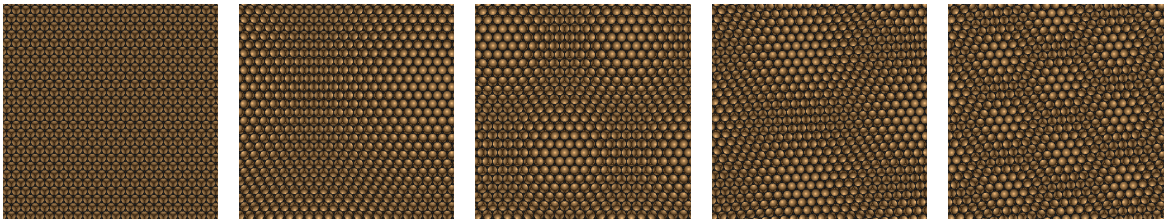

Figure 1.5|Moiré patterns of an adsorbate (black) on a surface (orange) resulting from varying lattice mismatch or rotation: (a) $\alpha = \phi = 0$, (b) $\alpha = 4\%$, (c) $\alpha = 8\%$, (d) $\phi = 4°$, (e) $\phi = 8°$.

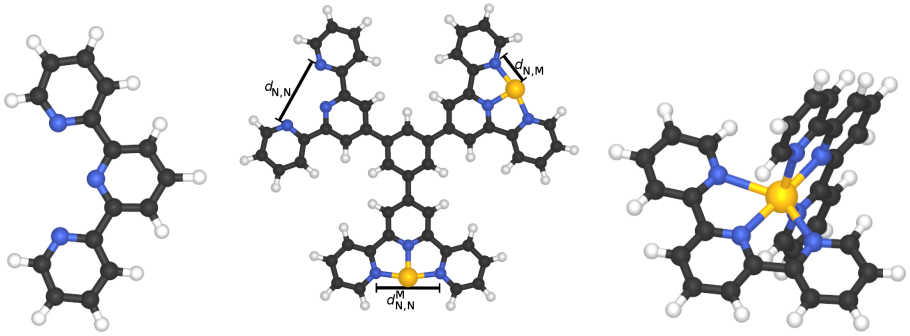

Figure 1.6|(a) Molecular structure of 2,2':6'2" terpyridine (terpy). (b) Sketch of 1,3,5-tris(4'(2,2':6'2"terpyridyl))benzene (TTPB). Two metal atoms bound by terpyridyl groups. N–metal ($d_{N,M}$) and N–N distances ($d_{N,N}$, $d^{M}_{N,N}$) in bound and unbound ligands indicated by black lines. (c) Two terpy ligands coordinating one metal ion. Atom colors: H, white; C, black; N, blue; Metal, yellow.

1.3 Metal-Organic Frameworks and Two-Dimensional Networks

Another class of tailored materials are Metal-Organic Frameworks (MOFs). They are composed of organic molecules connected with metal ions to form a well-defined network (essentially a *coordination polymer*), commonly in three dimensions.[60,61] Countless materials have been prepared with this approach, useful for many applications, e.g., catalysis,[62] gas (hydrogen) storage[63–66] and separation,[67] luminescence,[68] and magnetism.[69] MOFs are highly porous, and thus have large internal surface areas, making them suited for heterogenous processes. Due to the high tunability of both the organic linkers and the metal centers, one has a lot of flexibility in designing MOFs for a specific purpose. Moreover, since 3D MOFs are generally crystalline, characterization by X-ray crystallography is frequently possible.[60] As an example, catalysis in MOFs can be achieved in many different ways: incorporating catalytically active centers into the linker backbone[70] or attaching them to it, encapsulating catalysts in the framework,[71,72] or utilizing metal ions of the network nodes for catalysis.[73]

Frequently used functional groups in the linkers include[61] carboxylates, pyridyls, nitriles, and tertiary amines, which can coordinate to virtually any transition metals. Most commonly MOFs are prepared in solution and obtained as 3D crystals.[74] Thin films of MOFs can also be obtained, using various materials (e.g., silica, alumina, graphite) as support. Films with low regularity have been prepared by immersing the substrate in a solution of the MOF precursors,[75] while well-defined multilayered structures can be created by assembling precursors layer by layer.[74,76] Especially the latter approach is relevant in the context of 2D materials, where MOF membranes could be utilized as tailored functional sheets.

2,2':6',2'-terpyridine ("terpy", Fig.1.6 (a)) is a tricyclic molecule composed of three pyridyl groups. The three nitrogen atoms can coordinate to a metal center, making terpy a versatile tridentate ligand.[77,78] In recent decades, terpy and countless terpy derivatives have received a lot of attention in the context of supramolecular and coordination chemistry.[78] Compounds related to terpy and their metal complexes have been used in luminescent systems such as light-emitting diodes,[79,80] non-linear optical devices,[81,82] chemical sensors[83,84] and catalysts for various reactions in organic chemistry.[78,85]

Molecules incorporating two or more terpy units are of particular interest for the formation of linear polymers and sheet-like 2D MOFs, respectively. Extended chain-like oligo- and polymers have been prepared based on ligands containing two terpyridyl units separated by a spacer.[78] Two synthetic routes for these materials are possible: one can either polymerize bis-terpy metal complexes, or link bis-terpy

ligands with metal ions. Both of these approaches have been successful.[78] Extending this concept to molecules containing more than two terpy units (i.e. "dendrimers"), one can form metal-bridged sheets with tunable properties.

1,3,5-tris(4'(2,2':6',2"terpyridyl)) benzene (TTPB, Fig.1.6 (b)) incorporates three terpy units around a central phenyl ring (the 4'-phenyl-terpy fragment is referred to as a Kröhnke-type terpyridine[78]). The molecule is topologically planar (having only sp^2 centers), contains 10 rings connected by a total of 9 rotatable single bonds, and has 93 atoms giving a molecular weight of 771.9 g·mol^{-1}. Each of the "arms" of the terpyridyl groups can twist around the single bond to the central pyridyl, and adopt a *cis* or *trans* conformation. The terpy units can rotate around their bonds to the central phenyl ring. Two terpy moieties on different TTPB molecules can coordinate to one metal atom, forming a (distorted) octahedral coordination environment as shown in Fig.1.6 (c).

TTPB is a very practical building block for 2D MOFs, as described in detail in Section 4.1. It can be evaporated onto solid substrates, co-adsorbed with metal ions, and thus form a large 2D network. Furthermore, it is also a suitable model for monolayered MOFs prepared by confining precursor molecules on a liquid water surface and linking them with ions from the liquid phase (Section 4.1).

1.4 Research Questions

Recognizing the need for fundamental insight into the properties of 2D materials and adsorption systems, this thesis explores and seeks to answer a number of questions in two general areas: *Metal-supported h-BN* and *2D MOFs assembled on liquid and solid substrates*. The aim of this work is to (1) help to interpret and rationalize experimental results and (2) investigate new applications and new materials with improved functionality. The following chapters and their underlying publications address and answer a number of questions related to the two topic areas:

Metal-Supported h-BN

- What are the general properties of *h*-BN on metals, and can they be modelled with dispersion-corrected DFT?[34,86]
- Where does the electronic corrugation of *h*-BN/Cu(111) originate from?[12,13]
- What is the influence of this corrugation on adsorbed molecules?[14]
- How reactive is metal-supported *h*-BN towards gaseous species such as O_2?[86]
- What is the potential of *h*-BN/metal heterostructures as oxidation catalysts?[86]

2D MOFs on Water

- What are the properties of TTPB adsorbed on Au(111) and Cu(111)?
- What influence does the liquid substrate have on the structure of TTPB and *vice versa*?[16]
- How does the uptake of Zn^{2+} ions proceed from the liquid phase to surface-confined TTPB?[16]
- What is the free energy surface of this process?[16]
- How does formation of a metal-bridged dimer or network change the properties of TTPB and what influence does the water surface have?
- What is the free energy gain associated with forming a TTPB dimer?

2

Computational Methods

2.1 Density Functional Theory

This section briefly introduces the main underlying concepts of Density Functional Theory (DFT). After a cursory overview of the Kohn-Sham approach, some emphasis is placed on the particular approximations for the exchange-correlation energy ("XC functionals") that are used in this work. In this context a method for estimating the error of DFT calculations based on an ensemble of XC energies is introduced. The final part of this section describes the various approaches used to account for van der Waals interactions, which are not captured well with standard DFT.

Basics of Density Functional Theory

The foundation of all of (nonrelativistic) quantum mechanics is the Schrödinger equation. In its time-dependent form it reads[87]

$$\hat{H}(\vec{r},t)\Psi(\vec{r},t) = i\hbar\frac{\partial\Psi(\vec{r},t)}{\partial t}\,, \tag{2.1}$$

where $\hat{H}$ is the Hamiltonian and $\Psi(\vec{r},t)$ the wavefunction of the system. In bound systems where the potential energy is independent of time, also the Hamiltonian becomes time-independent and the wavefunction can be separated,

$$\Psi(\vec{r},t) = \Psi(\vec{r})\exp(-iEt)\,. \tag{2.2}$$

The time dependency can thus be written as a simple phase factor, which can be neglected in time-independent problems. One thus arrives at the time-independent Schrödinger equation,

$$\hat{H}(\vec{r})\Psi(\vec{r}) = E\Psi(\vec{r})\,. \tag{2.3}$$

In a system composed of n electrons and m nuclei, the Hamiltonian is given by the following equation:

$$\hat{H}(\vec{r}) = -\frac{1}{2}\sum_{i=1}^{n}\nabla_i^2 - \frac{1}{2}\sum_{A=1}^{m}\frac{1}{M_A}\nabla_A^2 - \sum_{i=1}^{n}\sum_{A=1}^{m}\frac{Z_A}{r_{i,A}} + \sum_{i=1}^{n}\sum_{j>i}^{n}\frac{1}{r_{i,j}} + \sum_{A=1}^{m}\sum_{B>A}^{m}\frac{Z_A Z_B}{r_{A,B}}\,, \tag{2.4}$$

containing the kinetic energy of electrons and nuclei and the Coulomb interactions between nuclei and electrons, electrons and electrons, and nuclei and nuclei.[88] $r_{\alpha,\beta}$ is a short notation for $|\vec{r}_\beta - \vec{r}_\alpha|$, where $\vec{r}_\alpha$ and $\vec{r}_\beta$ are position vectors of two particles, electrons or nuclei. M_A and Z_A refer to the mass and core charge of atom A. The above equations, as well as all of the following are expressed in atomic units. The square of the wavefunction can be interpreted as a probability of finding an electron at a particular point $\vec{r}$.

Atomic nuclei have a much greater mass than electrons and thus move at much slower velocities. Therefore, electronic and nuclear motions occur on two different timescales. The *Born-Oppenheimer*

approximation makes use of this fact and assumes a full separation of these degrees of freedom. Ψ is factorized into electronic and nuclear parts, and electrons are subject to the potential exerted by a set of stationary nuclei. The wavefunction thus depends *explicitly* on the position of the electrons and *parametrically* on the positions of the nuclei. $\hat{H}$ simplifies to[89]

$$\hat{H}(\vec{r}) = -\frac{1}{2}\sum_{i=1}^{n}\nabla_i^2 - \sum_{i=1}^{n}\sum_{A=1}^{m}\frac{Z_A}{\vec{r}_{i,A}} + \sum_{i=1}^{n}\sum_{j>i}^{n}\frac{1}{\vec{r}_{i,j}} \tag{2.5}$$

$$= \hat{T} + \hat{V}_{ne} + \hat{V}_{ee}\,. \tag{2.6}$$

The internuclear repulsion is added once the electronic energy E_{el} has been determined with this Hamiltonian, to yield the total energy:

$$E_{tot} = E_{el} + \sum_{A=1}^{m}\sum_{B>A}^{m}\frac{Z_A Z_B}{R_{A,B}}\,. \tag{2.7}$$

The electron density $\rho(\vec{r})$ of a system, i.e. the number of electrons per unit volume is given by the following expression, based on the wavefunction:[89]

$$\rho(\vec{r}) = n\int\cdots\int|\Psi(r_1, r_2, \cdots r_n)|^2 dr_2 dr_3\cdots dr_n\,. \tag{2.8}$$

ρ is a function of only 3 spatial coordinates, x, y and z, drastically reducing the $3n$-dimensionality of Ψ. Integration of ρ over all space yields the total number of electrons,

$$\int\rho(\vec{r})d\vec{r} = n\,. \tag{2.9}$$

If the density could be used directly in electronic structure calculations, rather then the complicated many-dimensional wavefunction, the computational complexity of quantum mechanics could be immensely reduced.

According to the first *Hohenberg-Kohn theorem*,[88,90] the electron density uniquely determines the Hamiltonian, and therefore all properties of a system. The ground state energy is a functional of the ground state density, and can be decomposed into its constituents,

$$E_0[\rho_0] = T[\rho_0] + E_{ee}[\rho_0] + E_{ne}[\rho_0]\,, \tag{2.10}$$

where T is the electron kinetic energy, and E_{ee} and E_{ne} are the potential energies due to electron-electron and electron-nuclei interaction. The first two terms are independent of the nuclear positions and charges, and are collectively termed the Hohenberg-Kohn functional, F_{HK}. If this functional were known, it would be possible to solve the Schrödinger equation of the system exactly. However, for all but the most simple systems,[91] F_{HK} is unknown and can only be approximated.

The second Hohenberg-Kohn theorem is the first step towards putting density-based calculations in practice. According to this theorem, E_0 is minimal only for the true ground-state density ρ_0.[88,90] In other words, the energy is variational with the input density, $\tilde{\rho}$,

$$E_0 \leq E[\tilde{\rho}]\,. \tag{2.11}$$

Any input density will be an upper bound to the true ground-state density, and ρ_0 can be found by minimizing $E[\tilde{\rho}]$.

The problem has now been reduced to finding a trial density and iteratively changing it until the minimal energy has been reached. A convenient way to do this is the *Kohn-Sham Method*.[92] This approach (re)introduces a set of non-interacting orbitals $\{\phi_i\}$, which make up a wavefunction represented

as a Slater determinant. The orbital energies are determined by the one-electron Kohn-Sham operator:

$$\hat{f}_{\mathrm{KS}}\phi_i = \epsilon_i\phi_i\,, \tag{2.12}$$

$$\hat{f}_{\mathrm{KS}} = -\frac{1}{2}\nabla^2 + V_s(\vec{r})\,. \tag{2.13}$$

The effective potential V_s now has to be chosen in such a way that the density resulting from the summation of the Kohn-Sham orbitals equals the true ground state energy of the system of interacting electrons.[88]

The total ground-state energy in Kohn-Sham DFT is given by

$$E[\rho(\vec{r})] = T_S[\rho] + J[\rho] + E_{\mathrm{XC}}[\rho] + E_{\mathrm{ne}}[\rho]\,. \tag{2.14}$$

The non-interacting kinetic energy T_S can readily be computed from the Kohn-Sham orbitals, as can the electron-electron term $J[\rho]$ and the electron-nuclear term E_{ne}. No explicit form for the E_{XC} term, the exchange correlation energy, is known. This quantity contains the residual electron kinetic energy (the difference between the non-interacting and "true" T) as well as exchange and correlation energies and a self-interaction correction.[88] E_{XC} is determined from the corresponding XC potential, ϵ_{XC}:

$$E_{XC} = \int \rho(\vec{r})\epsilon_{XC}(\vec{r})\,. \tag{2.15}$$

The following section discusses the exchange-correlation contribution in greater detail.

Exchange-Correlation Functionals

Any practically usable implementation of DFT requires a sufficiently accurate approximation to $E_{XC}[\rho(\vec{r})]$. The last four decades have seen a lot of effort in developing XC functionals of increasing quality and sophistication. Following a scheme by Perdew, XC functionals can be classified in a hierarchy, the "Jacob's Ladder" of density functional approximations.[93] At the lowest rung of this ladder ϵ_{XC} depends only on the value of the density at a given point in space, $\rho(\vec{r})$, termed the *Local (Spin) Density Approximation (LSDA)*. One step higher, ϵ_{XC} also depends on the gradient of the density, $\nabla\rho(\vec{r})$, constituting the *Generalized Gradient Approximation (GGA)*. As a further step towards higher accuracy, *meta-GGA* functionals include also the orbital kinetic energy density τ, or the Laplacian of the density.[93] The final rungs of the ladder contain fully nonlocal approximations: *hyper-GGA*, include the exact exchange energy density, and the random-phase approximation adds unoccupied orbitals.[93] In practice, GGA functionals, with the inclusion of possible corrections and improvements, are generally considered a good compromise between computational cost and accuracy for applications in materials science with systems of more than a few atoms. In the rest of this section, we therefore focus on the few GGA functionals used in this work.

Different strategies may be applied when designing XC functionals.[94,95] Firstly, fully non-empirical functionals are derived by requiring a particular approximation to satisfy certain constraints that are known to apply to the universal density functional. Such constraints might include sum rules for the exchange and correlation holes, scaling relations, and correct asymptotic behavior.[88] The PBE[96] functional is a well-known approximation of this type. Secondly, one can fit sufficiently flexible analytic functions to experimental or quantum chemical reference data, in a slightly empirical spirit.[94] One example of this approach is the BEEF-vdW[97] functional described below, but many other functionals have also been reported.[98–100] Thirdly, functionals can also rely on a mixture of these approaches, such as fitting to reference data, while still respecting some constraints. The revised PBE functional, for instance, forsakes one rigorously defined parameter from PBE in favor of a fitted one, leading to a claimed factor 10 improvement for atomic total energies (*vide infra*).[101]

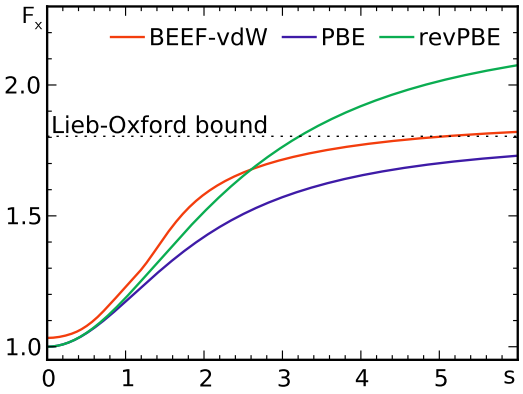

Figure 2.1|Exchange enhancement factors F_x of the PBE,[96] revPBE,[101] and BEEF-vdW[97] functionals as a function of reduced density gradient s.

As a first improvement on the LDA, the *Generalized-Gradient Approximation* methods use the gradient of $\rho(\vec{r})$ as an additional variable in the integral kernel. As was already the case for LDA, E_{XC} is typically split into E_X and E_C, which are determined independently (eq. 2.16). The gradient typically enters the expressions in the form of the *reduced density gradient* $s(\vec{\rho})$ (eq. 2.17):

$$E_{XC}^{\mathrm{GGA}} = E_X^{\mathrm{GGA}}[s] + E_C^{\mathrm{GGA}}[s]\,, \tag{2.16}$$

$$s(\vec{r}) = \frac{|\nabla\rho(\vec{r})|}{\rho^{4/3}(\vec{r})}\,. \tag{2.17}$$

The GGA exchange energy is typically expressed as a factor multiplied on top of the E_X from LDA,

$$E_X[s] = \int \rho\epsilon_X^{\mathrm{LDA}}(\rho)F_X(s(\vec{r}))d\vec{r}, \tag{2.18}$$

where $F_X(s(\vec{r}))$ is usually referred to as the exchange enhancement factor. In the zero-gradient limit, F_X should approach 1, to recover the LDA behavior. An upper bound to F_X was given by Lieb and Oxford, with a value of 1.804.[102]

PBE and revised PBE

The PBE functional, proposed by Perdew, Burke and Ernzerhof, is fully based on obeying physical constraints, containing no empirical parameters.[96] It is an improvement on the PW91-GGA,[103] chosen to satisfy fewer conditions in order to allow more flexibility in reproducing the features of the exact functional. The functional provides separate expressions for E_X and E_C, and the form of the exchange enhancement factor is shown in Fig. 2.1 and in the following equation:

$$F_X(s) = 1 + \kappa - \frac{\kappa}{1 + \frac{\mu s^2}{\kappa}}\,, \tag{2.19}$$

where $\kappa = 0.804$ and $\mu = 0.21951$. F_X reduces to the LDA in the low-gradient limit and obeys the Lieb-Oxford bound[96,102] at large s.

The original paper finds no significant improvement of the accuracy of PBE relative to PW91. However, the ease of implementation and the fully non-empirical origin of all parameters have since made PBE the most commonly used XC functional in solid-state physics and materials science.[95,104]

In a comment on the original PBE publication, Zhang and Yang[101] proposed a different choice of the parameter κ in the exchange term of PBE, resulting in a new functional termed *revised PBE* (revPBE).

They choose $\kappa = 1.245$, based on data fitted to exact-exchange energies for the noble gases He, Ne and Ar. This taints the originally fully non-empirical character of the functional. However, the mean absolute error in atomic total energies was shown to decrease by a factor of 10 relative to the original PBE formulation. For comparison, F_X of revPBE is also plotted in Fig. 2.1.

By tuning the parameters in the PBE form, one can in principle generate a multitude of different PBE-like functionals,[104] and many have been proposed beyond revPBE. Among these, PBEsol[105] and RPBE[106] are more commonly used. A recent study highlighted a fairly large variation between lattice constants computed with different PBE flavors,[104] but concluded that none of them represents a universal improvement over the others.

BEEF-vdW

Numerous studies have evaluated XC functionals for their accuracy for particular systems.[32,104,107–109] Depending on the problem at hand, different functionals exhibit very different errors, and no universally accurate functional is available. The ability to estimate the error of a given DFT calculation is thus a very important feature that greatly raises confidence in a functional. The van der Waals-corrected *Bayesian Error Estimation Functional* (BEEF-vdW) provides a convenient way to quantify the accuracy of the calculation using a large ensemble of computed XC energies.[97]

BEEF-vdW is predominantly designed for applications in surface science, following an advanced fitting approach using regularization and validation methods from machine learning. The functional is of the GGA-type and includes an additional nonlocal correlation term to account for van der Waals interactions. Numerous data sets were used in the construction of the functional, in order to allow the model to accurately describe many different types of interactions: The G3/99 data set of molecular formation energies,[110] the RE42 data set of reaction energies, the DBH24/08 data set of reaction barriers,[111] the S22 set of noncovalent interactions[112,113] (including potential energy curves), the CE17 set for chemisorption on solid surfaces and several data sets of solid state structures.[97]

The exchange enhancement factor F_X is expressed as a linear combination of Legendre polynomials B_m up to a degree $m = 30$, as a function of a modified reduced density gradient,

$$t(s) = \frac{2s^2}{4 + s^2} - 1\,, \tag{2.20}$$

giving:

$$F_X(s) = \sum_m a_m B_m[t(s)]\,. \tag{2.21}$$

Additionally, the correlation energy is expressed as a mixture of PBE and LDA correlation terms, as well as the nonlocal correlation energy computed with the vdW-DF2 functional. The BEEF-vdW XC energy is thus

$$E_{XC}^{\mathrm{BEEF-vdW}} = \sum_m a_m E_{X,m}^{\mathrm{BEEF}}[s] + \alpha_c E_C^{\mathrm{LDA}} + (1 - \alpha_c) E_C^{\mathrm{PBE}} + E_C^{\mathrm{vdW-DF2}}\,, \tag{2.22}$$

containing a total of 31 parameters $[a_0 \ldots a_{29}, \alpha_c]$. They are fitted by minimizing a cost function containing an error term (deviation from the reference data) and a regularization term (to penalize spurious "wiggling" of the parameters and thus reduce overfitting). The final functional has $\alpha_c \approx 0.6002$ and the form of F_X shown in Fig. 2.1. At $s = 0$, the LDA limit, F_X does not precisely obey the theoretical requirement of $F_X(0) = 1$, but overshoots by 3.4%. For large s, F_X is only slightly greater than what would be required by the Lieb-Oxford bound. The curvature of the exchange enhancement factor is slightly different from that of the previously discussed functionals, and a change in slope can be seen at $s \approx 1.3$.

The employed form of F_X is sensitive to changes in the expansion coefficients a_m. By varying them, one can arbitrarily generate a "new" XC functional. The reliability of a DFT calculation can be assessed by comparing a number of functionals for the same system, and the generated set ("ensemble") of functionals differing in a_m allows one to do this in a systematic way, if the coefficients are chosen systematically. This can be exploited to estimate the error of the functional in the following way: A perturbation δa is applied to the set of coefficients a_m. The magnitude of δa is proportional to a "Boltzmann factor" based on its influence on the cost function. The ensemble is generated by constructing 2000 perturbed new sets a_m, from random numbers following a normal distribution. The spread of the ensemble model predictions is chosen to reproduce the known computational errors for the training set. F_X can then be evaluated for all a_m non-selfconsistently for an available converged density, yielding a set of XC energies. The standard deviation over these energies then gives a measure of the confidence in the calculated results.[97]

BEEF-vdW has proven valuable for a number of problems in surface science and catalysis, particularly for its error estimation capabilities. The original publication focused on graphene adsorption on Ni(111) and trends in adsorption and surface energies of CO on TMs[97] as case studies. The functional's accuracy was found to be similar to that of other GGAs, with the additional benefit of computing confidence intervals for the results. Further studies of reactions in ammonia synthesis[114] showed the uncertainty of results to strongly depend on reaction conditions and catalyst materials. For this application the BEEF-vdW ensemble originally presented was modified to more strongly emphasize chemisorption energies in the training data. Consequently, errors obtained with the original ensemble are scaled by a factor 0.684. Using the BEEF-vdW functional provides a straightforward and robust way to estimate the error on calculated energies at negligible computational cost.

Van der Waals Interactions in DFT

Weak interactions are of particular importance in nanoscience. Many molecules on surfaces are only physisorbed or weakly chemisorbed, with interactions governed by hydrogen bonding and van der Waals interactions. H-bonds form between permanent dipoles and are thus electrostatic in nature. This is generally well-reproduced in DFT.[88] In contrast, dispersion or van der Waals interactions occur between induced dipoles, and are not captured by DFT. In the long range limit, binding energy curves calculated with DFT decay exponentially with $r_{A,B}$, rather than proportional to $\frac{1}{r_{A,B}^6}$, which is the correct behavior of van der Waals interactions.[95] Due to the predominance of these forces in the regimes at interest, they cannot be neglected, so that one is forced to use approximations and corrections beyond DFT.

In analogy to Perdew's Jacob's Ladder, dispersion corrections have also been categorized in a hierarchy ("Stairway to Heaven") based on their complexity and expected accuracy.[115] Simple force fields occupy the first step of this stairway, followed by force field approaches that utilize environment-dependent coefficients. The third step in accuracy and complexity are van der Waals functionals, which compute nonlocal correlation within DFT. Finally, the most involved methods to calculate dispersion include many-body dispersion and the random phase approximation.[115] The following sections briefly introduce the first through third levels of this hierarchy, and approaches based on levels 2 and 3 are used in the rest of this work.

Pair Potential-Based Dispersion Correction

A way to correct for the missing dispersion interactions is to include (pairwise) force field terms on top of the interactions computed with DFT.[95,116] Generally, the dispersion energy is expressed as

$$E_{\mathrm{vdW}} = -\frac{1}{2}\sum_{A,B} f_{\mathrm{damp}}(r_{A,B}, r_A^0, r_B^0) C_{6,AB} r_{A,B}^{-6}\,, \tag{2.23}$$

where f is a damping function, r^0 stands for the van der Waals radius of an atom, and $C_{6,AB}$ is the coefficient for the A-B interaction.[117] Since r^{-6} diverges for $r \to 0$, the damping function has to push E_{vdW} to zero for small interatomic separations. A simple force field does not depend and has no effect on the electronic structure, and its parameters have to be fitted to reference data. Furthermore, one has to balance the force field contributions with those from the XC functional, in order to avoid overbinding or a wrong correction at short range.

This approximation can be improved by introducing environment-dependent coefficients into the force field. Several approximate dispersion corrections based on this have been developed with varying degrees of empiricism. Two popular and recent schemes are the Tkatchenko-Scheffler (TS)[117] and Grimme DFT-D[118,119] methods.

The TS method computes the C_6 coefficients from the ground-state density and thus has no empirical parameters.[117] Starting from the exact expression for $C_{6,AB}$,

$$C_{6,AB} = \frac{3}{\pi}\int_0^\infty \alpha_A(i\omega)\alpha_B(i\omega)d\omega\,, \tag{2.24}$$

with $\alpha(i\omega)$ the frequency-dependent polarizability of an atom, the authors derive a formula for computing an effective C_6 coefficient for an atom in a molecule. This $C_{6,AA}^{\mathrm{eff}}$ is computed by scaling an accurately determined C_6 coefficient for a free atom, $C_{6,AA}^{\mathrm{free}}$,

$$C_{6,AA}^{\mathrm{eff}} = \left(\frac{V_A^{\mathrm{eff}}}{V_A^{\mathrm{free}}}\right)^2 C_{6,AA}^{\mathrm{free}}\,, \tag{2.25}$$

where the volume of the effective atom in the molecule V_A^{eff} is computed from a Hirshfeld partitioning of the electron density. The *inter*atomic coefficients $C_{6,AB}$ are then computed with a combination rule,

$$C_{6,AB} = \frac{2C_{6,AA}C_{6,BB}}{\frac{\alpha_B^0}{\alpha_A^0}C_{6,AA} + \frac{\alpha_A^0}{\alpha_B^0}C_{6,BB}}, \tag{2.26}$$

where α^0 is the static polarizability of an atom, taken from reference data.[117] Coupled with a suitable damping function, these calculated $C_{6,AB}$ coefficients can be used to define an almost fully non-empirical force field for van der Waals correction according to eq. 2.23. The TS method has been shown to significantly improve interatomic distances and binding energies over those computed with non-corrected functionals for various systems.[120] However, the method does not allow for a straightforward computation of the dispersion contribution to the interatomic forces.

Another family of force field based van der Waals corrections was introduced by Grimme et al., called the DFT-D, -D2 and -D3 methods. The initial formulation, DFT-D,[121] uses the following expression for the dispersion energy:

$$E_{\mathrm{disp}} = -s_6 \sum_{A,B}^{A<B} \frac{C_{6,AB}}{R_{A,B}^6} f_{\mathrm{damp}}(r_{A,B})\,. \tag{2.27}$$

This is essentially equivalent to eq. 2.23, with the exception of a scaling factor s_6, that is chosen according to the employed XC functional. The damping function is chosen to decay fast when $r_{A,B}$ is less than

the sum of the two atoms' van der Waals radii, so that interactions that are captured by DFT are not double-counted with the DFT correction. The diatomic dispersion coefficients $C_{6,AB}$ are also calculated from atomic C_6 coefficients with a combination rule. C_6 parameters for this method were obtained from a previous van der Waals correction by Wu and Yang,[116] determined by fitting to molecular data.

Two years after the introduction of DFT-D, a first "upgrade" was published, called the DFT-D2 method. The authors aimed to address issues with basic DFT-D, such as the lack of atomic parameters for elements beyond the second row, and inconsistencies in thermochemistry calculations.[118] The employed form of the pair potential remains the same as in DFT-D, but the parametrization was significantly revised. Particularly, a new combination rule of atomic coefficients with a geometric mean was introduced, and thus the functional-dependent s_6 coefficients were updated. The $C_{6,AA}$ coefficients were recomputed based on the London formula,

$$C_{6,AA} = 0.05 N I_A \alpha_A \,, \tag{2.28}$$

where N depends on the row of the periodic table in which element A is found, I is the atomic ionization potential and α the polarizability. The value 0.05 is a "fudge factor" adjusted to reproduce reference C_6 coefficients. Of particular note is how the coefficients are calculated for TMs. Rather than computing them from first principles according to eq. 2.28, they are set to the average C_6 coefficent of the preceding group VIII and following group III elements. The authors remark that the error of this approximation is negligible as long as the number of metal atoms in the system is small relative to the total number of atoms.[118] Furthermore, the C_6 coefficients are still treated as constant, without adjustment to the local environment of the atoms. This remains a significant source of error, since the C_6 coefficients depend on the hybridization of the atoms.

The third version, DFT-D3, is a further improvement over the preceding methods.[119] The method is less empirical, asymptotically correct and available for all elements. It explicitly determines atom pair-specific C_6 coefficients and uses coordination-number dependent coefficients to account for the chemical environment of an atom.[119] The coefficients $C_{6,AB}$ are computed for pairs of atoms from calculations of reference molecules (hydrides) using time-dependent DFT. The inclusion of environment-dependent dispersion coefficients is a major improvement over the D and D2 methods, and brings DFT-D3 on a comparable level with the TS approach. The D3 method uses the coordination number n_A (from a counting function) of an atom to quantify its environment,

$$n_{\mathrm{A}} = \sum_{\mathrm{A}\neq\mathrm{B}} \frac{1}{1+\exp(-k_1(k_2(R_A^{\mathrm{cov}}+R_B^{\mathrm{cov}})/r_{A,B}-1))}, \tag{2.29}$$

with R^{cov} the covalent radius of the elements, $k_1 = 16$ a steepness parameter, and $k_2 = 4/3$ a scaling factor for the covalent radii. Furthermore, R^{cov} are reduced by 10% for all metallic elements. The value of $C_{6,AB}$ is then calculated with a two-dimensional interpolation scheme,

$$C_{6,AB}(n_A, n_B) = \frac{Z}{W} \,, \tag{2.30}$$

$$Z = \sum_i^{N_A}\sum_j^{N_B} C_{6,AB}^{\mathrm{ref}}(n_A, n_B) L_{ij} \,, \tag{2.31}$$

$$W = \sum_i^{N_A}\sum_j^{N_B} L_{ij} \,, \tag{2.32}$$

$$L_{ij} = \exp(-k_3[(n_A - n_{A,i})^2 (n_B - n_{B,j})^2]) \,, \tag{2.33}$$

where N_A and N_B are the number of reference molecules for the atoms and $n_{A/B,j}$ are the coordination numbers of A or B in that reference molecule. Thus, the interatomic C_6 coefficients can be computed

for all elements in all bonding environments from the tabulated reference $C_{6,AB}$ values. The explicit calculation of the coordination numbers for each atom can be replaced by a predefined value specified as an input parameter from chemical knowledge of the system.

In addition to the $C_6 \cdot r^{-6}$ term, the D3 method also includes a higher-order $C_8 \cdot r^{-8}$ term.[119] The values of $C_{8,AB}$ are computed by scaling the $C_{6,AB}$ coefficients. Furthermore, a C_9 three-body term is also (optionally) part of the D3 approach. The final expression for the D3 energy correction is thus

$$E_{\text{disp}} = \sum_{A,B}^{A<B} \sum_{n=6,8} s_n \frac{C_{n,AB}}{R_{A,B}^n} f_{\text{damp},n}(r_{A,B}) + \sum_{ABC} f_{\text{damp},n}(\bar{r}_{ABC}) \frac{C_{9,ABC}(3\cos\theta_a \cos\theta_b \cos\theta_c - 1)}{(r_{AB} r_{BC} r_{CA})^3} \,. \tag{2.34}$$

$C_{9,ABC}$ is computed from the C_6 coefficients of the three atom pairs, s_6 is unity and s_8 is adjusted according to the XC functional used in combination with the method.

Compared to non-corrected DFT, DFT-D3 improves the mean absolute error for reference databases of non-covalent interactions by an order of magnitude and by up to a factor of 2 relative to DFT-D2.[119]

Nonlocal Correlation Functionals

An approach beyond classical pair potentials is to explicitly include nonlocal correlation effects, and compute dispersion interactions from there.[115] An obvious advantage of such methods is that they do not rely on precomputed parameters, but operate exclusively on the data intrinsically available from the DFT calculation at hand. The general expression for the non-local correlation energy E_c^{nl} is

$$E_c^{\text{nl}} = \int\int d\vec{r}_1 d\vec{r}_2 \rho(\vec{r}_1)\phi(\vec{r}_1,\vec{r}_2)\rho(\vec{r}_2) \,. \tag{2.35}$$

$\phi(\vec{r}_1,\vec{r}_2)$ is an integration kernel, with asymptotic behavior $\sim r_{1,2}^{-6}$.[115] This approach was first introduced by Langreth and Lundqvist,[122] but was initially only applicable to isolated fragments. Subsequently, Dion et al.[123] extended this method to work also for arbitrary geometries, termed the vdW-DF functional. The approach uses a pretabulated kernel ϕ in eq. 2.35. However, vdW-DF has a tendency to overbind in the long-range regime, as it overestimates C_6 coefficients.[115,124]

A subsequent improvement to address the overbinding issue is the vdW-DF2 functional.[125] It uses a more accurate exchange functional and a gradient correction in determining the kernel ϕ. vdW-DF2 has been shown to reproduce reference potential energy curves of van der Waals complexes quite well, and binding energies are within 0.05 eV of reference values for most of the benchmarked systems.[125] Further studies highlighted a good accuracy of vdW-DF2 also in a surface science context, for the adsorption of hydrogen on Cu(111).[126]

2.2 Molecular Dynamics

Typical *static* DFT calculations yield ground-state energies, forces and properties of systems consisting of stationary nuclei at zero temperature. Optimization techniques can be employed to find (local) minima corresponding to stationary points on this energy surface, in order to obtain quantities like relative energy differences and determine equilibrium bond lengths. Many materials properties, however, are of a dynamical nature, and thus cannot be properly described by such a static approach.

Condensed-phase systems at finite temperature (i.e. chiefly liquids) need to be treated with simulation methods that sample the phase space at finite temperature. In this context, both *Monte Carlo* (MC) and *Molecular Dynamics* (MD) methods are commonly employed. The former is a stochastic approach based on acceptance/rejection of trial moves, requiring only the computation of total energies, and yielding only time-averaged properties. This section, as the rest of the thesis, is concerned with the

latter, where – based on calculated forces – a system evolves in time, yielding a dynamical trajectory, starting from specified initial conditions. One can then extract dynamic properties of the system from this trajectory.

We first describe the basic approach to (classical) MD and then extend the idea to forces computed from quantum mechanical calculations (*ab initio* MD, AIMD). Finally, we briefly describe the *metadynamics* (MTD) method, used to accelerate the sampling of a free-energy surface in order to observe *rare events* in MD and determine energy barriers.

Basics of Molecular Dynamics

In its basic form, MD is concerned with the time evolution of a system of *classical* particles, based on defined interactions between them, starting from initial conditions. One solves Newton's equations for all constituents of the system, and (numerically) integrates them over time. This results in a trajectory of a certain length, an ensemble of configurations that samples the phase space. The trajectory is then analyzed using statistical mechanics to quantify properties of the ensemble.[127]

A system of N particles at a time t is specified by a set of positions $\vec{r}_i(t)$ and momenta $\vec{p}_i(t) = m_i\vec{v}_i(t)$, where m_i is the mass and $\vec{v}_i(t)$ the velocity of each particle $i \in [0 \cdots N]$. The positions of particles at a later time $t + \Delta t$ can be obtained by propagating it[127]

$$\vec{r}_i(t + \Delta t) = \vec{r}_i(t) + \vec{v}_i(t)\Delta t + \frac{\vec{f}_i(t)}{2m}\Delta t^2 + \cdots . \tag{2.36}$$

Here $f_i(t)$ is the force acting on a particle, which is given from the potential that describes the system:

$$\vec{f}_i = -\frac{\partial u}{\partial r} . \tag{2.37}$$

$\frac{\vec{f}_i}{m}$ is equal to $\vec{a}(t)$, i.e. the acceleration of a particle, following Newton's Second Law. This procedure is then repeated until a desired dynamic property of the system has converged, or the available computer time is exhausted. Care has to be taken to choose a sufficiently small timestep Δt to capture all relevant motions of the system and keep the integration numerically stable.

In practice, more stable integration algorithms have to be used, rather than the simple Euler scheme described above.[127] A common approach – also used in this work – is the *Velocity Verlet* algorithm. The positions at time $t + \Delta t$ are computed according to eq. 2.36, and subsequently the new velocities of particles are determined according to

$$\vec{v}_i(t + \Delta t) = v(t) + \frac{\vec{f}_i(t + \Delta t) + \vec{f}_i(t)}{2m}\Delta t\,, \tag{2.38}$$

where $f_i(t + \Delta t)$ is calculated at the new positions $r_i(t + \Delta t)$.

In an MD simulation of a closed system, without interaction with the external environment and with a conservative force field, the total energy E and the total momentum P are constants of motion.[127] Thus, such a simulation samples a microcanonical, i.e. NVE ensemble, where the number of particles, the total volume and total energy remain constant. Assuming *ergodicity*, an average over the entire MD trajectory is equal to an average over all the microstates of the ensemble. In many cases it is, however, convenient to perform a simulation in a different type of ensemble, such as at constant temperature (NVT) or constant pressure (NPT). Here, one typically uses thermostats and/or barostats to maintain a desired temperature and/or pressure. Conceptually, for an NVT ensemble this corresponds to coupling the system to a large heat bath, which adds or removes kinetic energy from a formerly NVE ensemble. A commonly used way to sample an NVT ensemble is the *Nosé-Hoover* thermostat, which is based on an extended Lagrangian formalism to restrain the system to a constant temperature.[127] Frequently, several

Nosé-Hoover thermostats are used together in a chain, improving the ergodicity of the sampling. In an NPT ensemble both heat and work are exchanged with the bath as the cell volume fluctuates during the simulation.

The basic steps to run and evaluate an MD simulation are the following:

1. Prepare the system in an initial configuration.
2. Run an MD trajectory to equilibrate the system. Atoms typically move to lower-energy positions, molecules change conformation and the consituents of a liquid rearrange into dynamically stable positions. The thermostat settles the temperature of the system.
3. Carry out the production run of the MD.
4. Postprocess the resulting trajectory to compute desired properties.

Care must be taken to minimize drift in the course of the simulation, i.e. to ensure the conservation of the constants of motion of the ensemble.

Ab initio MD

The above description does not specify how the forces in the system are computed. As long as all relevant interactions are described by a potential u, the derivative of which yields forces, MD can be used to propagate the system in time and produce a trajectory. In the case of classical MD, u is typically defined as a set of interatomic energy terms (a "force field"), descibring pairwise and many-body interactions. One example of such a potential is the Lennard-Jones potential, containing two parameters, ϵ and σ that can be tuned to describe the atom pair AB in question: [127]

$$u^{LJ}(|\vec{r}_{AB}|) = 4\epsilon \left[\left(\frac{\sigma}{|\vec{r}_{AB}|} \right)^{12} - \left(\frac{\sigma}{|\vec{r}_{AB}|} \right)^{6} \right] . \tag{2.39}$$

A disadvantage of pair potentials is the fact that all interactions between all atoms must be parametrized *a priori*. Any interaction that is not part of the force field cannot be computed, unless the force field is fully re-parametrized for all pairs. Furthermore, qualitative changes of these interactions during the simulation (e.g., bond breaking and formation) cannot be captured. An obvious way to circumvent this problem is to compute the interactions with a general-purpose *ab initio* method that requires no parametrized interactions. [128]

Various schemes to utilize *ab initio* energies and forces in MD have been designed and utilized:

- *Ehrenfest Dynamics*, is based on solving the *time-dependent* Schrödinger equation, while propagating the nuclei using classical mechanics. [128] This method can in principle handle also nonadiabatic transitions between electronic states, but may also be restricted to a single state, typically the ground state.
- *Born-Oppenheimer* MD (BOMD), the method used throughout this thesis, assumes the electrons to be fully decoupled from the nuclear motion, i.e. in the ground state at every MD step. Thus the time-independent electronic Schrödinger equation can be solved independently at each step, and the nuclei subsequently propagated according to the forces obtained from the electronic structure calculation. [128] Essentially, a BOMD trajectory is thus a series of ground-state DFT calculations, with slowly changing atomic coordinates from timestep to timestep.
- The *Car-Parinello* (CP) method [129] was arguably the first widely employed approach to combine DFT and MD. This method introduces an extended Lagrangian, containing time derivatives of both the orbitals and the nuclear coordinates. Equations of motion are introduced also for the orbitals, which carry a fictitious mass or adiabaticity parameter. [128] Hence, both nuclei and electrons are propagated in time simultaneously, the latter having a ficititous "temperature", i.e. they are not on the the Born-Oppenheimer surface, [129] but suffieciently close.

A significant drawback to AIMD is its considerably increased computational cost. Assuming a simple pair potential, the cost of a classical MD simulation of N particules will scale as N^2 using the most naive approach, and can be brought close to linear scaling for large N using methods such as truncation of interactions, neighbor lists, and cell lists. In contrast the cost of DFT calculations typically scales as n^3 with n being the number of basis functions, generally much larger than N, and the requirement for self-consistency means that typically several SCF iterations will take place during each MD timestep (with the exception of CPMD). Depending on the chosen AIMD method, the chosen MD timestep may also have to be significantly smaller than what is needed in classical MD. In the extreme case of Ehrenfest dynamics, Δt has to be on the timescale of electronic fluctuations, on the order of attoseconds.[130] In CPMD, in order to keep the "hot" electrons sufficiently close to the Born-Oppenheimer surface, a typical value for Δt may be 0.1 fs. BOMD has the advantage that the magnitude of the timestep is determined only by the nuclear motion, since the electronic wavefunction is not propagated, but recomputed at each step. Due to these two factors, cost per step and step length, the overall length of obtainable AIMD trajectories is orders of magnitude shorter than what can be achieved with classical MD.

Metadynamics

Taking advantage of massively parallel DFT implementations, large supercomputers, and algorithmic techniques such as wavefunction extrapolation and the orbital transformation method, systems with $\gg$1000 atoms can be simulated for 10^5 timesteps with AIMD. However, certain fluctuations and processes occur on longer timescales, as they require crossing high barriers or are composed of a small number of microstates, making them statistically unlikely. These phenomena are referred to as *rare events*, and require accelerated techniques to be accessible in MD (unless one is able to simulate sufficiently long time scales for the event to occur spontaneously).

Several options exist for the sampling of rare events: *Thermodynamic Integration*[131] samples a system where one degree of freedom, described by a collective variable (CV), is constrained at several constant values of the CV. The force that the system exerts against the constraint can then be integrated to yield an estimate of the free energy of the system in that macrostate. The *Umbrella Sampling* approach is closely related.[132] Another way to simulate a system crossing a barrier, provided that the initial and final states are known, is *Transition Path Sampling*.[133] Alternative approaches to crossing a high barrier are *Replica Exchange*[134] and *Parallel Tempering*.[135] In both methods, a trajectory is simultaneously evolved at different temperatures, and the coordinates of two trajectories are periodically exchanged with a probability proportional to a Boltzmann factor.

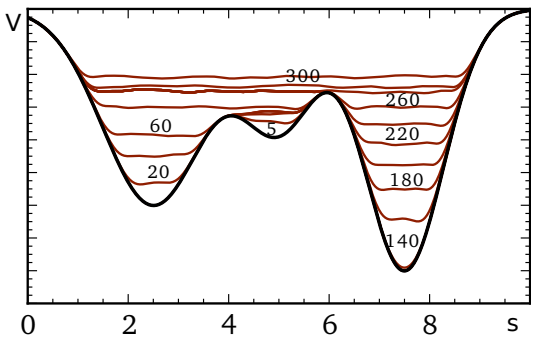

Figure 2.2|Schematic depiction of the metadynamics method in a one-dimensional potential with 3 minima (black line). The bias potential (the sum of deposited Gaussians) at certain time intervals (black numbers) is shown in red. See text for details.

The *metadynamics* method, originally introduced by Parinello and Laio,[136] is a versatile approach to sample free energy surfaces based on a history-dependent bias potential. The FES is described through CVs, several of which can be used simultaneously. The simulation typically starts from an equilibrium in a local minimum in the space of the CVs. As the trajectory progresses, a bias potential is dynamically constructed by placing Gaussian functions ("hills") at positions on the FES.[137] These functions give rise to a force that slowly increases while the system remains in the vicinity of the hills. Eventually, a local minimum in the FES is filled up with Gaussians, at which point the system easily overcomes the barrier, escapes the minimum and falls into

another nearby local minimum. Then this minimum gets filled up and the next one is entered. One assumes that all Gaussians deposited up to a particular time t constitute an unbiased estimator of the FES explored by the trajectory up to that point.[137] Thus, the shape and depth of the FES can be reconstructed from the deposited hills. The advantages of MTD are thus two-fold. Firstly, the trajectory samples rare events, as the system is induced to escape local minima *via* the lowest-lying saddle points. And secondly, the entire FES in the space of the CVs can be reconstructed with arbitrary accuracy from the history-dependent potential.[137]

Fig. 2.2 shows a one-dimensional potential $V(s)$ as a function of a single CV s. The system starts out at the bottom of the central well. As hills are deposited, the minimum slowly fills up until, after about 10 Gaussians have been placed, the system can transition downhill into the leftmost minimum. Subsequently this minimum gets filled up. After deposition of 80 Gaussians, the central and left wells are full, and the system experiences a very flat potential landscape, essentially free to adopt any macrostate with $s \in [1.5, 6]$. Once also this region of the phase space has been filled up, the system drops into the final, rightmost minimum, having now crossed both barriers. This minimum gets progressively filled up, until the FES once again is flat, and the system can oscilate within $s \in [1.5, 9]$. All relevant parts of the FES have now been sampled, and the surface can be reconstructed from the 300 deposited hills.

The total bias potential of a FES with d dimensions (i.e. CVs) is given by[137]

$$V_G(S(x), t) = w \sum_{t>t'=\tau_G, 2\tau_G, \ldots} \exp\left(- \sum_{\alpha=1}^{d} \frac{(S_\alpha(x) - s_\alpha(t'))^2}{2\delta s_\alpha^2} \right) , \tag{2.40}$$

where τ_G is the interval of Gaussian deposition, $S(x)$ is the value of the CVs at time t, $s(t')$ is the position of the hill (in terms of CV) at a time t' in the past and δs^2 is the width and w is the height of the Gaussians. Importantly, the number of Gaussians to fill a well of a particular size is proportional to $\left(\frac{1}{\delta s}\right)^d$, so that the cost of an MTD exploration scales exponentially with the dimensionality of the reduced FES. For a truthful sampling of the process and reliable reconstruction of the FES, w and δs should be as small as possible, while τ_G should be large. Evidently, the higher the desired accuracy, the slower will be the progress in sampling the FES.

A CV can essentially be any continuously differentiable function that maps a particular microstate of the system to a scalar. Common choices include interatomic distances, bond angles, dihedral angles and the like.[138] CVs can also be defined as linear combinations of these individual quantities. A very versatile CV is the coordination number of a particular atom Y around a central atom X, $n_{\mathrm{X,Y}}$, if it changes in the course of the simulated process. It is typically modelled with a distance-dependent counting function,[137]

$$n_{\mathrm{X}} = \frac{1}{N_{\mathrm{X}}} \sum_{\mathrm{X,Y}} \frac{1 - (r_{\mathrm{X,Y}}/r_0)^n}{1 - (r_{\mathrm{X,Y}}/r_0)^m} , \tag{2.41}$$

with the sum running over all X and Y atoms and steepness parameters n and m. More specialized CVs that describe subtle aspects of particular transformations have also been employed.[139] On the other hand, very general CVs such as the potential energy of the system are also useful.[140]

Numerous extensions and improvements to MTD have been proposed and developed, and there is continuous progress in the field. Particularly, *Lagrangian* MTD can reduce potential temperature inhomogeneity issues arising from the injection of large energy quantities into the degrees of freedom described by the CVs.[137] The method introduces auxiliary collective variables that are coupled to the system through harmonic restraining potentials and associated with a fictitious mass. One can then independently control the fluctuations of the CVs with a thermostat. Other improvements include the concept of *bias exchange* MTD, where the bias potential is periodically swapped between independently evolving trajectories[141] and well-tempered MTD, using the potential energy as a CV, yielding the density of states of the system.[140]

2.3 Computational Set-Up

This section describes the particular settings and methods parameters used for the work presented in the later chapters.

Adsorption Calculations with revPBE+D3

All calculations are carried out using DFT within the Gaussian-plane wave formalism as implemented in the Quickstep module[142] of the CP2K[143] program package. The valence electrons (11, 5, and 3 electrons for Cu, N, and B respectively) are described using Double-Zeta Valence Polarized basis sets of the MOLOPT[144] type. Dual-space Goedecker-Teter-Hutter pseudopotentials[145] are used to approximate the atomic cores. The Brillouin zone is sampled only at the Γ point. The electron density is expanded in plane waves (PW) up to a cut-off energy of 500 Ry. The same grid, as defined by the PW cut-off, is also used to evaluate the XC functional and its derivative. Here, a nearest-neighbor smoothing procedure is employed in order to improve the accuracy. In order to facilitate convergence, fractional occupation numbers and a Fermi–Dirac smearing with electronic temperatures of 300–1000 K are used. Furthermore, we employ Broyden mixing thoughout the SCF procedure. The exchange-correlation energy is treated using the revised PBE functional,[101] and the DFT-D3 dispersion correction[119] is applied to take into account long-range van der Waals-interactions.

Commensurate adsorption of *h*-BN on Ni(111) and Cu(111) is modelled with 7-layer slabs of lateral dimension 6×6 unit cells, where the monolayer is placed symmetrically on both sides of the slab. For systems of larger lateral size the slab is reduced to 4 vertical layers, with the bottom layer fixed at bulk interatomic distances, not covered by the adsorbate. Slab calculations typically include at least 20 Å of vacuum, in order to decouple the periodic replicas of the unit cell in the z direction.

Simulated STM images are produced using the Tersoff-Hamann approximation[146,147] with an *s*-type tip at an isolevel of $5{\cdot}10^{-7}$ electrons/Å^3. Here, the topography of the isocurrent surface is determined by calculating the height at which the local electron density, modulated by an exponential of the local work function, remains constant.[39]

Adsorption Calculations and Reaction Thermodynamics with BEEF-vdW

For all calculations we employ the Atomic Simulation Environment (ASE)[148] in connection with the QUANTUM ESPRESSO[149] program package. The electronic wavefunctions are expanded in PWs up to a cutoff energy of 500 eV, while the electron density is represented on a grid with an energy cutoff of 5000 eV. Core electrons are approximated with ultrasoft pseudopotentials.[150] We use the BEEF-vdW exchange-correlation functional,[97] that has been shown to accurately describe chemisorption as well as physisorption properties on TM surfaces.[114] Free energy corrections for adsorbed species are based on the harmonic approximation and calculated vibrational frequencies. We use a corrected total energy for gas-phase O_2 based on the formation enthalpy of H_2O.[151] BN/metal surfaces are modelled as slabs with 4 layers of metal (the bottom two layers are fixed at bulk atomic positions), one layer of *h*-BN, and adsorbed species atop *h*-BN. In order to achieve commensurate adsorption, the BN layer is fitted to match the surface lattice constant of the metal and used as a reference for adsorption energy calculations. A vacuum region of about 20 Å is used to decouple the periodic replicas. For adsorption studies we generally use supercells of lateral size 3×3, and sample the Brillouin zone[152] with a mesh of $4\times4\times1$ k-points.

We estimate the uncertainty of the presented DFT energies through an ensemble of 2000 exchange-correlation functionals, derived by perturbing the BEEF-vdW exchange potential (see Section 2.1), representing the known computational errors of the BEEF-vdW functional.[97,114] This yields an ensemble of

2000 energy values normally distributed around the DFT total energy. The error in the respective free energy is taken as the standard deviation of this ensemble.

Error Estimation for Electrochemical Reactions

BEEF-vdW ensemble energies are determined for all species participating in a particular reaction. Each ensemble contains 2000 non-selfconsistent energies, E_i. An energy difference for the reaction, ΔE_i, is calculated for each energy i in the ensemble. For the simple case of h-BN adsorption on Ni(111), ΔE_i is given as

$$\Delta E_i = E_i(h{-}\mathrm{BN/Ni}) - E_i(h{-}\mathrm{BN}) - E_i(\mathrm{Ni})\,, \tag{2.42}$$

yielding a set of 2000 energy differences, $\{\Delta E_i\}$. The error bars on the calculated DFT energy are then computed as the standard deviation over all elements in this set.

The same procedure is applied to compute the ensemble of overpotentials for the oxygen reduction reaction (ORR). For each ensemble member, potential differences are calculated for individual ORR steps.

$$U1_i = 1.23\,\mathrm{V} - [\Delta G_i(\mathrm{O_2^*}) - \Delta G_i(\mathrm{OOH^*})]\,, \tag{2.43}$$

$$U2_i = 1.23\,\mathrm{V} - [\Delta G_i(\mathrm{OOH^*}) - \Delta G_i(\mathrm{O^*})]\,, \tag{2.44}$$

$$U3_i = 1.23\,\mathrm{V} - [\Delta G_i(\mathrm{O^*}) - \Delta G_i(\mathrm{OH^*})]\,, \tag{2.45}$$

$$U4_i = 1.23\,\mathrm{V} - [\Delta G_i(\mathrm{OH^*}) - \Delta G_i(^*)]\,, \tag{2.46}$$

where $\Delta G_i = \Delta G + \Delta E_i$. ΔG is the free energy of a species and ΔE_i is the associated non-selfconsistent energy difference from the BEEF-vdW ensemble as defined above. The overpotential for a particular member of the ensemble is then given as

$$U_i = \max(U1_i, U2_i, U3_i, U4_i), \tag{2.47}$$

and the set $\{U_i\}$ can then be analyzed and visualized using a histogram. Note that due to the $\max()$ function, the resulting $\{U_i\}$ does not follow a normal distribution any more as $\{U1_i\}, \{U2_i\}\ldots$ do.

We employ a BEEF-vdW ensemble optimized for chemisorption energies as described in Section 2.1 and in ref. 114.

MD and MTD of Water-Supported TTPB

We perform *ab initio* molecular dynamics (AIMD) simulations based on DFT using the CP2K code.[142,143] The entire system is treated quantum-mechanically, representing valence and core electrons with Double-Zeta basis sets (including polarization functions) of the MOLOPT type[144] and Goedecker-Teter-Hutter pseudopotentials,[145] respectively. The electron density is represented with plane waves up to a cutoff energy of 500 Ry. The exchange-correlation contribution to the DFT energy is approximated using the Perdew-Burke-Ernzerhof (PBE) XC functional.[96] The D3 method[119] is used to account for dispersion interactions in an approximate way, which considerably improves the density of simulated water.[153,154]

The AIMD simulations are carried out at 300 K using a Nosé-Hoover thermostat chain and a timestep of 0.5 fs. We obtain NVT trajectories of at least 15 ps for all systems (starting from a pre-equilibrated water slab and statically optimized TTPB). For calculations in the gas phase, the ionic charge is compensated by a uniform background charge rather than solvated counterions.

3

Metal-Supported Hexagonal Boron Nitride

As discussed in Section 1.2, *h*-BN readily adsorbs on various TM surfaces, forming heterostructures of varying stability and properties. Depending on the interaction and lattice mismatch, widely different interface structures can be realized, ranging from strongly corrugated nanomeshes[21,28] to extended flat overlayers.[12,23] This chapter presents the results of several computational studies of *h*-BN adsorbed on TM surfaces. Section 3.1 describes the general energetic, structural and electronic properties of commensurate *h*-BN heterostructures on Ni(111), Cu(111) and Co(0001). Motivated by STM results, Section 3.2 then examines the electronic corrugation of *h*-BN/Cu(111) and its emergence without a concomitant structural corrugation of the overlayer. The final section, 3.3, focuses on possible applications of *h*-BN-based heterostructures in chemical technology: utilizing supported BN as a catalyst for the oxygen-reduction reaction in fuel cells.

3.1 Commensurate Adsorption

Based on references 34 and 86.

In the simplest case of small lattice mismatch and sufficiently strong interaction, *h*-BN forms a commensurate overlayer on TMs. This condition is satisfied on the three hexagonal surfaces Ni(111), Cu(111), and Co(0001). We study the former two with two different DFT approaches using the dispersion-corrected revPBE and the more recently published BEEF-vdW functional. Co(0001) is only examined with BEEF-vDW. Both methods tend to agree with each other, and the results are in line with previously published work.[23,37,46,50,51,54,155] Generally speaking, *h*-BN binds to TMs with two different binding modes, *chemisorption* or *physisorption*. Chemisorption is characterized by short monolayer-metal distances (< 2.3 Å), noticeable vertical buckling of the BN layer ($\sim$0.1 Å) and stronger adsorption energies compared to physisorption. Depending on the lateral placement of *h*-BN, both modes can be realized on the studied TM surfaces.

In the following, each *h*-BN-metal heterostructure is characterized in terms of a few parameters, for all six high-symmetry adsorption registries described in Section 1.2.

- The adsorption energy, ΔE_{ads}, defined as $\frac{1}{n_{\mathrm{BN}}} \cdot \left(E_{\mathrm{BN/metal}} - E_{\mathrm{BN}} - E_{\mathrm{metal}}\right)$ where E denotes the energy of the various components of the systems, each at corresponding optimized atomic coordinates.
- The strain-free adsorption energy, $\Delta E^{*}_{\mathrm{ads}}$, defined as $\frac{1}{n_{\mathrm{BN}}} \cdot \left(E_{\mathrm{BN/metal}} - E^{*}_{\mathrm{BN}} - E_{\mathrm{metal}}\right)$ where E denotes the energy of the various components of the systems, each at corresponding optimized atomic coordinates and E^{*} is the energy of BN stretched to match the lattice constant of the substrate (only for results obtained with BEEF-vdW).
- The interaction energy, ΔE_{int}, defined as $\frac{1}{n_{\mathrm{BN}}} \cdot \left(E_{\mathrm{BN/metal}} - E'_{\mathrm{BN}} - E'_{\mathrm{metal}}\right)$ where E denotes the energy of the total system, and E' denotes the energy of the respective subsystems at the same atomic coordinates as in the optimized full heterostructure.

- The minimum distances between the metal surface and the B and N atoms, $d_{\mathrm{M,B}}$, and $d_{\mathrm{M,N}}$.
- The intra-layer buckling of the BN sheet, i.e. the vertical distance between B and N, $d_{\mathrm{B,N}}$.
- The work function, Φ, of the heterostructure surface (only for results obtained with revPBE). Φ is calculated from the difference between vacuum electrostatic potential and the Fermi energy.
- The magnetic moment of atoms at the metal surface (only for Ni and Co).

These results provide fundamental insight into the properties and stability of *h*-BN/metal heterostructures. They set the stage for the following further studies in the later sections of this chapter, where we explore subtle influences on the electronic structure, as well as applications in catalysis.

h-BN on Ni(111)

Table 3.1 lists the properties of *h*-BN/Ni(111) as obtained with the revPBE+D3 method for the six lateral registries.[34]

A clear difference can be discerned between $N_{top}B_{fcc}$ and $N_{top}B_{hcp}$ and the other registries. The former two are characterized by about 0.1 eV stronger binding energies, about 1 Å shorter adsorbate-metal distances and $d_{\mathrm{B,N}}$ around 0.12 Å. Furthermore, the surface magnetic moment and the work function are both reduced in these two systems, compared to the four other monolayer registries. Already from this cursory look at the data it becomes evident that *h*-BN adopts a chemisorbed or physisorbed configuration depending on its lateral placement.

The two chemisorbed configurations are very similar to each other, as are the four physisorbed ones. Within these two groups, energies vary only on the order of meV and distances by 0.1 Å. The determining factor for chemi- vs. physisorption appears to be the *on-top* placement of the N atom.

Fig. 3.1 presents plots of the projected density of states (PDOS) for *h*-BN/Ni(111) in the $N_{top}B_{fcc}$ registry. In particular, the left panel shows projections on the p states of N in the BN layer, for both adsorbed and free-standing *h*-BN. Upon adsorption, states emerge in the band gap, as a result of the interaction with the surface. As expected, the p_z orbitals are most strongly affected by the binding to the metal. The gap states are mostly of p_z character, and the occupied p_z states shift to higher energies upon binding. The p states of free-standing BN are aligned to match the lowest-energy states of the heterostructure. For the $p_{x,y}$ states, there is little difference between the adsorbed and free-standing systems, except for a small shift of all peaks. In contrast, the p_z peaks are significantly more shifted (by >1 eV) and have different intensities. This indicates that the orbitals perpendicular to the BN plane respond more strongly to the binding of the surface, presumably due to interaction with the Ni d_{z^2} states. Overall, however, the peak shape is not strongly modified, hinting at the limited magnitude of the BN–Ni interaction. A very small spin polarization of the N orbitals can be seen in the PDOS.

Table 3.1|Adsorption and interaction energies (eV/BN), work function Φ (eV), adsorbate-surface distances and BN buckling (Å), and surface magnetic moment (μ_B) for *h*-BN/Ni(111) in six adsorption registries. Results obtained with the revPBE+D3 setup presented in Section 2.3. Data published in ref. 34.

N	B	ΔE_{ads}	ΔE_{int}	Φ	$d_{\mathrm{M,B}}$	$d_{\mathrm{M,N}}$	$d_{\mathrm{B,N}}$	μ_{surf} per Ni
top	fcc	-0.390	-0.470	3.58	2.006	2.130	0.123	0.519
top	hcp	-0.392	-0.473	3.55	2.008	2.132	0.124	0.503
fcc	hcp	-0.285	-0.269	3.90	3.015	3.028	0.016	0.651
fcc	top	-0.283	-0.257	3.84	2.903	2.921	0.022	0.635
hcp	top	-0.283	-0.268	3.84	2.923	2.944	0.021	0.630
hcp	fcc	-0.293	-0.270	3.91	2.996	3.008	0.016	0.649

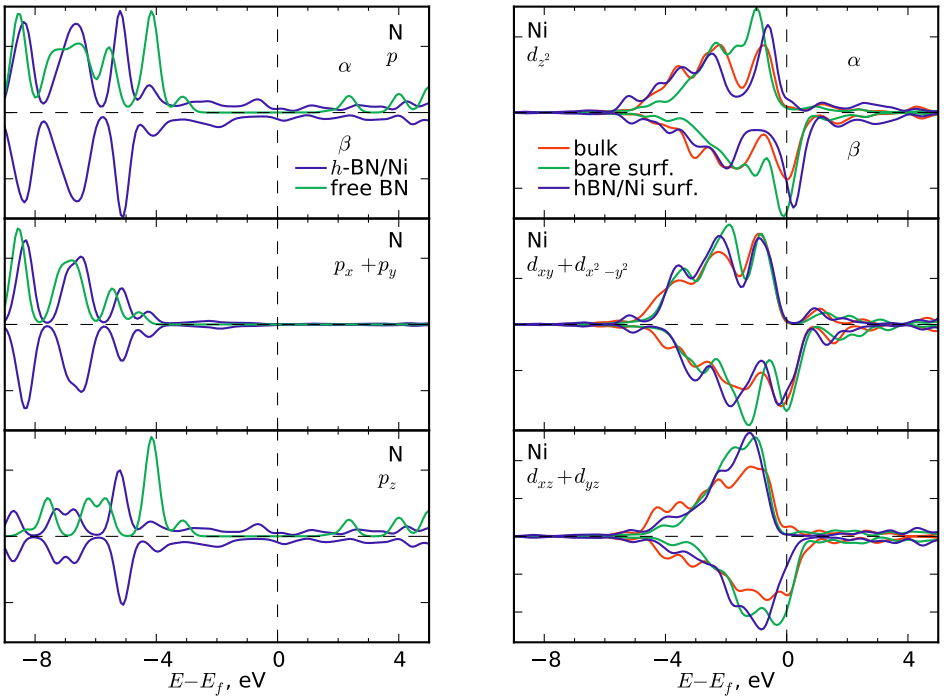

Figure 3.1|Projected Density of States (PDOS) of *h*-BN/Ni (spin resolved). Left panel: Projections on N p-states, total and separated by angular momentum. Comparison of adsorbed (blue) with free-standing (green) *h*-BN. Right panel: Projections on Ni d states for various angular momenta. Comparison of bulk (red) and surface (blue) atoms in *h*-BN/Ni with atoms on the bare Ni(111) surface (green).

An electron density difference map for *h*-BN/Ni is shown in Fig. 3.2. The electron accumulation and depletion resulting from the binding of *h*-BN to the surface is visualized as isosurfaces. Most of the electron redistribution occurs in the *h*-BN layer and the first metal layer; the second Ni layer is only weakly polarized and deeper layers remain inert. In agreement with the interpretation of the PDOS, most of the electronic effects of binding are related to the Ni d orbitals. The d_{z^2} orbitals lose electrons, while the $d_{xz,yz}$ orbitals gain them. Some electron density is also transferred to the interlayer space. The N atoms become somewhat polarized, losing electrons from the p_z orbitals. The B atoms behave in an opposite way, as they become polarized towards the metal and electron density accumulates in the *fcc* hollow site. The B–N bonds lose some electron density.

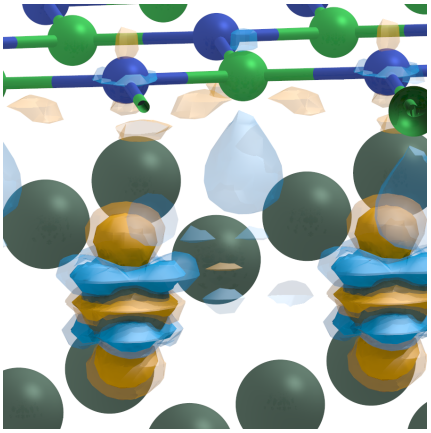

Figure 3.2|Electron density difference map of *h*-BN/Ni(111). Isosurfaces of positive (i.e. electron accumulation) and negative (electron depletion) differences shown in blue and orange, respectively. Isovalues at $\pm 0.01\,\mathrm{e/Bohr^3}$ and $\pm 0.005\,\mathrm{e/Bohr^3}$. Atom colors: B, light green; N, blue; Ni, dark green.

Table 3.2 lists the properties of *h*-BN/Ni(111) as determined with the BEEF-vdW method. Also in this case, the different adsorption registries give rise to two different binding modes. *h*-BN is chemisorbed in the $N_{top}B_{fcc}$ and $N_{top}B_{hcp}$ registries and physisorbed in the others, as can be seen from the monolayer-substrate distances and the buckling of the BN layer. The *h*-BN layer resides about 2.2 Å and 3.7 Å from the metal surface in the chemisorbed and physisorbed cases, respectively. The buckling of the monolayer is negligible in the latter case, even smaller than observed

Table 3.2|Adsorption energy, strain-free adsorption energy and interaction energy (eV/BN), adsorbate-surface distances and BN buckling (Å), and surface magnetic moment (μ_B) for *h*-BN/Ni(111) in six adsorption registries. Results obtained with the BEEF-vdW setup presented in Section 2.3. Data published in ref. 86

N	B	$\Delta E^*_{\mathrm{ads}}$	ΔE_{ads}	ΔE_{int}	$d_{\mathrm{M,B}}$	$d_{\mathrm{M,N}}$	$d_{\mathrm{B,N}}$	μ_{surf} per Ni
top	fcc	-0.005±0.102	-0.009±0.104	-0.062	2.146	2.233	0.087	0.351
top	hcp	0.001±0.088	-0.003±0.090	-0.042	2.217	2.293	0.076	0.353
fcc	hcp	-0.079±0.021	-0.083±0.019	-0.078	3.699	3.701	0.002	0.390
fcc	top	-0.079±0.022	-0.083±0.020	-0.078	3.696	3.698	0.002	0.390
hcp	top	-0.078±0.023	-0.082±0.022	-0.077	3.616	3.619	0.003	0.389
hcp	fcc	-0.079±0.019	-0.083±0.018	-0.079	3.747	3.748	0.001	0.390

above. Again, the chemisorbed configurations exhibit lower surface magnetic moments of the metal. Contrary to what would be expected, here the chemisorbed configurations have lower (i.e. more positive) ΔE_{ads} than the physisorbed ones. This may partially be due to the energy cost of buckling the BN structure ($\sim$60 meV), which energetically penalizes the N_{top} registries. When this value is taken into account, all adsorption energies become approximately equal. The strain of the BN layer to match the Ni surface lattice is negligible, as seen from the minute difference between $\Delta E^*_{\mathrm{ads}}$ and ΔE_{ads}. In fact, when free-standing BN at its optimized lattice constant is taken as the energy reference, the adsorption energy is even slightly smaller.

Using the BEEF-vdW ensemble, error bars can be estimated for the calculated energies. The errors are on the order of 0.02 eV for the physisorbed configurations, and around 0.1 eV for the chemisorbed ones. Especially for the latter, they are large relative to the energy values. On an absolute scale, however, they are roughly in the expected accuracy range of DFT calculations. The effect of larger estimated errors at closer adsorption distances has been noted previously for the case of graphene on Ni(111).[97]

Both differences and similarties between the revPBE+D3 and BEEF-vdW approach become apparent from the presented data. Qualitatively, the two methods agree on the two regimes of chemisorption and physisorption and find the same adsorption configurations in each category. Quantitatively, there is quite good agreement for the adsorption distances in the $N_{top}B_{fcc}$ and $N_{top}B_{hcp}$ registries and for the magnitude of the buckling. In general, BEEF-vdW finds equilibrium positions for the monolayer that are further away from the metal surface, giving smaller buckling and reduction of the magnetic moment.

The largest difference between the two methods, however, is found for ΔE_{ads} and ΔE_{int}. BEEF-vdW predicts much smaller binding energies, and reverses the trend of higher ΔE_{ads} for chemisorbed species as noted above. A significant reason for this behavior is probably the different methods for dispersion correction employed in the two approaches. The force field employed in the D3 correction likely tends towards overbinding in the present systems, giving too strongly negative adsorption energies and compressed bond distances.

Several experimental studies have examined the *h*-BN/Ni(111) heterostructure. Using low-energy electron diffraction (LEED), Gamou et al. determine a Ni–B distance of 2.04 Å, and a vertical buckling of 0.18 Å.[46] They propose that the *h*-BN layer adopts the $N_{top}B_{fcc}$ registry and note a fairly strong interaction between the monolayer and substrate due to mixing of the *h*-BN-π and Ni d_{z^2} states.[46] Values found with x-ray photoelectron diffraction (XPD) are in a similar range, $d_{\mathrm{Ni,B}}$ being 1.88 Å and $d_{\mathrm{B,N}}$ 0.07 Å.[24,47] Also these results point to an $N_{top}B_{fcc}$ adsorption registry, elucidated by examining scattering from surface metal atoms. Our results for the interlayer spacing and corrugation are in the range given by these experiments, somewhat closer to the LEED data. The preference for N_{top} registries is also confirmed by the experiments.

Table 3.3|Adsorption energy, (eV/BN), adsorbate-surface distances and BN buckling (Å), and change in surface magnetic moment (μ_B) for *h*-BN/Ni(111) as determined with various computational and experimental methods. Value marked with * is the metal–N, rather than metal–B distance. Extended based on ref. 34.

Method	XC	ΔE_{ads}	$d_{\mathrm{M,B}}$	$d_{\mathrm{B,N}}$	$\Delta\mu_{\mathrm{surf}}$ per Ni	Ref.
LEED		–	2.04	0.18	–	46
XPD		–	1.88	0.07	–	47, 24
DFT	PBE	–	2.08	0.11	-0.08	50
DFT	PW91	-0.021 – +0.038	2.18 – 3.97	–	-0.00 – -0.23	155
	LDA	-0.420 – -0.141	1.95 – 3.11	–	-0.02 – -0.43	155
DFT	PBE	-0.04	2.04	0.11	-0.06	37
	WC	-0.19	2.03	0.11		37
	LDA	-0.27	2.01	0.11		37
DFT	PBE	-0.04	1.99	0.10	–	156
DFT	WC	-0.36	1.99	0.12	–	54
DFT	PBE	+0.02	2.16*	–	–	52
DFT	PBE+D2	-0.28	2.00	0.11	–	52
DFT	PBE+D2	-0.38	1.99	0.12	0.11	157
DFT	PBE+D2	-0.29	2.82	0.02	–	157

Experimentally, the electronic structure of *h*-BN/Ni(111) has been investigated with numerous methods.[23,48–50] Initially it was reported that the interaction between the monolayer and substrate is weak and occurs without substantial electronic mixing.[51] Subsequent phonon spectra obtained with HREELS, however, show evidence of electronic interaction due to $3d$-π hybridization.[25] Preobrajenski et al. applied a number of spectroscopic techniques to elucidate the electronic effect of *h*-BN binding to Ni(111).[48] They observe a strong hybridization between the $3d$ states of Ni and π states of *h*-BN, and suggest the emergence of interlayer conduction bands, causing *h*-BN to have a metallic character.[48] In later work, they observe gap states in *h*-BN due to adsorption on the surface, noting a strong modification of the XES spectrum of *h*-BN/Ni compared to free *h*-BN. The gap states fill the entire energy range from the valence band maximum to E_F, which the authors rationalize with strong mixing of N $2p$ states and the Ni d bands.[49] Another study combining theory and photoemission found that no additional states emerge during adsorption.[50] Our PDOS plots indicate some modification of the electronic structure due to adsorption, gap states, and an increased metallic character of the *h*-BN sheet.

From the computational perspective, Ni(111) is probably the most investigated substrate for *h*-BN adsorption, as it forms a commensurate heterostructure with fairly strong adsorbate-substrate interactions. Initial work focused on the *h*-BN/Ni(111) system itself, characterizing the structure, energetics and magnetic properties of the interface and seeking to relate them to experimental findings.[37,50,155] Subsequently, studies also started including adsorbates atop *h*-BN, among them C_{60}[156] and O_2.[52,54] Table 3.3 gives an overview of quantities published in recent theoretical work. Calculated adsorption energies vary rather widely, between -0.42 eV/BN and +0.04 eV/BN, depending on the employed method and the adsorption registry of the monolayer. As is commonly the case, the LDA yields very high ΔE_{ads}.[106,107,158] Among GGA methods, the spread of ΔE_{ads} is also very large. In particular, the use of dispersion corrections has a very large influence on the adsorption energies. Without employing e.g., the D2 method, ΔE_{ads} tends to be zero or even positive. An exception to this appears to be the Wu-Cohen XC functional,[159] which yields ΔE_{ads} comparable to that of PBE+D2 even without an additional vdW correction. Dispersion-corrected GGA values for ΔE_{ads} tend to be around -0.3– -0.4 eV/BN.

Our results for ΔE_{ads} are in the reported range with both the revPBE+D3 and BEEF-vdW methods. However, as noted above, the two methods differ fairly strongly among each other as far as adsorption energetics are concerned.

There appears to be less variation for the structural properties determined with various methods. In general the N_{top} registries are found to be the most stable for the *h*-BN layer. Energy differences between $N_{top}B_{fcc}$ and $N_{top}B_{hcp}$ are too small, however, to distinguish between the two. The B atoms typically reside at a distance of around 2 Å from the metal. The buckling of the monolayer is uniformly predicted to be on the order of 0.1 Å, with the N atoms further away from the surface. Generally, our results are in good agreement with these findings with both the revPBE+D3 and BEEF-vdW methods.

h-BN on Cu(111)

The properties of *h*-BN/Cu(111), as determined with the revPBE method, are given in Table 3.4. ΔE_{ads} ranges from -0.23 eV to -0.27 eV, $d_{\mathrm{M,BN}}$ is typically around 3.0 Å and the BN layer is buckled by less than 0.02 Å. Φ lies in the range from 3.62 to 3.71 eV, about 1 eV less than that of the free Cu(111) surface (4.69 eV as calculated with the same method). The properties of the heterostructure show little variation with the adsorption registry, and in all cases the BN–Cu interaction can be characterized as physisorption.

The predominantly dispersive interactions that bind the monolayer to the surface are largely unspecific, leading to small differences between the adsorbate configurations. Registries where N is placed atop a surface atom are more stable by about 0.03–0.04 eV, likely due to a small electronic effect that contributes in addition to the van der Waals interaction. Within the accuracy of the present calculations, it is not possible to confidently distinguish which of the N_{top} registries is more stable, and a definitive hierarchy of stability cannot be established. In terms of electronic properties, differences between the adsorption registries are also minor. However, in the PDOS of the nitrogen p_z states in *h*-BN/Cu, one can observe a shift of the bands above and below the gap, depending on the lateral position of the monolayer. The difference between the $N_{top}B_{fcc}$ and $N_{fcc}B_{hcp}$ registries amounts to 0.3 eV, large enough to be measured and impact the electronic corrugation of the material as described in Section 3.2.

Table 3.5 gives the properties of *h*-BN/Cu(111) as determined with BEEF-vdW. $\Delta E^{*}_{\mathrm{ads}}$ is around -0.075 – -0.080 eV for all registries, monolayer-surface distances vary between 3.4 and 3.8 Å, and the corrugation of the BN layer is negligible. The estimated error on $\Delta E^{*}_{\mathrm{ads}}$ is uniformly on the order of 0.025 eV. It should be noted that the $\Delta E^{*}_{\mathrm{ads}}$ values become slightly positive, when free-standing *h*-BN is taken as the energy reference (as is done for ΔE_{ads}). The interaction between *h*-BN and Cu(111) as calculated with BEEF-vdW is evidently smaller than the strain energy needed to adjust *h*-BN to the Cu lattice. Confidence in the ΔE_{ads} values is also lower, as indicated by the error bars that are on the order

Table 3.4|Adsorption and interaction energies (eV/BN), work function Φ (eV), adsorbate-surface distances and BN buckling (Å) for *h*-BN/Cu(111) in six adsorption registries. Results obtained with the revPBE+D3 setup presented in Section 2.3. Data published in ref. 34.

N	B	ΔE_{ads}	ΔE_{int}	Φ	$d_{\mathrm{M,B}}$	$d_{\mathrm{M,N}}$	$d_{\mathrm{B,N}}$
top	fcc	-0.270	-0.298	3.62	2.962	2.977	0.015
top	hcp	-0.265	-0.262	3.63	2.966	2.980	0.015
fcc	hcp	-0.234	-0.281	3.71	3.023	3.036	0.013
fcc	top	-0.244	-0.284	3.66	2.959	2.976	0.016
hcp	top	-0.229	-0.273	3.67	2.969	2.985	0.016
hcp	fcc	-0.234	-0.280	3.69	3.019	3.032	0.013

Table 3.5|Adsorption energy, strain-free adsorption energy and interaction energy (eV/BN), adsorbate-surface distances and BN buckling (Å) for *h*-BN/Cu(111) in six adsorption registries. Results obtained with the BEEF-vdW setup presented in Section 2.3. Data published in ref. 86

N	B	$\Delta E^*_{\mathrm{ads}}$	ΔE_{ads}	ΔE_{int}	$d_{\mathrm{M,B}}$	$d_{\mathrm{M,N}}$	$d_{\mathrm{B,N}}$
top	fcc	-0.079±0.029	0.075±0.072	-0.075	3.427	3.433	0.006
top	hcp	-0.080±0.027	0.074±0.072	-0.075	3.496	3.500	0.004
fcc	hcp	-0.077±0.024	0.077±0.071	-0.072	3.819	3.820	0.001
fcc	top	-0.076±0.025	0.078±0.072	-0.071	3.736	3.738	0.002
hcp	top	-0.075±0.023	0.078±0.072	-0.072	3.784	3.785	0.001
hcp	fcc	-0.076±0.023	0.077±0.071	-0.072	3.817	3.818	0.001

of the energy value itself. Differences between the adsorption registries are again minor. In terms of adsorption distances, the N_{top} registries are predicted to have 0.3–0.4 Å smaller $d_{\mathrm{M,BN}}$ than the others. A smaller difference can also be seen for the B_{top} registries, having almost 0.1 Å smaller $d_{\mathrm{M,BN}}$ than the registries with N and B in hollow sites. The N_{top} registries are also slightly more stable energetically, but differences are on the order of only 5 meV. BEEF-vdW also predicts all configurations to be physisorbed.

The differences between revPBE+D3 and BEEF-vdW are similar as noted for *h*-BN/Ni. Again, ΔE_{ads} values from BEEF-vdW are significantly smaller, while the monolayer-surface distances are larger. It appears, however, that BEEF-vdW is more sensitive to the adsorption registry, as it gives much larger differences of $d_{\mathrm{M,BN}}$.

Relatively few experimental characterizations of the *h*-BN/Cu(111) heterostructure exist. From EXAFS data, Preobrajenski et al. conclude that the interaction between *h*-BN and Cu(111) is much weaker than that between *h*-BN and Ni(111).[23] Using scanning tunneling spectroscopy Joshi et al. determine a binding energy of 0.0597 eV per BN unit cell.[12] This value is between ΔE_{ads} determined with revPBE+D3 and with BEEF-vdW.

DFT studies have provided values of -0.296 eV (PBEsol+D2[160]), -0.0165 eV (PBEsol[160]), -0.19 eV (LDA[37]), +0.01 eV (PBE[37]), -0.05 eV (WC-GGA[37]), and -0.07 eV (WC[53]). Our values obtained with revPBE+D3 are at the strong-binding end of this range, while those computed with BEEF-vdW are at the weaker end, or even somewhat repulsive, depending on whether the strain energy of BN is accounted for. In this case, the importance of appropriate treatment of the vdW interactions is even greater than for *h*-BN/Ni(111). Calculations without dispersion corrections give binding energies around zero, contradicting the experimental observation of stable heterostructures. On the other hand, semiempirical corrections such as the D2/D3 methods appear to overestimate the binding, and the vdW-DF as a part of BEEF-vdW underestimates it.

Monolayer-surface distances have been reported to be 2.838±0.021 Å (PBEsol+D2[160]), 3.341±0.007 Å (PBEsol[160]), 3.10±0.02 Å (LDA[37]), 3.00±0.01 Å (WC[37]), and 2.65±0.03 Å (WC[53]), expressed as $d_{\mathrm{N,Cu}} \pm d_{\mathrm{B,N}}$. Also in this case the range of distances is rather wide, with dispersion-corrected calculations giving much closer attachment to the surface. Our values of 2.98±0.015 Å (revPBE+D3, $N_{top}B_{fcc}$) and 3.43±0.006 Å (BEEF-vdW, $N_{top}B_{fcc}$) are in the middle and far range of distances, respectively. Indeed, adsorption distances from BEEF-vdW are the largest among the reported values, in spite of the included dispersion correction.

Table 3.6|Adsorption energy, strain-free adsorption energy and interaction energy (eV/BN), adsorbate-surface distances and BN buckling (Å) for *h*-BN/Co(0001) in six adsorption registries. Results obtained with the BEEF-vdW setup presented in Section 2.3. Data published in ref. 86

N	B	$\Delta E^*_{\mathrm{ads}}$	ΔE_{ads}	ΔE_{int}	$d_{\mathrm{M,B}}$	$d_{\mathrm{M,N}}$	$d_{\mathrm{B,N}}$
top	fcc	-0.115±0.136	-0.097±0.148	-0.242	1.970	2.097	0.126
top	hcp	-0.100±0.136	-0.082±0.148	-0.228	1.973	2.100	0.127
fcc	hcp	-0.082±0.022	-0.064±0.028	-0.082	3.890	3.891	0.001
fcc	top	-0.082±0.021	-0.064±0.028	-0.082	3.898	3.899	0.001
hcp	top	-0.081±0.021	-0.064±0.028	-0.082	3.898	3.899	0.001
hcp	fcc	-0.082±0.022	-0.064±0.028	-0.082	3.812	3.813	0.001

h-BN on Co(0001)

The properties of *h*-BN/Co(0001) were calculated with the BEEF-vdW method, analogously to the other two substrates. Table 3.6 lists the obtained properties of the optimized structure.* The N_{top} configurations fall into a separate regime from the others, as is the case for Ni(111). They are more stable by 0.2–0.3 eV and the monolayer is approximately 1.9 Å closer to the metal surface. Additionally, *h*-BN is rather strongly buckled in these two configurations, which also indicates stronger binding.

The *h*-BN/Co system is very similar to *h*-BN/Ni. The monolayer is bound slightly more strongly and closely in the chemisorbed cases, but somewhat further away in the physisorbed ones. Contrary to *h*-BN/Ni, ΔE_{ads} is stronger for the N_{top} configurations, following the expectation for a chemisorbed heterostructure. As seen above, the N_{top} configurations have larger error bars for ΔE_{ads} than the others.

Quite different values for ΔE_{ads} have been published in previous work. Using dispersion-corrected PBE, Joshi et al. obtained values between -0.42 and -0.73 eV for different adsorption registries.[157] Zhou et al. found a broad range of ΔE_{ads} between 0.293 eV and -0.509 eV (using a 2-layer Co(111) slab and a not further specified GGA approximation).[161] In their extensive study of *h*-BN/metal heterostructures, Laskowski and co-workers[37] report values of -0.32, -0.06, and -0.23 eV with the LDA, PBE and Wu-Cohen approximations, respectively. BN-Co distances tend to be more uniform, ranging from 2.14[37] to 2.81 Å,[161] but not all authors report this distance. The finding of two different binding regimes is supported by previous work, although the energy differences between are smaller than those previously reported.[157] It should be noted, however, that other investigators typically either used force-field based dispersion corrections with the danger of overbinding, or no dispersion corrections, giving larger $d_{\mathrm{M,BN}}$.

Experimental results for *h*-BN on Co are even more rare than for Cu. The available LEEM data indicates that *h*-BN adsorbs in $N_{top}B_{fcc}$ and $N_{top}B_{hcp}$ configurations, supporting our results.[26]

Summary: Commensurate h-BN on Transition Metals

h-BN forms stable commensurate heterostructures on Ni(111), Cu(111), and Co(0001). Their structure and energetics are governed by the placement of the monolayer on the metal: The $N_{top}B_{fcc}$ registry is typically most stable. Ni and Co adsorb *h*-BN strongly, while Cu does so weakly. The revPBE+D3 and BEEF-vdW functionals give somewhat different results quantitatively, but largely agree in their predictions of chemi- and physisorption and interface structures. Our data show that dispersion interactions are particularly important for these systems.

*Properties were obtained with spin-restricted calculations, neglecting the magnetic properties of Co. While there may be some influence of the monolayer on the surface magnetism of the metal, restricting spin polarization should not strongly affect the adsorption energies and distances.

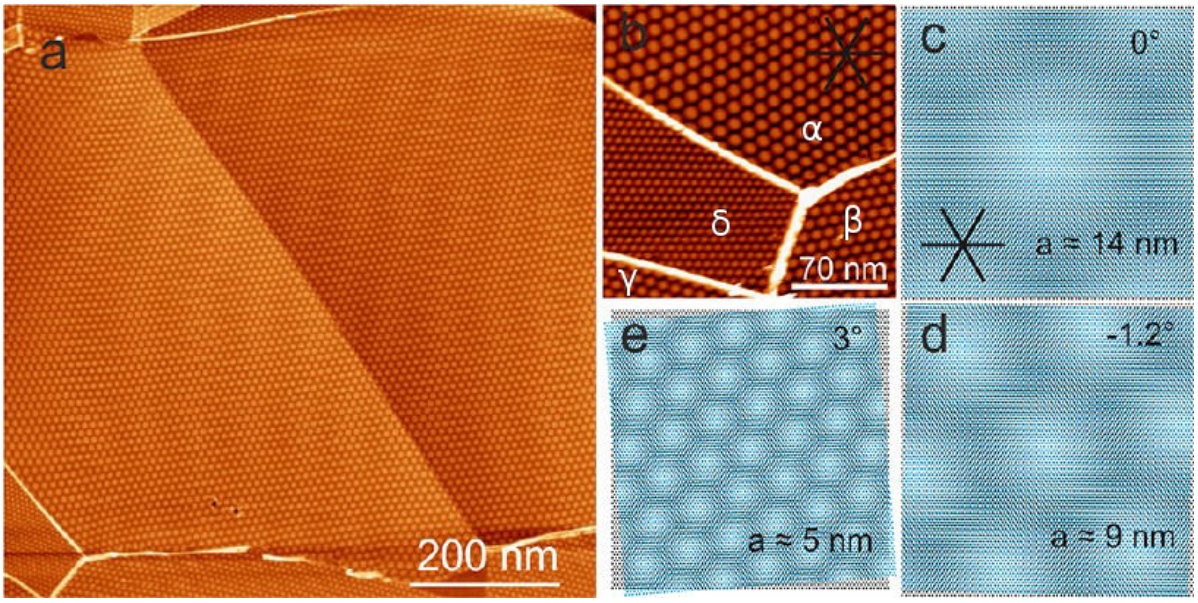

Figure 3.3|STM image of an *h*-BN monolayer on Cu(111). (a) Large-scale image of the corrugated surface, showing different coexisting domains. (b) Several domains of varying periodic corrugation labelled α–δ. (c) - (e) Modelled Moiré superstructures due to superposition of the slightly mismatched (1.8%) and rotated (0–3°) surface lattices (see 1.2). Image from ref. 12

3.2 The Electronic Corrugation of *h*-BN on Cu(111)

Based on references 12, 13, and 14.

While *h*-BN can form commensurate adsorption structures on Cu(111) as shown in the previous section, experimental evidence indicates that there is more to this interface.

Using chemical vapor deposition, Barth et al. were able to grow monolayer films of *h*-BN on a Cu(111) substrate.[12] Subsequent STM investigation of this material revealed domains of periodically modulated contrast across the surface. The periodicity of the pattern varied in different domains, which was ascribed to varying rotation angles of the monolayer relative to the metal surface. This rotation would lead to a Moiré-like interference of the *h*-BN and Cu lattices, therefore to contrast modulation and thus an apparent corrugation of the surface. Figure 3.3 shows STM images of the surface, with corrugation domains of varying periodicity. The surface exhibits a hexagonal array of bright "hills" surrounded by darker "valley" regions.

During further investigation of this system, it was found that the contrast was inverted depending on the bias voltage V_b. At low bias between -4 and 3 V, essentially no corrugation could be observed, while at $V_b = 4\,\mathrm{V}$ the corrugation reached a maximum value of 1.5 Å. Further increase of V_b led to inversion of the contrast. At $V_b = 3.7\,\mathrm{V}$ the hills appeared bright and the valleys dark, but with $V_b = 4.7\,\mathrm{V}$ the situation changed to the opposite. This observation led to the conclusion that the corrugation of the surface was *not topographic*, but mainly *electronic* in nature.[12]

In the following, we explore the origin of the observed electronic corrugation using large-scale DFT calculations.

Modeling Incommensurate Adsorption

As discussed in Section 1.2, when a periodic lattice is superimposed on one with a mismatched periodicity and/or a rotation angle, long-range periodic superstructures are formed. Due to the small mismatch between Cu(111) and *h*-BN, the smallest such Moiré superstructure is formed by a 24×24 cell of *h*-BN

adsorbed on a 23×23 metal surface, with a rotation angle of 2.11°. Here, planar lattice constants of 2.571 Å for Cu(111) and 2.515 Å for *h*-BN are used, in order to make the large supercell fully commensurable. The additional BN units in the monolayer compensate for its smaller lattice constant. The metal surface is modelled as a 4-layer slab, fixing the bottom layer at bulk interatomic distances. The simulated system contains 3222 atoms in total, with 27 700 electrons treated at the revPBE+D3 level (Section 2.3). The *h*-BN layer is placed at a distance of 2 Å from the surface and the system is fully relaxed in a geometry optimization.

Energetics and Structure of the Adsorption System

Table 3.7 summarizes a number of structural and energetic parameters for the Moiré system. The definitions of the various energetic quantities and distances are given in Section 3.1. In addition, the reorganization energies, E_{r}, are given for the metal and BN subsystem. This quantity is defined as

$$\Delta E_r = E_{\mathrm{opt}} - E_0 \,,$$

where E_0 refers to the energy of the respective system at bulk ("unoptimized") atomic positions.

There is a fairly large binding interaction between the monolayer and the surface, as indicated by ΔE_{int} of -0.243 eV. The predominant contribution to this is the van der Waals energy as determined with the Grimme D3 dispersion correction. At this optimized geometry, the *h*-BN–Cu interaction would be repulsive without the large dispersion term. It has been previously established that dispersion effects need to be taken into account for such adsorption systems.[34,162] However, due to the dominance of this type of interaction, one can expect the monolayer–surface binding to be mostly laterally unspecific, as shown in Section 3.1 for the case of commensurate *h*-BN on Cu(111). The comparatively much smaller values for $E_r^{\mathrm{BN,Cu}}$ indicate that both the monolayer and the metal are only slightly perturbed upon adsorption.

The structural changes induced by the adsorption are also rather small. The average monolayer–surface distance, $d_{\mathrm{Cu,BN}}$, is approximately 3 Å, while the vertical buckling of the BN layer, $d_{\mathrm{B,N}}$, is negligible. In this context, $d_{\mathrm{B,N}}$ is defined as the average displacement of a B atom out of the plane formed by its 3 surrounding N atoms, and *vice versa*. The maximum difference in *h*-BN–surface distance, $\Delta d_{\mathrm{Cu,BN}}$ is also small compared to the large lateral dimensions of the cell. Interestingly, this difference originates not only from a change of the vertical B and N positions, but to a lesser extent also from a corrugation of the Cu surface on the order of 0.1 Å. $\Delta d_{\mathrm{Cu,BN}}$ is smaller by a factor 10 compared to the equivalent distance in graphene/Ru(0001), 1.5 Å,[163] and *h*-BN/Rh(111), 1.0 Å.[34] All these quantities indicate that the monolayer remains flat both locally and over the entire supercell despite the variation of the registry. All these quantities indicate that the monolayer remains flat both locally and over the entire supercell despite the variation of the registry. We attribute this to the mostly unspecific and weak

Table 3.7|Energetic and structural characteristics of the Moiré system consisting of rotated 24×24 *h*-BN on a 23×23 4-layer Cu(111) slab. Data published in ref. 13.

Interaction energy, ΔE_{int}, eV/BN	-0.243
van der Waals correction in ΔE_{int}, eV/BN	-0.351
h-BN reorganization energy $\Delta E_{\mathrm{r}}^{\mathrm{BN}}$, eV/BN	0.001
Cu reorganization energy, $\Delta E_{\mathrm{r}}^{\mathrm{Cu}}$, eV/BN	-0.017
Average *h*-BN–Cu separation, $d_{\mathrm{Cu,BN}}$, Å	3.006
Average B–N buckling, $d_{\mathrm{B,N}}$, Å	0.013
Difference min–max height, $\Delta d_{\mathrm{Cu,BN}}$, Å	0.120
B–N bond length min/avg/max, $d_{\mathrm{B-N}}$, Å	1.450/1.452/1.454

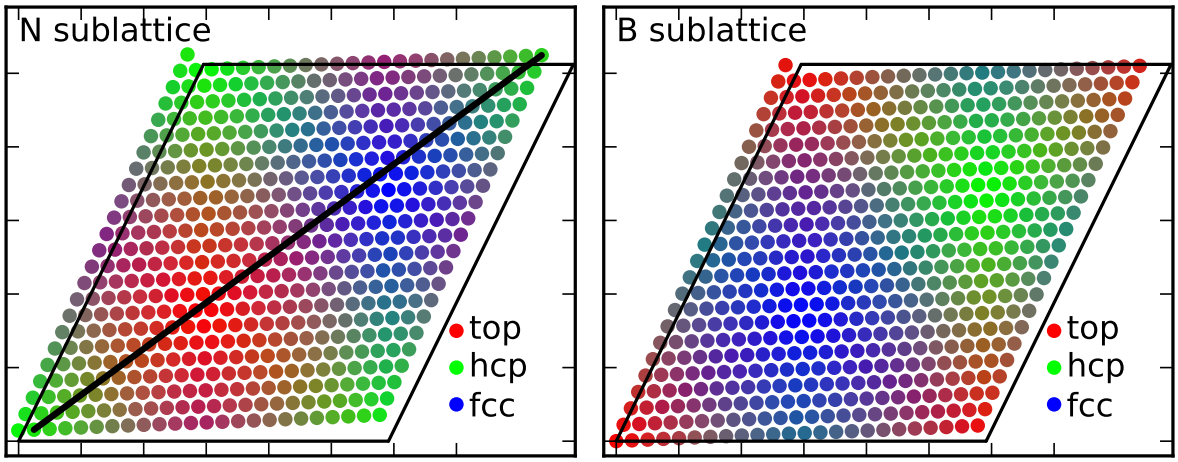

Figure 3.4|Lateral variation of the adsorption registry of the N (left panel) and B (right panel) atoms in the rotated Moiré supercell. The *top*, *hcp*, and *fcc* registries are shown in red, green and blue, respectively. Intermediate color shades indicate atomic positions in-between those registries. The (11) diagonal of the surface as analyzed in the subsequent work is indicated with the black line. The black frame shows the unit cell of the underlying metal substrate. The axis ticks are drawn every 10 Å. Data published in ref. 13.

h-BN–metal interaction, leading to a lack of preferential attraction of particular regions of the cell. In contrast, similar systems of both large and small lattice mismatches tend to be either periodically corrugated (*h*-BN nanomesh[21]) or locally buckled (*h*-BN/Ni(111)[50]).

Laterally, the B–N bond lengths, $d_{\mathrm{B-N}}$, are narrowly distributed around an average value of 1.452 Å, corresponding to a planar lattice constant of 2.515 Å. The additional unit cell compared to the metal (24-on-23) and the rotation of the monolayer thus make it possible to retain a commensurate lattice without an appreciable stretching of bonds to accommodate the 2% mismatch with Cu(111). Also, $d_{\mathrm{B-N}}$ remains uniform across the entire surface area, exhibiting an almost negligible modulation.

The six high-symmetry adsorption registries present in the Moiré system, are described in detail in Section 3.1. For those systems, ΔE_{int} ranges from -0.262 to -0.298 eV/BN, slightly larger than what we obtain for the Moiré cell. However, the monolayer has to stretch by 2% in order to remain commensurate in that case. For free-standing *h*-BN this stretching energy amounts to 0.045 eV/BN, shifting the ΔE_{int} range to bracket the Moiré value. Structural parameters of the large system, such as $d_{\mathrm{Cu,BN}}$ and $d_{\mathrm{B,N}}$, are also within the spread of values from the various 1×1 calculations. Thus, it seems that the Moiré cell averages properties of the different single-registry structures (which are locally present in the supercell). Commensurate adsorption, however, necessitates a much stronger stretching of the overlayer and does not yield the intermediate adsorption registries of the extended Moiré cell.

Based on the mathematical relations for Moiré patterns derived by Hermann,[59] the lattice mismatch and overlayer rotation in the presented system give rise to a "Moiré factor" κ of 23.05, in very good agreement with the actual dimensions of the supercell. Due to the misalignment of the layers, the adsorption registry of *h*-BN varies across the surface of the cell. An atom in the monolayer can occupy positions above one in the first (*top* registry), second (*hcp*), or third (*fcc*) substrate layer, as well as intermediate (*bridging*) sites. Fig. 3.4 shows the registry of each atom in the N- and B-sublattices of the monolayer by color. The lateral distance of an atom to its closest partners in the first three layers is plotted as the red, green, and blue components, respectively. Thus, points with the brightest shade of red indicate atoms closest to *top* positions, *hcp* are green and *fcc* blue. This allows for a straightforward overview of the registries occurring in the supercell.

It is immediately evident that both B and N atoms occupy all three adsorption registries relative to Cu in approximately equal proportions. Additionally, there are boundary regions (3 to 4 BN units wide).

They indicate atoms in bridging and intermediate sites. Note furthermore the differences between the two sublattices, which follow a cyclic pattern; regions with B_{top} contain N_{hcp}, B_{hcp} contain N_{fcc}, and B_{fcc} contain N_{top}. The strongest variation of the adsorption registry occurs along the cell diagonal. Here, both atom species occupy all three registries and the corresponding transition zones. For future reference, the diagonal starting at the top-right nitrogen atom is indicated in the figure with a black line.

Simulated STM Images and Electronic Structure

Figure 3.5(a) shows a simulated STM image for the *h*-BN/Cu Moiré system at a bias of +1.0 V. The image shows a pattern of rounded hexagonal regions with higher STM topography profile (brighter color) surrounded by darker, lower areas. The area directly above the elevated "hill" region contains more pronounced atom-like points with slightly greater height than the rest of the dark areas. The hill is surrounded by a fringe of lower elevation.

The central hill area corresponds approximately to the region with mostly $N_{top}B_{fcc}$ adsorption registry. The other two discernable areas are those with $N_{fcc}B_{hcp}$ (dark red) and $B_{top}N_{hcp}$ (red–orange points) registries. The overall variation of apparent height is approximately 0.3 Å, comparable to what is found experimentally for these bias voltages. As the topographic height is calculated from both the electron density and the electrostatic potential, the structural and electronic corrugations are convoluted. Therefore, the peak-to-peak height difference is larger in the simulated STM than in the optimized structure.

The electrostatic potential (ESP) above the surface can give further insight into the electronic structure of the studied system. Expressed relative to the Fermi energy, it reflects the local work function Φ. Fig. 3.5(b) shows a map of the ESP-derived work function across the surface of the supercell, cut at a height of about 3.4 Å above the *h*-BN layer. The potential varies in a range of 0.14 eV, showing an approximately circular minimum in the region of $N_{top}B_{fcc}$ configurations and a maximum further along the cell diagonal, around the $N_{fcc}B_{hcp}$ atoms. The other areas (of different registry) show roughly intermediate values for the ESP.

The three distinct regions of ESP are largely coincident with the three main areas of different contrast in the simulated STM images, although their shapes tend to be more rounded. The lateral variation in Φ is smaller than that indicated by experiments (0.3 eV[12]), but qualitatively comparable as the hill is characterized by a lower work function than the valley. We find values of 3.64 eV and 3.78 eV for the minimum and maximum work functions, respectively. These values are also somewhat smaller than what is found experimentally (3.8 and 4.1 eV).

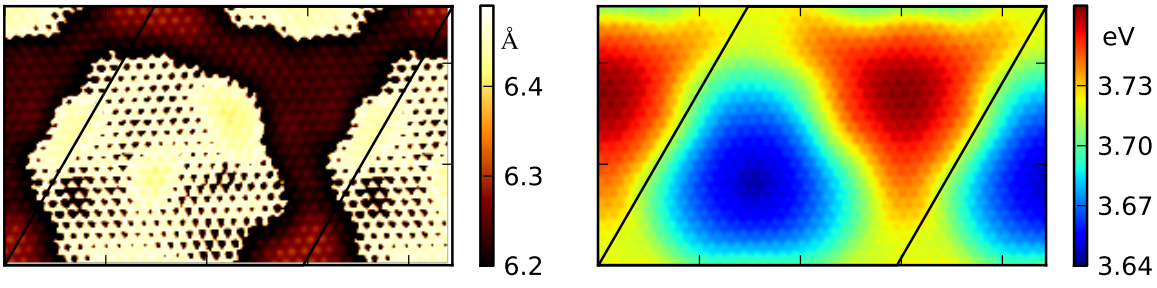

Figure 3.5|(a) Simulated STM using Tersoff-Hamann approximation at a bias of +1.0 V. Color bar is in units of Å relative to the topmost Cu layer, x and y axis ticks at intervals of 10 Å. (b) Lateral map of the electrostatic potential relative to the Fermi energy (eV) at constant height, approx. 3.4 Å above the *h*-BN layer. Both panels show the same lateral area, the black lines indicate the unit cell. Data published in ref. 13.

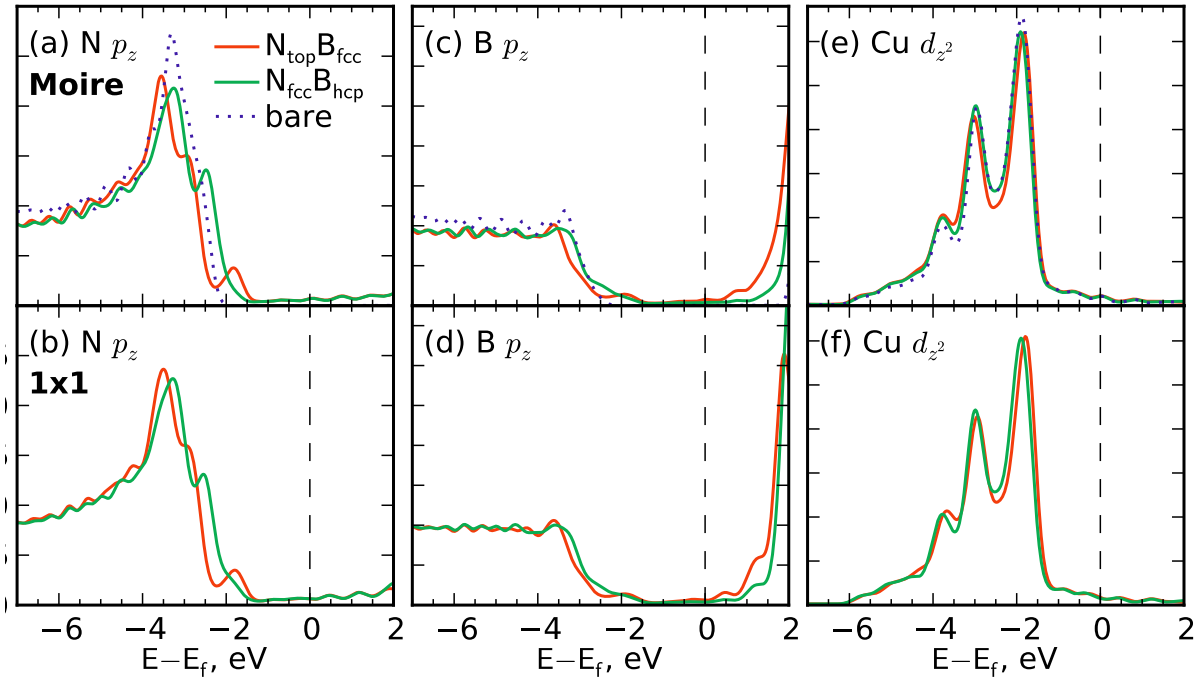

Figure 3.6|Plots of the PDOS projected on various atoms in *h*-BN/Cu in the Moiré (top row) and commensurate adsorption systems (bottom row). Data published in ref. 13.

Fig. 3.6 shows plots of the projected densities of states (PDOS) on various atoms on the cell diagonal. We only indicate those states most strongly involved in the metal–substrate bonding, i.e. the p_z states of B and N and the d_{z^2} states of Cu. We focus on two regions of differing adsorption registry, N_{top} and N_{fcc}, and indicate for comparison the PDOS of these atoms in the isolated BN or metal. The lower panels in Fig. 3.6 show the PDOS from commensurate (6×6) calculations of $N_{top}B_{fcc}$ and $N_{fcc}B_{hcp}$ arrangements.

The PDOS on nitrogen appears to be the one most affected by binding to the substrate. Compared to the p_z states of the free-standing layer, the main band at approx. -3 eV broadens and lowers upon adsorption, indicating some polarization away from N. An additional peak at about -1.9 eV appears in the PDOS of N in the *fcc* position, absent from both the *bare* and the $N_{top}B_{fcc}$ curves.

As this N atom is closest to the underlying Cu in the topmost layer, this peak presumably appears due to the increased interaction with the metal orbitals. Besides the emergence of this new feature, the p_z bands are also shifted by approximately 0.2 eV. The $N_{top}B_{fcc}$ curve remains closer to the Fermi level, and is even somewhat up-shifted from the band of the free monolayer. Note, however, that the N_{top} region of the cell has a lower work function. The down-shift of the N_{top} band and the emergence of the additional small peak can also be seen in the corresponding 1×1 PDOS data. This would indicate that the local environment within the Moiré pattern is the major influence on the PDOS.

The PDOS for the B atoms in the same regions are shown in Fig. 3.6(c). Here, amplitudes are lower by approximately a factor of 2 from the nitrogen case, and the curves are generally flat, with a gentle onset between -2 and -4 eV. The effect due to the adsorption is less visible, but we still observe a lowering and broadening of the PDOS curve. It should be noted that here B is found in B_{fcc} and B_{hcp} positions, being in both cases laterally distant from the topmost Cu, which presumably leads to weaker interactions. Close similarities with the 1×1 PDOS are also evident here, such as the relative shift of peaks and the position and width of the band gap.

The metal d_{z^2} states (Fig. 3.6(e)) appear to be least affected by the adsorption of the monolayer. The bands largely retain their double-peak structure and do not shift. Only a small depletion may be

observed in the N_{top} case, hinting at the polarization from N to Cu noted above. By and large, the situation on the Moiré is comparable to the 1×1 case, with some small changes in the finer structure of the features.

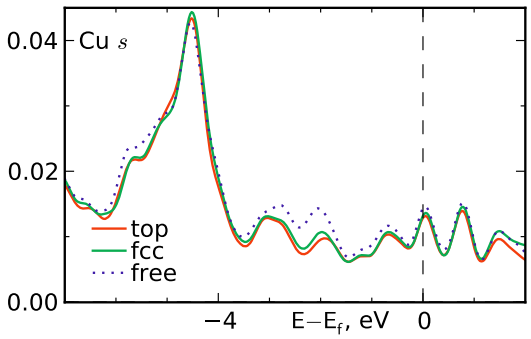

Figure 3.7|4s PDOS for Cu atoms on the diagonal of the Moiré supercell in the N_{top} and N_{fcc} regions and a free surface for comparison. Vertical axis in units of states/eV. Data published in ref. 13.

It has been suggested[23] that the Cu d_{z^2} orbitals are largely unaffected by the *h*-BN–substrate interaction, which is instead dominated by p_z–4s hybridization. In Fig. 3.7 we show the 4s PDOS of surface Cu atoms on various positions of the cell diagonal and a free surface. Our data support the notion that p_z–4s interactions dominate, showing on the one hand only marginal changes in the d_{z^2} bands, and on the other hand, a lowering and broadening of the 4*s* states in the range between -4 and -2 eV. This is indeed evidence of some s–p_z hybridization, which, although subtle, is the major contribution to the binding between monolayer and substrate aside from the van der Waals interaction. Also these states remain mostly unaffected by a change of the N registry, showing only slight broadening in the N_{top} configuration, compared to the N_{fcc} case.

Our results are in good agreement with electronic-structure data published by Laskowski and coworkers.[37] Qualitatively, our data confirm that the DOS of the metal surface remains mostly unchanged upon adsorption and that changes are minor also in the adlayer. However, they only report adsorption in one registry, so that the effect of the relative placement of *h*-BN cannot be directly compared. Also quantitatively, our results are similar to theirs, with Cu-d_{z^2} band onsets just above -2 eV, a N-p_z peak at roughly the same position, and the gentle B-p_z onset between -4 and -2 eV.

Relationships Between the Geometric and Electronic Structure

As shown in the preceding sections, the electronic structure varies across the Moiré supercell, while the adsorbed monolayer is largely flat throughout. Our results are thus in contrast to previous studies of related adsorption systems, which have commonly rationalized a corrugation of the electronic structure with the pronounced concomitant corrugation of the monolayer.[39,163,164] From a comparison of Figs. 3.5(a) and (b) with Fig. 3.4, it becomes evident that the patterns of the electronic structure resemble those produced by the lateral variation of the adsorption registry. It has already been suggested[12] that the modulation of the registry is responsible for the observed electronic corrugation of the surface. In this context our calculations serve to provide an atomic-scale rationalization for this observation.

The most pronounced variation of the adsorption registry occurs along the diagonal of the surface (*vide supra*), which we therefore examine in greater detail as a model for the entire supercell. In the top-left panel of Fig. 3.8 we plot the lateral distance of N atoms to their closest partners in the *top, hcp* and *fcc* layers along the diagonal (black line in Fig. 3.4). For comparison, the vertical distance d_{Cu} to the metal surface is also plotted on the same vertical scale (shifted down by 2.5 Å). This plot illustrates the registry variation in greater detail than Fig. 3.4; the lower a point, the closer is a particular N atom to the ideal registry of that layer. We observe three minima, corresponding to almost "pure" N_{top}, N_{hcp}, and N_{fcc} sites and three intersections of curves indicating interstitial positions. Over the same lateral distance, the topographic height remains largely unchanged, with a peak-to-peak difference of 0.12 Å. The right panel in Fig. 3.8 shows the analogous plot for the registry of B along the same diagonal. The same picture emerges, with the exception of a phase shift, putting the B_{fcc} minimum at the position of the N_{top} minimum, corresponding to the co-occurrence of these registries noted above.

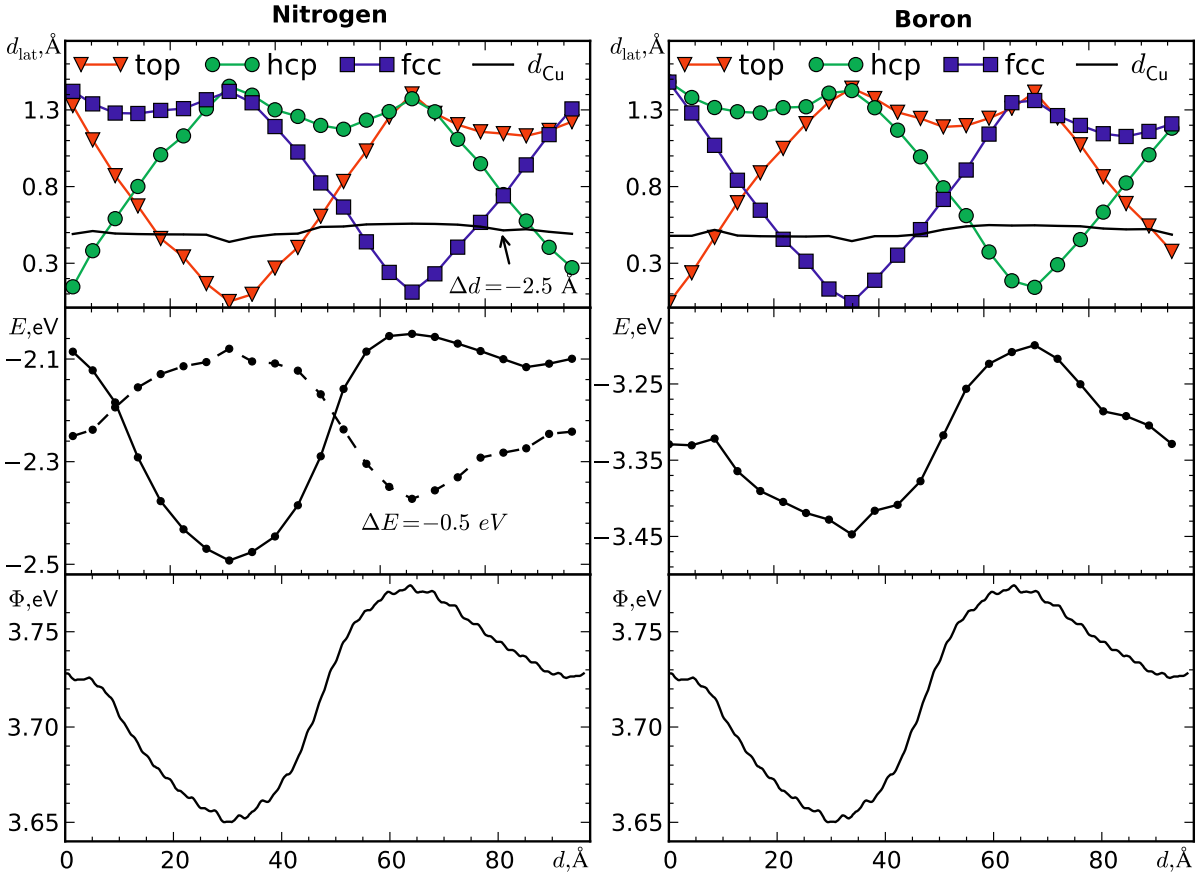

Figure 3.8|Relationship between the geometric and electronic structure in the *h*-BN Moiré on Cu(111) along the cell diagonal indicated in Fig. 3.4. Left panel, from top to bottom: Lateral distance (Å) of N atoms to the closest atoms in the underlying *top*, *hcp*, and *fcc* layers and vertical distance d_{Cu} to the surface. Energy (eV) of the p_z flank (continuous line) and peak (dashed line) onsets of PDOS projected on N atoms along the cell diagonal. Local work function, Φ, from electrostatic potential at 3.4 Å above the surface. Horizontal axis shows distance (Å) from the bottom left N atom in the cell. Right panel, from top to bottom: Lateral distance of B atoms, as in left panel. Energy (eV) of the p_z flank onset in B-PDOS. Local work function as in left panel. Data published in ref. 13.

In the preceding discussion of the p_z PDOS of nitrogen, we remarked the shift of the band onset and emergence of a small secondary peak for two registry extremes. The second plot in the left panel of Fig. 3.8 shows the position (in eV) of the flank of the band onset and the position of the peak in the PDOS projected on each atom along the diagonal. For this purpose, we have arbitrarily defined the onset of the flank (E_{fl}) as the point where the value of the PDOS is equal to 0.040 states/eV, and the onset of the peak (E_{p}) as the point with a value of 0.020 states/eV. E_{fl} varies in a range greater than 0.4 eV, with one pronounced minimum, while E_{p} follows an inverted trend with a somewhat smaller range of onset energies. By comparing this plot with the variation of the surface registry, it is obvious that E_{fl} closely tracks the curve of the *top* registry, and E_{p} follows it with the opposite sign. Thus, at the point where the N atoms are closest to an underlying Cu, their p_z flanks are most strongly shifted to lower energies, while the smaller feature is closest to the Fermi level. In the opposite extreme of a large lateral N–Cu separation, the two features are closest together and the peak disappears into the flank (note the shift of curves in Fig. 3.8).

Evidently, the distance between an N atom and its closest Cu strongly influences the local electronic structure of that atom. In the present system, however, it is the lateral rather than the vertical distance which is responsible for the shift of the PDOS features, as it is much more strongly modulated along the

cell diagonal. Additionally, when the metal slab is removed, the variation of the electrostatic potential is reduced by a factor of 3.5, confirming that the monolayer corrugation plays a minor role in modulating the electronic structure.

For the B atoms along the cell diagonal, only the position of the PDOS flank (E_{fl}) is modulated with position, as shown in the middle right panel of the same figure. Here, E_{fl} is defined as the position where the PDOS has a value of 0.035 states/eV. The curve follows a similar trend as the corresponding one in the left panel, but the magnitude of the modulation is approximately half of that observed for the N atoms. E_{fl} is minimal in the $\mathrm{N}_{top}\mathrm{B}_{fcc}$ region, and has a maximum at $\mathrm{N}_{fcc}\mathrm{B}_{hcp}$. The modulation of the B p_z onset may be an effect related to the adjacent polarized N atoms that propagates to B.

The bottom panels in Fig. 3.8 show a cut through the electrostatic potential (cf. Fig. 3.5(b)) on the cell diagonal, 3.4 Å above the surface. While the variation is smaller than that based on the PDOS features, it also follows the same characteristic trend related to the N_{top} registry. Thus, the work function reaches a minimum at N_{top} and a maximum at $\mathrm{N}_{\mathrm{fcc}}$ positions. We relate this to the trend of E_{fl}, indicating that the conduction band is down-shifted furthest exactly at positions of smallest Φ, and vice versa. The absolute value of the work function should decrease as cuts of the electrostatic potential are considered further away from the surface. This is also the reason why the peak-to-peak difference of the ESP gets progressively smaller at larger distances, as the local features of the electronic structure are increasingly smeared out. A difference of 0.14 eV at 3.4 Å is reduced to 0.092 eV at 4.8 Å and 0.073 eV at 6.3 Å.

Based on these data, it becomes evident that the adsorption registry connects the electronic structure with the underlying geometry. The lattice mismatch and rotation of the monolayer cause a modulation of the adsorption registry over the cell. This in turn results in a periodic variation of the (lateral) B,N–Cu distances, changing the hybridization between metal and BN. Consequently, features of the PDOS change depending on the position of each atom, resulting finally in a modulated electrostatic potential at considerable distance above the surface. Therefore, the experimentally observed electrostatic corrugation can originate without significant structural changes.

Adsorption and Electronic Level Alignment of Porphine on *h*-BN/Cu

The electronic corrugation of *h*-BN/Cu combined with the weak metal-substrate interaction and the inertness of *h*-BN make this material a good candidate as adsorption substrate. Templating and selective adsorption are essential for nanoscience applications.[7] Here, the electronic corrugation and topographical flatness consititute an ideal combination: adsorbed molecules are not sterically confined by the substrate, but experience a modulated electronic environment that may serve to align them. On the other hand, the *h*-BN layer serves as an insulating sheet that decouples adsorbates from the metal, which can protect the substrate from degradation by reactive molecules, and the adsorbate from defects in the metal.

A number of studies have investigated epitaxial graphene and *h*-BN for their potential of aligning and supporting adsorbates. For instance, the topographical corrugation of the *h*-BN nanomesh has been used to align and confine various adsorbates.[40–42] The Moiré superstructure of graphene on Rh(111) was used as an adsorption template for PTCDI molecules to align them as extended arrays.[165] Ruthenium-supported graphene was used to confine and separate individual TCNQ molecules and to induce long-range magnetic order.[166] Schulz et al. investigated cobalt-phthalocyanine on Ir-supported *h*-BN, a rather similar system to the one presented here.[27] At low coverage they observed that the Moiré superstructure favors adsorption of the molecules in the pores. In denser layers the electronic structure of the molecule is altered based on its lateral position on the Moiré pattern, as evidenced by a change of the STM contrast.[27] Very recently, the *h*-BN/Cu heterostructure was also utilized to control the formation of extended networks resembling 2D MOFs.[167]

Experimental Results

Free-base porphine (2H–P, Fig. 3.9) is the simplest member of the porphyrin family, a very common class of compounds in biological systems.[168] Numerous reports of adsorbed porphyrins as arrays, chains, and supramolecules have been published.[169–174] 2H–P itself has been studied less extensively. Some studies have reported about the adsorption of 2H–P on Cu(110)[174] and Cu(111),[175] as well as on Ag(111).[176] The adsorbed molecules undergo significant electronic changes induced by the metallic substrate and tend to repel each other, preventing the formation of islands or even networks (Fig. 3.10(a),(b)).[176]

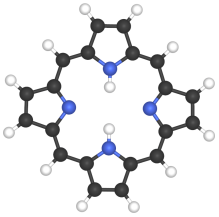

Figure 3.9|Molecular structure of free-base porphine, 2H–P. Atom colors: N, blue; C, black; H, white.

Auwärter and co-workers studied 2H–P adsorbed on the *h*-BN/Cu Moiré system described previously.[14] The molecules were deposited using organic molecular beam epitaxy at elevated temperatures and then analyzed by STM and STS at 6 K. Fig. 3.10(c) shows individual 2H–P molecules and the underlying corrugated surface. At low coverage the porphines preferentially adsorb on the hills of the Moiré pattern, forming small aggregates. The trapping of the molecules was confirmed by inducing the 2H–P to jump by injecting electrons from the stationary STM tip. They remained within the hill area throughout.[14]

Fig. 3.11(a) shows dI/dV spectra of 2H–P on various substrates, as well as of bare *h*-BN/Cu. When the molecule is in direct contact with a metal substrate (Ag, Cu), the spectrum appears featureless, without obvious resonances. In contrast, two sharp peaks are observed for 2H–P on *h*-BN/Cu, at bias voltages -2.4 and 1.45 V, indicating a HOMO-LUMO gap of ∼3.5 eV. The smaller features within the gap can be attributed to the substrate. This leads to the conclusion that the porphine is largely decoupled from the metal by the *h*-BN layer. The 2H–P molecules show a certain amount of intramolecular contrast, depending on the bias voltage (Fig. 3.11(b)). At biases below the gap resonance, the molecule exhibits a fourfold symmetry, analogous to the HOMO of isolated porphine as calculated with DFT.

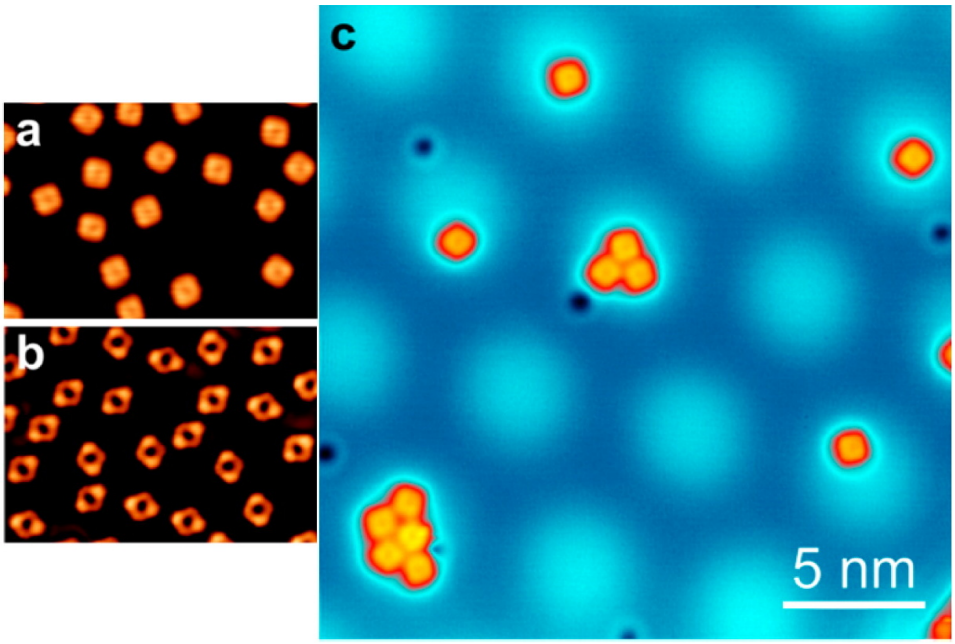

Figure 3.10|(a) STM image of 2H–P on Ag(111), V_b = -0.8 V. (b) STM image of 2H–P on Ag(111), V_b = -0.1 V. The molecules repel each other, preventing aggregation and island formation. (c) Trapping of 2H–P on the hills of *h*-BN/Cu(111), formation of small aggregates. Image adapted from ref. 14.

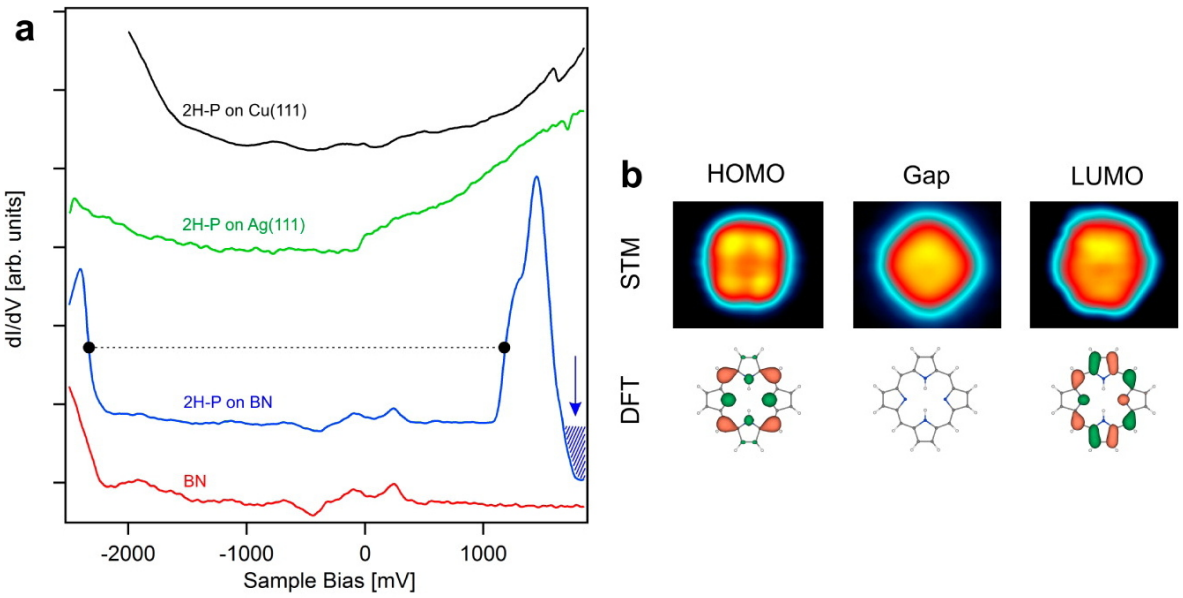

Figure 3.11|(a) dI/dV spectra of adsorbed 2H–P on Cu(111) (black), Ag(111) (green), *h*-BN/Cu and of bare *h*-BN/Cu (red). An electronic gap is only seen for 2H–P on *h*-BN/Cu, indicated by dashed line. (b) STM images of a 2H–P monomer on *h*-BN/Cu at -2.45 V, 1.0 V, 1.25 V and HOMO and LUMO of 2H–P from our DFT calculations. Image adapted from ref. 14.

With bias voltages within the gap, the molecule looks like a square, without intramolecular features. At higher bias, the molecule is characterized by two-fold symmetry, in agreement with the calculated LUMO. One can thus identify the resonances in panel (a) with the HOMO and LUMO of adsorbed 2H–P.

Besides the pronounced trapping of the molecules (which in turn led to cluster formation on the hill areas of the surbstrate), it was also observed that the molecules appear differently, depending on their lateral position. In a range of bias voltages between 0.9 and 1.65 V, the apparent height of porphine molecules varied with their distance from the center of the hill area. From dI/dV spectra of porphins at different lateral positions, it was observed that the LUMO-related peak appeared at different energies. For 2H–P at the center of the hill, the LUMO is found at a 0.3 eV lower energy than for 2H–P on a "bridge" site. The position-dependent apparent height of the molecules could thus be rationalized with this LUMO shift, which is induced by the modulation of the surface potential of *h*-BN/Cu.[14]

Adsorption Properties from DFT

Using commensurate adsorption models in the $N_{top}B_{fcc}$ and $N_{fcc}B_{hcp}$ registries as well as the computational model of the *h*-BN/Cu Moiré system described before, we simulate the position-dependent adsorption of 2H–P on *h*-BN/Cu. Of particular interest were the adsorption and interaction energies of the molecule on *h*-BN/Cu, the structure of the system, as well as the effect of the adsorption position (i.e. the registry of the underlying *h*-BN) on the porphine's electronic properties.

Isolated 2H–P is optimized in the gas phase, in order to characterize its electronic structure. The HOMO-LUMO gap of the molecule is found to be 1.93 eV, significantly smaller than the reference values of 5.2 and 5.3 eV from high-accuracy calculations.[177] This quantity is generally underestimated by GGA methods, such as the one used here. The experimental gap of 3.5 eV on the *h*-BN/Cu substrate was rationalized to be smaller due to interactions with the support.[14] As discussed above, the calculated HOMO and LUMO wavefunctions of 2H–P are in good agreement with the STM results in terms of symmetry and appearance.

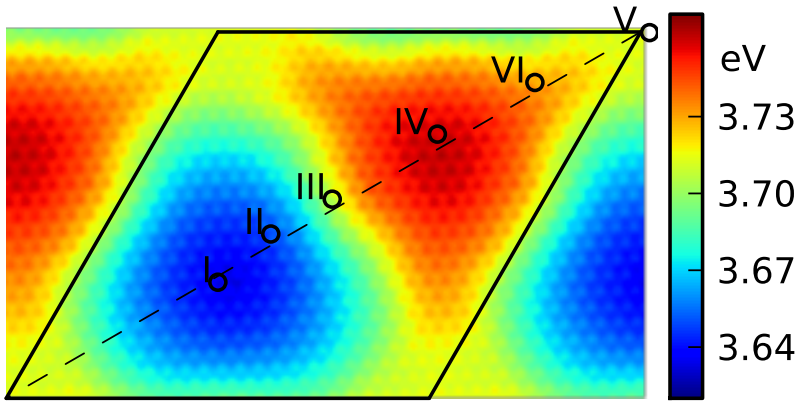

(a)

Point	Site	ΔE_{int}, eV
I	hill	-2.040
II	rim	-2.042
III	bridge	-2.013
IV	valley	-2.014
V	bridge	-2.040
VI	bridge	-2.025

(b)

Figure 3.12|(a) Map of the local work function Φ, i.e. a slice of the local ESP - E_f 3.4 Å above the *h*-BN surface (at the height of the porphine molecules). Continuous lines indicate the unit cell of the substrate, dashed line indicates the surface diagonal, with points I–VI on which the porphine molecule is placed. (b) Site types and interaction energy of 2H–P on points I–VI along the Moiré diagonal. Data published in ref. 14.

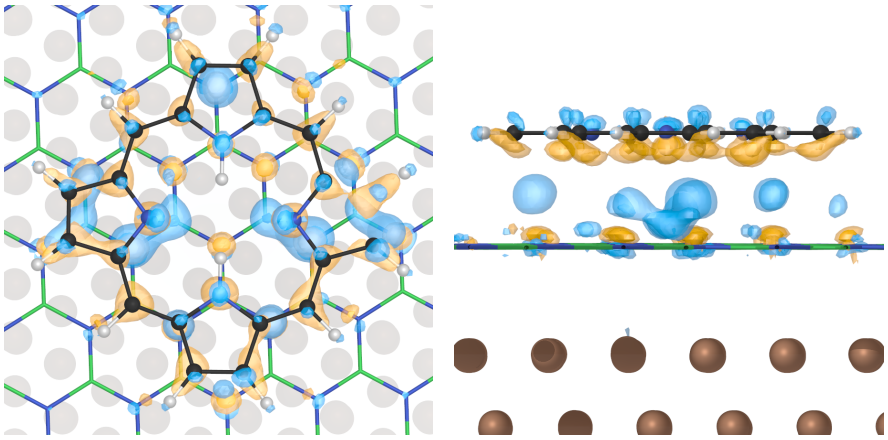

(a) (b)

Figure 3.13|Electron density difference for 2H–P on *h*-BN/Cu Moiré. Isosurfaces of positive (i.e. electron accumulation) and negative (electron depletion) differences shown in blue and orange, respectively. Isovalues at ± 0.001 e/Bohr^3 and ± 0.0005 e/Bohr^3. (a) Top view. (b) Side view. Atom colors: B, green; N, blue; Cu, brown; C, black; H, white.

2H–P is placed atop commensurate *h*-BN/Cu(111) in the $N_{top}B_{fcc}$ and $N_{fcc}B_{hcp}$ registries, with the porphine N atoms laterally close to underlying B atoms and the structure fully optimized. The molecule remains flat, at a distance of 3.20 Å above the *h*-BN layer. ΔE_{ads} for both adsorption registries are nearly indistinguishable: -1.932 eV for $N_{top}B_{fcc}$ and -1.933 eV for $N_{fcc}B_{hcp}$. The major contribution to these values is the van der Waals energy, amounting to -3.349 eV ($N_{top}B_{fcc}$) and -3.196 eV ($N_{fcc}B_{hcp}$). At this optimized geometry, the electronic contribution to ΔE_{ads} is positive, and exactly compensates the difference in ΔE_{vdW}. Thus, the trapping of 2H–P on specific areas of the Moiré pattern cannot be rationalized with differing ΔE_{ads} (for the small commensurate models). The variation of the *h*-BN registry also has a negligible effect on the peak positions in the PDOS on the porphine atoms.

Based on the optimized geometry of 2H–P on commensurate *h*-BN/Cu, the molecule is then placed at various positions (I–VI, Fig. 3.12(a)) atop the large Moiré cell. Vertically, the molecule is kept at

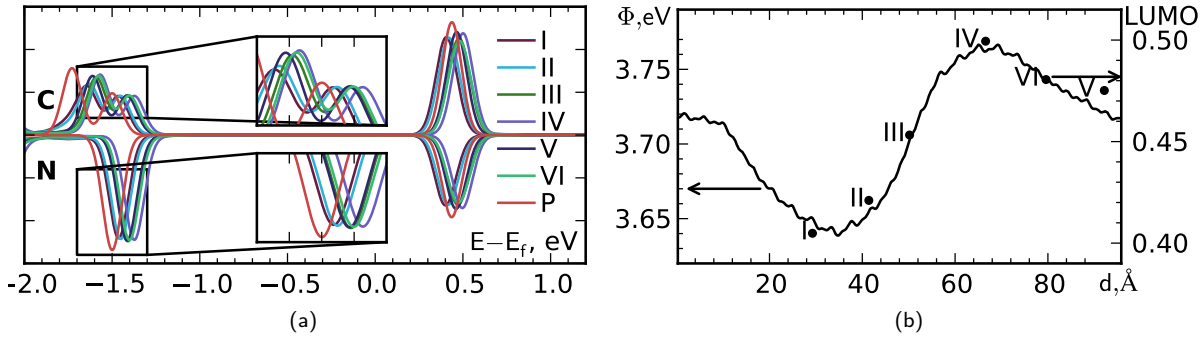

Figure 3.14|(a) PDOS on C (positive y axis) and N (negative y axis) atoms of 2H–P placed at points I–VI on the Moiré surface. PDOS of free 2H–P plotted for comparison (curve "P"). Insets show zooms around HOMO peak. (b) Position of LUMO peak of 2H–P at points I–VI (right vertical axis), superimposed on the ESP-derived work function at the height of the porphine molecule (continuous line, left vertical axis). Data published in ref. 14.

the optimized distance. Due to the prohibitive computational cost, full geometry optimizations were not performed for this system. However, in all but two cases the residual average forces on the 2H–P molecule are less than 10^{-4} hartree/bohr. When they exceed that threshold, the molecule is vertically moved by at most 0.1 Å to manually reduce the forces. This manual approach can be considered an adequate optimization for this system.

The table in Fig. 3.12(b) presents the interaction energies ΔE_{int} for 2H–P at the different points of the surface, as well as an approximate identification of the adsorption site as hill, valley, rim or bridge site. The variation in ΔE_{int} with the lateral placement of the molecule is very small, with only 0.027 eV separating the most and least stable positions. The van der Waals energy dominates the interaction.

An electron density difference plot for this system is shown in Fig. 3.13. The amount of charge redistribution upon adsorption of the molecule is small, with all changes confined to the porphine and the *h*-BN sheet. A small accumulation of charge occurs in the space between the substrate and adsorbate, while 2H–P is polarized vertically, with excess charge pointing to the vacuum and charge depletion on the underside. Placement of the molecule at different lateral positions on the Moiré does not result in significant changes of the electron density difference.

Electronic Properties from DFT

While DFT calculations cannot confidently reproduce the trapping effect observed experimentally on *h*-BN/Cu, they show the effect of the molecule's lateral position on its electronic structure. The adsorption positions I–VI are placed on the diagonal of the Moiré cell, where the electronic corrugation, i.e. the variation of the local work function Φ, is the strongest (Fig. 3.12(a)). Φ varies from 3.64 eV on the hill area to 3.77 eV in the valley, a range of 0.13 eV, approximately 43% of the experimental value (0.3 eV).

The resulting curves in the region of the band gap are plotted in Fig. 3.14(a) with the PDOS of the gas phase molecule for comparison. Depending on the position of the molecule, the HOMO and LUMO peaks are shifted over a range of about 0.1 eV. In particular, the HOMO and LUMO at point IV are at the highest energies, while at point I they are the lowest.

Fig. 3.14(b) shows Φ along the cell diagonal, with the LUMO positions superimposed. The LUMO energy is strongly correlated with Φ at the height of the 2H–P molecule, i.e. with its lateral position on the electronically corrugated surface. In positions with low Φ, the LUMO peak is found at lower energies, and in positions with high Φ at higher energies. The variation of LUMO energies is a factor of 3 smaller than experimentally observed, but qualitatively reproduces the trend well. Also spatially the

calculations agree well with the points sampled by STS, as the lowest LUMO is found on the hills, and is shown to increase in the direction away from them.

Summary: The Electronic Corrugation of h-BN on Cu(111)

h-BN binds weakly to Cu(111) *via* predominantly dispersive interactions. The small lattice constant mismatch of 2 % combined with a rotation of the overlayer leads to Moiré superstructures with long periodicities. DFT calculations of a 24-on-23 superstructure reveal a lateral modulation of the local work function in the absence of structural buckling in agreement with STM experiments. We rationalize this with the varying lateral distance of B and N atoms to the top metal layer, which leads to local modifications of the electronic structure (as seen in the PDOS) that, in turn, alter the local work function. The electrostatic potential modulation is also reflected in the orbital energies of porphine adsorbed on *h*-BN/Cu, which vary by 0.1 eV depending on the lateral position of 2H–P.

3.3 The Oxygen Reduction Reaction on *h*-BN/Metal

Based on reference 86.

In the final part of the preceding section, we presented evidence, that *h*-BN/Cu(111) can successfully be used as an substrate for molecules. We now explore the potential of metal-supported *h*-BN beyond simple adsorption, namely for small-molecule activation and catalysis. For this study we choose the O_2 molecule and its reduction to water, which is briefly introduced in the following.

Sustainable power generation beyond fossil fuels is a critical necessity for the future, particularly in the transportation sector. Fuel cells that produce electricity from the reaction of hydrogen and oxygen constitute one of the most promising options for this purpose.[178] The overall reaction for this process is

$$2H_2 + O_2 \rightarrow 2H_2O + 4.92\,\text{eV}.$$

A schematic of a fuel cell is shown in Fig. 3.15. The set-up consists of an anode and a cathode, separated by an electrolyte membrane. Gaseous H_2 enters the cell at the anode where it is oxidized to protons.[178] They migrate through the electrolyte layer, while the electrons pass through an external circuit (at a potential of 1.23 V) and power an electrical appliance. At the cathode, both protons and electrons then react with gaseous O_2 to yield water. Overall, the fuel cell consumes H_2 and O_2, and emits water, electricity and heat.[178]

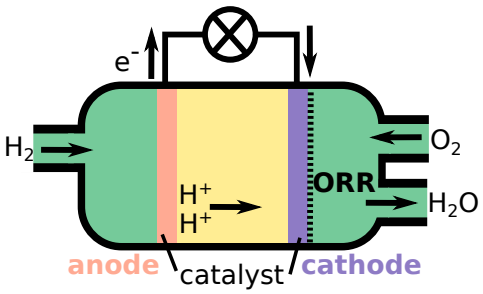

Figure 3.15|Schematic of a hydrogen/oxygen fuel cell. See text for details.

H_2 oxidation at the anode is comparatively fast and straightforward.[179] The key process occurring at the cathode is the electrochemical reduction of O_2 to H_2O, the so-called *oxygen reduction reaction* (ORR). This 4-electron, 4-proton process is slow and impeded by high electrode overpotentials. In order to make it practically viable, suitable catalysts have to be employed that are efficient, stable, and cost-effective.[180] Scarce metals such as palladium and platinum are currently most often used, leading to a high overall cost that prevents widespread adoption.[178,181,182] While Pd and Pt can be alloyed with other metals to reduce cost and increase efficiency,[183–185] alternative catalysts based on non-precious metals or metal-free materials are still highly desirable.

Research into advanced ORR catalysts is on-going. Catalysts based on doped carbon materials such as nanotubes and graphene have been experimentally[186–188] and computationally[189] shown to be par-

ticularly promising. Metal-supported *h*-BN is also a good candidate for O_2 activation and ORR catalysis. It was found that *h*-BN has to be supported on a (transition) metal to show catalytic activity, as free-standing *h*-BN is inactive.[190] In particular, *h*-BN/Ni has been predicted to favorably adsorb and activate[52] O_2, and has also been investigated for the ORR.[54] Moreover, *h*-BN/Au(111) has been investigated experimentally, and shown to significantly reduce the ORR overpotential compared to unfunctionalized Au.[191] *h*-BN/metal heterostructures thus have the potential to serve as alternatives to current precious-metal ORR catalysts.

The computational hydrogen electrode (CHE) is a model to compute electrochemical potentials from calculated free energies (from DFT).[192] The CHE has been successfully applied to the ORR on transition metals,[192] transition-metal oxides,[193] and doped carbon materials[189] as well as for other electrochemical processes like CO_2 and N_2 reduction.[194,195] Within this model, zero voltage is defined based on the reversible hydrogen electrode, where the protons and electrons are in equilibrium with gas-phase H_2 so that the chemical potential of a proton/electron pair equals 1/2 H_2(g). The influence of the applied potential can then be calculated from

$$\Delta G = -eU\,, \tag{3.1}$$

where e is the number of transferred electrons and U is the applied potential.[192] The ideal ORR catalyst should exhibit a free energy difference as close as possible to the reversible potential (-1.23 V) of the ORR between each intermediate step. Deviations from this optimal behaviour lead to an undesired overpotential for the reaction.

This section describes the adsorption of molecular O_2 on *h*-BN/Ni, *h*-BN/Co, and *h*-BN/Cu. The free energy profiles of the ORR on these materials are presented. Using the CHE, we calculate the overpotentials necessary to drive the ORR. We then analyze the available data to investigate trends and correlations that might be exploited to optimize the design of *h*-BN-based catalysts.

Adsorption and Activation of O_2

For the ORR to proceed, O_2 has to be adsorbed on the *h*-BN/metal surface, and be activated. Assuming a *side-on* binding of O_2 on BN, four adsorption configurations are possible in high-symmetry positions: The O_2 molecule can bridge two B atoms (denoted O_2-BB), two N atoms (O_2-NN), or a B-N pair, either adjacent (O_2-BN) or across a hexagon (O_2-BN') of the BN honeycomb. Fig. 3.16 shows these adsorption configurations schematically.

All calculations presented in this section are carried out with the BEEF-vdW set-up described in Section 2.3. O_2 was placed in the four configurations, 2 Å above the *h*-BN surface and the structure was subsequently fully relaxed. The adsorption energy of the molecule is defined as $E_{\mathrm{ads}} = E_{\mathrm{O_2/BN/M}} -$

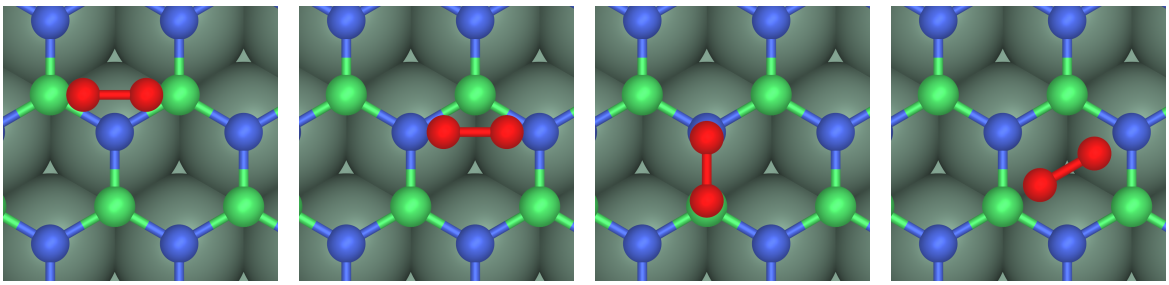

(a) (b) (c) (d)

Figure 3.16|Four binding configurations of O_2 on *h*-BN/Ni(111): (a) O_2-BB, (b) O_2-NN, (c) O_2-BN, (d) O_2-BN'. Atom colors: B, green; N, blue; metal, grey-green.

Table 3.8|Adsorption Energy E_{ads} (eV) of O_2 in various binding configurations on free-standing *h*-BN and *h*-BN/metal substrates. See Fig. 3.17 for sketches of the optimized positions of the molecule.

	h-BN	*h*-BN/Ni(111)	*h*-BN/Cu(111)	*h*-BN/Co(0001)
BB	-0.960	-2.043	-0.559	-1.971
NN	-0.954	-1.016	+0.058	-0.760
BN	+1.657	-1.278	+1.308	-1.288
BN'	-0.960	-1.451	+0.047	-1.342

$E_{\mathrm{BN/M}} - E_{\mathrm{O_2}}$, where $E_{\mathrm{O_2/BN/M}}$ is the total energy of the optimized system, $E_{\mathrm{O_2}}$ is the gas-phase energy of O_2, and $E_{\mathrm{BN/M}}$ is the energy of the optimized bare *h*-BN/metal heterostructure (or free-standing *h*-BN).

Table 3.8 presents an overview of the adsorption energies of O_2 in the 4 configurations on a free-standing *h*-BN sheet, *h*-BN/Ni(111), *h*-BN/Cu(111), and *h*-BN/Co(0001). O_2 binds weakly on free-standing *h*-BN, the value of ΔE_{ads} being around -0.95 eV for all adsorption configurations, except O_2-BN. ΔE_{ads} is almost +1.7 eV in the latter case, indicating a thermodynamically unbound state. The interaction of O_2 with free *h*-BN is thus weak and unlikely to lead to favorable activation of the molecule.

On all metallic substrates, the O_2 molecule binds most strongly in the BB configuration, with a difference of at least 0.5 eV to the nearest other ΔE_{ads}. *h*-BN/Ni and *h*-BN/Co show rather similar ΔE_{ads} values for all configurations. NN is the weakest, while the two BN configurations exhibit intermediate binding energies, around -1.2– -1.4 eV. In the case of *h*-BN/Cu, all configurations except O_2-BB lead to positive ΔE_{ads}, i.e. thermodynamically unfavorable interaction. ΔE_{ads}(O_2-BB) is also considerably weaker than for the other substrates.

Fig. 3.17 shows the optimized structures of O_2 on all substrates. On free-standing *h*-BN, O_2 typically is not adsorbed but remains far from the substrate at a distance of 3.3 Å from the nearest atom, and a bond length $d_{\mathrm{O,O}}$ practically unchanged from its gas-phase value (1.22 Å). The *h*-BN layer remains unperturbed by the O_2 molecule in its proximity. The O_2-BN configuration is the exception to this trend. In this case, O_2 is close to the substrate, with the O atoms at a distance of 1.52 Å to B and N and a bond length $d_{\mathrm{O,O}}$ = 1.48 Å. The large positive ΔE_{ads} (*vide infra*), indicates that this is not a stable structure, but rather a shallow local minimum.

On *h*-BN/Ni, the four starting configurations converge to rather different final structures. In the BB configuration, both O atoms remain close to the BN surface, which undergoes some distortion (*vide infra*). In contrast, the O_2 that was initially placed in the NN configuration detaches from the surface and comes to reside at a distance of 3.25 Å from the closest N atom. The molecule remains parallel to the surface, which stays flat and unperturbed. In the BN and BN' configurations, one O atom is attracted to the closest B atom, while the other points away from the surface at a small angle. The B–O distance is about 1.55 Å for both configurations, and the second O is either parallel to a B–N bond or oriented towards the middle of the B_3N_3 hexagon.

The optimized structures of O_2 on *h*-BN/Co(0001) are very similar to those on *h*-BN/Ni, as expected from the similar properties of the free heterostructures.

O_2 adsorption on *h*-BN/Cu(111) shows characteristics of both the adsorbed structures on free *h*-BN and *h*-BN/Ni. The NN and BN' configurations converge to weakly bound O_2 at a large distance (3.30 Å) from the surface. Similar to free-standing *h*-BN, O_2 binds differently in the BN configuration, with O atop N and B atoms and short bond lengths. Also in this case the adsorbed structure is not a stable minimum. The BB configuration, in contrast, resembles the situation on *h*-BN/Ni and *h*-BN/Co. The oxygen molecule is stretched and the substrate distorted as described below.

Only the BB configuration is considered for further analysis, as it is the most stable one. Table 3.9

Table 3.9|Adsorption energetics (ΔE_{ads}, ΔG_{ads} at 298 K, in eV), structural properties (O–O, O–B, B–B distances, d, in Å) and (average) Bader charges q for O_2 adsorbed on *h*-BN/metal substrates (OO-BB configuration). Data published in ref. 86.

	h-BN/Ni(111)	*h*-BN/Cu(111)	*h*-BN/Co(0001)
ΔE_{ads}	-2.043	-0.559	-1.971
ΔG_{ads}	-1.252	+0.243	-1.184
$d_{\mathrm{O,O}}$	1.51	1.51	1.50
$d_{\mathrm{B,O}}$	1.48	1.49	1.48
$d_{\mathrm{B,B}}$	2.33	2.33	2.30
$q_{\mathrm{O_2}}$	-1.15	-1.16	-1.13
q_{B}	+2.93	+2.94	+2.87
q_{N}	-2.60	-2.53	-2.56

shows the properties of O_2 on the three substrates in greater detail, giving the adsorption free energy ΔG_{ads}, bond lengths, and the Bader charges of the involved elements. ΔG_{ads} on both *h*-BN/Ni and *h*-BN/Co is approximately 1.2 eV, while it is slightly positive ($\sim$0.2 eV) on *h*-BN/Cu. In the latter, case entropic contributions to ΔG outweigh the enthalpic binding attraction. The energy cost of distorting the substrate upon adsorption is 3.41 eV for *h*-BN/Ni, and 3.37 eV for *h*-BN/Co, but 4.62 eV for *h*-BN/Cu. This accounts for most of the difference in ΔE_{ads} between Cu and the other substrates, providing an indication for the weaker binding in this case.

The partial charges on B and N nearly compensate each other, B loses about 2.6 e to N. The O_2 molecule is rather strongly reduced upon adsorption to a total partial charge of almost -1.2 e, receiving 0.3–0.4 e from B and 0.8–0.9 e from the metal slab. $d_{\mathrm{O,O}}$ and $d_{\mathrm{B,O}}$ are nearly identical for all three substrates. A closeup of adsorbed O_2 on *h*-BN/Ni with annotated bond lengths is shown in Fig. 3.18(a). The O–O bond is stretched by about 0.3 Å compared to its gas-phase value, corresponding to a 24% elongation. The two oxygen atoms are closer to the surface B atoms than to each other, forming a 5-membered B–O–O–B–N ring across the BN honeycomb (highlighted). The situation is very similar for O_2 on *h*-BN/Co and *h*-BN/Cu. The exothermic binding of O_2 with the large accompanying bond stretch and charge transfer is a first indication that O_2 can be activated by adsorption on metal-supported *h*-BN.

Fig. 3.18(b) shows the electron density difference map of O_2 on *h*-BN/Ni. A fairly large amount of electron density redistribution can be observed upon binding of the molecule. The O atoms accumulate negative charge, in accordance with the Bader charge analysis. Electron density is also found between the O and B atoms, indicating the formation of a bond. In contrast, the O–O bond loses electrons, as does the region within the B–O–O–B–N pentagon. Electron density depletion is observed also along the B–N bonds. The neighboring N atoms become somewhat polarized.

We have shown that free *h*-BN is unsuitable for O_2 activation, but metal-supported *h*-BN shows promise. The question remains, whether one could dispense with *h*-BN altogether, and activate O_2 directly on the transition metal surface. We answered this for the case of Ni(111) with some exploratory calculations. Molecular O_2 is bound on Ni with ΔG_{ads} = -0.84 eV with a 12% bond stretch and a partial charge of -0.27 e. However, O_2 is much more stable on Ni(111) as two dissociated O atoms, with ΔG_{ads} = -3.78 eV and $q_{\mathrm{O_2}}$ = -1.17 e. This is indicative of a surface oxidation, as it commonly occurs on transition metals. Rather than activation of O_2, a deactivation of the catalyst surface occurs. It appears, therefore, that the *combination of h-BN with a transition metal* is crucial to achieve catalytic activity.

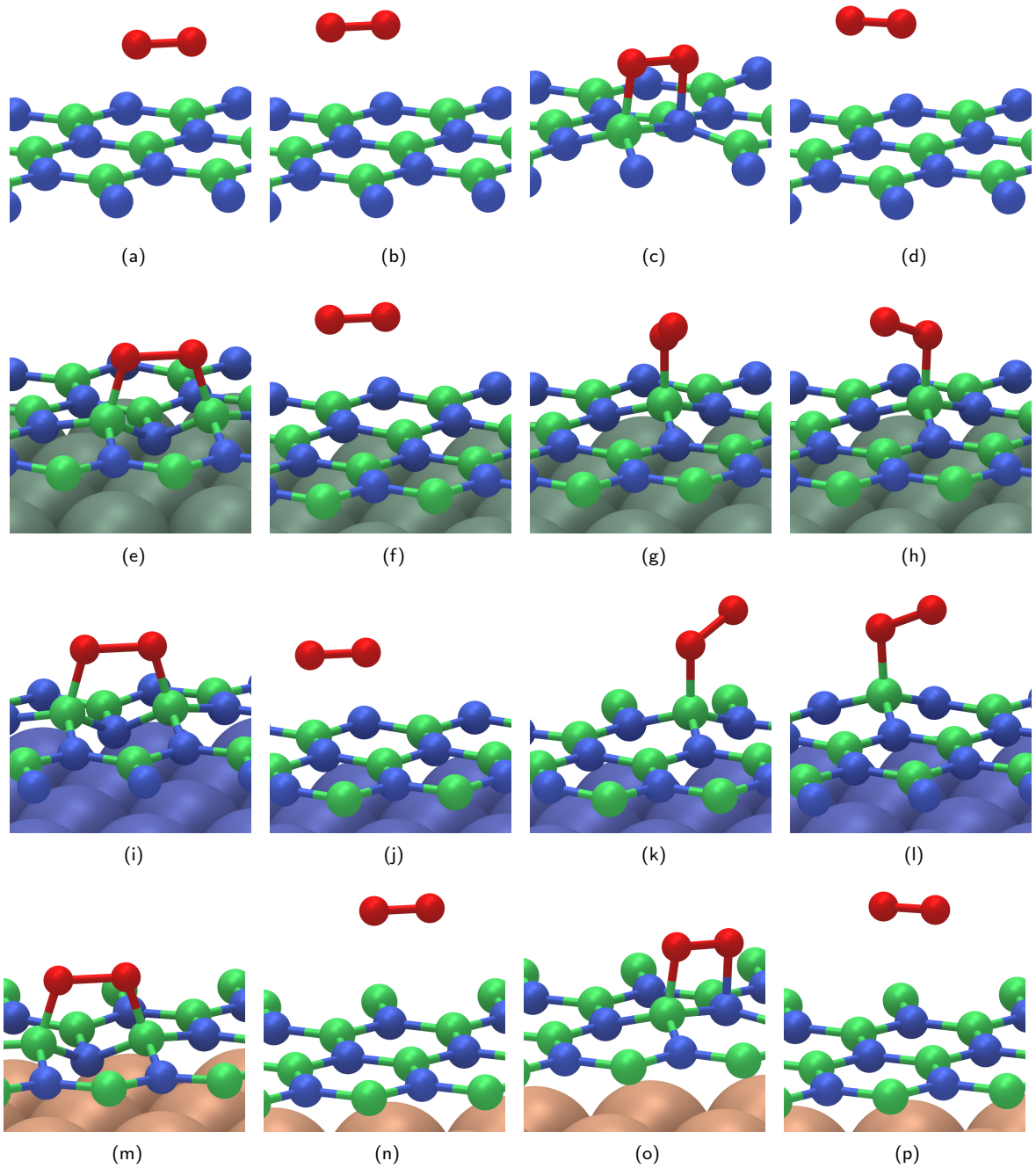

Figure 3.17|Optimized structures of O_2 in configurations O_2-BB (first column), O_2-NN (second column), O_2-BN (third column), O_2-BN' (fourth column) on free-standing *h*-BN (first row), and *h*-BN/Ni(111) (second row), *h*-BN/Co(0001) (third row), and *h*-BN/Cu(111) (fourth row). Atom colors: B, green; N, blue; O, red; Ni, grey-green; Co, blue; Cu, beige.

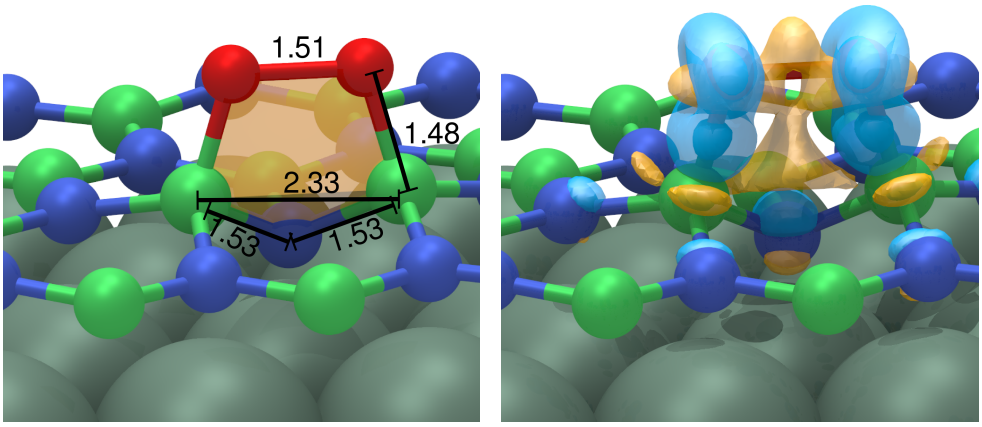

(a) (b)

Figure 3.18|Optimized structure of O_2 on *h*-BN/Ni(111): (a) O–O, O–B, and B–B bond lengths in Å and highlighted B–O–O–B–N pentagon (orange). (b) Electron density difference map of O_2 on *h*-BN/Ni(111). Isosurfaces of positive (i.e. electron accumulation) and negative (electron depletion) differences shown in blue and orange, respectively. Atom colors: B, green; N, blue; O, red; Ni, grey-green.

Thermodynamics of the ORR on *h*-BN/Ni and *h*-BN/Co

We now employ DFT calculations to elucidate the reaction mechanism of the ORR. The ORR proceeds through four consecutive proton/electron transfer steps

$$4H^+ + 4e^- + 2O_2 \rightarrow 2H_2O$$

via the intermediates OOH*, O*, OH*. The * indicates adsorbed species. We calculate the free energies at 298 K for the adsorbates on all 3 *h*-BN/metal substrates to determine overpotentials according to the CHE model.

Free-standing *h*-BN is rather unreactive towards O_2, as shown above.[190,196] Its activity for the ORR is also very low, as indicated by the very low binding energies of OOH*, O*, and OH* (shown in Fig. 3.19). The ORR intermediates are located at distances far exceeding those expected of covalent bonds, and leave the monolayer unperturbed. The interactions between adsorbate and substrate are very small, or in fact thermodynamically non-binding. If entropic contributions were added to the binding enthalpies, the ORR intermediates are expected to be unbound. Unsupported *h*-BN is therefore not a suitable ORR catalyst.

These results agree with the conclusions by Lyalin et al.,[190] who find, e.g., a similarly large value of $d_{\mathrm{B,O}} \approx 3$ Å for OOH* and ∼1.5 Å for O*.[54] On the other hand, their adsorption energies differ from the values presented here, in particular for O* (ΔE_{ads} = -1.67 eV).[54] They also note that defects in free-standing *h*-BN can increase its reactivity enough to show potential for catalytic applications.[190]

When supported on transition metals, however, *h*-BN becomes much more active. The optimized structures of the three intermediates for the ORR on *h*-BN/Ni(111) and *h*-BN/Co(0001) are shown in Fig. 3.20. On *h*-BN/Ni(111), the first intermediate, OOH*, is bound to a B atom with a bond length of 1.48 Å. The O-O bond points away from the surface plane at an angle of about 39°. The bond is stretched ($d_{\mathrm{O,O}}$ = 1.49 Å), staying at essentially the same length as in adsorbed O_2, resembling a peroxo species. For comparison, the gas phase O–O bond length in H_2O_2 is 1.47 Å. The B atom bound to O is displaced from the *h*-BN plane by about 0.5 Å, stretching the corresponding B–N bonds by about 0.07 Å (4.8%). The rest of the *h*-BN sheet, further away from the binding position of OOH*, remains largely unperturbed. The second intermediate, O*, is located directly above a surface B atom, at a distance somewhat shorter than for OOH*. As in O* there is no more O–O covalent bond, this reduction of $d_{\mathrm{B,O}}$ can be rationalized with the formation of a (partial) double bond to B. The binding B atom is slightly buckled outward from the BN layer (0.6 Å). Lastly, the OH* species exhibits $d_{\mathrm{B,O}}$ and $d_{\mathrm{O,H}}$ bond lengths similar to those in OOH*. Due to the single bond to H, the double bond character of B–O is lost and $d_{\mathrm{B,O}}$ elongates again.

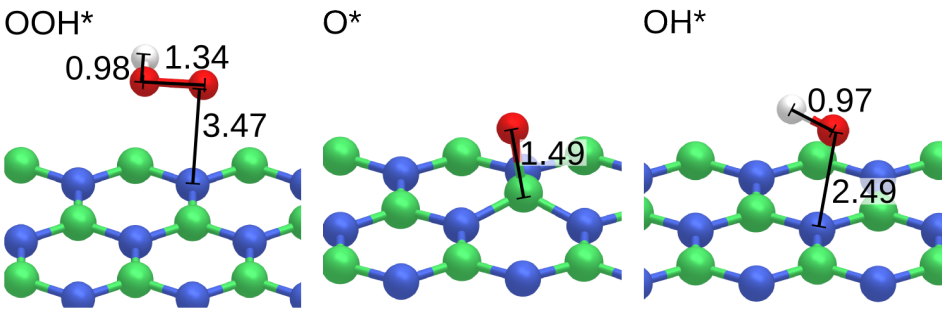

(a) ΔE_{ads} = -0.854 eV (b) ΔE_{ads} = +1.755 eV (c) ΔE_{ads} = -0.194 eV

Figure 3.19|(a)–(c) ORR intermediates on free-standing *h*-BN. Numbers indicate bond lengths in Å, panels labelled with the species' adsorption energies. Atom colors: B, green; N, blue; O, red; H, white. Data published in ref. 86.

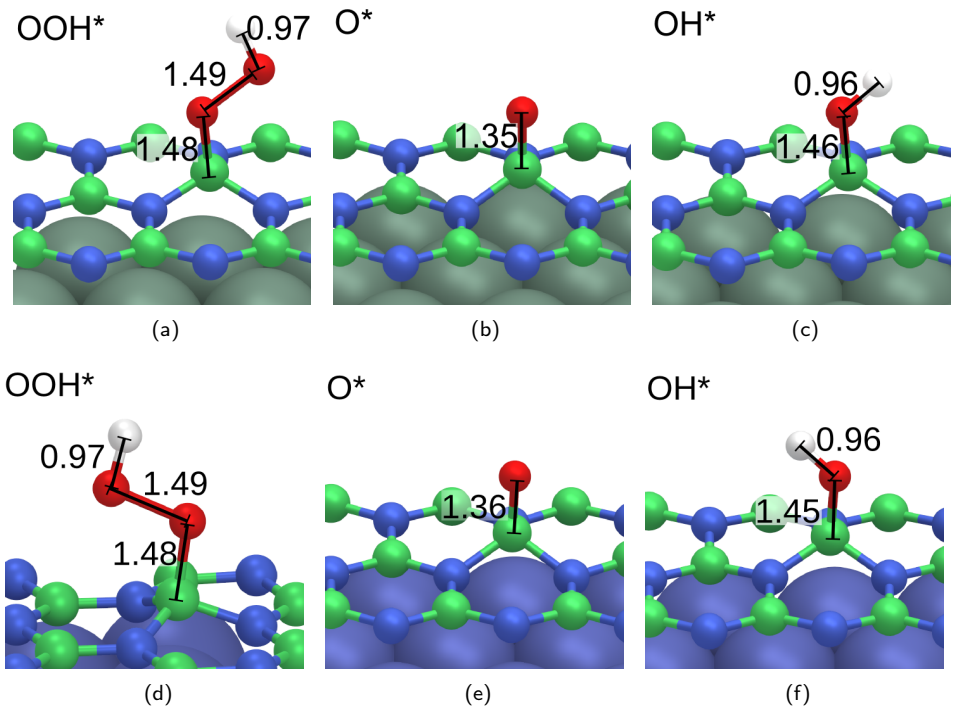

Figure 3.20|ORR intermediates on *h*-BN/Ni(111), (a)–(c), and *h*-BN/Co(0001), (d)–(f). Numbers indicate bond lengths in Å. Atom colors: B, green; N, blue; Ni, grey-green; Co, dark blue; O, red; H, white. Data published in ref. 86.

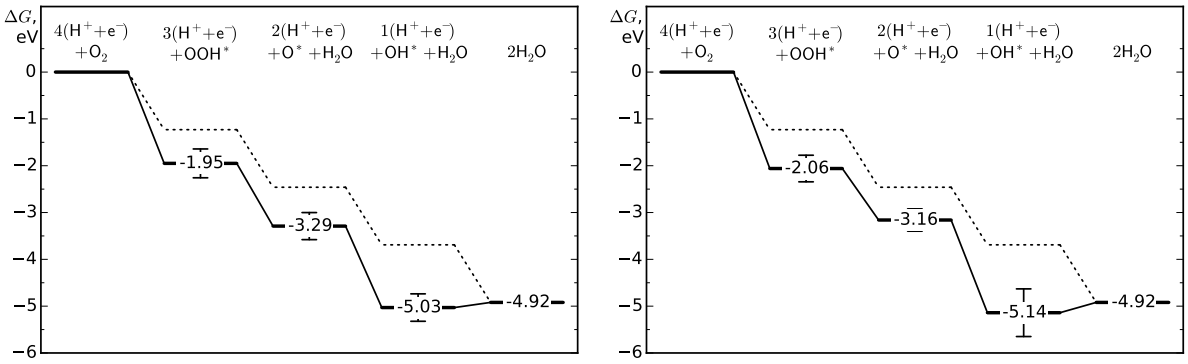

(a) *h*-BN/Ni(111) (b) *h*-BN/Co(0001)

Figure 3.21|Free energy profile of the ORR on (a) *h*-BN/Ni and (b) *h*-BN/Co. ΔG in eV, error bars indicate standard deviation obtained from the BEEF-vdW ensemble. Dashed line shows the profile for an ideal ORR catalyst. Data published in ref. 86.

These structural results are in good agreement with previous theoretical analyses.[54] On *h*-BN/Ni $d_{\mathrm{B,O}}$ is reported as 1.47 Å, 1.36 Å and 1.45 Å for OOH*, O*, and OH*, respectively. The authors note a similar deformation of the *h*-BN sheet around the bound species. In addition to the on-top binding configuration of O*, their study also identified a bridging configuration between 2 B atoms, with almost the same binding energy.[54]

The free energy profile of the ORR on these two substrates is shown in Fig. 3.21, along with the energetics of an ideal catalyst. The first step, $O_2(g) + 1/2\ H_2 \rightarrow$ OOH*, is downhill in free energy by -1.95 eV, noticeably more than for the ideal ORR catalyst (see dashed line in Fig. 3.21(a)). The

Table 3.10|Entropy contributions to the free energy of ORR steps on metal-supported *h*-BN, relative to *h*-BN/metal + O_2 + 2 H_2, in analogy to the free energy profiles (Figures 3.21 and 3.23). Data published in ref. 86.

	h-BN/Ni(111)	*h*-BN/Co(0001)	*h*-BN/Cu(111)
ΔS(OOH*), eV	-0.694	-0.704	-0.737
ΔS(O*), eV	-0.450	-0.401	-0.404
ΔS(OH*), eV	-0.587	-0.587	-0.593
ΔS(2H_2O), eV	-0.272	-0.272	-0.272

following reduction of OOH* to O* (while releasing an H_2O molecule) is exothermic by -1.34 eV. The third step, O* + 1/2 $H_2 \rightarrow$ OH*, is downhill by -1.94 eV, reaching a minimum of -5.03 eV relative to gas-phase O_2, lower than the overall free energy of the ORR. Adsorbed OH* on *h*-BN/Ni thus constitutes a thermodynamic sink that would prevent the reaction from continuing. This result is in line with previous findings that indicate a too strong adsorption of OH* on h-BN/Ni.[54]

The ORR intermediates on h-BN/Co(0001) is very similar to h-BN/Ni(111) (see Fig. 3.20(d)–(f)). The interatomic distances of the adsorbed species are comparable to those on h-BN/Ni in terms of bond lengths and structure. The reaction profile (Fig. 3.21(b)) is qualitatively the same as that observed on h-BN/Ni(111). The first step is downhill in free energy by -2.06 eV, followed by the O* intermediate at -3.16 eV and OH* at -5.14 eV. As for *h*-BN/Ni, the OH* species is bound too strongly for the ORR to proceed. Generally, it appears that *h*-BN/Co is comparable to *h*-BN/Ni as an ORR catalyst, with only minor quantitative differences in the thermodynamics. The Co(0001) substrate is equally able to activate the boron nitride overlayer, but also results in overall too strong adsorption relative to the ideal behavior of an ORR catalyst.

The confidence intervals indicated by the error estimates from the BEEF-vdW ensemble are of an acceptable magnitude, typically around $\pm$0.3 eV. They are somewhat larger than the errors found for commensurate *h*-BN adsorption on metals in absolute terms, but smaller relative to the much larger ΔG values. It should be noted that the error estimates are only computed for the enthalpic contributions to ΔG, and not the entropic corrections (which are a significant, but not dominant contribution).

Table 3.10 lists the entropic contributions to ΔG presented in the energy profiles. The values are very similar for all substrates, indicating a significant entropic decrease of 0.4 – 0.7 eV per reaction step. One can expect the thermodynamics of the ORR to improve at lower temperatures (more negative ΔG), while they will worsen as temperatures are increased. To a first approximation, the overall reaction would cease to be exergonic at a temperature of T $\approx$ 1000 K on *h*-BN/Ni and *h*-BN/Co (assuming S to be independent of temperature).

The effect of lateral strain on the ORR on *h*-BN/Ni

In order to elucidate the influence of the metal–metal bonding on the ORR, we artificially expanded the Ni surface and adsorbed *h*-BN laterally by a strain factor α = 2, 4, and 6%. Applying compressive strain (as small as 1%) led to the detachment of the *h*-BN layer from the metal surface, i.e. breakdown of the chemisorbed heterostructure. Table 3.11 lists the free energies of the ORR intermediates at the different degrees of strain. ΔG(OOH*) is largely independent of the strain, remaining near the value for $\alpha = 0$ (-1.95 eV). ΔG(OH*) also shows little variation with α, decreasing slightly from -5.03 to -5.12 eV as α is increased to 2%, then remaining the same. We find the stretching of the lattice constant to have the greatest effect on ΔG(O*), which is stabilized by 0.16 eV at $\alpha = 6$%, following an approximately linear trend. However, also this effect is rather minor, considering that a strain of 6% corresponds to an increase of the in-plane interatomic distances by 0.15 Å. The approach of stretching the material allows

Table 3.11|Free energies ΔG of ORR intermediates adsorbed on *h*-BN/Ni(111) at various magnitudes of lateral expansion (α) of the substrate. Data published in ref. 86.

Strain, α, %	ΔG(OOH*)	ΔG(O*)	ΔG(OH*)
0.0	-1.949	-3.287	-5.031
2.0	-1.990	-3.372	-5.116
4.0	-1.969	-3.391	-5.104
6.0	-1.965	-3.451	-5.101

for some control over the intermediates' binding energies, but tends to stabilize rather than destabilize them as would be desirable for improving the ORR.

Thermodynamics of the ORR on *h*-BN/Cu

Fig. 3.22 shows the optimized structures of ORR intermediates on *h*-BN/Cu. In all cases, the bond lengths and adsorption distances are very similar to those found on *h*-BN/Ni(111) and *h*-BN/Co(0001). The O* species is adsorbed noticeably closer to the surface (1.35 Å) than the others and the O-O bond length in OOH* is equally long as the O-B bond length in the same species. The B atom binding the adsorbate is slightly displaced out of the *h*-BN plane in all cases.

Fig. 3.23 shows the free energy diagram for the ORR on *h*-BN/Cu(111). In addition to the free energy profile (at $U = 0$) we also show the maximum potential at which all steps of this reaction are still downhill in energy, which is 0.89 V, computed according to the CHE model. Without an external potential, the OOH* species is bound with a ΔG of -0.99 eV, O* with -1.89 eV and OH* with -3.95 eV. Compared to *h*-BN/Ni(111) and *h*-BN/Co(0001), all intermediates are bound less strongly by at least 1 eV, which significantly changes the overall profile of the reaction. The free energy differences between each step are -0.99 eV, -0.90 eV, -2.06 eV, and -0.97 eV. These energy differences are fairly close to the ideal -1.23 eV. The O* $\rightarrow$ OH* transformation deviates most strongly from this value, by 0.83 eV. The free energy of the last step is comparable to the value of -0.80 eV on Pt(111),[192] and constitutes a major improvement compared to the overbinding noted above.

The weaker adsorption of all the intermediates compared to *h*-BN/Ni and *h*-BN/Co improves the usability of *h*-BN/Cu as an ORR catalyst. Since the profile is relatively smoothly downhill in energy for all 4 steps, the reaction proceeds easily from a thermodynamic point of view. The binding of OOH* and O* is somewhat weaker than it should be on an ideal catalyst, while is OH* bound more strongly.

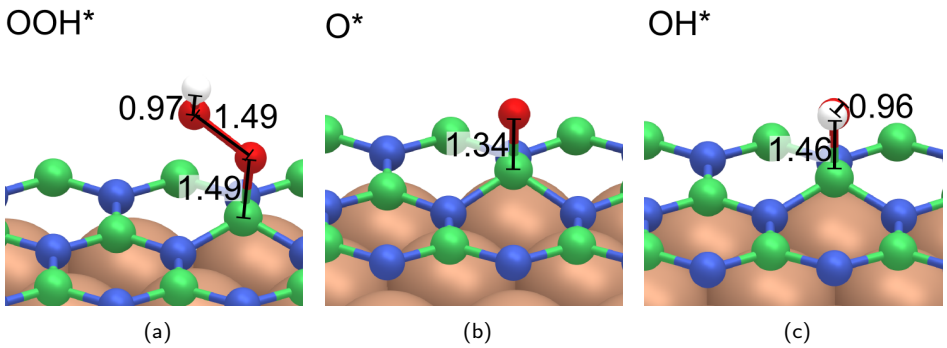

Figure 3.22|(a)–(c) ORR intermediates on *h*-BN/Cu(111). Numbers indicate bond lengths in Å. Atom colors: B, green; N, blue; Cu, beige; O, red; H, white. Data published in ref. 86.

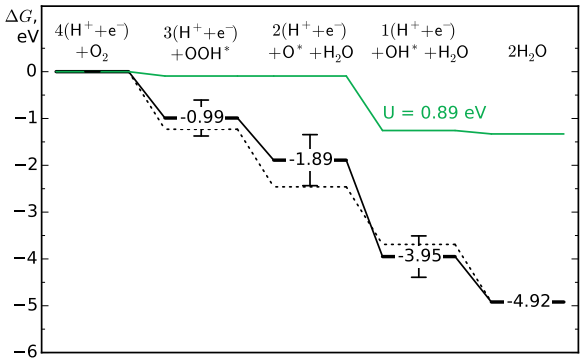

Figure 3.23|Free energy profile of the ORR on *h*-BN/Cu(111). ΔG in eV, error bars indicate standard deviation obtained from the BEEF-vdW ensemble. Dashed line shows the profile for an ideal ORR catalyst. Green line shows the reaction profile at an external potential of $U = 0.89$ eV, the highest at which all steps are still exothermic. Data published in ref. 86.

The external potential U can be increased up to a value of 0.89 V, until the reduction of OOH* to O* ceases to be exothermic. The energy profile at this value of U is shown in Fig. 3.23 in green. It is a measure of the lost energy and thus of the quality of the catalyst. The calculated overpotential of the ORR on *h*-BN/Cu is 0.34 V, which is somewhat lower than the theoretical[192] (0.45 V) and experimental[197] (0.40 V) values on Pt(111).† For the ORR on Pt, the reduction of OH* determines the overpotential and weakening OH binding has been proposed to improve catalytic activity. In contrast, on *h*-BN/Cu the reduction of OOH* is the limiting step, which could be alleviated by increasing the catalyst's affinity to O*.

The free energy difference between OOH* and OH* is about 3 eV which is close to values found for transition metals[151] and transition metal oxides.[198] This value is substantially above the theoretical minimum of 2.46 eV, but among the best reported so far. ΔG(OOH*)-ΔG(OH*) serves as an instructive descriptor in oxygen electrocatalysis and is found to be approximately 3.2 eV across a broad range of materials. We analyze this quantity in greater detail below.

The error bars computed with BEEF-vdW are larger than those for the other *h*-BN/TM substrates. Using the entire set of energies in the ensemble, we calculated a derived ensemble of overpotentials for the reaction (see Section 2.3). This provides a distribution of values characterizing the confidence in the predicted ORR activity of h-BN/Cu(111). The distribution of overpotentials for the ORR is shown in Fig. 3.24(a). Each bar represents the probability with which *h*-BN/Cu(111) is predicted to have an ORR overpotential in a particular voltage interval. Due to the uncertainty of the DFT calculations, the overpotentials show a certain spread. And since each individual overpotential is a "worst-case" value derived from four energy quantities, the distribution is wider than the error bars on the individual ΔG values. There is an almost 50% probability that the ORR overpotential is smaller than 0.5 V, and 84% probability that it is smaller than 0.7 V. This gives us high confidence that *h*-BN/Cu is a viable catalyst also after accounting for potential calculation errors.

As mentioned above, the binding free energies and overpotentials do not take into account solvation effects at the electrode–water interface. Previous calculations have shown that ΔG may have to be corrected by 0.25 eV for OH* and 0.50 eV for O*.[192] When these corrections are applied, the theoretical overpotential would increase to 0.59 V and the difference ΔG(OOH*)-ΔG(OH*) would increase to ∼3.21 eV. The ensemble of solvation-corrected binding energies then yields a distribution of overpo-

†For the cases of *h*-BN/Ni and *h*-BN/Co examined above, the overpotential is in fact negative, implying that one would have to "drive" the fuel cell with external voltage, rather than utilize its voltage output.

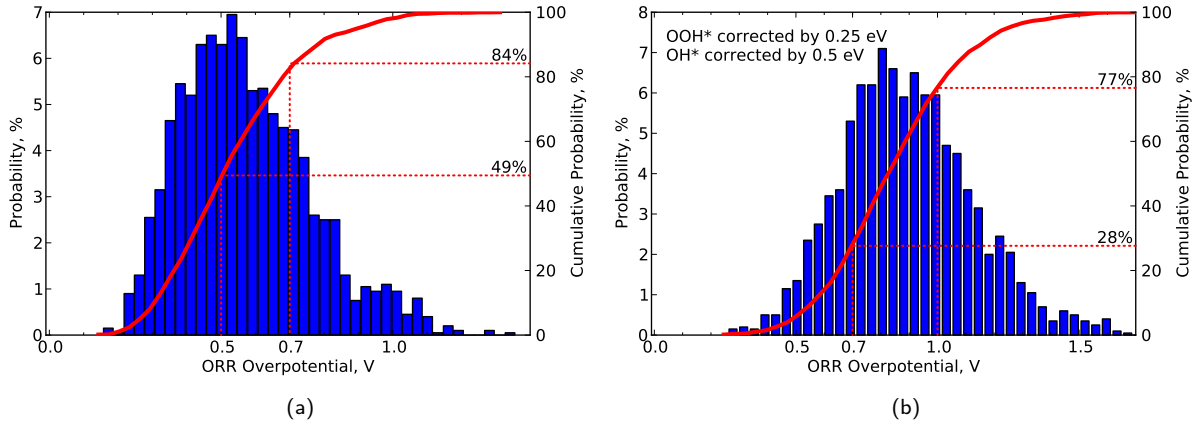

Figure 3.24|Histogram of ORR overpotentials on *h*-BN/Cu determined with the BEEF-vdW ensemble: (a) Overpotentials calculated directly from free energies. (b) Overpotentials calculated from free energies where ΔG(OOH*) and ΔG (OH*) were shifted by 0.25 and 0.50 eV, respectively, in order to account for solvation effects. The red line indicates the integrated histogram, i.e. the cumulated probability up to a given overpotential (right vertical axis). Data published in ref. 86.

tentials as shown in Fig. 3.24(b). Solvation effects may thus be significant enough to partially offset the catalytic activity of the *h*-BN/Cu(111) surface, but accurate quantification is needed before these conclusions can be drawn.

Trends and Correlations in ORR catalysis on supported *h*-BN

Looking at the complete data set of ORR intermediates, we identify trends that might allow one to optimize the catalyst materials.

In the context of the O_2 evolution reaction, it was found that materials generally obey the relation ΔG(OOH*)-ΔG(OH*) = 3.2 eV.[198] When comparing our data, we find an average difference ΔG(OOH*)-ΔG(OH*) of 3.09 eV for the various materials, largely in line with what is observed for transition metals[151] and oxides[198] and slightly closer to the ideal value of 2.46 eV.

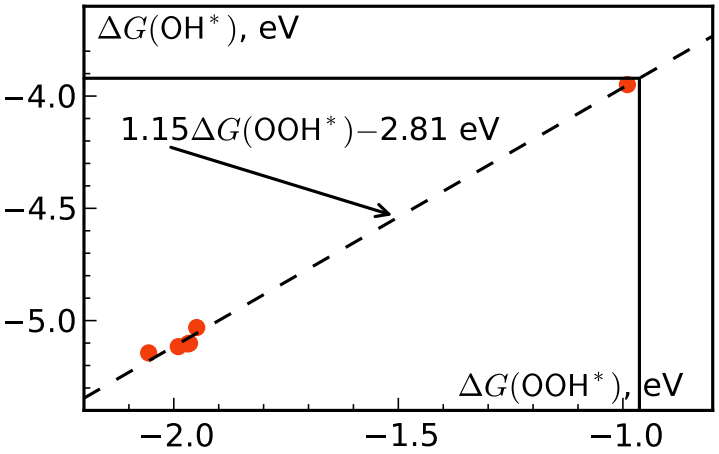

Figure 3.25|ΔG(OH*) plotted as a function of ΔG(OOH*) for all substrate materials. Dashed line is a linear fit to the data points, labelled with the corresponding equation. Solid lines indicate the point on the fitted curve where the overall deviation of ΔG(OH*) and ΔG(OOH*) from their respective ideal values is minimal.

We observe a linear relationship between ΔG(OH*) and ΔG(OOH*), as shown in Fig. 3.25. *h*-BN/Cu lies in the top right corner of the plot, with small (in absolute value) free energies, and *h*-BN/Co and (strained) *h*-BN/Ni reside at the left side with larger adsorption free energies. An ideal ORR catalyst with ΔG(O0H*) = -1.23 eV can be interpolated to have ΔG(OH*) = -4.23 eV, which is about 0.54 eV too low compared to the ideal value. The ideal ΔG(OH*) corresponds to a ΔG(OOH*) of -0.76 eV – significant underbinding compared to the ORR catalyst. The ideal catalyst material as given by the fitted function (with minimal overall deviation from both ideal binding energies) has values of ΔG(OOH*) = -0.96 and ΔG(OH*) = -3.92 eV (shown by the black lines in Fig. 3.25). According to the correlation identified here, *h*-BN/Cu is essentially an optimal ORR material, where any improvement of one ΔG value would worsen the other. The fairly large gap between *h*-BN/Cu and the other data points would suggest that a number of materials with intermediate values of ΔG may still be found.

Summary: Oxygen Activation and Reduction on h-BN/Metal

The heterostructures *h*-BN/Ni(111), *h*-BN/Co(0001), and *h*-BN/Cu(111) can adsorb molecular O_2 with ΔG_{ads} up to -1.25 eV. This activates the molecule as indicated by a 24% elongation of the O–O bond. Crucially, neither free *h*-BN nor the bare metal can cause this on their own. A promising application for such a catalytic material is the oxygen reduction reaction. Our results indicate that *h*-BN/Ni and *h*-BN/Co bind the final ORR intermediate, OH* too strongly to be viable, but *h*-BN/Cu shows promise. We calculate an ORR overpotential of 0.34 V, comparable to that of the ORR on platinum.

4

Two-Dimensional Metal-Organic Frameworks

As outlined in Chapter 1, well-defined two-dimensional materials are of prime importance for applications in nanoscience and technology. In this chapter we discuss one example of 2D materials beyond the purely sp^2-bonded covalent sheets like graphene and h-BN: 2D MOFs, obtained by interlinking suitable multifunctional ligands with metal ions.

4.1 Introduction

TTPB and Metal-supported Networks

Using solid surfaces as a substrate to adsorb and prepare self-assembled networks is one of the major research areas in surface science. Experimental characterization techniques such as STM and AFM offer partial atomic-scale insight into the structure of these materials and are often complemented by computational investigations.

TTPB has a sufficiently low molecular weight to be evaporated and deposited onto surfaces *in situ* in an ultra-high vacuum STM chamber. Dienel et al. applied this technique to deposit TTPB on metallic substrates (Au and Cu) in various conditions with different results. Fig. 4.1(a) shows individual TTPB molecules adsorbed on an Au(111) surface at low coverage, evaporated at 385° C onto the room-temperature substrate. Under these conditions the molecules do not aggregate and show no preferential orientation. On the other hand, on Cu(111), most (>95%) TTPB molecules adsorb with the same rotational orientation relative to the surface. Well-defined and selective adsorption is highly desirable

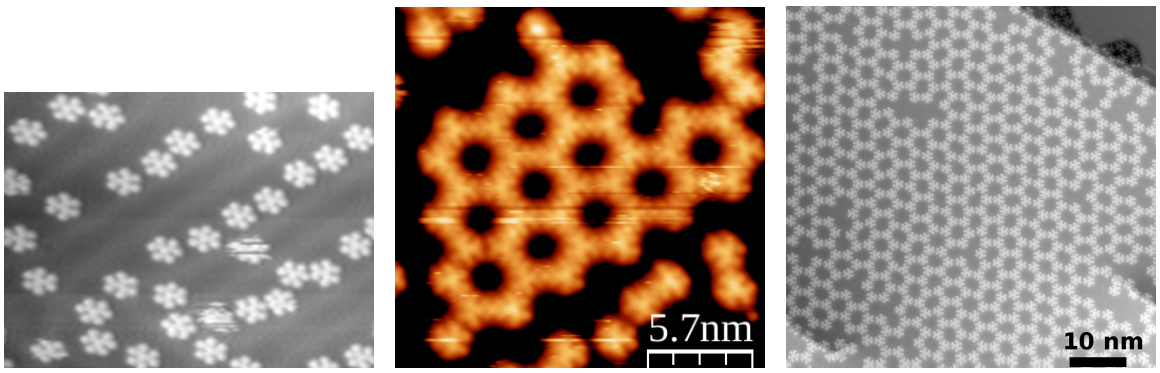

(a) (b) (c)

Figure 4.1|STM Images of: (a) Isolated TTPB molecules on a terraced Au(111) surface. (b) A small network of TTPB molecules co-deposited with Fe atoms on Au(111) (c) A larger network of TTPB on Cu(111), achieved through co-deposition of NaCl.

to control the formation of ordered structures. Therefore, the alignment of TTPB on Cu(111) merits further investigation.

As shown in Fig. 4.1(b), TTPB can form small porous aggregates on Au(111) when co-deposited with Fe atoms. The observed islands are limited to lateral dimensions of a few repeat units. The STM image faintly shows bridging metal atoms in the space between the terpyridyl groups, although the metal could not be confirmed to be Fe. In contrast, when TTPB is co-deposited with NaCl on Cu(111), large extended networks with lateral dimensions of 10s of nm are formed (Fig. 4.1(c)). The aggregates appear to be bridged by metal atoms, forming a hexagonal lattice with pores of 2 nm diameter and 2 nm distances between the centers of adjacent molecules. The number of bridging atoms, as well as their identity and coordination number could not be determined experimentally.

The first part of this chapter explores the adsorption of TTPB on Au(111) and Cu(111), both with and without metal atoms. Different lateral and rotational positions are considered, in order to investigate the site-selectivity of the adsorption. Furthermore, the effect of adsorption on the electronic structure of the molecule is thoroughly investigated, as is the preference for and impact of *cis* and *trans* conformations of TTPB.

Assembly of 2D Networks on a Water Surface

A popular method to synthesize extended 2D sheets is through the decomposition and/or assembly of precursor molecules on suitable surfaces.[199,200] However, some aspects of this approach limit its usefulness. Firstly, substrates are typically only reactive at the surface, leaving the bulk of the solid unutilized for the reaction. Secondly, the solid with its rigidly placed binding sites limits the conformational flexibility of adsorbed species and thus the range of accessible reaction products.[201,202] Thirdly, removing the final extended sheet from the support may be challenging.[203] Alternative approaches to prepare 2D sheets are thus highly desirable.

A promising route to prepare extended 2D coordination polymers or 2D MOFs using liquid water as a substrate has recently been presented.[15,204–206] The monomeric precursors are confined on the surface of water, induced to form a dense layer by increasing lateral pressure, and linked with metal ions present in the liquid phase to form large sheets.[15,205] This way the liquid-vapor interface of water is used as a "surface" on which the reaction occurs, while metal ions can be supplied from the bulk of the solution and used to assemble an extended sheet. Such a substrate provides reactants from the bulk liquid by diffusion, lightly and dynamically stabilize adsorbates, and allows easy removal of the sheet by drying. Therefore all three issues mentioned above are overcome.

Fig. 4.2 shows a sketch of the steps involved in the formation of an extended network on a water

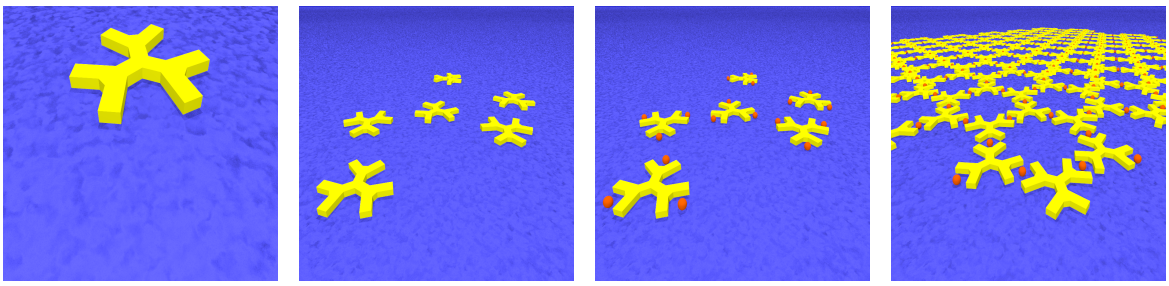

Figure 4.2|Assembly of a 2D MOF on a water surface: (a) Individual molecule confined at the surface. (b) Disordered film of multiple molecules. (c) Metal ions from the liquid phase bound to ligand sites of the molecules. (d) Aggregation of monomers into an ion-bridged extended network.

surface. Molecules are spread on the surface, where they remain due to their insolubility (panel (a)). As the lateral pressure is increased, molecules loosely aggregate into a disordered film (panel (b)). After a solution of a metal salt has been added to the mixture, the ions diffuse to the surface and are coordinated by the ligands (panel (c)). Finally, since the monomers are multifunctional, they are cross-linked by the ions into a dense, topologically two-dimensional sheet supported by the water surface (panel (d)).

Makiura et al. first used this technique for the layer-by-layer fabrication of MOFs with Co-porpyhrin and pyridine building units, linked by Cu^{2+} ions.[206] They were able to obtain a highly crystalline MOF on a quartz substrate with exact control over the thickness (by repeating the reaction on water, a single layer is deposited at each iteration). They also examined the structure and properties of this material using various spectroscopic and x-ray techniques, finding that the 2D layers are laterally dense aggregates whose optical adsorption increases linearly with the number of deposited layers.[205] Schlüter et al. made use of different precursor molecules, containing up to 6 terpyridyl units as ligands, interconnected with metal ions (Co^{2+}, Ru^{2+}, Zn^{2+}, Pb^{2+}, Ni^{2+}, Fe^{2+}).[15] They were able to obtain large two-dimensional monolayer sheets of sizes $> 500\times500$ μm^2 and to transfer them onto solid substrates for characterization by TEM and AFM. The sheets were found to be of uniform single-layer thickness and mechanically stable to span over 20×20 μm^2 large holes of a TEM grid. Subsequent characterization of these terpyridine-based sheets indicated that between 60 and 80% of ligand sites are occupied by ions, depending on the specific monomer and metal.[207] The linking ions can be easily exchanged (Zn^{2+} to Fe^{2+}) also after the synthesis by exploiting the dynamic equilibrium between ions in the sheet and in solution. This transmetalation can be targeted to specific parts of the sheet by applying lithographic techniques.[207] Related DFT studies were able to rationalize the partial metalation of the sheet with the fact that only part of the counterions can be incorporated into the sheet, making it energetically unfavorable to occupy more than 66% of ligand sites with ions. Furthermore, the elastic modulus of the sheet could be computed in good agreement with AFM nanoindentation results.[207] More recently, also other types of networks assembled on water have been reported. In particular, Schlüter et al. were able to produce a covalently linked sheet by photochemically polymerizing anthracene-based monomers at an air/water interface.[208]

In order to understand the properties and assembly of terpyridine-based 2D MOFs from the on-water polymerization described in here, detailed knowledge is needed at the molecular scale. This chapter presents detailed studies of several aspects of this material. We perform MD simulations of free and Zn-coordinated TTPB in the gas phase and on a substrate of liquid water, in order to elucidate the dynamic properties of the monomer. Subsequently, we use MTD to quantify the free energy and the details of Zn^{2+} uptake from the bulk water phase. The next step towards the assembly of extended 2D networks is the formation of a TTPB-Zn-TTPB dimer, which we also study with MD and MTD methods. Finally, we investigate the dynamics of a fully periodic (TTPB-Zn_3)$_n$ polymer.

4.2 TTPB in the Gas Phase

As a preliminary study of the possible binding of metal atoms and ions to TTPB, we considered isolated molecules in the gas phase. All stoichiometries of TTPB-M_n are computed for n = 1,2,3, with M = Fe^{2+}, Co^{2+}, Ni^{2+}, Cu^{2+}, Zn^{2+}, and the molecules were optimized, constrained to be planar, as expected for adsorbed molecules.* The employed computational set-up is described in Section 2.3, with the revPBE functional replaced by the canonical PBE[96] formulation.

*This constraint considerably facilitates convergence of the geometry optimization and simplifies the selection of an energy reference for free TTPB. As will be seen in later sections, TTPB has a very high conformational flexibility with soft torsional modes, leading to strong deformation of the molecule unless it is forced to remain planar.

Ion Binding: Structure and Energetics

Table 4.1 shows the ion binding energy, ΔE_{bnd}, and the distances between N and the closest metal ($d_{\mathrm{N,M}}$) and between the uncoordinated ($d_{\mathrm{N,N}}$) and coordinated N atoms ($d^{\mathrm{M}}_{\mathrm{N,N}}$) of terpy units (sketched in Fig. 4.3). Depending on the number and species of bound metal ions, the properties of the resulting coordination compounds vary to a considerable degree. Without any bound metal, the terpy units are widest, i.e. their $d_{\mathrm{N,N}}$ is maximal. The pyridyl nitrogen atoms tend to repel each other and the terpy site is thus spread wide. If allowed, the pyridyl arms would likely turn to assume a (partial) *trans* conformation in order to reduce this repulsive energy (this is explored further in the next section). Bonding to a metal ion strongly compresses the involved ligand moieties. The N atoms are about 0.6–0.8 Å closer to each other than without a metal. This compression is strongest for Ni, and least pronounced for Zn and Cu. $d_{\mathrm{N,M}}$ is on the order of 1.9 Å for all metal species.

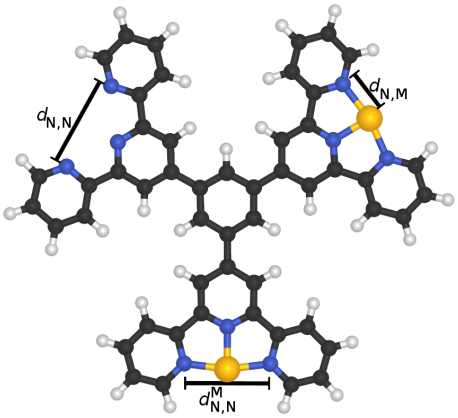

Figure 4.3|Sketch of 1,3,5-tris(4'(2,2':6'2''-terpyridyl))benzene (TTPB). Two metal atoms bound by terpyridyl groups. N–metal ($d_{\mathrm{N,M}}$) and N–N distances ($d_{\mathrm{N,N}}$, $d^{\mathrm{M}}_{\mathrm{N,N}}$) in bound and unbound ligands indicated by black lines. Atom colors: H, white; C, black; N, blue; Metal, yellow.

When a metal is bound somewhere in the molecule, also those terpy groups that are not coordinated adopt narrower $d_{\mathrm{N,N}}$. Largely independent of the identity of the metal, $d_{\mathrm{N,N}}$ is about 4.33–4.39 Å in the case of $n = 1$, and somewhat shorter for $n = 2$. This corresponds to a reduction by 0.2 Å compared to unbound TTPB. The coordination of a metal to one terpy unit thus seems to have a long-reaching effect also on the others.

The distances $d_{\mathrm{N,M}}$ compare well with available structural data, but tend to be shorter by about 0.1–0.2 Å, likely due to the fact that Zn is only coordinated by 1 ligand rather than 2. The corresponding value from an x-ray structure of $Zn(terpy)_2$ is $d_{\mathrm{N,M}} \approx 2.15$ Å.[209] The Ni bis-terpy analog has $d_{\mathrm{N,M}} = 2.08$ Å.[210] Similarly, $d_{\mathrm{N,M}}$ for a bis-terpy Fe compound is reported as ~1.96 Å[211] and 2.25 Å for a derivative with similar ligand group but bulkier substituents.[212] For a $Co(terpy)_2$ derivative, the experimental $d_{\mathrm{N,M}}$ is reported as 2.01 Å[213] and 2.11 Å for a related Cu analog.[214]

The values of ΔE_{bnd} show a substantial variation with the coordinated metal ion. The absolute values of ΔE_{bnd} are difficult to quantify accurately due to the challenge of computing an accurate energy reference for a free ion. However, we can determine a hierarachy of relative binding strengths for the ions (considering ΔE_{bnd} for $n = 1$):

$$Ni^{2+} > Co^{2+} > Fe^{2+} > Cu^{2+} > Zn^{2+}$$

with Ni bound about twice as strongly to TTPB as Zn. This is somewhat at odds with an experimental dataset on the binding enthalpies[78] of $M(terpy)_2$, that suggests the order

$$Cu^{2+} > Fe^{2+} > Ni^{2+} > Co^{2+} > Zn^{2+}.$$

Here, the Cu > Fe group is transposed to the beginning of the hierarchy and Cu and Fe exchange places. It should be noted, however, that only rough comparisons can be made from this data, since the experimental values are determined at ambient temperature, in solution, for somewhat different ligands bound in a 2:1, rather than 1:1 ratio.

It is also instructive to compare ΔE_{bnd} of a specific ion for different values of n. The higher the loading of TTPB with metal ions, the weaker is each ion bound. The effect can be as large as 200–300 kJ·mol^{-1} per bound ion between $n = 1$ and $n = 3$. This is further evidence of a long range influence

Table 4.1|Properties of flat TTPB with n coordinated metal cations M in the gas phase: Binding energy per ion (ΔE_{bnd}), N–ion distance ($d_{\mathrm{N,M}}$), N–N distance in terpyridyl groups with ($d^{\mathrm{M}}_{\mathrm{N,N}}$) and without ($d_{\mathrm{N,N}}$) ions as shown in Fig. 1.6.

M	n	$\Delta E_{\mathrm{bnd}}/n$, kJ·mol^{-1}	$d_{\mathrm{N,M}}$, Å	$d_{\mathrm{N,N}}$, Å	$d^{\mathrm{M}}_{\mathrm{N,N}}$, Å
	0	—	—	4.559, 4.544, 4.562	—
Fe	1	-548.5	1.877	4.340, 4.326	3.832
	2	-461.6	1.886, 1.884	4.058	3.833, 3.829
	3	-347.1	1.878, 1.881, 1.881	—	3.815, 3.811, 3.816
Co	1	-580.6	1.848	4.340, 4.333	3.748
	2	-445.5	1.851, 1.851	4.296	3.763, 3.762
	3	-278.1	1.921, 1.857, 1.892	—	3.807, 3.846, 3.769
Ni	1	-607.0	1.903	4.321, 4.332	3.826
	2	-482.4	1.865, 1.865	4.363	3.770, 3.768
	3	-390.5	1.849, 1.851, 1.851	—	3.738, 3.737, 3.738
Cu	1	-473.6	1.991	4.340, 4.349	3.956
	2	-367.9	1.968, 1.966	4.193	3.923, 3.923
	3	-251.1	1.937, 1.935, 1.935	—	3.867, 3.873, 3.870
Zn	1	-292.3	1.962	4.393, 4.395	3.943
	2	-232.6	1.973, 1.973	4.225	3.947, 3.951
	3	-169.7	1.980, 1.982, 1.984	—	3.947, 3.945, 3.944

among the binding sites, a type of inverse cooperative effect that disfavors binding of an ion, if other binding sites are already occupied.

We also quantify the energy cost of bending the terpy ligand *in-plane* upon coordination of the metal. For M = Zn, the energy cost of rearrangement of TTPB is 53.1 kJ·mol^{-1} for $n = 1$, 99.8 kJ·mol^{-1} for $n = 2$, and 131.6 kJ·mol^{-1} for $n = 3$. This trend is not quite linear, as the average distortion energy per terpy decreases with rising n. However, the mutual repulsion of the terpy-N atoms is significant in terms of energetic cost associated with the reduction of $d_{\mathrm{N,N}}$.

Ion Binding: Inter-Site Effects

In order to elucidate the nature of the influence that an ion in one binding site has on the structure of the other binding site, and on the binding of the subsequent ions, we examine the charge distribution in TTPB with different degrees of metal loading. Table 4.2 lists the Hirshfeld charges of the N (averaged for each terpy unit) and metal atoms for various degrees of metal binding. As would be expected, in the absence of any bound ions, all pyridyl N atoms carry a negative partial charge of equal magnitude (-0.35 e). Upon binding of 1 ion, the average N partial charge of that ligand group is reduced to a value close to zero (-0.11–0.08 e), as electron density is redistributed to form coordinative bonds to the ion. Furthermore, the partial charge on the other remaining (unbound) terpy groups decreases, typically by about 15%. Binding of the second ion again significantly diminishes the partial charges of the corresponding group, as well as that of the remaining unbound ligand. As the negative charge on the free pyridyl groups is reduced, they repel each other less and the terpy unit contracts (as seen by the decrease of $d_{\mathrm{N,N}}$ with increasing n).

With increasing metal loading, less negative charge becomes available for each coordinative bond.

Table 4.2|Average charges on N and metal atoms of the three terpy units in TTPB with different number of ions bound. Charges determined according to Hirshfeld partititioning.

M	n	0	1	2	3
Fe	q_{N}	-0.350	0.033	0.030	0.043
	q_{N}	-0.351	-0.304	0.031	0.042
	q_{N}	-0.351	-0.304	-0.257	0.043
	q_{M}	—	-0.663	-0.482	-0.419
Co	q_{N}	-0.350	0.081	0.087	0.040
	q_{N}	-0.351	-0.306	0.087	0.087
	q_{N}	-0.351	-0.305	-0.265	0.061
	q_{M}	—	-0.799	-0.733	-0.502
Ni	q_{N}	-0.350	0.061	0.099	-0.118
	q_{N}	-0.351	-0.304	0.099	-0.117
	q_{N}	-0.351	-0.303	-0.278	-0.117
	q_{M}	—	-0.822	-0.766	-0.694
Cu	q_{N}	-0.350	-0.113	-0.099	-0.079
	q_{N}	-0.351	-0.306	-0.098	-0.078
	q_{N}	-0.351	-0.306	-0.260	-0.078
	q_{M}	—	-0.257	-0.149	-0.039
Zn	q_{N}	-0.350	-0.056	-0.050	-0.042
	q_{N}	-0.351	-0.317	-0.050	-0.043
	q_{N}	-0.351	-0.316	-0.285	-0.044
	q_{M}	—	-0.265	-0.195	-0.137

The average partial charge on the bound metal decreases with growing n. Therefore, the terpy-metal bonding per ion becomes weaker. Those metals where the change in binding energy with loading is most pronounced also exhibit the greatest reduction in q_{M}.

We therefore conclude that the long-range influence among the 3 terpy sites on TTPB is due to the redistribution of partial charge and electron density. An incoming ion draws electrons away from the entire molecule, thus reducing the binding capability of the remaining sites. Conceivably, this could be ameliorated by augmenting TTPB with additional electron-rich groups that offset the charge lost due to ion binding.

4.3 TTPB on Metal Substrates

As outlined above, experiments have focused on TTPB and its aggregates on Au(111) and Cu(111). Particularly the function of Fe atoms for binding TTPB on Au(111) and the preferential orientation of the molecule on Cu(111) can be further elucidated with calculations. This section presents adsorption studies of TTPB on Au(111) and Cu(111), focusing on adsorption energetics, structural parameters and the electronic structure of the adsorbate.

Laterally, the TTPB molecule can be placed in three high-symmetry adsorption positions, defined by the center of the central phenyl ring: *top*, *hcp*, *fcc*. When the center is placed on an *hcp* site, the six

C atoms of the phenyl ring alternate between *fcc* and *top* positions. Conversely, with the center in a *top* position, the phenyl ring occupies *hcp* and *fcc* sites, and when the center is in the *fcc* position, the adjacent C atoms are in *hcp* and *top* sites (for an illustration see Fig. 4.6).

TTPB on Au(111)

As observed with STM, TTPB readily adsorbs on Au(111), forming an unordered arrangement of molecules at low coverage and small Fe-bridged networks. We model this by placing a single TTPB molecule on Au(111) in the *top*, *hcp*, *fcc* positions, both with and without coordinated iron atoms. The computational parameters are identical to the revPBE+D3 set-up described in Section 2.3, but the standard PBE approximation[96] is employed. Fig. 4.4 shows side and top views of optimized structures of TTPB$_{hcp}$/Au and TTPB$_{hcp}$-Fe$_3$/Au. In the former case, the molecule drifts from its starting position to a nearly *top* configuration, during the geometry optimization and the pyridyl groups rotate slightly towards the metal. For the latter, TTPB-Fe$_3$ remains laterally in the initial *hcp* position and the pyridyl groups also rotate slightly towards the metal surface. A similar lateral movement as for TTPB$_{hcp}$/Au also occurs for TTPB$_{fcc}$-Fe$_3$/Au, but in all other cases TTPB remains in its starting position. We rationalize the movement of the molecule with the tendency to minimize the distance between N and surface atoms.

Table 4.3 summarizes the adsorption energies of TTPB (ΔE_{ads}), intramolecular N–N distances ($d_{\mathrm{N,N}}$) and N–Au and Fe–Au distances for TTPB and TTPB-Fe$_3$ in the three lateral positions. ΔE_{ads} ranges between -470 and -500 kJ·mol^{-1} for free TTPB and is around -1100 kJ·mol^{-1} for TTPB-Fe$_3$. When adsorbed without coordinated metal atoms, TTPB is most stable in the *top* position, which is preferred by 30 kJ·mol^{-1} compared to *fcc*, the least stable one. The geometry optimization started from the *hcp* position converges to an intermediate configuration between *hcp* and *top* (Fig. 4.4(a)), indicating that the *hcp* configuration is not a (local) minimum. The major contribution to the binding of free TTPB to Au is due to dispersion interactions (for the *top* configuration, the vdW part of ΔE_{ads} amounts to -539.1 kJ·mol^{-1}).

Energy differences between the various lateral positions are less pronounced for TTPB-Fe$_3$, but the *top* position is again preferred. The three added Fe atoms more than double the ΔE_{ads} of TTPB, due to the strong binding of Fe to the surface, and the stable coordination of Fe to TTPB. Additional calculations show that the binding energy of a single Fe atom on Au is between -638 kJ·mol^{-1} (in a *top* position) and -502 kJ·mol^{-1} (on a *bridge* site). In the TTPB-Fe$_3$ system (*hcp* configuration), the Au atoms are found in intermediate positions, laterally about 0.7 Å from the closest high-symmetry site (*top*). With TTPB-Fe$_3$ in the *top* configuration, the Au atoms come to reside about 0.5 ang from *fcc* sites, and for the molecule in the *fcc* position, the metal atoms are closest to the *hcp* sites. The large energy differences between

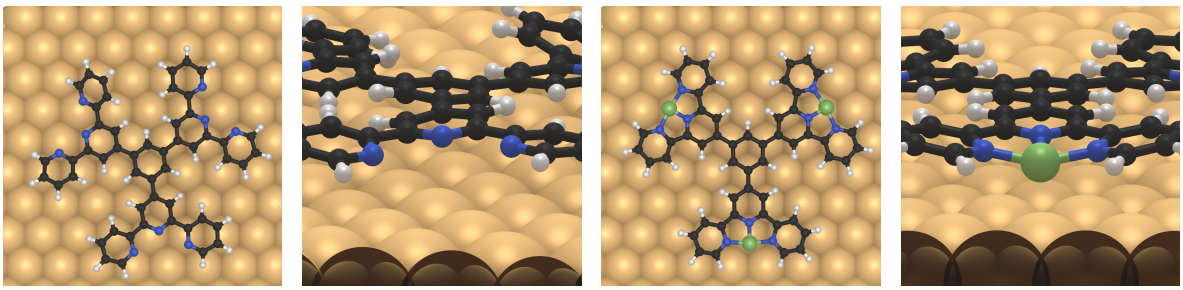

(a) *hcp* (b) *hcp*, side view (c) *hcp*, Fe$_3$ (d) *hcp*, Fe$_3$, side view

Figure 4.4|Examples of optimized structures of TTPB and TTPB-Fe$_3$ on Au(111). Atom colors: H, white; C, black; N, blue; Fe, green.

Table 4.3|Properties of TTPB and TTPB-Fe_3 on Au(111) in several lateral positions: Adsorption energy (ΔE_{ads}), average N–Fe distance ($d_{\mathrm{N,M}}$), average N–N distance in terpyridyl groups with ($d^{\mathrm{M}}_{\mathrm{N,N}}$) or without ($d_{\mathrm{N,N}}$) ions as shown in Fig. 1.6., distance of N to closest Au, $d_{\mathrm{N,Au}}$ (min/avg/max), height difference Δz between N atoms and central phenyl ring of TTPB.

Adsorbate	Position	ΔE_{ads}, kJ·mol^{-1}	$d_{\mathrm{N,M}}$, Å	$d_{\mathrm{N,N}}/d^{\mathrm{M}}_{\mathrm{N,N}}$, Å	$d_{\mathrm{N,Au}}$, Å	Δz, Å
TTPB	*hcp*	-487.1	—	4.624	2.687 / 3.260 / 3.667	-0.189
TTPB	*top*	-500.3	—	4.589	2.941 / 3.101 / 3.360	-0.295
TTPB	*fcc*	-470.5	—	4.508	3.515 / 3.620 / 3.750	-0.001
TTPB-Fe_3	*hcp*	-1128.2	1.885	3.775	3.189 / 3.247 / 3.323	-0.400
TTPB-Fe_3	*top*	-1138.8	1.908	3.707	2.941 / 2.990 / 3.084	-0.636
TTPB-Fe_3	*fcc*	-1134.7	1.891	3.753	3.050 / 3.214 / 3.469	-0.482

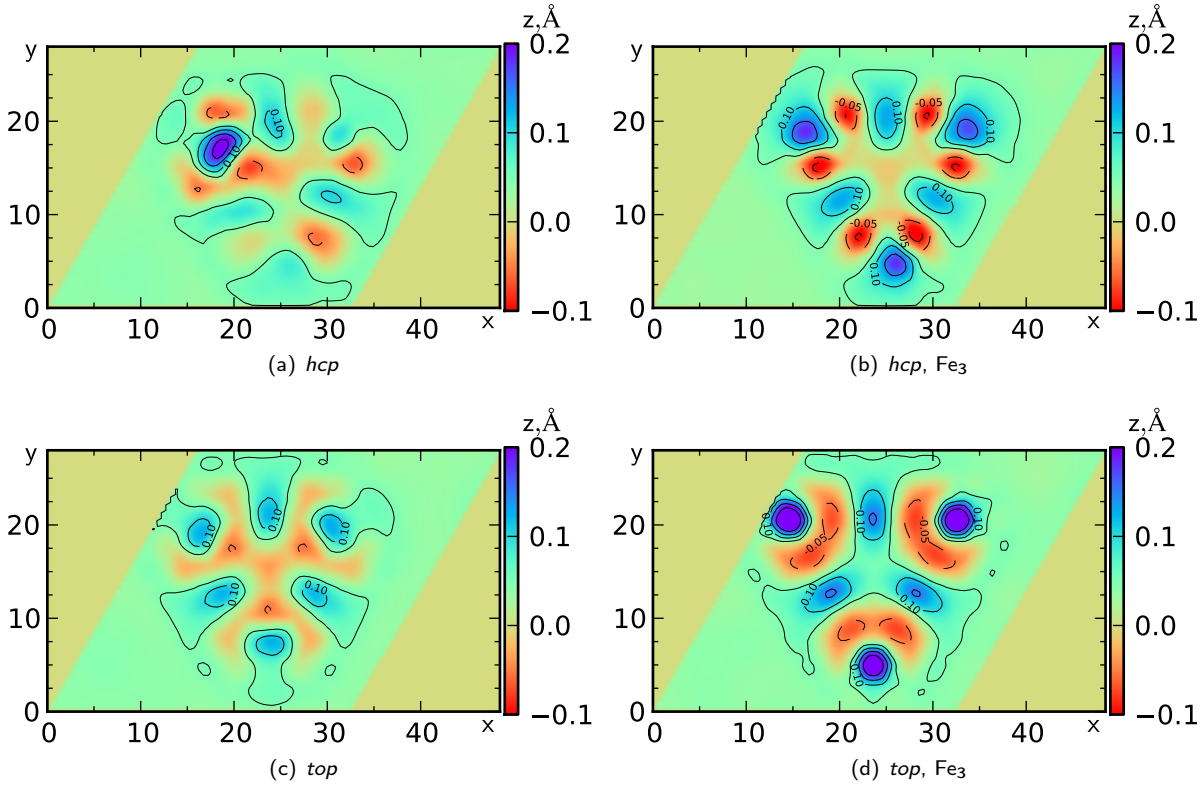

Figure 4.5|Elevation map of top layer Au atoms for TTPB and TTPB-Fe_3 in various lateral positions on Au(111).

various placements of the Fe atoms are not reflected in the ΔE_{ads} differences between the various placements of TTPB-Fe_3.

As noted above for gas-phase TTPB, coordination to a Fe brings the outer N atoms of the pyridyl groups closer together by ∼0.8 Å also when TTPB is adsorbed on Au. For TTPB-Fe_3, the variation of $d^{\mathrm{M}}_{\mathrm{N,N}}$ with the lateral position is slightly less pronounced than for TTPB, presumably because binding to the metal restricts the conformational freedom of the pyridyl groups. The lateral position of TTPB strongly influences the magnitude and variation of $d_{\mathrm{N,Au}}$ in the optimized structures. The minimum $d_{\mathrm{N,Au}}$ is smallest for TTPB_{hcp}, and largest for TTPB_{fcc}. The latter is characterized by a small spread of $d_{\mathrm{N,Au}}$ (0.24 Å), while the former exhibits a fourfold larger spread of about 1 Å. The average $d_{\mathrm{N,Au}}$ is typically

somewhat above 3 Å, spanning a range of 0.52 Å for TTPB and 0.26 Å for TTPB-Fe_3. This compares to N–Au distances in Au terpy complexes (1.99 Å[215]) and for adsorbed pyridine on Au (2.46 Å[216]). The average $d_{\mathrm{N,Au}}$ correlates with ΔE_{ads}, which is strongest for the lateral configuration with the smallest $d_{\mathrm{N,Au}}$. $d_{\mathrm{N,M}}$ is around 1.9 Å, largely independent of the lateral position of TTPB-Fe_3, and is in the range measured for Fe–terpy complexes.[211]

Upon adsorption, TTPB is distorted by rotating the pyridyl N atoms towards the surface to a varying extent. This is captured by Δz, the average difference in z coordinate between the central phenyl ring of TTPB and the pyridyl N atoms. Without coordinated Fe atoms, TTPB is somewhat distorted ($\Delta z \approx 0 - -0.3$ Å) or almost undistorted, depending on its lateral position. The most strongly adsorbed configuration exhibits the highest Δz, while the most weakly bound configuration is characterized by an almost undistorted adsorbate. This trend is also observed for TTPB-Fe_3, with a noticeably higher magnitude of Δz.

The different lateral positions of TTPB allow for a variation of N–Au distances and a different degree of "bending" of the pyridyl groups towards the metal. As the N atoms are "active" for coordinative bonds to the metal, the adsorption energies are thus modulated.

While there is a significant distortion of the flat molecule upon adsorption, the Au surface is also deformed as TTPB interacts with it. Fig. 4.5 shows the z coordinate of the surface atoms optimized structures with TTPB in several positions. In the case of TTPB$_{hcp}$, the surface distortion is rather asymmetric, as one surface atom near the top-left terpy unit is "pulled out" of the surface by $\sim$0.2 Å, due to a strong interaction with the pyridyl nitrogen (cf. the atomic positions in Fig. 4.4 (a)). Gold atoms around the one pulled out recede back below the level of the surface. For the other cases, the heightmap approximately visualizes the "footprint" of TTPB, as the distortion preserves the general shape and symmetry of the molecule (Fig. 4.5(b)–(d)). The overall effect on the surface is stronger for TTPB-Fe_3, as the coordinated iron atoms strongly interact with their direct Au neighbors, and displace them from the surface. TTPB$_{fcc}$ causes the smallest distortion of the surface (about 50% of the magnitude of TTPB$_{top}$, not shown), presumably due to the weaker interaction, and significantly larger N–Au distances.

In conclusion, our results show that TTPB can adsorb rather strongly on Au(111), with some lateral selectivity, as shown by the differences in ΔE_{ads}. Coordination of Fe atoms significantly improves the binding of TTPB to the surface, since the molecule strongly coordinates Fe, and Fe provides additional interactions with surface atoms. Δz and $d_{\mathrm{N,Au}}$ indicate a deformation of the molecule, as N atoms tend toward the surface where sterically possible. At the same time, depending on the interaction strength, TTPB also distorts the topmost metal layer by pulling out and depressing Au atoms.

TTPB on Cu(111)

The second substrate studied for TTPB adsorption is Cu(111). The in-plane lattice constant of Cu (2.55 Å) is significantly smaller than that of Au (2.88 Å), providing a better match with the interatomic length scales in TTPB and thus the periodicity of a possible network. For example, the distance between C1 and C3 in the TTPB-phenyl is 2.41 Å, so that both atoms can adopt an optimal adsorption position, nearly commensurate with the surface lattice. This better match with the underlying lattice may serve as a rationalization for the observed preferential orientation of TTPB on Cu(111).

Structures and Energetics

In order to elucidate the selectivity of the adsorption of TTPB on Cu, we placed the molecule in the 3 different lateral positions on the surface (Fig. 4.6), and rotated it by a varying angle. The center of the central benzene ring was placed atop *fcc*, *top*, and *hcp* positions, and the molecule turned by Θ = 0, 30, 60, 90° relative to the (01) axis of the surface. The adsorption energies of TTPB in these various configurations, ΔE_{ads} are given in Fig. 4.7(a). The most stable configuration is that with the center

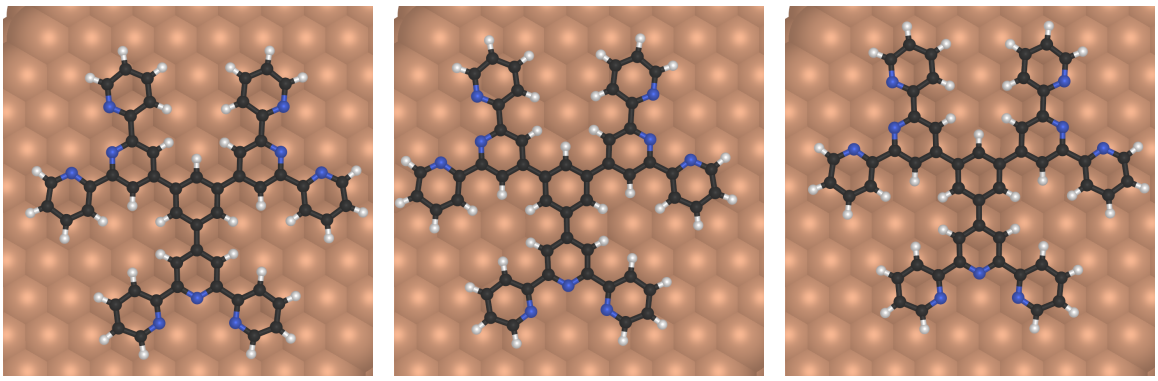

(a) *hcp* (b) *top* (c) *fcc*

Figure 4.6|Optimized structures of TTPB in 3 different lateral positions on a Cu(111) surface. The adsorption position is defined by the center of the central benzene ring relative to the surface metal atoms. For all molecules $\Theta = 0°$. Atom colors: H, white; C, black; N, blue; Cu, pink.

Φ, °	*hcp*	*top*	*fcc*
0	-556.6	-464.0	-534.0
30	-527.6	-524.0	-540.3
60	-538.0	-512.7	-541.5
90	-542.3	-522.9	-542.5

(a)

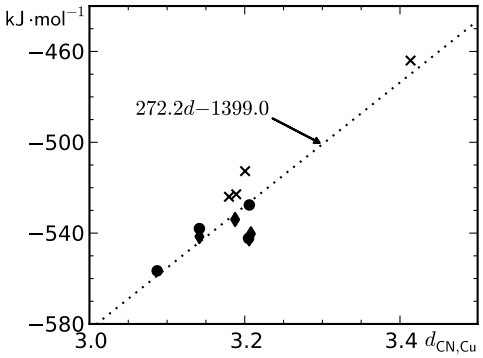

(b)

Figure 4.7|(a) Adsorption energies (ΔE_{ads}, kJ·mol^{-1}) of TTPB on Cu(111) as a function of adsorption registry (of the central benzene ring) and rotation angle of the molecule. (b) ΔE_{ads} (TTPB) as a function of the average distance of C and N atoms to substrate Cu. Dotted line shows linear fit. Markers indicate registry: crosses, *top*; circles, *hcp*; diamonds, *fcc*.

of the molecule atop an *hcp* site and $\Theta = 0°$, with ΔE_{ads} = -556.6 kJ·mol^{-1}, while a lateral shift to the *fcc* position leads to the lowest ΔE_{ads} of -464.0 kJ·mol^{-1}. The other investigated configurations exhibit intermediate values of ΔE_{ads}, in the range -512– -542 eV. These differences in ΔE_{ads} can rationalize the preferential orientation of TTPB on Cu(111), since at low temperatures the *hcp*/0° configuration should be most strongly populated.

In the search for an explanation of the different ΔE_{ads}, the different adsorbate-substrate distances due to the variation in position and rotation, may play a role. In Fig. 4.7(b) we plot ΔE_{ads} as a function of the average distance of C and N atoms ($d_{CN,Cu}$) to the closest substrate Cu atom. The trend is not perfectly linear, as the points at intermediate $d_{CN,Cu}$ show some variation in ΔE_{ads}, but a correlation is still rather apparent. The hcp/0° configuration is set apart from the others by a 0.05 Å smaller adsorbate-surface distance, while *top*/0° has about 0.2 Å longer $d_{CN,Cu}$ than any other configuration. From this we infer that for particular position/rotation combinations, the distances between TTPB and "active" binding atoms on the surface are optimal and for others badly matching. Given the structure

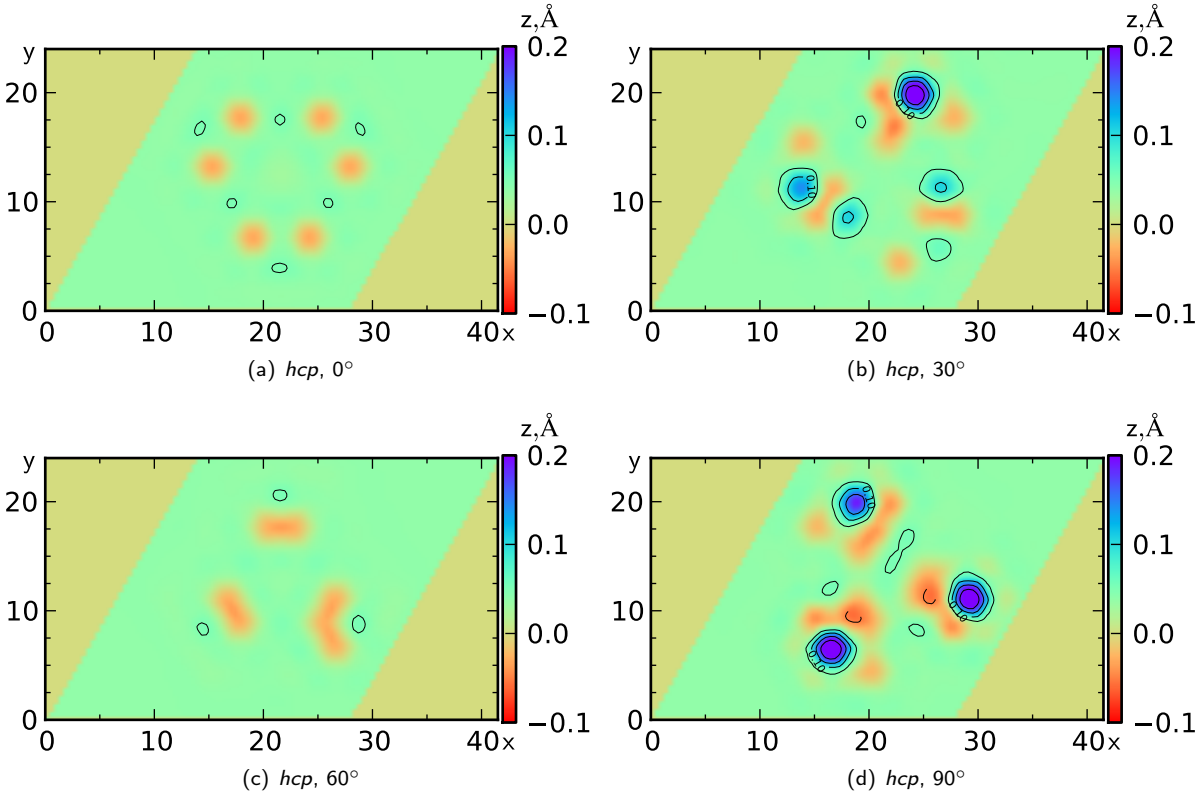

(a) *hcp*, 0° (b) *hcp*, 30°

(c) *hcp*, 60° (d) *hcp*, 90°

Figure 4.8|Elevation map of top layer Cu atoms for TTPB at 4 rotation angles in the *hcp* position on Cu(111).

of TTPB and the surface, this can rationalize the preferential orientation observed in the experiment.

In analogy to the presented results for TTPB/Au, Fig. 4.8 shows elevation maps for the series of rotation angles with TTPB in the *hcp* position. The molecule leaves a footprint on the Cu surface, as various surface atoms are displaced from their equilibrium positions. At $\Theta = 0°$, the height map reflects the symmetry of the molecule very well, with six Cu atoms slightly depressed into the plane of the surface. These displaced atoms are located under the C atoms with which the arms of terpy are attached to the central pyridyl group. At 30°, one particular Cu atom is pulled out from the surface rather far by a pyridyl N, while two others also move upward somewhat. Comparing 0° and 60°, the latter exhibits a similar magnitude of distortion, but with a different symmetry. Here, the atoms underneath the central pyridyl of terpy are slightly depressed, since there the molecule is closest to the surface. Finally, for the case of $\Theta = 90°$, three Cu atoms are significantly pulled out of the substrate, partially conforming to the symmetry of TTPB. One of the pyridyl arms rotates toward the surface, forming a $\sim$2.3 Å bond with the closest metal atom. This is is the same observation as for the 30° case, now occurring on all three terpy arms. As ΔE_{ads} is significantly lower for $\Theta = 90°$, it is likely that the 30° system is in a metastable configuration, and would energetically benefit from forming the full set of 3 N–Cu bonds. However, the energetic cost of displacing atoms from the surface apparently (partially) compensates the gain from forming stronger bonds, since the most stable system *hcp*/0° does not exhibit any such bonds or signifcant distortions of the surface.

We conclude that the interaction between TTPB and Cu is governed by subtle variations of the "fit" of the atoms of TTPB onto the Cu surface due to the lateral position and rotation. Configurations with a good fit exhibit strong ΔE_{ads}, and *vice versa*. This effect is especially pronounced as the surface lattice constant of Cu matches the dimensions of TTPB well, leading to large effects of the molecule placement.

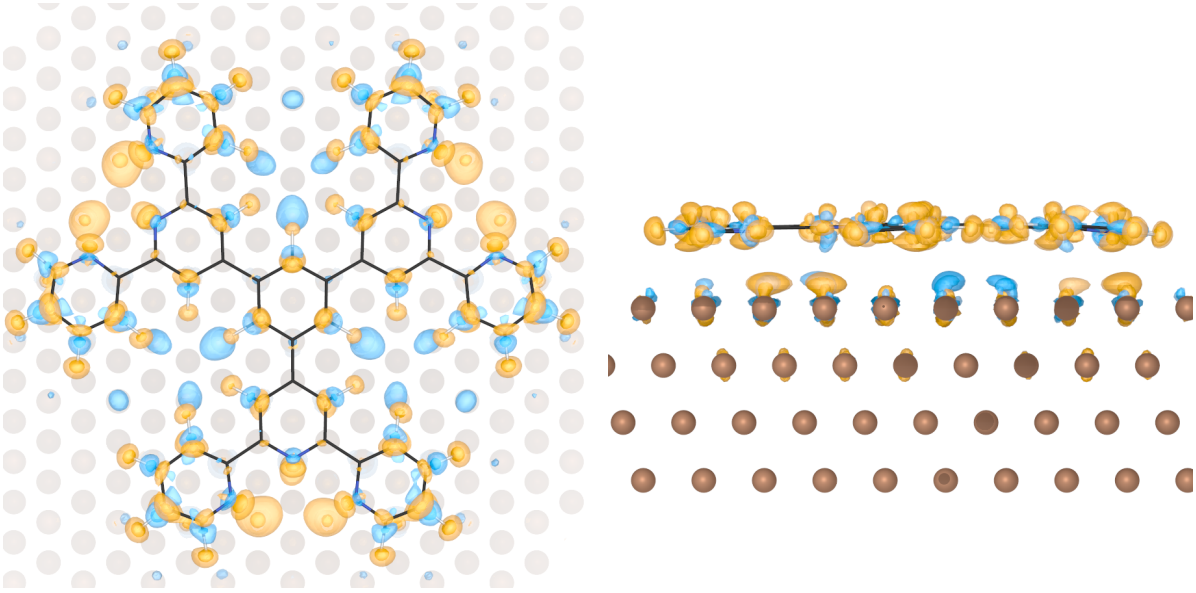

(a) (b)

Figure 4.9|Top (a) and side (b) views of the electron density difference for TTPB$_{hcp}$ at 0° rotation. Blue isosurface indicates accumulation of e-density, orange indicates depletion. Isovalues at ±0.005 and ±0.001 e/Bohr^3

Electron Density Difference

While the interaction of TTPB with Cu is largely of a physisorptive nature (indicated by the ∼3 Å separation between the molecule and metal, and the modest ΔE_{ads} of -5– -6 kJ·mol^{-1} per atom), some electron redistribution occurs upon adsorption. Fig. 4.9 shows an electron density difference map for the TTPB$_{hcp}$ 0° system. Particularly, one observes a polarization of the pyridyl-N atoms, which lose some electron density upon binding. This may indicate a partial coordinative bond of these N to the metal, which would provide some additional chemisorptive contribution to the adsorbate-substrate interaction. At the same time some electron accumulation is found around the central phenyl ring, and the C atoms of the pyridyl groups. The side view of the electron density difference (panel (b)) shows the vertical polarization of the molecule, with some electron accumulation between the surface and TTPB. The overall magnitude of these effects is rather minor.

Projected Density of States

In order to examine the effects of adsorption on the electronic structure of TTPB, we plot the PDOS on the pyridyl N atoms in Fig. 4.10 in the *hcp* and *top* positions for all considered rotation angles Θ. In general, the molecular HOMO-LUMO gap is on the order of 1.8 eV, the highest occupied states having predominantly p_{x} and p_{y} character and the lowest unoccupied states p_{z}. The most stable configuration, TTPB$_{hcp}$/0°, is characterized by a PDOS with three approximately equally spaced peaks between -1.8 and -2.8 eV, originating from p_{x} and p_{y} states.

As the molecule is rotated at this lateral position, the structure of this feature of the PDOS changes markedly. At Θ = 30°, the two deeper peaks largely merge into a single peak at an intermediate position. Upon further rotation to Θ = 60°, the three-peak structure of the initial configuration is restored. Finally, at Θ = 90° the feature once again collapses to two peaks. The same behavior can be observed for the s states, while the p_{z}-DOS remains mostly unaffected by the rotation of the molecule.

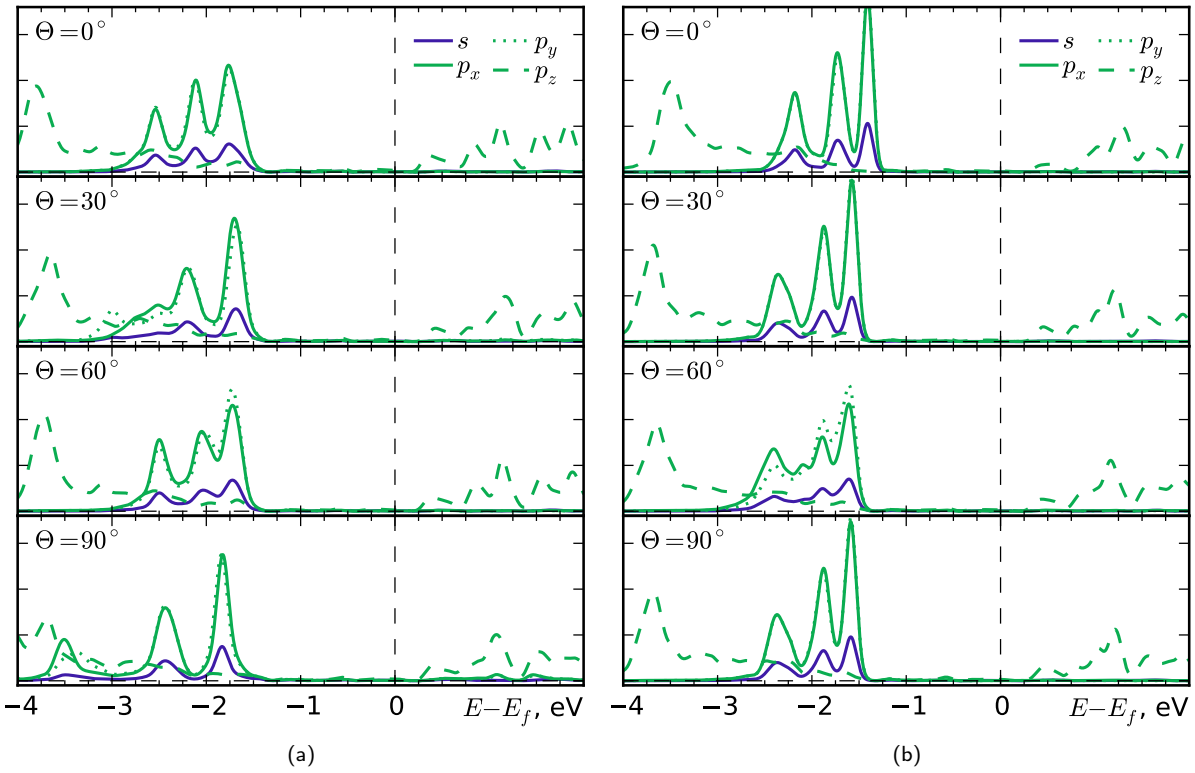

Figure 4.10|PDOS on N atoms and separated by angular momentum components for TTPB/Cu(111) in (a) *hcp*, (b) *top* position as a function of rotation angle Θ.

Fig. 4.10(b) shows the same data for TTPB in a different lateral position, *top*. The rotation-dependent structure of the occupied states close to the Fermi level is largely absent, and the three-peak structure of the s and p_x, p_y feature is conserved for all rotation angles. A small exception to this is the PDOS at $\Theta = 60°$, where the shape of these peaks slightly changes and the degeneracy of p_x and p_y is not preserved.

Conformation of the Pyridyl Groups

An additional structural property of adsorbed TTPB that is not readily accessible experimentally is the conformation of terpy. STM imaging cannot distinguish between the *cis* and *trans* conformations of the pyridyl arms. In order to form extended networks, terpy has to adopt an all-*cis* conformation, which is what the study above exclusively focused on. However, isolated monomers may also be present in full or partial *trans* conformations, making it instructive to see the different properties and adsorption characteristics of these species.

Alongside all-*cis* TTPB_{hcp}, we prepared conformations with 1, 2, 3 and 6 of the pyridyl arms in *trans* conformations, and optimized their structures. The relative energies of these species are plotted in Fig. 4.11(a). As the graphic shows, an increasing number of *trans* pyridyl groups (n_{trans}) proportionally reduces the total energy of the system. The increase very closely follows a linear trend, where each flipping of a pyridyl group contributes $\sim$30 kJ·mol^{-1} of conformational stabilization energy. This is evidence that TTPB will likely be present in (partial) *trans* conformations at finite temperatures. Since the magnitude of the stabilization is rather substantial, relative to the overall variation in ΔE_{ads}, *trans*-TTPB will likely be more stable also as an adsorbed monomer.

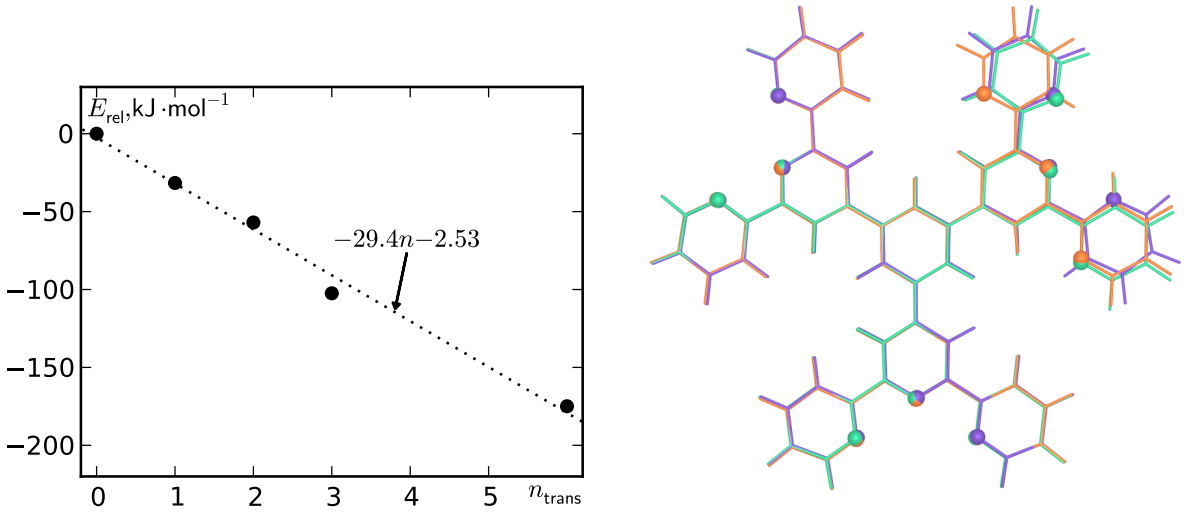

Figure 4.11|(a) Relative energies of TTPB as a function of the number of *trans* pyridyl groups. (b) Overlay of optimized geometries of TTPB on Cu(111) with different pyridyl conformations: all-*cis* (purple), 1-*trans* (light green), 2-*trans* (orange). Spheres indicate N atoms.

Fig. 4.11(b) shows optimized structures of all-*cis* , 1-*trans* and 2-*trans* TTPB superimposed onto each other. It is evident that the changes due to the flipping of the pyridyl groups are localized only on that group, and the rest of the molecule remains essentially unaltered.

The effect of the pyridyl conformation is also apparent in the electronic structure of the molecule. As in the previous section, Fig. 4.12 shows the PDOS projected on TTPB N atoms, for all flipped conformations. The top panel shows the all-*cis* conformation, with the 3-peak structure as described above. When one pyridyl group is switched, the overall symmetry of the molecule is broken, affecting the degeneracy of the p_x and p_z states, altering chiefly the p_x peak shape. This effect is larger still for the 2-*trans* TTPB, where now also the p_y peak changes, compared to the top and second panels. When three pyridyl groups are flipped (each on one of the terpy arms), the overall symmetry of the molecule is restored – each terpy arm now has 1 *cis* and 1 *trans* pyridyl rest. Thus the p_x and p_y states become indistinguishable once more, and the 3-peak shape of the PDOS resembles that shown in the top panel, with somewhat changed amplitudes.

Summary: TTPB on Metal Substrates

Experimental evidence indicates that TTPB readily adsorbs on noble metal surfaces, with the possibility to form networks by co-adsorption with Fe or NaCl. Our calculations of TTPB on Au(111) indicate a preferred lateral position, with the center of the molecule in a *top* position. The addition of Fe atoms significantly strengthens the binding to the metal. On Cu(111), TTPB is found to adsorb with a preferential orientation. Our calculations confirm this observation, rationalizing it with a significantly reduced N–Cu distance when TTPB is in the *hcp* position, oriented along the (01) axis of the surface. The rotation of the molecules also influences their electronic structure, as seen in the PDOS. The conformation of TTPB (*cis* or *trans*) influences its stability, each *trans* pyridyl group stabilizes the molecule by $\sim$30 kJ·mol^{-1}.

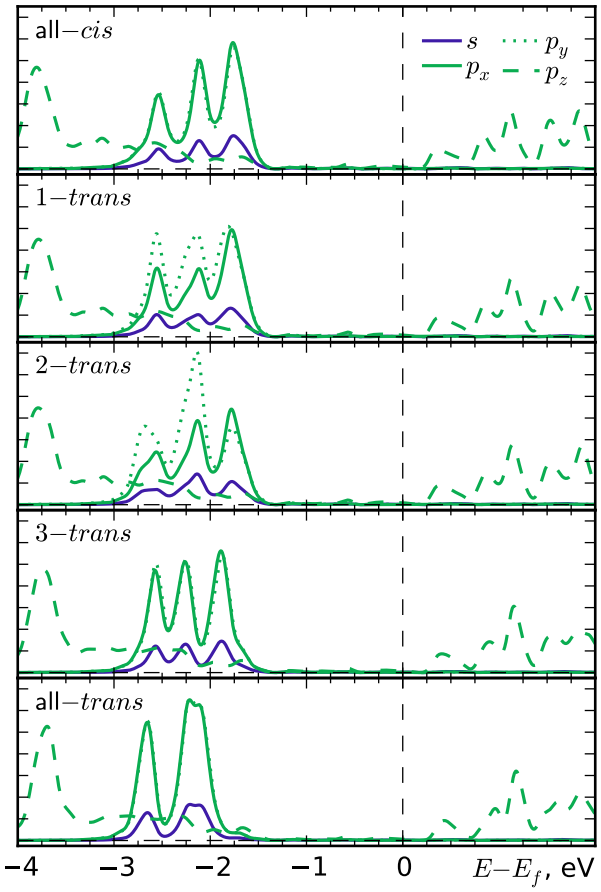

Figure 4.12|PDOS on N atoms and by angular momentum components for TTPB/Cu(111) in *hcp* position ($\Theta = 0°$) for different numbers of *trans* pyridyl groups.

4.4 TTPB Confined on a Water Surface

Based on reference 16.

Aside from metallic substrates, molecular networks of TTPB-like molecules have also been realized on the surface of liquid water, by interlinking confined monomers.[15] Also in this case, simulations can provide valuable atomic-scale insight into processes that are not observable experimentally, and thus complement the available results.

Before interlinking the monomers with metal ions, they are confined on the water surface as outlined in Section 4.1. In this section we examine the dynamic properties of TTPB on H_2O and the influence of the adsorbate on the water surface. We then use MTD simulate the migration from the water bulk to the ligand pocket of TTPB, quantify the free energy surface of the Zn^{2+} and study the diffusion and binding process in detail. These results then provide the basis for the final section of this chapter, which examines the properties and energetics of Zn-bridged TTPB dimers and networks on water.

Model

We carry out DFT-based MD and MTD simulations of an individual TTPB molecule adsorbed on a water surface. The latter is modelled as a periodic slab of 482 H_2O molecules occupying a volume of $30\times30\times16\,\text{Å}^3$, with a vacuum region of $\sim$60 Å in the direction perpendicular to the surface. The di-

ameter of the TTPB molecule is approximately 19 Å, which allows for a sufficient distance to decouple the periodic replicas of the molecule. Fig. 4.13 shows the simulation cell with water and TTPB atop it. The entire system is treated quantum-mechanically, using DFT with a dispersion-corrected PBE XC functional, as introduced in Section 2.3.

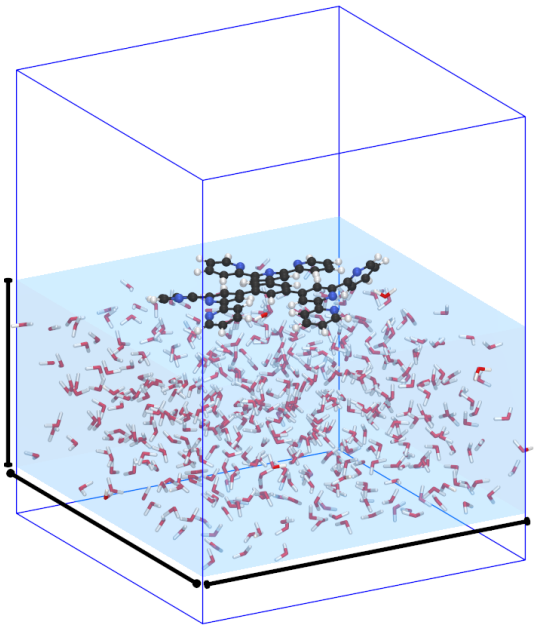

Figure 4.13|Simulation cell with TTPB supported by 482 water molecules (shaded in blue). Vacuum region not to scale. Atom colors: O, red; H, white; C, black; N, blue.

We simulate three different systems: A TTPB molecule adsorbed on the water slab ("$TTPB_w$"), a TTPB molecule with 3 Zn^{2+} ions coordinated to the terpy groups and Cl^- counterions in the liquid phase ("$TTPB_w$-Zn_3"), and, for comparison, a free TTPB molecule in the gas phase ("$TTPB_g$"). The $TTPB_w$ system consists of one molecule in close proximity to the water surface and we use MD to examine its dynamic properties. In order to study the effect of the coordinated Zn ion, we carry out the same simulation for the $TTPB_w$-Zn_3 system, which is expected to show somewhat different dynamics on the water surface. We also simulate a trajectory of $TTPB_g$, which we then compare to the water-supported systems in order to quantify the influence of the liquid substrate. For each system, we obtain NVT trajectories of at least 15 ps length, starting from a pre-equilibrated water slab and statically optimized TTPB.

Because of the dynamics of the liquid and the lack of rigid adsorption sites, we expect a milder influence of the surface than, e.g., on a metal or semiconductor substrate. The confined molecule is larger and heavier than water and can be expected to have an effect on the structure of the water surface. In the first part of this section, we examine the properties of adsorbed TTPB and H_2O, respectively.

Besides the dynamics of TTPB, we also investigate the reaction of the molecule with Zn^{2+} taken up from the liquid phase. As this reaction is a "rare event" on the timescale of our simulations, we employ MTD.[136] Here, an adaptive bias potential is applied in the reduced phase space of two CVs to energetically discourage already explored regions of the configurational space and thus accelerate the sampling (see Section 2.2). As CVs we choose the Zn–TTPB distance and Zn–N coordination number. They are expected to span a configurational space in which the processes of interest here are well described. The MTD trajectory is computed for a total of 60 ps, with deposition of hills every 50 steps, beginning after 7.3 ps of unbiased MD. A quadratic wall potential is used to limit the distance between Zn and TTPB to less than about 13 Å. The deposited hills are subsequently integrated to reconstruct the underlying free energy surface (FES).

Dynamic Properties of TTPB

We monitor two structural parameters describing water-supported TTPB: intramolecular dihedral angles and the out-of-plane distortion of the molecule.

The rotation of the pyridine rings of TTPB makes up a large part of its structural flexibility. The "outer" pyridyl groups of TTPB can rotate around the C–C single bond connecting them to the central pyridine, as shown by the yellow arrow in Fig. 4.14 (a). There are six such N–C–C–N dihedral angles per TTPB molecule, which we collectively refer to as Φ. Furthermore, each terpy unit can rotate around the

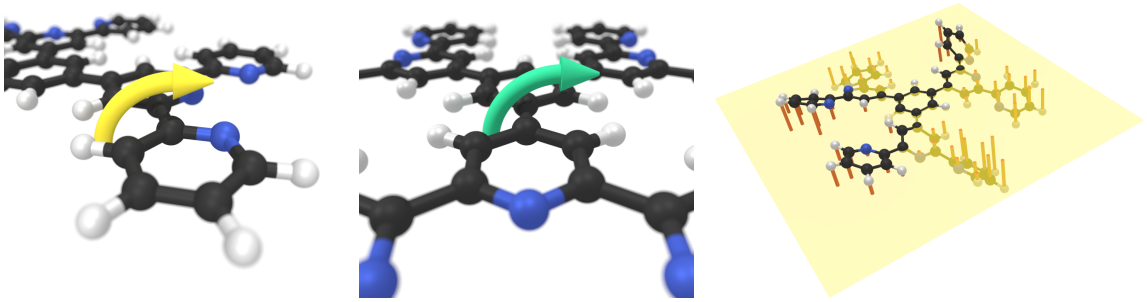

(a) (b) (c)

Figure 4.14|(a) Rotation of a pyridyl unit around its C–C bond, described by the N–C–C–N dihedral angle Φ. (b) Rotation of an entire terpyridyl unit around the central C–C bond, described by the C–C–C–C dihedral angle Θ. (c) Out-of-plane distortion of TTPB, described by the perpendicular distances of atoms (red) to a best-fit plane (yellow) defined by the central benzene ring. Atom colors: H, white; C, black; N, blue.

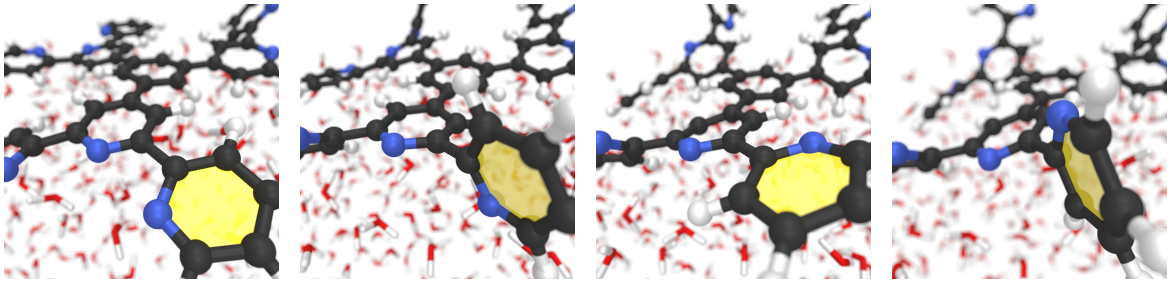

(a) (b) (c) (d)

Figure 4.15|Rotation of a pyridyl group (yellow highlight) of TTPB around its C–C bond. (a)–(d) 4 snapshots from MD trajectory, with $\Phi \approx 0°$, 90°, 180°, and 270°, respectively. Atom colors: O, red; H, white; C, black; N, blue.

single bond to the central benzene unit, giving rise to three equivalent C–C–C–C angles, Θ, indicated by the green arrow in Fig. 4.14 (b). As there are no other single bonds in the molecule (besides those to hydrogen), Φ and Θ together describe the entire intramolecular rotational flexibility of TTPB.

Another way to quantify the dynamics of the structure of TTPB is based on the deviation from the molecule's equilibrium shape. In the absence of external influences such as temperature, TTPB remains flat, and is stable with the pyridyl units in both all-*cis* and all-*trans* conformations. We define the distortion of the molecule, Δ_d, as the mean distance over all atoms from a plane of best fit through the central benzene ring,

$$\Delta_d = \sum_{i=1}^{N} \frac{|r_i - r_{0,i}|}{N}, \tag{4.1}$$

where r_i is the position of atom i, and $r_{0,i}$ is its projection on the plane (Fig. 4.14(c)). In the limit of a perfectly flat molecule, Δ_d is zero and rises as the molecule is distorted and loses planarity.

The two quantities, Φ and Δ_d, are complementary, as various conformations of the molecule may give rise to identical Φ or Θ, while having different values for Δ_d, and *vice versa*. E.g., as long as the molecule remains flat, $\Phi = 0°$ and $\Phi = 180°$ are characterized by the same $\Delta_d = 0$. Conversely, an upward "bulging" of TTPB gives rise to nonzero Δ_d, while preserving $\Phi = \Theta = 0$.

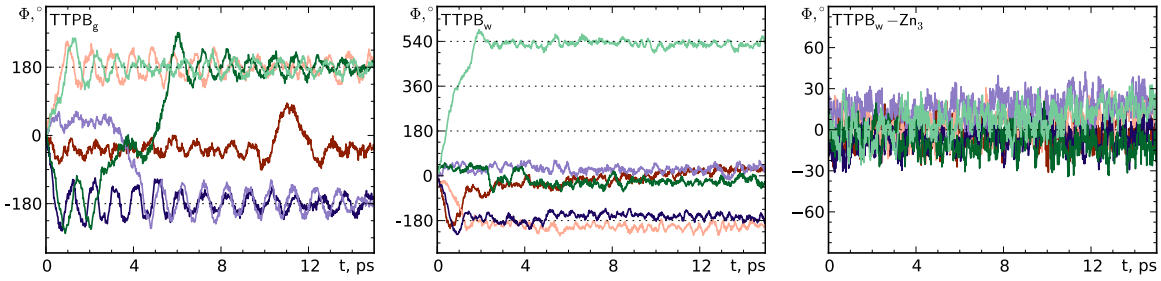

Figure 4.16|Inner (Θ) dihedral angles of TTPB (C-C-C-C and N-C-C-N) for the (a) $TTPB_g$, (b) $TTPB_w$, and (c) $TTPB_w$-Zn_3 systems, respectively, as a function of time. Data published in ref. 16.

Dihedral Angles

Fig. 4.15 shows four snapshots from the MD trajectory of $TTPB_w$, highlighting the rotation of a pyridyl group around the single bond. This occurs rather rapidly, as TTPB is not stable in the all-*cis* conformation at the temperature of the simulation. Instead, some pyridyls adopt and remain in a *trans* conformation, as the one shown in Fig. 4.15(c). In this case Φ has a value of 180°. Typically, each terpy remains with one pyridyl group in a *cis* and one in a *trans* conformation relative to the central pyridine.

Fig. 4.16(a)-(c) show the six angles Φ in $TTPB_g$, $TTPB_w$, and $TTPB_w$-Zn_3 as a function of time. In $TTPB_g$, most pyridine rings rotate outward within 1 ps, maximizing the distance between the N atoms. This partial *trans* conformation then remains largely stable, with sizable fluctuations around the mean dihedral angles and even 180° flips of some pyridyl groups. The $TTPB_w$ system is also characterized by a similar number of *trans* pyridyl units, one of which in fact undergoes a 360° turn and only thereafter adopts the *trans* conformation (shown in the sequence in Fig. 4.15). Compared to $TTPB_g$, however, the fluctuations around the equilibrium angles are significantly smaller in amplitude. In $TTPB_w$-Zn_3, the coordination of the Zn ion by the 3 ligands leads to stable bonds that prevent large rotations. Fluctuations of Φ are centered around zero for all six angles. Evidently, all pyridyls remain in the *cis* conformation, held there by the bound ions. Metal coordination can thus successfully and selectively restrain the torsional flexibility of the molecule.

The angles Θ show slightly different behavior (not pictured). In $TTPB_g$, the terpyrdine units rotate almost freely around the single bonds, without settling into a stable conformation on the timescale of the simulation. In contrast, in both $TTPB_w$ and $TTPB_w$-Zn_3, the terpy moieties adopt a mean $\Theta \leq \pm 30°$ and fluctuate around it with a small amplitude. As for the case of Φ, the dominating stabilizing influence is the presence of the water substrate, whereas the coordination of Zn ions to terpy does not significantly affect rotation of the whole unit.

After the pyridyl and terpy groups have adopted a stable conformation (*cis* or *trans* for the pyridyls), they fluctuate around an average dihedral angle Φ_{avg}. Similarly, the terpy units fluctuate around Θ_{avg}, determined from the overall trajectory, excluding the first 2 ps. In Fig. 4.17(b) and (c) we plot the distributions of the deviations $\Delta\Phi = \Phi - \Phi_{\mathrm{avg}}$ and $\Delta\Theta = \Theta - \Theta_{\mathrm{avg}}$, aggregrated for all equivalent angles in the molecule, for $TTPB_g$, $TTPB_w$, and $TTPB_w$-Zn_3. The distributions follow a clear trend in the first instance, obvious from the shape of the curves, and well-represented also by the full width at half maximum (FWHM) of the peaks. The greatest fluctuation of angles occurs in the gas phase. The distribution significantly narrows once the molecule is brought into contact with the water surface. The peak width is reduced by almost 60% for ΔΦ. Coordination of Zn additionally increases the conformational rigidity of the molecule, keeping all fluctuations within 30° of the equilibrium angles, further reducing the FWHM by 28%.

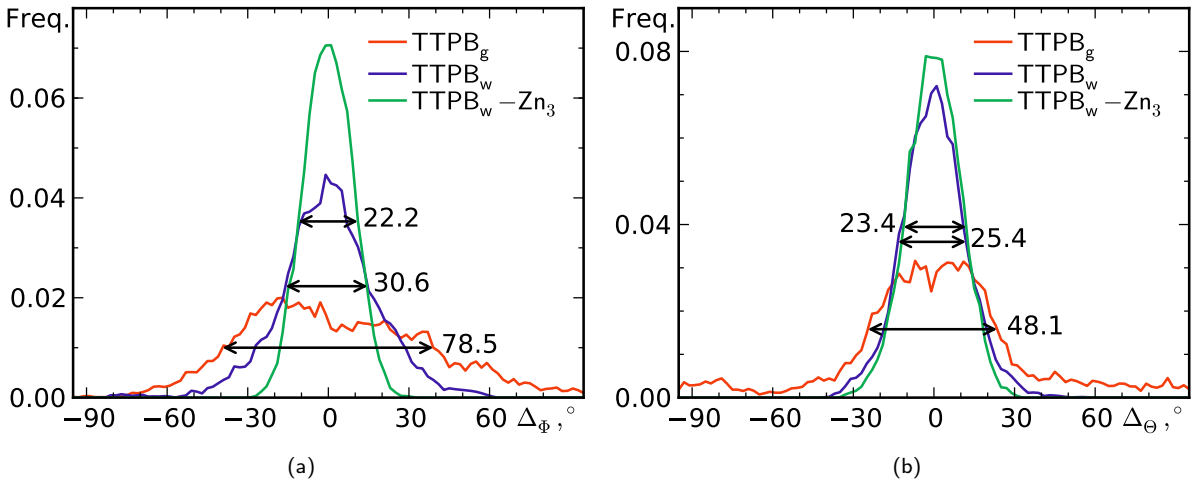

Figure 4.17|Histograms of deviation of dihedral angles from equilibrium value for $TTPB_g$, $TTPB_w$, and $TTPB_w$-Zn_3: (a) Outer dihedral angles ($\Delta\Phi$). (b) Inner dihedral angles ($\Delta\Theta$). Data updated based on ref. 16, where the distribution of one angle Θ in $TTPB_w$-Zn_3 included an error that made the histogram appear narrower.

For the dihedral angles Θ, the distribution narrows by 47% with adsorption. Subsequent metal coordination has little influence on the distribution of $\Delta\Phi$, reducing the FWHM by only 2°. This is consistent with the intuition that ion binding in the terpy pocket should not influence the rotation around the central benzene. Overall, the $\Delta\Theta$ distributions are narrower than those of $\Delta\Phi$, because the rotation of the whole terpyridine unit is sterically hindered compared to that of an invidiual pyridyl group. The terpyridine moiety is significantly larger and heavier, and thus rotates more slowly, and is more strongly impeded by the water substrate.

These data indicate that the liquid substrate exerts a stabilizing and confining influence on the TTPB molecule. Intramolecular rotations of TTPB are restricted and reduced, as shown by both the distributions of $\Delta\Phi$ and $\Delta\Theta$.

Distortion of the Molecule

In Fig. 4.18(a) we plot the time dependence of Δ_d for all three simulations. It rapidly increases from its initial value of zero in the first ps. At equilibrium, the distortion fluctuates around $\Delta_d \approx 2$ Å for $TTPB_g$, and $\Delta_d \approx 1$ Å for $TTPB_w$ and $TTPB_w$-Zn_3. The molecule in the gas phase reaches a much higher distortion, and exhibits stronger variations. $TTPB_w$ and $TTPB_w$-Zn_3 fluctuate with a smaller amplitude around a mean Δ_d only about half as large as that of free TTPB. Fig. 4.18(b) shows distributions of Δ_d. $TTPB_g$ shows the highest FWHM (0.47 Å), while the distributions for $TTPB_w$ and $TTPB_w$-Zn_3 are rather similar, with FWHM 0.353 and 0.408 Å, respectively.

In contrast to the fluctuation of the dihedral angles Φ, the coordination of the metal ion has little effect on the molecule's out-of-plane distortion. This is an indication that the predominant contributions to the distortion of the molecule are the rotation and deformation of the entire terpy units, rather than of the individual pyridyl groups. In fact, fixing these groups with Zn does not reduce Δ_d. The rotation of the terpy unit has a greater contribution to Δ_d, as the atoms far from the axis of rotation are further away from the best-fit plane (Fig. 4.14(c)). Additionally, this quantity also captures "vertical" displacement of the atoms, due to bending of the molecule, which is presumably greater in $TTPB_w$-Zn_3, due to the greater torsional rigidity of the terpy units.

The influence of the substrate on the out-of-plane distortion of TTPB is evident. The water surface confines the molecule while still allowing a certain degree of structural freedom. In this respect the liq-

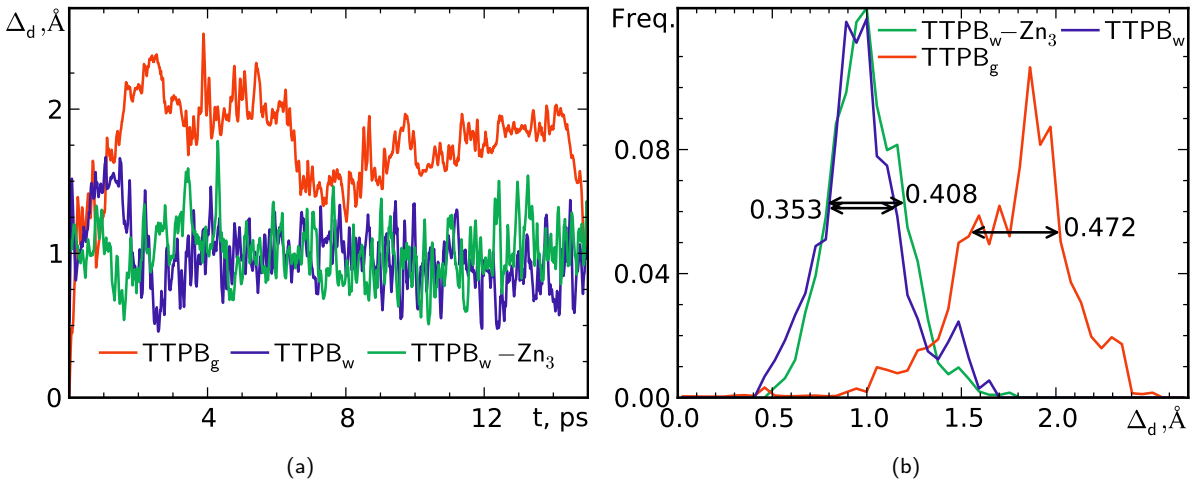

Figure 4.18|Distortion of the adsorbate (a) Distortion Δ_d of $TTPB_g$, $TTPB_w$, and $TTPB_w$-Zn_3 as a function of time. (b) Distribution of molecular distortions. Horizontal bars indicate estimates of the FWHM. Data published in ref. 16.

uid surface acts as an intermediate-strength support, between a rigid solid surface and the unrestrained gas phase molecule.

Influence of TTPB on the Water Support

Having quantified the influence of the support on TTPB, we now examine the reverse, i.e. the adsorbate's impact on the structure and properties of H_2O. It has been shown that structural and dynamic properties of water change near an interface with air or vacuum.[153,217,218] In our simulation, roughly 30% of one side of the water slab is covered by the TTPB molecule, while the opposite side is a bare water surface. It is thus possible that the presence of the adsorbate changes the interface properties, compared to those of the bare interface. We compare the two sides in order to characterize the effect of the adsorbate.

For this purpose we monitor the liquid density as a function of depth and the internal structure of the liquid as characterized by the hydrogen bonding network.

Density Profile

We compute the density of the water slab as a function of depth (z) in intervals of 2 Å. By fitting the expression

$$\rho(z) = \frac{\rho_0}{2}\left(1 + \tanh\left(-\frac{z - z_G}{\delta}\right)\right) \tag{4.2}$$

to the density data (from both sides), we obtain values for the bulk density $\rho_0 = (1.05 \pm 0.01)$ g·cm^{-3}, the interface thickness $\delta = (1.46 \pm 0.20)$ Å and the location of the Gibbs' dividing surface, z_G, at values of -16.34 Å and -1.01 Å (averages for[217] tpw and $TTPB_w$-Zn_3 simulations). The presented $\pm$values correspond to standard deviations for the four independently obtained fitted quantities. ρ_0 and δ are nearly identical on both sides of the slab for $TTPB_w$ and $TTPB_w$-Zn_3, and the averages agree well with previously reported data ($\delta = 1.1$,[153] 1.71 Å,[217] $\rho_0 = 0.98$,[153] 1.01 g·cm^{-3} [217]).

Fig. 4.19 shows the density profiles and fitted functions for $TTPB_w$ and $TTPB_w$-Zn_3. The right-hand side of the plots (values around $z = 0$ Å) are those in contact with the TTPB molecule. In general, the curves fit the points very well and converge essentially to the same bulk densities from left and right. Both visually and quantitatively, the TTPB-exposed sides show no difference to the bare surfaces. The

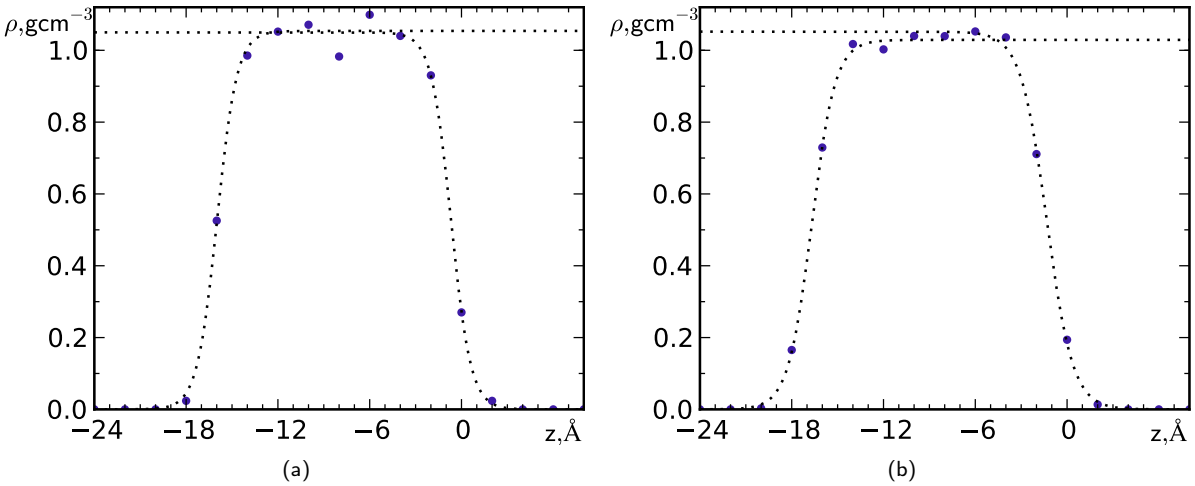

Figure 4.19|Density profile of water slabs along the direction perpendicular to the surface. Points fitted to Eq. 4.2. (a) $TTPB_w$, (b) $TTPB_w$-Zn_3. Data published in ref. 16.

slightly lower bulk density found for $TTPB_w$-Zn_3 (left curve), is likely due to the presence of counterions in the liquid, which displace water molecules and thus lower the density.

Based on the density profiles, we observe no significant effect of the adsorbate on the overall structure of the water slab.

Hydrogen Bond Populations

We subdivide the water slab into 4 vertical regions with a thickness of 4 Å (Fig. 4.20), and investigate differences between the hydrogen bonding (H-bonding) network in the bulk and near the free and covered surfaces. An H-bond is defined by two H_2O molecules, for which $d_{OO} < 3.5$ Å and $\angle_{OHO} > 140°$.[153] In the H-bond network, water molecules can be categorized based on the number of donor (D) and acceptor (A) H-bonds. Most are bound by 2–4 H-bonds: 1 donor/1 acceptor (DA), 2 donors/1 acceptor (DDA), 1 donor/2 acceptors (DAA), 2 donors/2 acceptors (DDAA).[153]

Fig. 4.21(a) and (b) show the probabilities for the various donor/acceptor combinations as a function of depth for $TTPB_w$ and $TTPB_w$-Zn_3, respectively. In both simulations, the two middle regions contain predominantly DDAA species, as expected in bulk water. The probability of DDAA bonding in the regions II and III ranges from 0.62 to 0.67, with slightly higher values found in the $TTPB_w$ simulation. This value is in line with previous reports. Using the BLYP functional, Baer et al.[153] determine a value around 0.5 using the same H-bond definition as this work, while other studies find 0.40[218] and 0.84,[217] using different definitions and methods. The free surface is characterized by an increased incidence of the other three species, reducing the number of DDAA by approximately one third ($TTPB_w$) to one quarter ($TTPB_w$-Zn_3). Qualitatively this agrees well with previous reports,[217] but it should be noted that we use a rather coarse vertical partitioning of the water slab, which may not fully capture the rapid change in the species' distribution.

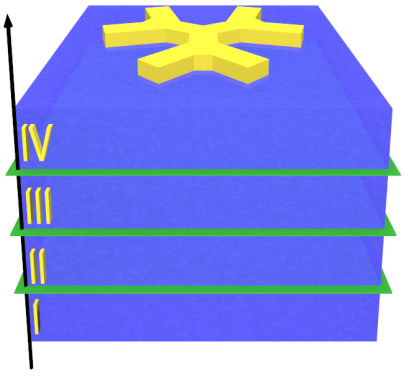

Figure 4.20|Vertical subdivision of H_2O slab into regions I–IV. Data published in ref. 16.

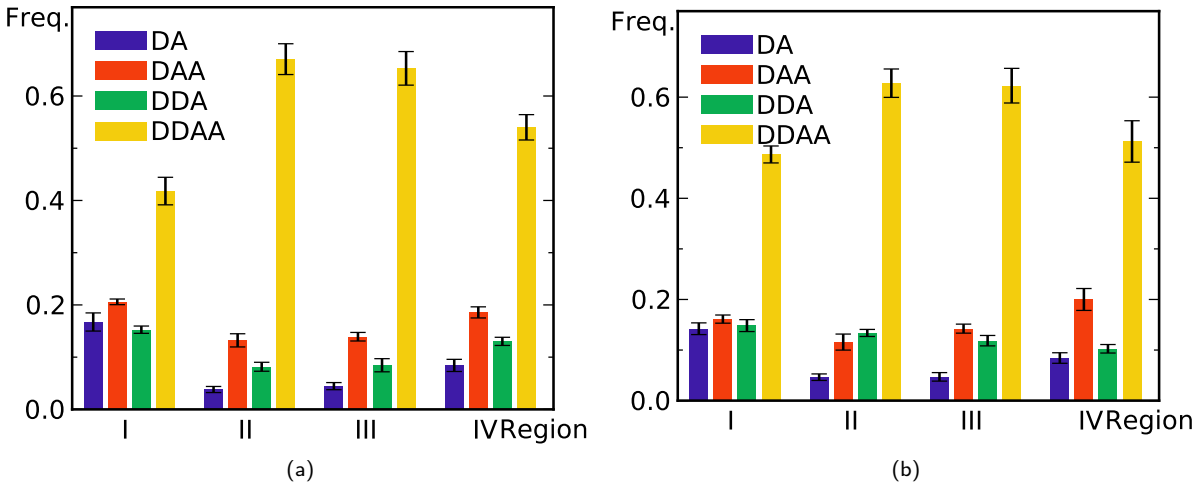

Figure 4.21|Hydrogen bond patterns in the water slab. Populations of H_2O molecules in particular H-bond envrionments in the 4 vertical regions for (a) $TTPB_w$, (b) $TTPB_w$-Zn_3. The error bars indicate the standard deviation of the H-bond population over 2 ps sub-blocks of the trajectories. Data published in ref. 16.

For the case of $TTPB_w$ the surface covered by the adsorbate exhibits a distribution of H-bonds roughly half-way between those of the free surface and the bulk regions. Compared to the free surface, the fraction of DDAA species increases from 0.41 to 0.54, while the fraction of DA species decreases by approximately 50%. Compared to the bulk-like region, the fraction of DDAA species decreases from 0.65 and the occurrence of DA molecules roughly doubles. On the other hand, the DAA and DDA water molecules are approximately equally common on the free and covered surface sides, exhibiting increased probabilities compared to the bulk. In the $TTPB_w$-Zn_3 simulations, the differences in DDAA frequencies between the covered and free surfaces are less pronounced. The fraction of DA species is about 40% lower on the TTPB-covered side and the occurrence of DAA species is somewhat higher. Furthermore, we note a small number of double-acceptor (AA) species on the TTPB-covered side, that are almost completely absent from all other vertical regions. Generally, the $TTPB_w$ and $TTPB_w$-Zn_3 systems exhibit quite similar depth-dependencies of their H-bond distributions. It should be noted that in the $TTPB_w$-Zn_3 simulation, a total of 6 Cl^- ions are present in the bulk liquid, which may account for some of the differences in H-bonding patterns between the two simulations.

Our results agree with previous conclusions about the distributions of H-bonds near the air-water interface. Furthermore, they suggest that the adsorbate has a subtle influence on the H-bonding pattern of near-surface water molecules, reordering them to affect the frequencies of different donor/acceptor combinations.

Zn^{2+} Ion Insertion from the Liquid Phase

Once the TTPB monomer is confined at the water surface, the next step in the formation of a MOF is the coordination of metal ions, which serve as linkers between molecules. This process involves diffusion of the ions from the liquid phase to the surface and subsequent formation of 3 coordinative N_{terpy}–Zn bonds. Having established that Zn^{2+} binds to the terpy moieties of TTPB in a stable way (*vide supra*), we now examine the transition

$$\mathrm{TTPB}(ads) + \mathrm{Zn}^{2+}(aq) \rightleftharpoons \mathrm{TTPB}-\mathrm{Zn}(ads)$$

in detail, focusing on one isolated ion uptake rather than the saturation of all three ligand sites.

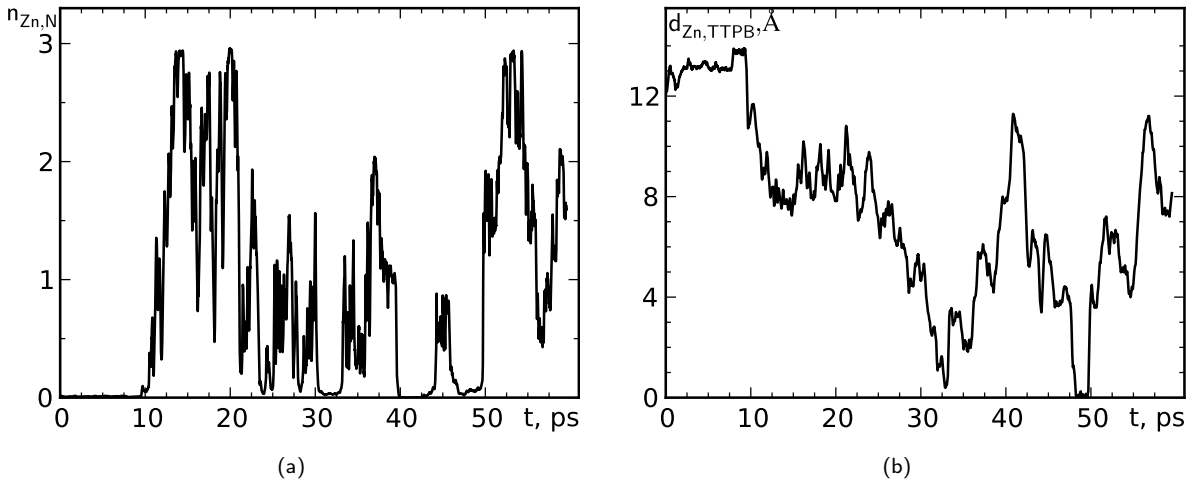

Figure 4.22|Collective variables in MTD run as a function of time: (a) $n_{\mathrm{Zn,N}}$ and (b) $d_{\mathrm{Zn,TTPB}}$. Data published in ref. 16.

We use MTD to accelerate the simulation of the process. As CVs, we choose the distance from Zn to the center of TTPB, $d_{\mathrm{Zn,TTPB}}$ and the Zn–N coordination number, $n_{\mathrm{Zn,N}}$. Starting from a configuration with Zn^{2+} rather far away from the molecule, along the metadynamics trajectory we expect $d_{\mathrm{Zn,TTPB}}$ to decrease and eventually $n_{\mathrm{Zn,N}}$ to increase from 0 to 3, i. e. full coordination of Zn by terpyridine. As the simulation goes on, the bias potential should drive Zn^{2+} out of the complex back into the solution. We can thus elucidate the molecular details of ion binding and describe the energy landscape of the process.

Fig. 4.22 shows the 2 CVs as a function of time. After the bias potential is activated ($t \approx 7.3$ ps) and some hills have been deposited, the coordination number rapidly increases to full binding at $n_{\mathrm{Zn,N}} = 3$, concurrently with a drop of $d_{\mathrm{Zn,TTPB}}$ from 12 to 8 Å. The bias potential then partially breaks the N–Zn bonds again, leading to intermittently decreased n (at a constant distance d), until Zn eventually leaves the ligand completely and reaches a position under the center of mass of TTPB ($d_{\mathrm{Zn,TTPB}} \approx$ 0 Å). Subsequently, the ion oscillates between partially bound and unbound configurations, reaching a situation of full coordination again after ∼55 ps. This indicates that the space spanned by the CVs has been sampled to a sufficient degree.

Ion Insertion: Free Energy and Mechanism

We plot the free energy data as a function of the two CVs, as well as a minimum-energy path for the first Zn^{2+} uptake event in Fig. 4.23(a). The free energy profile along this path is shown in Fig. 4.23(b), with minima and barriers labelled for comparison. Starting from bulk water (point 1) the ion has to escape a minimum of 430 kJ·mol^{-1} due to the solvation free energy, overcomes a barrier of about 165 kJ·mol^{-1} (point 2) and settles into a wider and deeper minimum somewhat closer to TTPB (-520 kJ·mol^{-1}, point 3). The ion then traverses a second barrier (point 4) until it is bound by the first pyridyl group ($n_{\mathrm{Zn,N}} = 1$). After a final, smaller barrier (127 kJ·mol^{-1}, point 6), $TTPB_w$-Zn_3 is formed, characterized by a very narrow minimum with a depth of -388 kJ·mol^{-1} (point 7).

The FES exihibits a number of minima. Most notable is a broad and deep “valley” with uncoordinated Zn ($n_{\mathrm{Zn,N}} \approx 0$) at the center of mass of TTPB up to $d_{\mathrm{Zn,TTPB}} \approx 8$ Å with Zn solvated by H_2O in a bulk-like environment. There is also a broad minimum for $n_{\mathrm{Zn,N}}$ between 1 and 2 (point 5), where the ion is partially coordinated by TTPB and still has substantial freedom of movement.

Among the configurations with coordinated Zn, full binding to the terpyridine unit has the narrowest

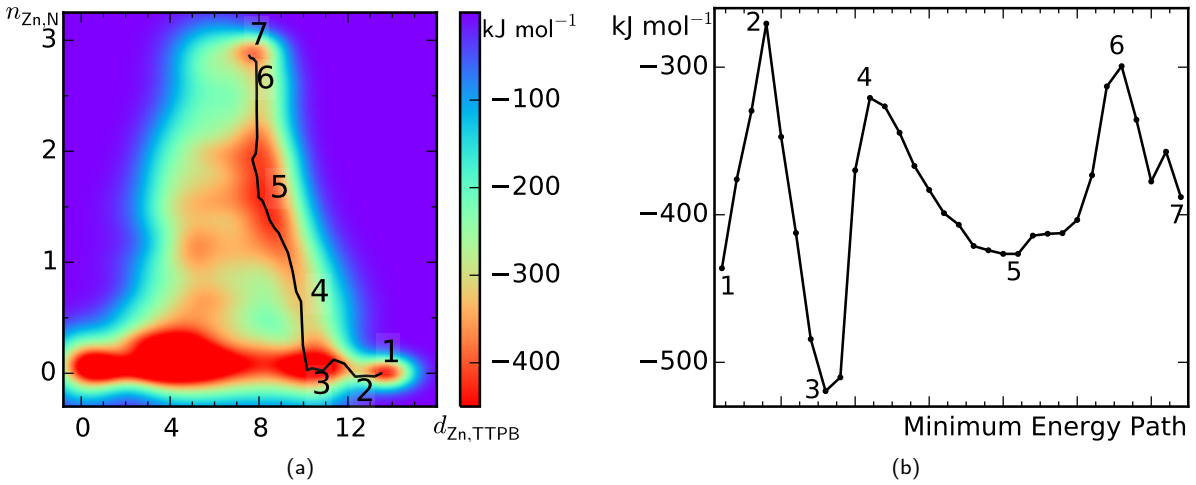

Figure 4.23|(a) Reconstructed free energy surface (FES) of Zn^{2+} uptake from solution, as a function of Zn–N coordination number, $n_{Zn,N}$, and distance from Zn to the center of the TTPB molecule, $d_{Zn,TTPB}$. Minimum energy path representing the first Zn^{2+} uptake event from bulk water (black). Significant points (minima, barriers) numbered 1–7. (b) Free energy profile along the minimum energy path shown in (a). Data published in ref. 16.

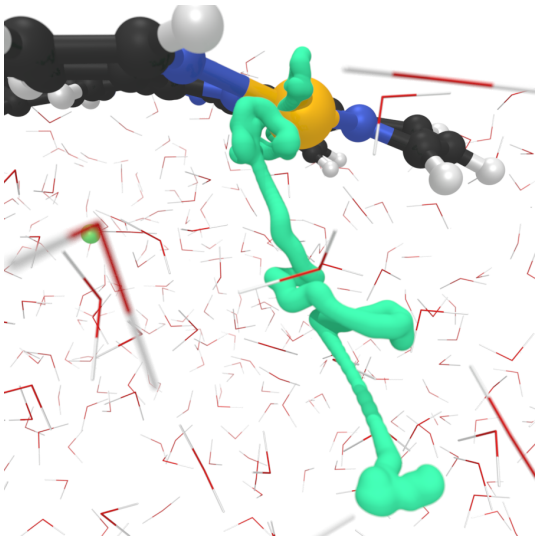

Figure 4.24|Path of Zn^{2+} ion from the bulk liquid to TTPB until the first ion binding occurs. Atom colors: O, red; H, white; C, black; N, blue; Zn, yellow.

and steepest minimum. We rationalize this situation with the competition between entropy and binding enthalpy. While configurations with a higher number of Zn–N bonds are energetically more stable, they also increasingly restrict the conformational freedom of TTPB and the movement of Zn, making these microstates entropically disfavored. Furthermore, the vastly larger *number* of configurations with Zn in solution increases the statistical probability of the unbound state, thus leading to deeper free energy minima for dissolved Zn. The unbound states are sampled more frequently by the MTD trajectory, producing the corresponding minima in the MTD representation of the free energy surface.

The fact that the $TTPB_w$-Zn_3 complex is thermodynamically higher in energy than the unbound state does not preclude the formation of larger clusters and extended networks. In the single metal-linker complex Zn is coordinated by three pyridyl groups and the binding interaction is exceeded by the

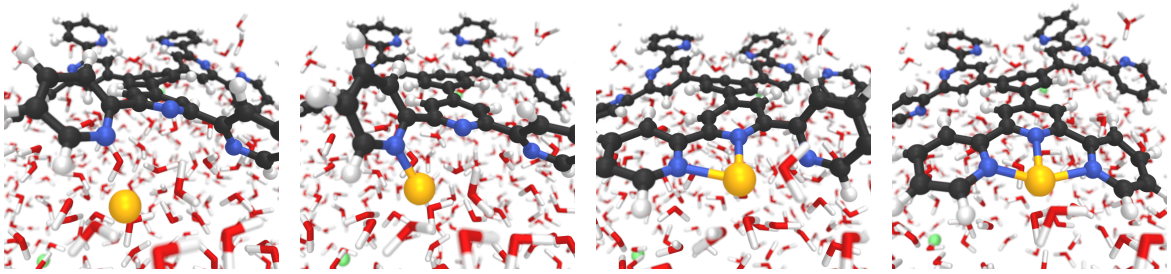

(a) (b) (c) (d)

Figure 4.25|Snapshots of MTD trajectory illustrating the first Zn^{2+} binding event to TTPB. (a) Ion approach; Formation of (b) first, (c) second, and (d) third N–Zn bonds. Atom colors: O, red; H, white; C, black; N, blue; Zn, yellow. Data published in ref. 16.

entropic contributions described above. When the Zn ion bridges two TTPB molecules, it is coordinated by six pyridyls, which should approximately double the binding enthalpy. Furthermore, when fully coordinated by pyridyls, Zn is shielded from water molecules, and less likely to re-enter the aqueous phase. Thus, the lower thermodynamic stability of $TTPB_w$-Zn_3 is due to the conditions imposed in the simulation, but should not adversely affect our conclusions on the mechanism of ion insertion as such. Ion insertion is a necessary first step towards the formation of 2D sheets, which will be discussed further in the last section of this chapter.

Fig. 4.24 shows the path of the Zn ion through the liquid from the start of MTD hill deposition up to the first full binding to TTPB. The ion spends some time at its initial position in the bulk of the liquid and then follows a straight line to a point roughly halfway to the terpy group (corresponding to point 3 in Fig. 4.23). It spends some time there, as the bias potential increases to overcome the barrier (at point 4 of the MEP). From there, Zn again follows a straight line, all the way up to the terpy group. In terms of free energy, this step goes downhill, approaching the wide minimum around point 5. Once the ion has traversed most of the distance to the pyridyl ligands, it begins to bind.

The 4 snapshots shown in in Fig. 4.25 illustrate the relevant steps of the binding process. Zn approaches the binding site (panel (a)), and the first pyridyl group coordinates the ion (panel (b)), effectively pulling it farther out from solution. Then the central ligand forms the second bond to Zn (panel (c)). The final pyridine ring, taking advantage of the conformational flexibility allowed by the liquid substrate, rotates by 180° (between panels (b) and (d)) and completes the 3-fold coordination.

Solvation and Coordination of Zn^{2+}

In order to bind to the molecule at the surface, Zn diffuses from the bulk towards the surface. We define the first solvation shell of Zn^{2+} as containing all water molecules whose oxygen atoms are within 2.2 Å of the ion. Conceivably, the ion can either move independently of its solvation shell and transiently bind different H_2O molecules along the diffusion path, or move along with its first solvation shell, coordinated by the same H_2O over extended time and distance. The barriers for each of these mechanisms should determine the preferred one. As a first step towards answering this question, we plot the distribution of Zn–O_{H_2O} ($n_{Zn,O}$) versus the Zn–N_{terpy} coordination (Fig. 4.26(a)). As expected, there is an inverse relationship between the two quantities. In bulk-like situations with a 4- to 5-fold solvation of Zn, the ion is not coordinated by the N_{terpy} atoms. Conversely, the bound Zn retains on average two solvating water molecules that coordinate axially from below and at the fourth equatorial position on the open side of the terpyridine.

Between the limits of full solvation and full complexation, the two coordination numbers are inversely correlated, with several spots of particularly high occurrence. The combinations of integer

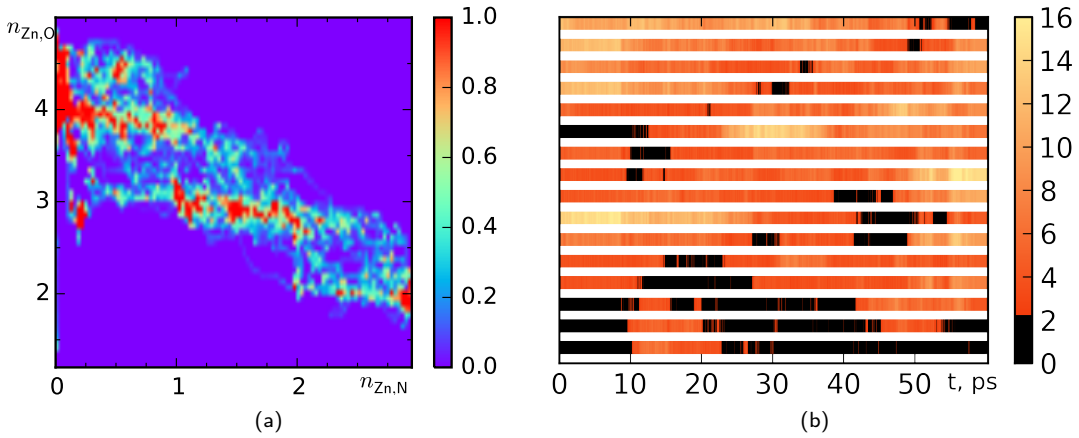

Figure 4.26|(a) Correlation of Zn solvation (O coordination, $n_{\mathrm{Zn,O}}$) with Zn binding (N coordination, $n_{\mathrm{Zn,N}}$) to TTPB, throughout the MTD simulation. Color bar shows frequency per x/y bin times 1000. (b) Time-resolved structure of the Zn solvation shell. Each horizontal bar represents one H_2O molecule in the vicinity of the metal. Colors indicate the O–Zn distance of that molecule over time. An estimate of the number of solvating molecules can be calculated by counting the number of black spots at a particular time. Data published in ref. 16.

numbers 4/0, 3/0, 4/1, 3/1, 3/2, 2/2, 2/3 ($n_{\mathrm{Zn,O}}/n_{\mathrm{Zn,N}}$) can be recognized in the plot. Thus, Zn maintains an environment of 4 to 5 ligands at all times. Particularly, while the ion is partially bound to 1 or 2 N_{terpy}, it remains coordinated by 3 water molecules.

The structure of the bulk solvation shell of Zn^{2+} has not been unambiguously determined, 4-, 5-, and 6-fold coordination by water are all possible. Our results point to a solvation shell consisting of 4 H_2O molecules, with additional solvent located in close proximity (partially contributing to the counting function we use to determine n). This is consistent with a recent study that determined the free energy minimum for $Zn(H_2O)_4{}^{2+}$ to be the lowest of the three solvation modes by a narrow margin, and found low barriers of interconversion.[219]

Over the course of the entire simulation, 16 water molecules come to reside within 2.2 Å of Zn, and thus make up a part of the ion's solvation shell. The O–Zn distance of each of those molecules is plotted as a function of time in Fig. 4.26(b). Each row represents one H_2O molecule, and the color indicates $d_{\mathrm{Zn,H_2O}}$. Yellow to orange shows varying degrees of proximity, while black signifies solvation of the ion. Some molecules only solvate Zn very briefly, but others remain attached to the ion for most of the simulation.

At the start of the trajectory, 4 molecules surround Zn, moving upward through the solution with the ion until it is fully bound by TTPB (at approx. 10 ps). Subsequently, it is other molecules that partially solvate the complexated ion. As the metal then leaves the ligand, it "picks up" three of the water molecules that initially solvated it in the bulk, and maintains a transient attachment to a fourth molecule that is replaced multiple times. After some time in a bulk-like solvation environment, Zn is once again taken up by terpyridine, reducing its solvation to two and three water molecules. At the end of the simulation, half of the initial solvation shell has been exchanged, while the other half is still comprised of molecules that solvated Zn at the outset.

This behavior leads us to conclude that instead of overcoming the solvation free energy and reattaching in a different solvation environment, Zn can move with its first solvent shell largely intact as it diffuses through the solution. Apparently, it is energetically preferable to move a large $Zn(H_2O)_4$ quasiparticle through loosely bound water, rather than to break the comparatively stronger Zn–OH_2 bonds while moving the Zn ion by itself. Water exchange in the ion's solvation shell appears to be independent of the diffusional movement of Zn, occurring on longer timescales. Eventually, assisted

by the intermittent binding to the ligand, the solvent shell would be fully exchanged for "other" H_2O molecules.

Summary: TTPB Confined on a Water Surface

The liquid-gas interface of water can be used as a dynamic surface on which to adsorb/confine TTPB. This substrate mildly stabilizes the molecule, while maintaining a certain degree of conformational flexibility. TTPB's freely rotatable bond angles fluctuate considerably less than in the gas phase and the pyridine ligands can coordinate Zn^{2+} ions in a stable way. Due to the liquid nature of the substrate, solutes in the aqueous phase can diffuse upward to the surface and react with the adsorbate. For the prototypical case of Zn^{2+} uptake and coordination from water, a stepwise reaction with the three pyridine moieties leads to an energetically stable but entropically unfavorable bound state. Remarkably, as the metal ion migrates, it largely retains its first solvation shell and is also coordinated by the same water molecules after temporarily binding to TTPB.

4.5 TTPB Dimers and Networks on Water

Having exhaustively characterized an individual TTPB molecule on water and its ability to bind Zn, the focus now shifts to the Zn-bridged TTPB dimer and to fully periodic networks. As above, the section begins with an overview and comparison of the properties of the free and water-supported dimers, $TTPB_{2g}$-Zn and $TTPB_{2w}$-Zn, from MD simulations. Further, we use MTD to quantify the binding free energy of $TTPB_{2w}$-Zn, in order to assess the stability of the 2D MOF. Emphasis is also placed on the mechanism of breaking the dimer. The last part of this section introduces a model of a fully periodic 2D MOF based on a $TTPB_2$ unit cell, where all terpy units are bridged by Zn^{2+} to form the network.

Dynamic Properties of the TTPB Dimer

As an extension of the detailed characterization of the dynamic structure of $TTPB_w$ and $TTPB_w$-Zn_3 above, we examine a number of structural properties that are unique to $TTPB_{2g}$-Zn and $TTPB_{2w}$-Zn.

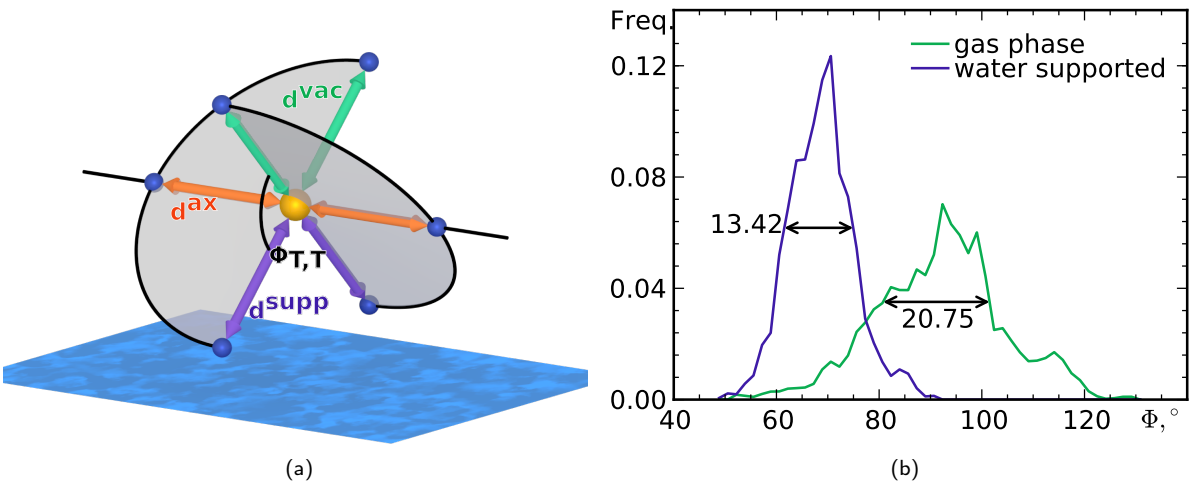

Figure 4.27|(a) Overview of distinct N–Zn distances in the binding region of a supported TTPB dimer: axial, $d^{ax}_{N,Zn}$, water-exposed, $d^{supp}_{N,Zn}$ and vacuum-exposed, $d^{vac}_{N,Zn}$ and inter-terpy angle $\Phi_{T,T}$. (b) Distributions of $\Phi_{T,T}$.

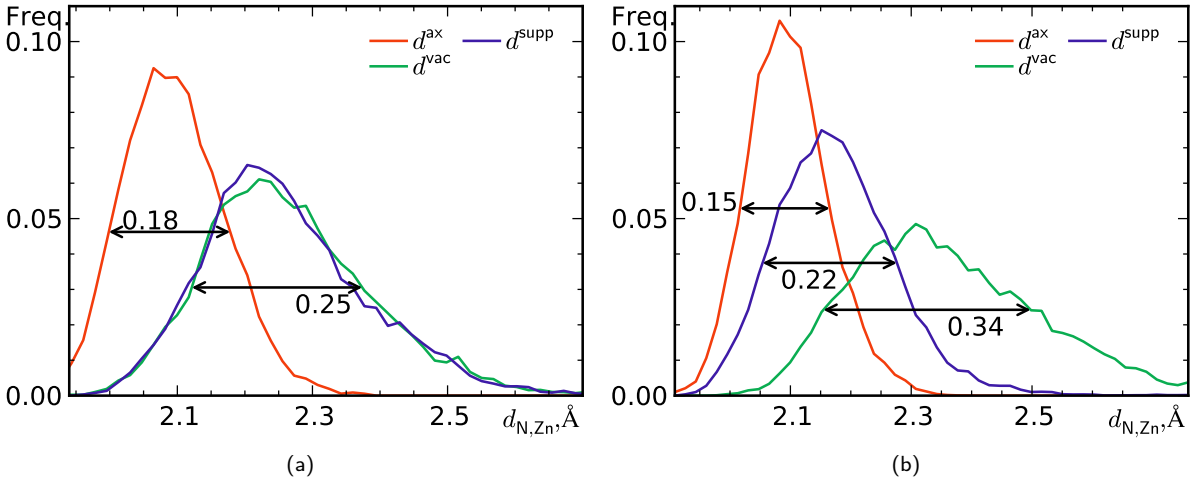

Figure 4.28|Distributions of N–Zn distances (Å): axial: $d^{ax}_{N,Zn}$, water-exposed: $d^{supp}_{N,Zn}$ and vacuum-exposed: $d^{vac}_{N,Zn}$ for (a) $TTPB_{2g}$-Zn and (b) $TTPB_{2w}$-Zn.

The Zn binding site, with the ion coordinated by two terpy units from different TTPB, is schematically shown in Fig. 4.27(a). The two terpy units form an interplanar angle $\Phi_{T,T}$, modeled here as the angle between two best-fit planes through the central pyridine and the two adjacent carbon atoms to the pyridyl arms. Overall the binding site has six N–Zn distances: Two of them are "axial" bonds, to the central pyridyl groups of each terpy, referred to as $d^{ax}_{N,Zn}$. Two of the "equatorial" bonds point "up", i.e. are exposed to the vacuum side of the dimer, $d^{vac}_{N,Zn}$, while two bonds face the water-supported side, $d^{supp}_{N,Zn}$.

Fig. 4.27 (b) shows the distribution of $\Phi_{T,T}$ for $TTPB_{2g}$-Zn and $TTPB_{2w}$-Zn. In the absence of the supporting water, $\Phi_{T,T}$ is approximately evenly distributed around a mean of 91.8° with a FWHM of 20.75°. For $TTPB_{2w}$-Zn, on the other hand, the angle is considerably sharper, with a mean value of $\Phi_{T,T}$ = 68.7°. The distribution is also significantly narrower, characterized by an FWHM of 13.42°.

Several conclusions about the dynamic structure of $TTPB_2$-Zn can be drawn from these data. Unsupported $TTPB_2$-Zn essentially maintains the octahedral environment expected around a sixfold coordinated metal ion, as there is no substrate that would make the system asymmetric and "flatten" the octahedron equatorially. On the other hand, $TTPB_{2w}$-Zn appears to lie flatter on the water substrate, as shown by the reduction of $\Phi_{T,T}$ in comparison to the value for $TTPB_{2g}$-Zn. Furthermore, the flattened binding site of $TTPB_{2w}$-Zn fluctuates considerably less than that of $TTPB_{2g}$-Zn. Evidently the water support exerts a similar conformational stabilization onto the dimer as noted above for $TTPB_w$. Without this support, it is only the N–Zn bonds and repulsion of terpy units that stabilize $\Phi_{T,T}$, giving rise to much larger fluctuations at 300 K around an expected angle of 90°.

The various interatomic distances found in the dimer binding site allow for further characterization. Fig. 4.28 (a) shows the distributions of Zn–N distances in $TTPB_{2g}$-Zn. The curves are slightly skewed towards greater distances, with mean values of 2.10 Å for $d^{ax}_{N,Zn}$, and 2.26 Å for $d^{supp}_{N,Zn}$ and $d^{vac}_{N,Zn}$.[†] The distributions of $d^{supp}_{N,Zn}$ and $d^{vac}_{N,Zn}$ are essentially identical, as all involved pyridyl arms are equivalent in the absence of the water surface. The same distributions are plotted in Fig. 4.28 (b) for $TTPB_{2w}$-Zn. Here, the mean values for $d^{ax}_{N,Zn}$, $d^{supp}_{N,Zn}$, and $d^{vac}_{N,Zn}$ are 2.10 Å, 2.18 Å, and 2.37 Å, respectively. Due to the water support, $d^{supp}_{N,Zn}$ and $d^{vac}_{N,Zn}$ now differ significantly in their behavior. $d^{vac}_{N,Zn}$ has a much broader distribution, shifted to a larger mean value.

[†]The shapes of the distance distributions are reminiscent of upside-down Lennard-Jones or Morse potential curves, with their steeper decay of the repulsive contributions compared to the attractive ones.

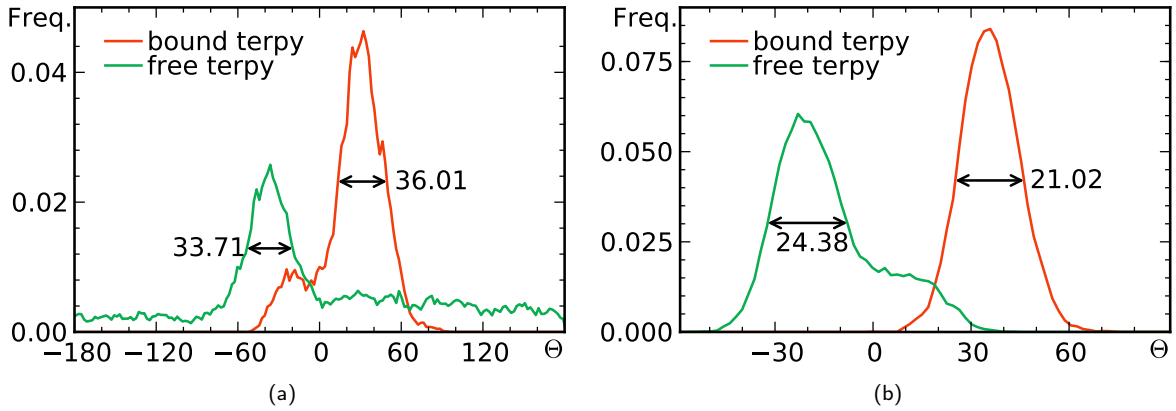

Figure 4.29|Distribution of Θ for the 2 bound and 4 unbound terpy groups in (a) $TTPB_{2g}$-Zn and (b)$TTPB_{2w}$-Zn.

Comparing $TTPB_{2w}$-Zn and $TTPB_{2g}$-Zn, the influence of the water substrate becomes obvious. The axial Zn–N bonds are essentially unaffected, whereas those exposed to water shorten and those near the vacuum region elongate. Evidently, besides flattening the binding site, H_2O also exerts a certain pressure onto the closest pyridyl groups, pushing them towards the metal. Equivalently, it may be argued that the charged Zn ion is attracted to the liquid, a question to be examined below. The vacuum-exposed pyridyl groups, on the other hand, are characterized by increased flexibility (i.e. fluctuations) and increased mean distance. Remarkably, the overall average N–Zn distance in the binding site is essentially the same for both $TTPB_{2w}$-Zn and $TTPB_{2g}$-Zn, 2.21 Å. This may be an indication that the water substrate changes the shape of the binding site, but not the overall energetics of the dimer binding.

A final parameter describing the dynamic structure of the $TTPB_2$-Zn dimer is the inclination of the terpy groups relative to the plane of the dimer. We define Θ as the C-C-C-C dihedral angle between the central phenyl ring and a terpy group, as shown in Fig. 4.14 (b). In $TTPB_2$-Zn, there are 2 Θ angles for terpy units that are part of the binding site, and 4 for free terpy units. Fig. 4.29 (a) shows distributions of these angles for $TTPB_{2g}$-Zn, and panel (b) shows the same for $TTPB_{2w}$-Zn. In $TTPB_{2g}$-Zn, Θ of the free terpy groups is spread around a mean value of -2.67° and 24.4° for the bound ones. Θ is very broadly spread for free terpy groups, as several of the groups undergo multiple rotations around the bond axis, and fluctuate strongly (cf. fig. 4.16(a) where, however, the deviation from the mean is plotted directly). The distribution of Θ is not well characterized by the mean in this case, which is rather sensitive to the very large outlier angles; the median of the distribution is -24.6°, and the peak of the histogram (i.e. the mode of the distribution) is at -36.6°. The two bound terpy groups making up the binding site are somewhat more stable with respect to rotation around the central benzene[‡], as they are bound from two sides, resulting in a heavier and less flexible unit. Both sets of terpy groups exhibit a preference for a particular conformation relative to the phenyl ring, rather than fully free rotation.

For $TTPB_{2w}$-Zn, the mean angles Θ of the free and bound terpy groups are -13.5° and 35.9°, respectively. The distribution of Θ for the free terpy groups is not symmetric, but characterized by a broad shoulder towards positive angles. These groups do not oscillate around an average of zero (requiring on average a planar conformation), but around a finite equilibrium value, indicating a nonplanar equilibrium conformation. In contrast, Θ_{bound} is highly symmetrically distributed around its mean value. In terms of absolute values, the free terpy groups tend to be "flatter" to the plane of the dimer, as the

[‡]Arguably, this should be more accurately classified as the rotation of the central benzene with two attached terpyridyl groups around the binding site.

geometry of the binding site imposes a larger rotation of the involved ligand group.

Comparing Θ for $TTPB_{2g}$-Zn and $TTPB_{2w}$-Zn, it is evident that the H_2O substrate has a similar stabilizing influence on the dimer as noted above for the monomer. The fluctuations of both the free and bound terpy groups are significantly restrained by the support, as shown by the FWHM of the distributions. The overall conformation of the binding site seems little affected by the water substrate, having approximately the same mean Θ. Θ is also centered around similar values for the free terpy groups, noting however, the much stronger fluctuations in the absence of the water support.

The above characterization of $TTPB_2$-Zn in terms of $\Phi_{T,T}$, $d_{N,Zn}$, and Θ, leads to the following picture of the dimer and its binding site. In the gas phase, the $terpy_2$-Zn binding moiety resembles a square bipyramid, which is slightly wider than tall. The diagonals of the base of the bipyramid form an approximately right angle $\Phi_{T,T}$ as noted above. The binding site fluctuates rather strongly in shape and dimensions, and is slightly rotated relative to the plane of the dimer (Θ). In contrast, the binding site in $TTPB_{2w}$-Zn is best described as a rectangular bipyramid, with the longer edge of the rectangle approximately parallel to the water surface. As noted above, the presence of the substrate introduces an asymmetry in the system and distorts the binding site.

Coupling and Decoupling Mechanism

In order to quantify the binding strength of the 2D MOF assembled on water, we rely on the binding free energy of the dimer as a model. We use MTD in a similar fashion as above, to reconstruct the FES of the reaction

$$\mathrm{TTPB_2{-}Zn} \rightleftharpoons \mathrm{TTPB} + \mathrm{TTPB{-}Zn}$$

as described by the following three collective variables:

- $n_{\mathrm{Zn,N}}$, the Zn–N coordination number, expected to transition from 6 to 3 in the course of the reaction.
- $d^{\mathrm{ax}}_{\mathrm{N,N}}$, the distance between the two axial N of the binding site, expected to sharply increase from the average value of 4.15 Å for the bound dimer.
- $n_{\mathrm{Zn,O}}$, the Zn–O coordination number, which may slightly increase, as some pyridyl groups coordinating Zn are replaced by water. This CV is later integrated out.

The series of images in Fig. 4.30 shows snapshots extracted from the MTD trajectory, depicting the breaking and reassembly of $TTPB_2$-Zn.

(a) Fully bound $TTPB_2$-Zn ($n_{\mathrm{Zn,N}} = 5.84$, $d^{\mathrm{ax}}_{\mathrm{N,N}} = 4.21$ Å, $n_{\mathrm{Zn,O}} = 0.09$).

(b) Partial break of the binding site, with 2 terpy groups temporarily rotating into a *trans* conformation ($n_{\mathrm{Zn,N}} = 3.96$, $d^{\mathrm{ax}}_{\mathrm{N,N}} = 4.53$ Å, $n_{\mathrm{Zn,O}} = 0.39$).

(c)–(e) Progressively increasing separation between the monomers.

(f) Dimer fully broken into constituents, TTPB-Zn and TTPB ($n_{\mathrm{Zn,N}} = 2.93$, $d^{\mathrm{ax}}_{\mathrm{N,N}} = 8.94$ Å, $n_{\mathrm{Zn,O}} = 1.43$).

(g) Transient rotation of one pyridyl group into the *trans* conformation ($n_{\mathrm{Zn,N}} = 2.03$, $d^{\mathrm{ax}}_{\mathrm{N,N}} = 8.04$ Å, $n_{\mathrm{Zn,O}} = 2.98$).

(h) Re-formation of a Zn–N bond with the second TTPB ($n_{\mathrm{Zn,N}} = 3.75$, $d^{\mathrm{ax}}_{\mathrm{N,N}} = 4.82$ Å, $n_{\mathrm{Zn,O}} = 1.21$).

(i) Two bonds from Zn to the second TTPB ($n_{\mathrm{Zn,N}} = 4.81$, $d^{\mathrm{ax}}_{\mathrm{N,N}} = 4.22$ Å, $n_{\mathrm{Zn,O}} = 0.75$).

(j) Quasi fully re-assembled dimer ($n_{\mathrm{Zn,N}} = 5.11$, $d^{\mathrm{ax}}_{\mathrm{N,N}} = 4.38$ Å, $n_{\mathrm{Zn,O}} = 1.01$).

(k) Fully re-assembled dimer ($n_{\mathrm{Zn,N}} = 5.75$, $d^{\mathrm{ax}}_{\mathrm{N,N}} = 3.95$ Å, $n_{\mathrm{Zn,O}} = 0.56$).

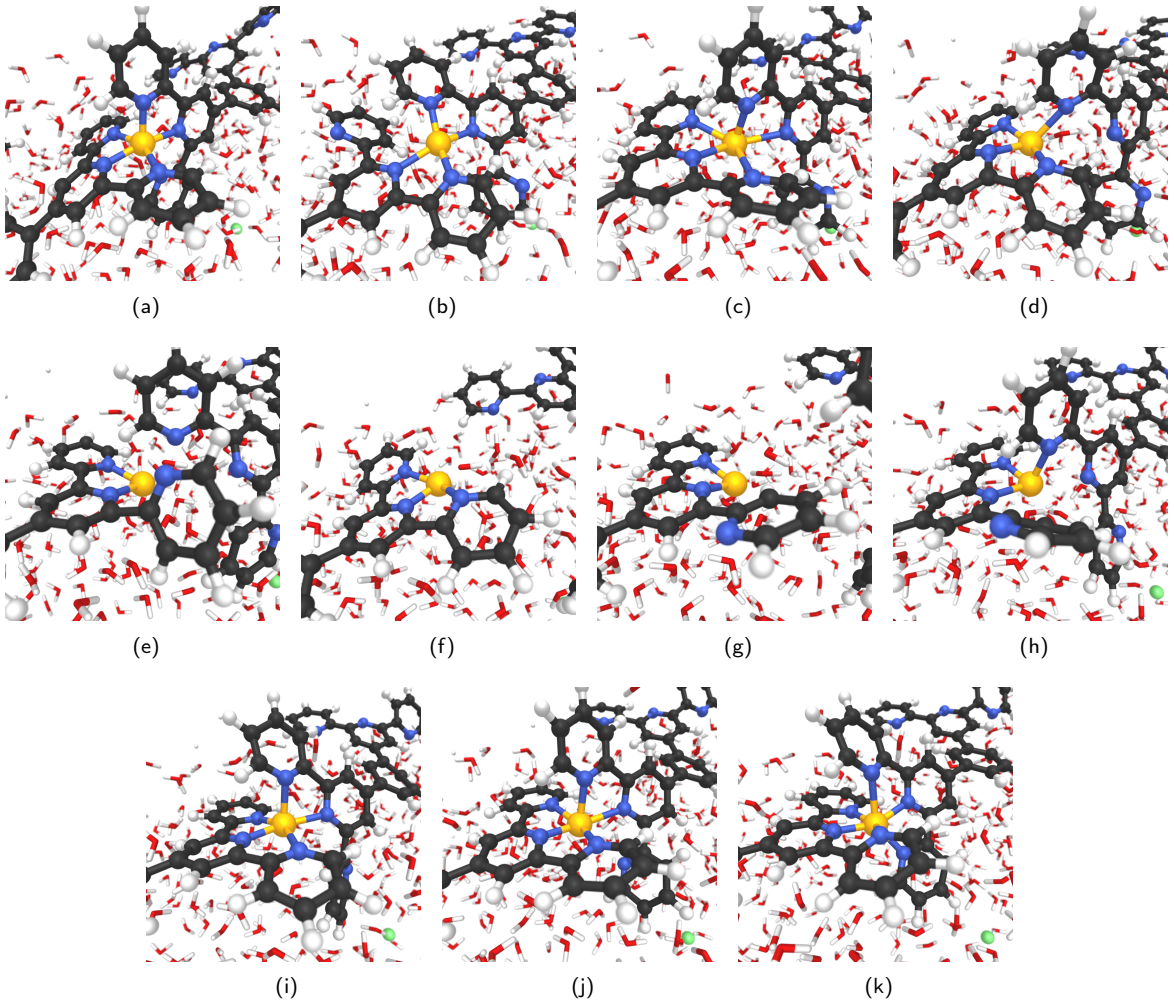

Figure 4.30|Snapshots from the MTD trajectory simulating the breaking of $TTPB_2$-Zn. See text for details. Atom colors: H, white; C, black; N, blue; Zn, yellow.

As can be seen from the snapshots, the breaking of the dimer follows a similar stepwise mechanism as the uptake of the Zn^{2+} from solution. The bias potential causes individual TTPB-Zn bonds to break and the monomers to separate until the dimer has fully broken. This is accompanied by the rotation of individual pyridyl groups, that intermittently reduce the Zn–N coordination (similar behavior was noted above during Zn insertion). The successful re-formation of the full dimer indicates that the bias potential covers the FES sufficiently well, having filled up all relevant minima.

Fig. 4.31 shows the time evolution of the 3 CVs throughout the simulation. Before the MTD potential is activated, the values remain constant around the equilibrium of $n_{\mathrm{Zn,N}} \approx 5.8$, $d^{\mathrm{ax}}_{\mathrm{N,N}} \approx 4.15$ Å, and $n_{\mathrm{Zn,O}} \approx 0$. When MTD is enabled after ∼10 ps, $n_{\mathrm{Zn,N}}$ decreases in a roughly stepwise fashion to a minimum around 2, before increasing again to the equilibrium value. It then decreases again, to as low as 3. $d^{\mathrm{ax}}_{\mathrm{N,N}}$ reaches a maximum at approximately the same moment as $n_{\mathrm{Zn,N}}$ reaches its minimum, then assumes the equilibrium values again, and does not deviate from it significantly any more. This may be an indication that the "second" decrease of $n_{\mathrm{Zn,N}}$ beyond 40 ps is not due to a breaking of the dimer, but rotation and deformation of the pyridyl groups, while keeping the inter-monomer distance constant. The behavior of $n_{\mathrm{Zn,O}}$ indicates that part of the coordination environment of Zn is replaced by H_2O

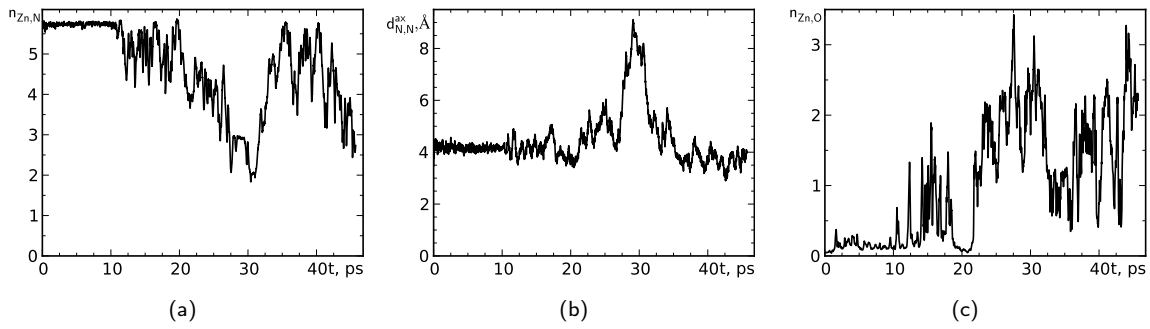

Figure 4.31|Time evolution of CVs during breaking and reassembly of $TTPB_2$-Zn dimer: (a) $n_{\mathrm{Zn,N}}$, (b) $d^{\mathrm{ax}}_{\mathrm{N-N}}$, and (c) $n_{\mathrm{Zn,O}}$.

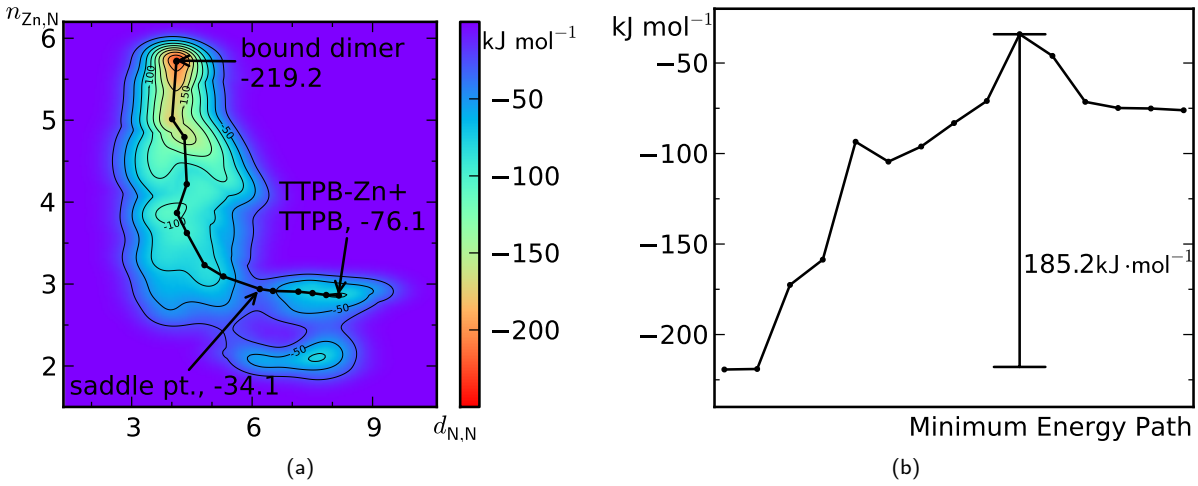

Figure 4.32|(a) Reconstructed MTD free energy surface of splitting $TTPB_{2w}$-Zn, as a function of CVs $d_{\mathrm{N,N}}$, $n_{\mathrm{Zn,N}}$. The third CV, $n_{\mathrm{Zn,O}}$, is integrated over its range. Black line indicates minimum energy path for dimer breaking. (b) Free energy profile along the MEP.

upon breaking of the dimer. This is consistent with the observation that Zn typically remains partially solvated when bound to a single TTPB, as shown in the previous section.

The reconstructed FES of the $TTPB_2$-Zn breaking process is shown in Fig. 4.32(a) as a function of $n_{\mathrm{Zn,N}}$ and $d^{\mathrm{ax}}_{\mathrm{N,N}}$. The system is characterized by two minima, one for the bound state (top left, $n_{\mathrm{Zn,N}} \approx 5.8$, $d^{\mathrm{ax}}_{\mathrm{N,N}} \approx 4.0$ Å) and one for the unbound state (bottom right, $n_{\mathrm{Zn,N}} \approx 3.0$, $d^{\mathrm{ax}}_{\mathrm{N,N}} \approx 8.0$ Å). Additionally, some smaller basins can also be seen. At reduced $n_{\mathrm{Zn,N}}$ and small $d^{\mathrm{ax}}_{\mathrm{N,N}}$, a bound dimer with undercoordinated Zn^{2+} is evident. Furthermore, at the distance of separated TTPB, Zn can also be undercoordinated, missing one bond to a pyridyl group.

The free energy difference between the bound and unbound dimer is ΔG = -143.1 kJ·mol^{-1}. Taking into account the higher entropy of TTPB + TTPB-Zn relative to $TTPB_2$-Zn, due to the higher number of particles and higher conformational flexibility, the binding enthalpy of the dimer should be appreciably larger than this. In comparison, the experimental binding enthalpy ΔH of $Zn(terpy)_2^{2+}$ is -60.7 kJ·mol^{-1},[78] somewhat smaller.

The highest saddle point of the FES is indicated in Fig. 4.32(a) with ΔG = -34.1 kJ·mol^{-1}. Panel (b) shows the free energy profile along the MEP. The breaking of the dimer is rather steeply uphill in energy, with a shallow local minimum of the undercoordinated dimer. A barrier of 185 kJ·mol^{-1} is crossed before reaching the shallow minimum of TTPB + TTPB-Zn.

These results indicate that the Zn-bridged TTPB dimer is stable on the surface of water. The significant barrier and low relative stability of the unbound state prove that these aggregates can persist and that stable networks are likely formed. Since Zn is the weakest-binding of all examined ions (see gas-phase results in Section 4.1), other ions such as Fe^{2+} should form significantly more stable dimers and networks.

Extended Networks

The extended Zn bridged TTPB network, $(TTPB_w\text{-}Zn_3)_n$, modeled based on a $TTPB_2$ unit cell, can be structurally characterized with similar quantities as $TTPB_{2w}$-Zn. Fig. 4.33 compares the distributions of N–Zn distances, $d^{ax}_{N,Zn}$, $d^{supp}_{N,Zn}$, $d^{vac}_{N,Zn}$ in $(TTPB_g\text{-}Zn_3)_n$ and $(TTPB_w\text{-}Zn_3)_n$. These quantities are essentially identical to those observed for $TTPB_{2g}$-Zn and $TTPB_{2w}$-Zn, respectively. The FWHM of the distributions are also not significantly different.

This is an indication that the binding site of the dimer represents the situation in the extended network very well, and that the dimer can be taken as a good model of the 2D MOF as a whole.

One aspect of the network structure that is not reflected in the dimer is the out-of-plane displacement of the metal ions relative to the network. This quantity is an indication of the overall "flatness" of the MOF and the short-range curvature of the surface. We model this by measuring the distance of Zn to the plane through the central benzene rings of the networks, $d_{Zn,net}$, as shown by the red bar in Fig. 4.34(a). As the system contains 3 Zn atoms, there are 3 equivalent such distances, carrying a positive or negative sign, depending on the position of Zn above or below the plane.

Fig. 4.33 (b) depicts the individual and aggregated distributions of $d_{Zn,net}$ for $(TTPB_w\text{-}Zn_3)_n$ and $(TTPB_g\text{-}Zn_3)_n$. For $(TTPB_w\text{-}Zn_3)_n$ the overall distribution is fairly symmetric, centered around the value of $d_{Zn,net} = 0$. The Zn atoms thus reside in the same plane as the rest of the network, on average. The fluctuations, indicated by an FWHM of 0.86 Å and fairly broad tails of the distribution up to 2 Å, indicate, however, that Zn is still relatively mobile in its binding site and can move up and down with a rather large amplitude. The residence time of the atoms is, however, essentially split evenly between positions above and below the network plane. The individual $n_{Zn,N}$ distributions of the Zn ions differ somewhat, in that one is centered around zero, while one peaks at $n_{Zn,N} \approx$ -0.6 and the other one at $n_{Zn,N} \approx 0.8$ Å.

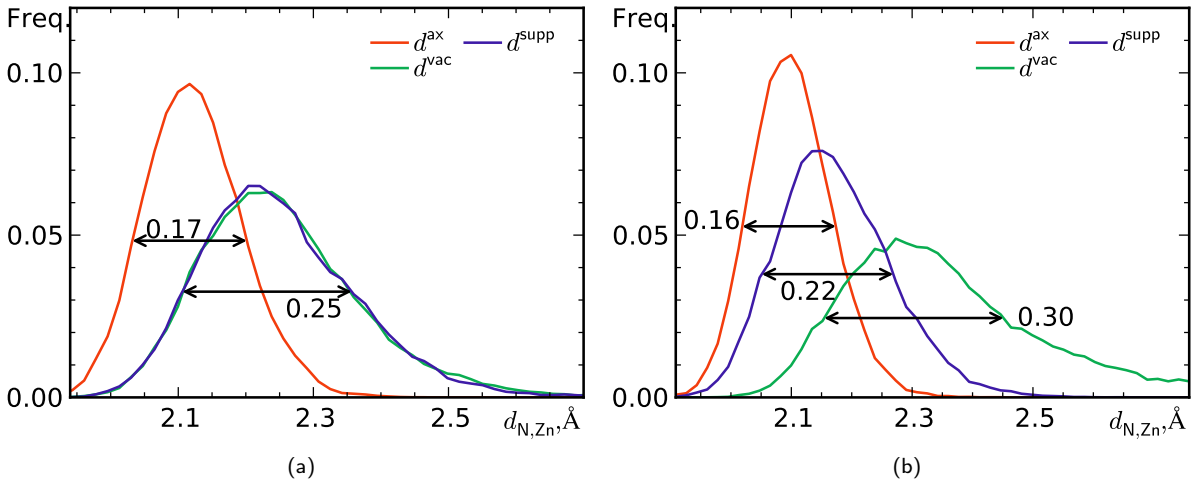

Figure 4.33|Distributions of N–Zn distances (Å): axial: $d^{ax}_{N,Zn}$, water-exposed: $d^{supp}_{N,Zn}$ and vacuum-exposed: $d^{vac}_{N,Zn}$ for (a) $(TTPB_g\text{-}Zn_3)_n$ and (b) $(TTPB_w\text{-}Zn_3)_n$.

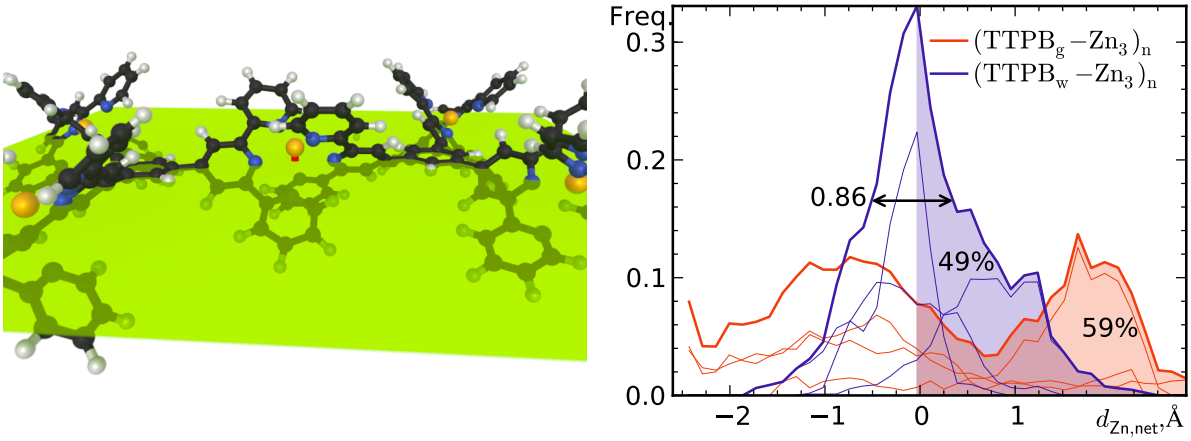

Figure 4.34|(a) Schematic of a best-fit plane through the central phenyl rings (i.e. the network plane) in $(TTPB_w\text{-}Zn_3)_n$ and the distance of Zn to that plane (red bar). (b) Distribution of $d_{Zn,net}$ in $(TTPB_g\text{-}Zn_3)_n$ and $(TTPB_w\text{-}Zn_3)_n$. Individual distances for the three Zn ions represented by thin lines; thick lines show aggregated distribution. Arrow indicates an estimate of the FWHM, percentages give the positive fraction of $d_{Zn,net}$ relative to the total distribution (shaded areas).

The distribution of $d_{Zn,net}$ is less well defined for $(TTPB_g\text{-}Zn_3)_n$. It is much broader than that for $(TTPB_w\text{-}Zn_3)_n$ and exhibits two peaks, at ∼-1 Å and 1.6 Å, making it overall unsymmetric. It appears that the ion frequently resides substantially above or below the plane of the network, giving rise to an out-of-plane distortion. There appears to be a barrier between those two extremes, so that positions near the plane of the network are less populated. It should be noted that the left peak of this distribution is composed primarily of the $n_{Zn,N}$ distances of two Zn atoms in the network, while the third is due to one Zn ion that predominantly occupies positions with large positive $n_{Zn,N}$. This strongly supports the existence of a barrier to interconversion, since each individual Zn ion largely remains on one side of the network plane.

In general it appears that the water substrate has a "flattening" effect on the network, as the overall distribution width is significantly reduced, and the individual Zn atoms remain closer to the network plane. The Zn^{2+} ion evidently does not experience a significant attraction to the liquid.We rationalize this with shielding of the ion from the liquid, by the hydrophobic terpy groups.

Summary: TTPB Dimers and Networks on Water

TTPB forms a stable dimer, $TTPB_2$-Zn, both in the gas phase and on the water substrate. The binding site is based on 6-fold coordination of Zn, in a bipyramidal geometry, which is flattened on one side by adsorption on water. The breaking and re-formation of the dimer is characterized by stepwise bond breaking, due to the high flexibility of the pyridyl groups, and associated with a binding free energy of -143.1 kJ·mol^{-1}. An extended network based on Zn bridged TTPB preserves the structural properties of the dimer, with the Zn ion remaining in-plane with the network with a high amplitude of fluctuation.

5

Conclusions and Outlook

Step by step, the preceding chapters have provided answers to the research questions posed at the beginning of this thesis. We found that *h*-BN, despite its alleged chemical inertness, readily forms stable heterostructures on transition metals. We rationalized the electronic corrugation of *h*-BN on Cu with the periodically modulated lateral BN–metal distances. We saw how this corrugation becomes manifest also in the electronic properties of adsorbed porphin. We observed metal-supported *h*-BN to be surprisingly reactive towards molecular O_2, able to substantially activate the adsorbate. We explored *h*-BN on Ni, Co, and Cu as oxidation catalysts, and predict the latter to be a promising competitor to platinum.

We studied the adsorption behavior of TTPB on Au and Cu, finding preferred adsorption sites and orientations. We quantified the dynamic structure of water-supported TTPB, observing the significant stabilizing and confining effect of the substrate. We watched a Zn ion make its way from the liquid phase to the surface to be bound by tridentate terpyridyl ligand. We surveyed the free energy landscape of this process. We studied dimers and aggregates of TTPB and how the liquid substrate influences their shape and dimensions. We let a Zn-bridged dimer break in order to see how strongly it was bound.

A goal of this work was to confirm and rationalize experimental observations using computational methods. This could be achieved in many instances throughout the study. Our computational models of metal-supported *h*-BN are in agreement with the available experimental evidence. Using DFT calculations of hitherto rarely seen system size, we could reproduce a large-scale Moiré pattern on *h*-BN/Cu and provide an explanation of the phenomena observed with STM. While there are few experimental results related to water-supported 2D MOFs that can directly be compared to our simulations, we can provide a level of atomistic detail far beyond conventional experimental techniques. The AIMD studies of water-supported TTPB characterize the dynamic properties of the MOF building blocks at the level of bond distances and distortion angles. Similarly, the mechanisms of ion insertion and dimer breaking could be quantified down to the details of metal-ligand bonds and individual solvent molecules, including the free energy landscapes of the processes.

A second goal was to use simulations to predict and improve the functionality of 2D materials. The study of catalysis on metal-supported *h*-BN was particularly promising in this respect. All of the studied materials activate molecular O_2, but *h*-BN/Cu also catalyzes its reduction to H_2O, as needed in a fuel cell. We predict overpotentials in the range of those found otherwise only for Pt, making *h*-BN/Cu a potential alternative. These are predictions in the absence of prior experimental evidence, but the promising results and high confidence in them may encourage more detailed explorations.

Doubtlessly, research can proceed in many directions based on the results presented here. The properties of metal-supported *h*-BN deserve further study from several points of view: 2D networks could recently be produced on *h*-BN/Cu[167] using linker ions, and on *h*-BN/Ni by catalyzed covalent polymerization.[220] The structure and properties of these materials as well as the details of their formation merit further computational investigation. Particularly, catalysis on *h*-BN/metal beyond oxygen activation may bring crucial new knowledge.

In the context of the ORR on *h*-BN/Cu we noted that potentially important solvation effects at the

electrode surface are typically neglected or approximated. Yet, from the MD study of MOFs on water it is obvious that the liquid plays an important role for chemical reactions. It would be instructive to apply MD and MTD techniques to the problem of the ORR. With the availability of large and fast supercomputers, *ab initio* simulation of an entire ORR cycle at an electrode with explicit solvation should be within reach. Such a simulation would go far beyond the currently dominating static calculations in terms of complexity and information gain.

As far as (2D) MOFs are concerned, obvious directions of further research include examining different ligands and ions, up to the extent of screening studies,[221] or perhaps different liquid substrates. Beyond that, it may be instructive to examine 2D MOFs at different interfaces, e.g., between water and an organic solvent. In such a system the MOF constitutes a tunable, covalent membrane, possibly suitable for separation applications, or a type of phase-transfer catalysis.

References

[1] Geim, A. K.; Novoselov, K. S. The Rise of Graphene. *Nat. Mater.* **2007**, *6*, 183–191.

[2] Wang, X.; Zhi, L.; Müllen, K. Transparent, Conductive Graphene Electrodes for Solar Cells. *Nano Lett* **2007**, *8*, 323–327.

[3] Gupta, A.; Sakthivel, T.; Seal, S. Recent Development in 2D Materials Beyond Graphene. *Progress in Materials Science* **2015**, *73*, 44–126.

[4] Avouris, P.; Freitag, M. Graphene Photonics, Plasmonics, and Optoelectronics. *IEEE Journal on Selected Topics in Quantum Electronics* **2014**, *20*.

[5] Machado, B. F.; Serp, P. Graphene-Based Materials for Catalysis. *Catal. Sci. Technol.* **2012**, *2*, 54–75.

[6] Xu, M.; Liang, T.; Shi, M.; Chen, H. Graphene-Like Two-Dimensional Materials. *Chem. Rev.* **2013**, *113*, 3766–3798.

[7] Barth, J. V. Molecular Architectonic on Metal Surfaces. *Annu. Rev. Phys. Chem.* **2007**, *58*, 375–407.

[8] Novoselov, K. S.; Geim, A. K.; Morozov, S. V.; Jiang, D.; Zhang, Y.; Dubonos, S. V.; Grigorieva, I. V.; Firsov, A. A. Electric Field Effect in Atomically Thin Carbon Films. *Science* **2004**, *306*, 666–669.

[9] Novoselov, K. S.; Jiang, D.; Schedin, F.; Booth, T. J.; Khotkevich, V. v.; Morozov, S. V.; Geim, A. K. Two-Dimensional Atomic Crystals. *Proc. Natl. Acad. Sci. USA* **2005**, *102*, 10451–10453.

[10] Cooper, D. R.; D'Anjou, B.; Ghattamaneni, N.; Harack, B.; Hilke, M.; Horth, A.; Majlis, N.; Massicotte, M.; Vandsburger, L.; Whiteway, E.; Yu, V. Experimental Review of Graphene. *ISRN Condensed Matter Physics* **2012**, *2012*, 1–56.

[11] Balandin, A. A.; Ghosh, S.; Bao, W.; Calizo, I.; Teweldebrhan, D.; Miao, F.; Lau, C. N. Superior Thermal Conductivity of Single-Layer Graphene. *Nano Lett.* **2008**, *8*, 902–907.

[12] Joshi, S.; Ecija, D.; Koitz, R.; Iannuzzi, M.; Seitsonen, A. P.; Hutter, J.; Sachdev, H.; Vijayaraghavan, S.; Bischoff, F.; Seuferd, K.; Barth, J. V.; Auwärter, W. Hexagonal Boron Nitride on Cu(111): An Electronically Corrugated Monolayer. *Nano Lett.* **2012**, *12*, 5821–5828.

[13] Koitz, R.; Seitsonen, A. P.; Iannuzzi, M.; Hutter, J. Structural and Electronic Properties of a Large-Scale Moire Pattern of Hexagonal Boron Nitride on Cu(111) Studied With Density Functional Theory. *Nanoscale* **2013**, *5*, 5589–5595.

[14] Joshi, S.; Bischoff, F.; Koitz, R.; Ecija, D.; Seufert, K.; Seitsonen, A. P.; Hutter, J.; Diller, K.; Urgel, J. I.; Sachdev, H.; Barth, J. V.; Auwärter, W. Control of Molecular Organization and Energy Level Alignment by an Electronically Nanopatterned Boron Nitride Template. *ACS Nano* **2014**, *8*, 430–442.

[15] Bauer, T.; Zheng, Z.; Renn, A.; Enning, R.; Stemmer, A.; Sakamoto, J.; Schlüter, A. D. Synthesis of Free-Standing, Monolayered Organometallic Sheets at the Air/Water Interface. *Angew. Chem. Int. Ed.* **2011**, *50*, 7879–7884.

[16] Koitz, R.; Iannuzzi, M.; Hutter, J. Building Blocks for Two-Dimensional Metal-Organic Frameworks Confined at the Air-Water Interface: An Ab Initio Molecular Dynamics Study. *J. Phys. Chem. C* **2015**, *119*, 4023–4030.

[17] Pease, R. S. An X-Ray Study of Boron Nitride. *Acta Cryst.* **1952**, *5*, 356–361.

[18] Kubota, Y.; Watanabe, K.; Tsuda, O.; Taniguchi, T. Deep Ultraviolet Light Emitting Hexagonal Boron Nitride Synthesized at Atmospheric Pressure. *Science* **2007**, *317*, 932–934.

[19] Watanabe, K.; Taniguchi, T.; Kanda, H. Direct-Bandgap Properties and Evidence for Ultraviolet Lasing of Hexagonal Boron Nitride Single Crystal. *Nat. Mater.* **2004**, *3*, 404–409.

[20] Jin, C.; Lin, F.; Suenaga, K.; Iijima, S. Fabrication of a Freestanding Boron Nitride Single Layer and Its Defect Assignments. *Phys. Rev. Lett.* **2009**, *102*, 195505.

[21] Corso, M.; Auwärter, W.; Muntwiler, M.; Tamai, A.; Greber, T.; Osterwalder, J. Boron Nitride Nanomesh. *Science* **2004**, *303*, 217–220.

[22] Kim, G.; Jang, A.-R.; Jeong, H. Y.; Lee, Z.; Kang, D. J. Growth of High-Crystalline, Single-Layer Hexagonal Boron Nitride on Recyclable Platinum Foil. *Nano Lett.* **2013**, *13*, 1834–1839.

[23] Preobrajenski, A. B.; Vinogradov, A. S.; Mårtensson, N. Monolayer of h-BN Chemisorbed on Cu(111) and Ni(111): The Role of the Transition Metal 3d States. *Surf. Sci.* **2005**, *582*, 21–30.

[24] Auwärter, W.; Kreutz, T.; Greber, T.; Osterwalder, J. XPD and STM Investigation of Hexagonal Boron Nitride on Ni(111). *Surf. Sci.* **1999**, *429*, 229–236.

[25] Rokuta, E.; Hasegawa, Y.; Suzuki, K.; Gamou, Y.; Oshima, C.; Nagashima, A. Phonon Dispersion of an Epitaxial Monolayer Film of Hexagonal Boron Nitride on Ni(111). *Phys. Rev. Lett.* **1997**, *79*, 4609–4612.

[26] Orofeo, C. M.; Suzuki, S.; Kageshima, H.; Hibino, H. Growth and Low-Energy Electron Microscopy Characterization of Monolayer Hexagonal Boron Nitride on Epitaxial Cobalt. *Nano Res.* **2013**, *6*, 335–347.

[27] Schulz, F.; Drost, R.; Hämäläinen, S. K.; Liljeroth, P. Templated Self-Assembly and Local Doping of Molecules on Epitaxial Hexagonal Boron Nitride. *ACS Nano* **2013**, *7*, 11121–11128.

[28] Goriachko, A.; He, Y.; Knapp, M.; Over, H.; Corso, M.; Brugger, T.; Berner, S.; Osterwalder, J.; Greber, T. Self-Assembly of a Hexagonal Boron Nitride Nanomesh on Ru(0001). *Langmuir* **2007**, *23*, 2928–2931.

[29] Vinogradov, A. S.; Zakharov, A. a.; Ng, M. L.; Mikkelsen, A.; Lundgren, E.; Mårtensson, N.; Preobrajenski, A. B. One-Dimensional Corrugation of the h-BN Monolayer on Fe(110). *Langmuir* **2012**, *28*, 1775–1781.

[30] Müller, F.; Hüfner, S.; Sachdev, H.; Laskowski, R.; Blaha, P.; Schwarz, K. Epitaxial Growth of Hexagonal Boron Nitride on Ag(111). *Phys. Rev. B* **2010**, *82*, 113406.

[31] Lu, G.; Wu, T.; Yuan, Q.; Wang, H.; Wang, H.; Ding, F.; Xie, X.; Jiang, M. Synthesis of Large Single-Crystal Hexagonal Boron Nitride Grains on Cu-Ni Alloy. *Nature Comm.* **2015**, *6*, 1–7.

[32] Haas, P.; Tran, F.; Blaha, P. Calculation of the Lattice Constant of Solids With Semilocal Functionals. *Phys. Rev. B* **2009**, *79*, 085104.

[33] Clendenen, G.; Drickamer, H. Effect of Pressure on the Volume and Lattice Parameters of Magnesium. *J. Phys. Chem. Solids* **1964**, *25*, 865–868.

[34] Gómez Díaz, J.; Ding, Y.; Koitz, R.; Seitsonen, A. P.; Iannuzzi, M.; Hutter, J. Hexagonal Boron Nitride on Transition Metal Surfaces. *Theor. Chem. Acc.* **2013**, *132*, 1350.

[35] Dong, G.; Fourré, E. B.; Tabak, F. C.; Frenken, J. W. M. How Boron Nitride Forms a Regular Nanomesh on Rh(111). *Phys. Rev. Lett.* **2010**, *104*, 096102.

[36] Laskowski, R.; Blaha, P.; Gallauner, T.; Schwarz, K. Single-Layer Model of the Hexagonal Boron Nitride Nanomesh on the Rh (111) Surface. *Phys. Rev. Lett.* **2007**, *98*, 106802.

[37] Laskowski, R.; Blaha, P.; Schwarz, K. Bonding of Hexagonal BN to Transition Metal Surfaces: An Ab Initio Density-Functional Theory Study. *Phys. Rev. B* **2008**, *78*, 045409.

[38] Laskowski, R.; Gallauner, T.; Blaha, P.; Schwarz, K. Density Functional Theory Simulations of B K and N K NEXAFS Spectra of h-BN/Transition Metal(111) Interfaces. *J. Phys.: Condens. Matt.* **2009**, *21*, 104210.

[39] Iannuzzi, M.; Hutter, J. Comparative Study of the Nature of Chemical Bonding of Corrugated Graphene on Ru(0001) and Rh(111) by Electronic Structure Calculations. *Surf. Sci.* **2011**, *605*, 1360–1368.

[40] Ding, Y.; Iannuzzi, M.; Hutter, J. Investigation of Boron Nitride Nanomesh Interacting With Water. *J. Phys. Chem. C* **2011**, *115*, 13685–13692.

[41] Fukamori, Y.; König, M.; Yoon, B.; Wang, B.; Esch, F.; Heiz, U.; Landman, U. Fundamental Insight Into the Substrate-Dependent Ripening of Monodisperse Clusters. *ChemCatChem* **2013**, *5*, 3330–3341.

[42] Dienel, T.; Gómez-Díaz, J.; Seitsonen, A. P.; Widmer, R.; Iannuzzi, M.; Radican, K.; Sachdev, H.; Müllen, K.; Hutter, J.; Gröning, O. Dehalogenation and Coupling of a Polycyclic Hydrocarbon on an Atomically Thin Insulator. *ACS Nano* **2014**, *8*, 6571–6579.

[43] Cun, H.; Iannuzzi, M.; Hemmi, A.; Roth, S.; Osterwalder, J.; Greber, T. Immobilizing Individual Atoms Beneath a Corrugated Single Layer of Boron Nitride. *Nano Lett.* **2013**, *13*, 2098–2103.

[44] Cun, H.; Iannuzzi, M.; Hemmi, A.; Osterwalder, J.; Greber, T. Implantation Length and Thermal Stability of Interstitial Ar Atoms in Boron Nitride Nanotents. *ACS Nano* **2014**, *8*, 1014–1021.

[45] Cun, H.; Iannuzzi, M.; Hemmi, A.; Osterwalder, J.; Greber, T. Two-Nanometer Voids in Single-Layer Hexagonal Boron Nitride: Formation via the "Can-Opener" Effect and Annihilation by Self-Healing. *ACS Nano* **2014**, *8*, 7423–7431.

[46] Gamou, Y.; Terai, M.; Nagashima, A.; Oshima, C. Atomic Structural Analysis of a Monolayer Epitaxial Film of Hexagonal Boron Nitride/Ni(111) Studied by LEED Intensity Analysis. *Sci. Rep. RITU A44* **1997**, 211–214.

[47] Muntwiler, M.; Auwärter, W.; Baumberger, F.; Hoesch, M.; Greber, T. Determining Adsorbate Structures From Substrate Emission X-Ray Photoelectron Diffraction. *Surface Science* **2001**, *472*, 125–132.

[48] Preobrajenski, A. B.; Vinogradov, A. S.; Mårtensson, N. Ni 3d-BN π Hybridization at the h-BN/Ni(111) Interface Observed With Core-Level Spectroscopies. *Phys. Rev. B* **2004**, *70*, 165404.

[49] Preobrajenski, A. B.; Krasnikov, S. A.; Vinogradov, A. S.; Ng, M. L.; Käämbre, T.; Cafolla, A. A.; Mårtensson, N. Adsorption-Induced Gap States of h-BN on Metal Surfaces. *Phys. Rev. B* **2008**, *77*, 085421.

[50] Grad, G.; Blaha, P.; Schwarz, K.; Auwärter, W.; Greber, T. Density Functional Theory Investigation of the Geometric and Spintronic Structure of h-BN/Ni(111) in View of Photoemission and STM Experiments. *Phys. Rev. B* **2003**, *68*, 085404.

[51] Nagashima, A.; Tejima, N.; Gamou, Y.; Kawai, T.; Oshima, C. Electronic Structure of Monolayer Hexagonal Boron Nitride Physisorbed on Metal Surfaces. *Phys. Rev. Lett.* **1995**, *75*, 3918–3921.

[52] Wasey, A. H. M. A.; Chakrabarty, S.; Das, G. P.; Majumder, C. h-BN Monolayer on the Ni(111) Surface: A Potential Catalyst for Oxidation. *ACS Appl. Mater. Interfaces* **2013**, *5*, 10404–10408.

[53] Lyalin, A.; Nakayama, A.; Uosaki, K.; Taketsugu, T. Adsorption and Catalytic Activation of the Molecular Oxygen on the Metal Supported h-BN. *Top. Catal.* **2014**, *57*, 1032–1041.

[54] Lyalin, A.; Nakayama, A.; Uosaki, K.; Taketsugu, T. Functionalization of Monolayer h-BN by a Metal Support for the Oxygen Reduction Reaction. *J. Phys. Chem. C* **2013**, *117*, 21359–21370.

[55] Kim, G.; Jung, S. C.; Han, Y.-K. Selectively Strong Molecular Adsorption on Boron Nitride Monolayer Induced by Transition Metal Substrate. *Curr. Appl. Phys.* **2013**, *13*, 2059–2063.

[56] Song, L.; Ci, L.; Lu, H.; Sorokin, P. B.; Jin, C.; Ni, J.; Kvashnin, A. G.; Kvashnin, D. G.; Lou, J.; Yakobson, B. I.; Ajayan, P. M. Large Scale Growth and Characterization of Atomic Hexagonal Boron Nitride Layers. *Nano Lett.* **2010**, *10*, 3209–3215.

[57] Kim, K. K.; Hsu, A.; Jia, X.; Kim, S. M.; Shi, Y.; Hofmann, M.; Nezich, D.; Rodriguez-Nieva, J. F.; Dresselhaus, M.; Palacios, T.; Kong, J. Synthesis of Monolayer Hexagonal Boron Nitride on Cu Foil Using Chemical Vapor Deposition. *Nano Lett.* **2012**, *12*, 161–166.

[58] Wang, M.; Kim, M.; Odkhuu, D.; Park, N.; Lee, J.; Jang, W. J.; Kahng, S. J.; Ruoff, R. S.; Song, Y. J.; Lee, S. Catalytic Transparency of Hexagonal Boron Nitride on Copper for Chemical Vapor Deposition Growth of Large-Area and High-Quality Graphene. *ACS Nano* **2014**, *8*, 5478–5483.

[59] Hermann, K. Periodic Overlayers and Moiré Patterns: Theoretical Studies of Geometric Properties. *J. Phys.: Condens. Matt.* **2012**, *24*, 314210.

[60] Long, J. R.; Yaghi, O. M. The Pervasive Chemistry of Metal-Organic Frameworks. *Chem. Soc. Rev.* **2009**, *38*, 1213–1214.

[61] James, S. L. Metal-Organic Frameworks. *Chem. Soc. Rev.* **2003**, *32*, 276–288.

[62] Lee, J.; Farha, O. K.; Roberts, J.; Scheidt, K. A.; Nguyen, S. T.; Hupp, J. T. Metal-Organic Framework Materials as Catalysts. *Chem. Soc. Rev.* **2009**, *38*, 1450–1459.

[63] Murray, L. J.; Dinca, M.; Long, J. R. Hydrogen Storage in Metal-Organic Frameworks. *Chem. Soc. Rev.* **2009**, *38*, 1294–1314.

[64] Barman, S.; Khutia, A.; Koitz, R.; Blacque, O.; Furukawa, H.; Iannuzzi, M.; Yaghi, O. M.; Jainak, C.; Hutter, J.; Berke, H. Synthesis and Hydrogen Adsorption Properties of Internally Polarized 2,6-Azulenedicarboxylic Acid Based MOFs. *J. Mat. Chem. A* **2014**, *2*, 18823–18830.

[65] Suh, M. P.; Park, H. J.; Prasad, T. K.; Lim, D.-W. Hydrogen Storage in Metal-Organic Frameworks. *Chem. Rev.* **2012**, *112*, 782–835.

[66] Sumida, K.; Rogow, D. L.; Mason, J. A.; McDonald, T. M.; Bloch, E. D.; Herm, Z. R.; Bae, T. H.; Long, J. R. Carbon Dioxide Capture in Metal-Organic Frameworks. *Chem. Rev.* **2012**, *112*, 724–781.

[67] Li, J.-R.; Kuppler, R. J.; Zhou, H.-C. Selective Gas Adsorption and Separation in Metal-Organic Frameworks. *Chem. Soc. Rev.* **2009**, *38*, 1477–1504.

[68] Allendorf, M. D.; Bauer, C. A.; Bhakta, R. K.; Houk, R. J. T. Luminescent Metal-Organic Frameworks. *Chem. Soc. Rev.* **2009**, *38*, 1330–1352.

[69] Kurmoo, M. Magnetic Metal-Organic Frameworks. *Chem. Soc. Rev.* **2009**, *38*, 1353–1379.

[70] Cho, S.-H.; Ma, B.; Nguyen, S. T.; Hupp, J. T.; Albrecht-Schmitt, T. E. A Metal-Organic Framework Material That Functions as an Enantioselective Catalyst for Olefin Epoxidation. *Chem. Commun.* **2006**, 2563–2565.

[71] Alkordi, M. H.; Liu, Y.; Larsen, R. W.; Eubank, J. F.; Eddaoudi, M. Zeolite-Like Metal-Organic Frameworks as Platforms for Applications: On Metalloporphyrin-Based Catalysts. *J. Am. Chem. Soc.* **2008**, *130*, 12639–12641.

[72] Choi, K. M.; Na, K.; Somorjai, G. A.; Yaghi, O. M. Chemical Environment Control and Enhanced Catalytic Performance of Platinum Nanoparticles Embedded in Nanocrystalline Metal-Organic Frameworks. *J. Am. Chem. Soc.* **2015**,

[73] Llabres I Xamena, F. X.; Abad, A.; Corma, A.; Garcia, H. MOFs as Catalysts: Activity, Reusability and Shape-Selectivity of a Pd-Containing MOF. *J. Catal.* **2007**, *250*, 294–298.

[74] Stock, N.; Biswas, S. Synthesis of Metal-Organic Frameworks (MOFs): Routes to Various MOF Topologies, Morphologies, and Composites. *Chem. Rev.* **2012**, *112*, 933–969.

[75] Zacher, D.; Shekhah, O.; Wöll, C.; Fischer, R. A. Thin Films of Metal-Organic Frameworks. *Chem. Soc. Rev.* **2009**, *38*, 1418–1429.

[76] Shekhah, O.; Wang, H.; Kowarik, S.; Schreiber, F.; Paulus, M.; Tolan, M.; Sternemann, C.; Evers, F.; Zacher, D.; Fischer, R. A.; Wo, C.; Uni, V. Step-By-Step Route for the Synthesis of Metal-Organic Frameworks. *J. Am. Chem. Soc.* **2007**, *129*, 15118–15119.

[77] Schubert, U. S.; Hofmeier, H.; Newcome, G. R. *Modern Terpyridine Chemistry*, 1st ed.; Wiley-VCH: Weinheim, 2006.

[78] Schubert, U. S.; Winter, A.; Newkome, G. R. *Terpyridine-Based Materials*, 1st ed.; Wiley-VCH: Weinheim, 2011.

[79] Williams, J. A. G.; Wilkinson, A. J.; Whittle, V. L. Light-Emitting Iridium Complexes With Tridentate Ligands. *Dalton Trans.* **2008**, 2081–2099.

[80] Winter, A.; Friebe, C.; Chiper, M.; Hager, M. D.; Schubert, U. S. Self-Assembly of Pi-Conjugated Bis(terpyridine) Ligands With Zinc(II) Ions: New Metallosupramolecular Materials for Optoelectronic Applications. *J. Polym. Sci., Part A: Polym. Chem.* **2008**, *46*, 830–843.

[81] Dumur, F.; Mayer, C. R.; Hoang-Thi, K.; Ledoux-Rak, I.; Miomandre, F.; Clavier, G.; Dumas, E.; Méallet-Renault, R.; Frigoli, M.; Zyss, J.; Sécheresse, F. Electrochemical, Linear Optical, and Nonlinear Optical Properties and Interpretation by Density Functional Theory Calculations of (4-N,N- Dimethylaminostyryl)-Pyridinium Pendant Group Associated With Polypyridinic Ligands and Respective Multifunctional Me. *Inorg. Chem.* **2009**, *48*, 8120–8133.

[82] Scarpaci, A.; Monnereau, C.; Hergué, N.; Blart, E.; Legoupy, S.; Odobel, F.; Gorfo, A.; Pérez-Moreno, J.; Clays, K.; Asselberghs, I. Preparation and Characterization of Second Order Non-Linear Optical Properties of New "Push-Pull" Platinum Complexes. *Dalton Trans.* **2009**, 4538–4546.

[83] Wadas, T. J.; Wang, Q. M.; Kim, Y. J.; Flaschenreim, C.; Blanton, T. N.; Eisenberg, R. Vapochromism and Its Structural Basis in a Luminescent Pt(II) Terpyridine-Nicotinamide Complex. *J. Am. Chem. Soc.* **2004**, *126*, 16841–16849.

[84] Wenger, O. S. Vapochromism in Organometallic and Coordination Complexes: Chemical Sensors for Volatile Organic Compounds. *Chem. Rev.* **2013**, *113*, 3686–3733.

[85] Liu, P.; Zhou, C.-Y.; Xiang, S.; Che, C.-M. Highly Efficient Oxidative Carbon-Carbon Coupling With SBA-15-Support Iron Terpyridine Catalyst. *Chem. Commun.* **2010**, *46*, 2739–2741.

[86] Koitz, R.; Nørskov, J. K.; Studt, F. A Systematic Study of Metal-Supported Boron Nitride Materials for the Oxygen Reduction Reaction. *Phys. Chem. Chem. Phys.* **2015**, *17*, 12722–12727.

[87] Jensen, F. *Introduction to Computational Chemistry*, 2nd ed.; Wiley: Chichester, 2007.

[88] Koch, W.; Holthausen, M. C. *A Chemist's Guide to Density Functional Theory*; Wiley-VCH: Weinheim, 2001.

[89] Parr, R. G.; Yang, W. *Density-Functional Theory of Atoms and Molecules*; Oxford University Press: New York, 1989.

[90] Hohenberg, P.; Kohn, W. Inhomogeneous Electron Gas. *Phys. Rev.* **1964**, *136*, 864–871.

[91] Wagner, L. O.; Baker, T. E.; Stoudenmire, E. M.; Burke, K.; White, S. R. Kohn-Sham Calculations With the Exact Functional. *Phys. Rev. B* **2014**, *90*, 045109.

[92] Kohn, W.; Sham, L. J. Self-Consistent Equations Including Exchange and Correlation Effects. *Phys. Rev.* **1965**, *385*, 1133–1138.

[93] Perdew, J. P.; Ruzsinszky, A.; Constantin, L. A.; Sun, J.; Csonka, G. I. Some Fundamental Issues in Ground-State Density Functional Theory: A Guide for the Perplexed. *J. Chem. Theory. Comput.* **2009**, *5*, 902–908.

[94] Scuseria, G. E.; Staroverov, V. N. *Theory and Applications of Computational Chemistry*; 2005; pp 669–724.

[95] Burke, K. Perspective on Density Functional Theory. *J. Chem. Phys.* **2012**, *136*, 150901.

[96] Perdew, J. P.; Burke, K.; Ernzerhof, M. Generalized Gradient Approximation Made Simple. *Phys. Rev. Lett.* **1996**, *77*, 3865–3868.

[97] Wellendorff, J.; Lundgaard, K. T.; Møgelhøj, A.; Petzold, V.; Landis, D. D.; Nørskov, J. K.; Bligaard, T.; Jacobsen, K. W. Density Functionals for Surface Science: Exchange-Correlation Model Development With Bayesian Error Estimation. *Phys. Rev. B* **2012**, *85*, 235149.

[98] Zhao, Y.; Truhlar, D. G. Applications and Validations of the Minnesota Density Functionals. *Chem. Phys. Lett.* **2011**, *502*, 1–13.

[99] Zhao, Y.; Truhlar, D. G. A New Local Density Functional for Main-Group Thermochemistry, Transition Metal Bonding, Thermochemical Kinetics, and Noncovalent Interactions. *J. Chem. Phys.* **2006**, *125*, 194101.

[100] Snyder, J. C.; Rupp, M.; Hansen, K.; Müller, K. R.; Burke, K. Finding Density Functionals With Machine Learning. *Phys. Rev. Lett.* **2012**, *108*, 1–5.

[101] Zhang, Y.; Yang, W. Comment on "Generalized Gradient Approximation Made Simple". *Phys. Rev. Lett.* **1998**, *80*, 890.

[102] Lieb, E. H.; Oxford, S. Improved Lower Bound on the Indirect Coulomb Energy. *Int. J. Quantum Chem.* **1981**, *19*, 427–439.

[103] Perdew, J.; Chevary, J.; Vosko, S.; Jackson, K.; Pederson, M.; Singh, D.; Fiolhais, C. Atoms, Molecules, Solids, and Surfaces: Applications of the Generalized Gradient Approximation for Exchange and Correlation. *Phys. Rev. B* **1992**, *46*, 6671–6687.

[104] Haas, P.; Tran, F.; Blaha, P.; Silva, A. J. R.; Odashima, M. M.; Capelle, K. Systematic Investigation of a Family of Gradient-Dependent Functionals for Solids. *Phys. Rev. B* **2010**, *81*, 125136.

[105] Perdew, J. P.; Ruzsinszky, A.; Csonka, G. I.; Vydrov, O. A.; Scuseria, G. E.; Constantin, L. A.; Zhou, X.; Burke, K. Generalized Gradient Approximation for Solids and Their Surfaces. *Phys. Rev. Lett.* **2007**, *136406*, 1–4.

[106] Hammer, B.; Hansen, L.; Nørskov, J. Improved Adsorption Energetics Within Density-Functional Theory Using Revised Perdew-Burke-Ernzerhof Functionals. *Phys. Rev. B* **1999**, *59*, 7413–7421.

[107] Koitz, R.; Soini, T. M.; Genest, A.; Trickey, S. B.; Rösch, N. Scalable Properties of Metal Clusters: A Comparative Study of Modern Exchange-Correlation Functionals. *J. Chem. Phys.* **2012**, 034102.

[108] Koitz, R.; Soini, T. M.; Genest, A.; Trickey, S. B.; Rösch, N. Structure-Dependence of the Magnetic Moment in Small Palladium Clusters: Surprising Results From the M06-L Meta-GGA Functional. *Int. J. Quantum Chem.* **2011**, *112*, 113–120.

[109] Haas, P.; Tran, F.; Blaha, P.; Schwarz, K.; Laskowski, R. Insight Into the Performance of GGA Functionals for Solid-State Calculations. *Phys. Rev. B* **2009**, *80*, 195109.

[110] Curtiss, L. S.; Raghavachari, K.; Redfern, P. C.; Pople, J. A. Assessment of Gaussian-3 and Density Functional Theories for a Larger Experimental Test Set. *J. Chem. Phys.* **2000**, *112*, 7374–7383.

[111] Zheng, J.; Zhao, Y.; Truhlar, D. G. The DBH24/08 Database and Its Use to Assess Electronic Structure Model Chemistries for Chemical Reaction Barrier Heights. *J. Chem. Theory. Comput.* **2009**, *5*, 808–821.

[112] Jurecka, P.; Sponer, J.; Cerny, J.; Hobza, P. Benchmark Database of Accurate (MP2 and CCSD(T) Complete Basis Set Limit) Interaction Energies of Small Model Complexes, DNA Base Pairs, and Amino Acid Pairs. *Phys. Chem. Chem. Phys.* **2006**, *8*, 1985–1993.

[113] Takatani, T.; Hohenstein, E. G.; Malagoli, M.; Marshall, M. S.; Sherrill, C. D. Basis Set Consistent Revision of the S22 Test Set of Noncovalent Interaction Energies. *J. Chem. Phys.* **2010**, *132*, 144104.

[114] Medford, A. J.; Wellendorff, J.; Vojvodic, A.; Studt, F.; Abild-Pedersen, F.; Jacobsen, K. W.; Bligaard, T.; Nørskov, J. K. Assessing the Reliability of Calculated Catalytic Ammonia Synthesis Rates. *Science* **2014**, *345*, 197–200.

[115] Klimes, J.; Michaelides, A. Perspective: Advances and Challenges in Treating van der Waals Dispersion Forces in Density Functional Theory. *J. Chem. Phys.* **2012**, *137*, 120901.

[116] Wu, Q.; Yang, W. Empirical Correction to Density Functional Theory for van der Waals Interactions. *J. Chem. Phys.* **2002**, *116*, 515–524.

[117] Tkatchenko, A.; Scheffler, M. Accurate Molecular van der Waals Interactions From Ground-State Electron Density and Free-Atom Reference Data. *Phys. Rev. Lett.* **2009**, *102*, 073005.

[118] Grimme, S. Semiempirical GGA-Type Density Functional Constructed With a Long-Range Dispersion Correction. *J. Comput. Chem.* **2006**, *27*, 1787–1799.

[119] Grimme, S.; Antony, J.; Ehrlich, S.; Krieg, H. A Consistent and Accurate Ab Initio Parametrization of Density Functional Dispersion Correction (DFT-D) for the 94 Elements H-Pu. *J. Chem. Phys.* **2010**, *132*, 154104.

[120] Zhang, G. X.; Tkatchenko, A.; Paier, J.; Appel, H.; Scheffler, M. van der Waals Interactions in Ionic and Semiconductor Solids. *Phys. Rev. Lett.* **2011**, *107*, 245501.

[121] Grimme, S. Accurate Description of van der Waals Complexes by Density Functional Theory Including Empirical Corrections. *J. Comput. Chem.* **2004**, *25*, 1463–1473.

[122] Andersson, Y.; Langreth, D.; Lundqvist, B. van der Waals Interactions in Density-Functional Theory. *Phys. Rev. Lett.* **1996**, *76*, 102–105.

[123] Dion, M.; Rydberg, H.; Schröder, E.; Langreth, D. C.; Lundqvist, B. I. van der Waals Density Functional for General Geometries. *Phys. Rev. Lett.* **2004**, *92*, 246401.

[124] Vydrov, O.; Voorhis, T. V. Nonlocal van der Waals Density Functional Made Simple. *Phys. Rev. Lett.* **2009**, *103*, 063004.

[125] Lee, K.; Murray, E. D.; Kong, L.; Lundqvist, B. I.; Langreth, D. C. Higher-Accuracy van der Waals Density Functional. *Phys. Rev. B* **2010**, *82*, 081101.

[126] Lee, K.; Kelkkanen, A. K.; Berland, K.; Andersson, S.; Langreth, D. C.; Schröder, E.; Lundqvist, B. I.; Hyldgaard, P. Evaluation of a Density Functional With Account of van der Waals Forces Using Experimental Data of H_2 Physisorption on Cu(111). *Phys. Rev. B* **2011**, *84*, 193408.

[127] Frenkel, D.; Smit, B. *Molecular Simulation: From Algorithms to Applications*, 2nd ed.; Academic Press: London, 2002.

[128] Marx, D.; Hutter, J. *Ab Initio Molecular Dynamics*, 1st ed.; Cambridge University Press: Cambridge, 2009.

[129] Car, R.; Parrinello, M. Unified Approach for Molecular Dynamics and Density-Functional Theory. *Phys. Rev. Lett.* **1985**, *55*, 2471–2474.

[130] Andrade, X.; Castro, A.; Zueco, D.; Alonso, J. L.; Echenique, P.; Falceto, F.; Rubio, A. Modified Ehrenfest Formalism for Efficient Large-Scale Ab Initio Molecular Dynamics. *J. Chem. Theory. Comput.* **2009**, *5*, 728–742.

[131] Sprik, M.; Ciccotti, G. Free Energy From Constrained Molecular Dynamics. *J. Chem. Phys.* **1998**, *109*, 7737–7744.

[132] Patey, G. N.; Valleau, J. P. A Monte Carlo Method for Obtaining the Interionic Potential of Mean Force in Solution. *J. Chem. Phys.* **1975**, *63*, 2334–2339.

[133] Dellago, C.; Bolhuis, P. G.; Csajka, F. S.; Chandler, D. Transition Path Sampling and the Calculation of Rate Constants. *J. Chem. Phys.* **1998**, *108*, 1964–1977.

[134] Sugita, Y.; Okamoto, Y. Replica Exchange Molecular Dynamics Method for Protein Folding. *Chem. Phys. Let.* **1999**, *314*, 141–151.

[135] Merlitz, H.; Wenzel, W. Comparison of Stochastic Optimization Methods for Receptor-Ligand Docking. *Chem. Phys. Lett.* **2002**, *362*, 271–277.

[136] Laio, A.; Parrinello, M. Escaping Free-Energy Minima. *Proc. Natl. Acad. Sci. USA* **2002**, *99*, 12562–12566.

[137] Laio, A.; Gervasio, F. L. Metadynamics: A Method to Simulate Rare Events and Reconstruct the Free Energy in Biophysics, Chemistry and Material Science. *Rep. Prog. Phys.* **2008**, *71*, 126601.

[138] Barducci, A.; Bonomi, M.; Parrinello, M. Metadynamics. *Wiley Interdisciplinary Reviews: Computational Molecular Science* **2011**, *1*, 826–843.

[139] Sega, M.; Autieri, E.; Pederiva, F. On the Calculation of Puckering Free Energy Surfaces. *J. Chem. Phys.* **2009**, *130*, 225102.

[140] Bonomi, M.; Parrinello, M. Enhanced Sampling in the Well-Tempered Ensemble. *Phys. Rev. Lett.* **2010**, *104*, 190601.

[141] Piana, S.; Laio, A. A Bias-Exchange Approach to Protein Folding. *J. Phys. Chem. B* **2007**, *111*, 4553–4559.

[142] VandeVondele, J.; Krack, M.; Mohamed, F.; Parrinello, M.; Chassaing, T.; Hutter, J. Quickstep: Fast and Accurate Density Functional Calculations Using a Mixed Gaussian and Plane Waves Approach. *Comput. Phys. Commun.* **2005**, *167*, 103–128.

[143] CP2K Developers Group Under the Terms of the GNU General Public Licence; See www.cp2k.org. 2014.

[144] VandeVondele, J.; Hutter, J. Gaussian Basis Sets for Accurate Calculations on Molecular Systems in Gas and Condensed Phases. *J. Chem. Phys.* **2007**, *127*, 114105.

[145] Goedecker, S.; Teter, M.; Hutter, J. Separable Dual-Space Gaussian Pseudopotentials. *Phys. Rev. B* **1996**, *54*, 1703–1710.

[146] Tersoff, J.; Hamann, D. R. Theory and Application for the Scanning Tunneling Microscope. *Phys. Rev. Lett.* **1983**, *50*, 1998–2001.

[147] Tersoff, J.; Hamann, D. R. Theory of the Scanning Tunneling Microscope. *Phys. Rev. B* **1985**, *31*, 805–813.

[148] Bahn, S. R.; Jacobsen, K. W. An Object-Oriented Scripting Interface to a Legacy Electronic Structure Code. *Comput. Sci. Eng.* **2002**, *4*, 56–66.

[149] Giannozzi, P.; Baroni, S.; Bonini, N.; Calandra, M.; Car, R.; Cavazzoni, C.; Ceresoli, D.; Chiarotti, G. L.; Cococcioni, M.; Dabo, I.; Dal Corso, A.; De Gironcoli, S.; Fabris, S.; Fratesi, G.; Gebauer, R.; Gerstmann, U.; Gougoussis, C.; Kokalj, A.; Lazzeri, M.; Martin-Samos, L.; Marzari, N.; Mauri, F.; Mazzarello, R.; Paolini, S.; Pasquarello, A.; Paulatto, L.; Sbraccia, C.; Scandolo, S.; Sclauzero, G.; Seitsonen, A. P.; Smogunov, A.; Umari, P.; Wentzcovitch, R. M. QUANTUM ESPRESSO: A Modular and Open-Source Software Project for Quantum Simulations of Materials. *J. Phys.: Condens. Matt.* **2009**, *21*, 395502.

[150] Ahmed Adllan, A.; Dal Corso, A. Ultrasoft Pseudopotentials and Projector Augmented-Wave Data Sets: Application to Diatomic Molecules. *J. Phys.: Condens. Matt.* **2011**, *23*, 425501.

[151] Rossmeisl, J.; Logadottir, A.; Nørskov, J. Electrolysis of Water on (Oxidized) Metal Surfaces. *Chem. Phys.* **2005**, *319*, 178–184.

[152] Pack, J. D.; Monkhorst, H. J. Special Points for Brillouin-Zone Integrations. *Phys. Rev. B* **1977**, *16*, 1748–1749.

[153] Baer, M. D.; Mundy, C. J.; McGrath, M. J.; Kuo, I.-F. W.; Siepmann, J. I.; Tobias, D. J. Re-Examining the Properties of the Aqueous Vapor-Liquid Interface Using Dispersion Corrected Density Functional Theory. *J. Chem. Phys.* **2011**, *135*, 124712.

[154] Schmidt, J.; VandeVondele, J.; Kuo, I.-F. W.; Sebastiani, D.; Siepmann, J. I.; Hutter, J.; Mundy, C. J. Isobaric-Isothermal Molecular Dynamics Simulations Utilizing Density Functional Theory: An Assessment of the Structure and Density of Water at Near-Ambient Conditions. *J. Phys. Chem. B* **2009**, *113*, 11959–11964.

[155] Huda, M. N.; Kleinman, L. h-BN Monolayer Adsorption on the Ni(111) Surface: A Density Functional Study. *Phys. Rev. B* **2006**, *74*, 075418.

[156] Che, J.; Cheng, H.-P. First-Principles Investigation of a Monolayer of C_{60} on h-BN/Ni(111). *Phys. Rev. B* **2005**, *72*, 115436.

[157] Joshi, N.; Ghosh, P. Substrate-Induced Changes in the Magnetic and Electronic Properties of Hexagonal Boron Nitride. *Phys. Rev. B* **2013**, *87*, 235440.

[158] Hammer, B.; Scheffler, M.; Jacobsen, K.; Nørskov, J. Multidimensional Potential Energy Surface for H_2 Dissociation Over Cu(111). *Phys. Rev. Lett.* **1994**, *73*, 1400–1403.

[159] Wu, Z.; Cohen, R. E. More Accurate Generalized Gradient Approximation for Solids. *Phys. Rev. B* **2006**, *73*, 235116.

[160] Feigelson, B. N.; Bermudez, V. M.; Hite, J. K.; Robinson, Z. R.; Wheeler, V. D.; Sridhara, K.; Hernández, S. C. Growth and Spectroscopic Characterization of Monolayer and Few-Layer Hexagonal Boron Nitride on Metal Substrates. *Nanoscale* **2015**, *7*, 3694–3702.

[161] Zhou, Y.; Zu, X.; Gao, F. Substrate-Induced Magnetism in BN Layer: A First-Principles Study. *Solid State Comm.* **2011**, *151*, 883–886.

[162] Stradi, D.; Barja, S.; Díaz, C.; Garnica, M.; Borca, B.; Hinarejos, J.; Sánchez-Portal, D.; Alcamí, M.; Arnau, A.; Vázquez De Parga, A.; Miranda, R.; Martín, F. Role of Dispersion Forces in the Structure of Graphene Monolayers on Ru Surfaces. *Phys. Rev. Lett.* **2011**, *106*, 186102.

[163] Wang, B.; Bocquet, M.-L.; Marchini, S.; Günther, S.; Wintterlin, J. Chemical Origin of a Graphene Moiré Overlayer on Ru(0001). *Phys. Chem. Chem. Phys.* **2008**, *10*, 3530–3534.

[164] Brugger, T.; Ma, H.; Iannuzzi, M.; Berner, S.; Winkler, A.; Hutter, J.; Osterwalder, J.; Greber, T. Nanotexture Switching of Single-Layer Hexagonal Boron Nitride on Rhodium by Intercalation of Hydrogen Atoms. *Angew. Chem. Int. Ed.* **2010**, *49*, 6120–6124.

[165] Pollard, A. J.; Perkins, E. W.; Smith, N. A.; Saywell, A.; Goretzki, G.; Phillips, A. G.; Argent, S. P.; Sachdev, H.; Müller, F.; Hüfner, S.; Gsell, S.; Fischer, M.; Schreck, M.; Osterwalder, J.; Greber, T.; Berner, S.; Champness, N. R.; Beton, P. H. Supramolecular Assemblies Formed on an Epitaxial Graphene Superstructure. *Angew. Chem. Int. Ed.* **2010**, *49*, 1794–1799.

[166] Garnica, M.; Stradi, D.; Barja, S.; Calleja, F.; Diaz, C.; Alcamí, M.; Martín, N.; Vazquez De Parga, A. L.; Martín, F.; Miranda, R. Long-Range Magnetic Order in a Purely Organic 2D Layer Adsorbed on Epitaxial Graphene. *Nat. Phys.* **2013**, *9*, 368–374.

[167] Urgel, J. I.; Schwarz, M.; Garnica, M.; Stassen, D.; Bonifazi, D.; Ecija, D.; Barth, J. v.; Auwärter, W. Controlling Coordination Reactions and Assembly on a Cu(111) Supported Boron Nitride Monolayer. *J. Am. Chem. Soc.* **2015**, *137*, 2420–2423.

[168] Milgrom, L. R.; Warren, M. J. *The Colours of Life: An Introduction to the Chemistry of Porphyrins and Related Compounds*; Oxford University Press: Oxford, 1997.

[169] Auwärter, W.; Weber-Bargioni, A.; Riemann, A.; Schiffrin, A.; Gröning, O.; Fasel, R.; Barth, J. V. Self-Assembly and Conformation of Tetrapyridyl-Porphyrin Molecules on Ag(111). *J. Chem. Phys.* **2006**, *124*, 194708.

[170] Auwärter, W.; Weber-Bargioni, A.; Brink, S.; Riemann, A.; Schiffrin, A.; Ruben, M.; Barth, J. V. Controlled Metalation of Self-Assembled Porphyrin Nanoarrays in Two Dimensions. *ChemPhysChem* **2007**, *8*, 250–254.

[171] Heim, D.; Seufert, K.; Auwärter, W.; Aurisicchio, C.; Fabbro, C.; Bonifazi, D.; Barth, J. V. Surface-Assisted Assembly of Discrete Porphyrin-Based Cyclic Supramolecules. *Nano Lett.* **2010**, *10*, 122–128.

[172] Heim, D.; Ecija, D.; Seufert, K.; Auwärter, W.; Aurisicchio, C.; Fabbro, C.; Bonifazi, D.; Barth, J. V. Self-Assembly of Flexible One-Dimensional Coordination Polymers on Metal Surfaces. *J. Am. Chem. Soc.* **2010**, *132*, 6783–6790.

[173] Jung, T. A.; Schlittler, R. R.; Gimzewski, J. K. Conformational Identification of Individual Adsorbed Molecules With the STM. *Nature* **1997**, *386*, 696–698.

[174] Dyer, M. S.; Robin, A.; Haq, S.; Raval, R.; Persson, M.; Klimes, J. Understanding the Interaction of the Porphyrin Macrocycle to Reactive Metal Substrates: Structure, Bonding, and Adatom Capture. *ACS Nano* **2011**, *5*, 1831–1838.

[175] Diller, K.; Klappenberger, F.; Allegretti, F.; Papageorgiou, A. C.; Fischer, S.; Wiengarten, A.; Joshi, S.; Seufert, K.; Ecija, D.; Auwärter, W.; Barth, J. V. Investigating the Molecule-Substrate Interaction of Prototypic Tetrapyrrole Compounds: Adsorption and Self-Metalation of Porphine on Cu(111). *J. Chem. Phys.* **2013**, *138*, 154710.

[176] Bischoff, F.; Seufert, K.; Auwärter, W.; Joshi, S.; Vijayaraghavan, S.; Ecija, D.; Diller, K.; Papageorgiou, A. C.; Fischer, S.; Allegretti, F.; Duncan, D. A.; Klappenberger, F.; Blobner, F.; Han, R.; Barth, J. V. How Surface Bonding and Repulsive Interactions Cause Phase Transformations: Ordering of a Prototype Macrocyclic Compound on Ag(111). *ACS Nano* **2013**, *7*, 3139–3149.

[177] Dabo, I.; Ferretti, A.; Park, C.-H.; Poilvert, N.; Li, Y.; Cococcioni, M.; Marzari, N. Donor and Acceptor Levels of Organic Photovoltaic Compounds From First Principles. *Phys. Chem. Chem. Phys.* **2013**, *15*, 685–695.

[178] Crabtree, G.; Dresselhaus, M. The Hydrogen Fuel Alternative. *MRS Bulletin* **2008**, *33*, 421–429.

[179] Zhang, M.; Dai, L. Carbon Nanomaterials as Metal-Free Catalysts in Next Generation Fuel Cells. *Nano Energy* **2012**, *1*, 514–517.

[180] Morozan, A.; Jousselme, B.; Palacin, S. Low-Platinum and Platinum-Free Catalysts for the Oxygen Reduction Reaction at Fuel Cell Cathodes. *Energy & Environmental Science* **2011**, *4*, 1238–1254.

[181] Berger, D. J. Fuel Cells and Precious-Metal Catalysts. *Science* **1999**, *286*, 49.

[182] Bashyam, R.; Zelenay, P. A Class of Non-Precious Metal Composite Catalysts for Fuel Cells. *Nature* **2006**, *443*, 63–66.

[183] Stamenkovic, V. R.; Fowler, B.; Mun, B. S.; Wang, G.; Ross, P. N.; Lucas, C. A.; Markovic, N. M. Improved Oxygen Reduction Activity on $Pt_3Ni(111)$ via Increased Surface Site Availability. *Science* **2007**, *315*, 493–497.

[184] Lefevre, M.; Proietti, E.; Jaouen, F.; Dodelet, J.-P. Iron-Based Catalysts With Improved Oxygen Reduction Activity in Polymer Electrolyte Fuel Cells. *Science* **2009**, *324*, 71–74.

[185] Greeley, J.; Stephens, I. E. L.; Bondarenko, A. S.; Johansson, T. P.; Hansen, H. A.; Jaramillo, T. F.; Rossmeisl, J.; Chorkendorff, I.; Nørskov, J. K. Alloys of Platinum and Early Transition Metals as Oxygen Reduction Electrocatalysts. *Nat. Chem.* **2009**, *1*, 552–556.

[186] Qu, L.; Liu, Y.; Baek, J. B.; Dai, L. Nitrogen-Doped Graphene as Efficient Metal-Free Electrocatalyst for Oxygen Reduction in Fuel Cells. *ACS Nano* **2010**, *4*, 1321–1326.

[187] Liu, R.; Wu, D.; Feng, X.; Müllen, K. Nitrogen-Doped Ordered Mesoporous Graphitic Arrays With High Electrocatalytic Activity for Oxygen Reduction. *Angew. Chem. Int. Ed.* **2010**, *49*, 2565–2569.

[188] Gong, K.; Du, F.; Xia, Z.; Durstock, M.; Dai, L. Nitrogen-Doped Carbon Nanotube Arrays With High Electrocatalytic Activity for Oxygen Reduction. *Science* **2009**, *323*, 760–764.

[189] Studt, F. The Oxygen Reduction Reaction on Nitrogen-Doped Graphene. *Catal. Lett.* **2012**, *143*, 58–60.

[190] Lyalin, A.; Nakayama, A.; Uosaki, K.; Taketsugu, T. Theoretical Predictions for Hexagonal BN Based Nanomaterials as Electrocatalysts for the Oxygen Reduction Reaction. *Phys. Chem. Chem. Phys.* **2013**, *15*, 2809–2820.

[191] Uosaki, K.; Elumalai, G.; Noguchi, H.; Masuda, T.; Lyalin, A.; Nakayama, A.; Taketsugu, T. Boron Nitride Nanosheet on Gold as an Electrocatalyst for Oxygen Reduction Reaction: Theoretical Suggestion and Experimental Proof. *J. Am. Chem. Soc.* **2014**, *136*, 6542–6545.

[192] Nørskov, J. K.; Rossmeisl, J.; Logadottir, A.; Lindqvist, L.; Kitchin, J. R.; Bligaard, T.; Jonsson, H. Origin of the Overpotential for Oxygen Reduction at a Fuel-Cell Cathode. *J. Phys. Chem. B* **2004**, *108*, 17886–17892.

[193] Rossmeisl, J.; Qu, Z. W.; Zhu, H.; Kroes, G. J.; Nørskov, J. K. Electrolysis of Water on Oxide Surfaces. *J. Electroanal. Chem.* **2007**, *607*, 83–89.

[194] Skulason, E.; Bligaard, T.; Gudmundsdottir, S.; Studt, F.; Rossmeisl, J.; Abild-Pedersen, F.; Vegge, T.; Jonsson, H.; Nørskov, J. K. A Theoretical Evaluation of Possible Transition Metal Electro-Catalysts for N_2 Reduction. *Phys. Chem. Chem. Phys.* **2012**, *14*, 1235.

[195] Peterson, A. A.; Abild-Pedersen, F.; Studt, F.; Rossmeisl, J.; Nørskov, J. K. How Copper Catalyzes the Electroreduction of Carbon Dioxide Into Hydrocarbon Fuels. *Energy Environ. Sci.* **2010**, *3*, 1311–1315.

[196] Bacle, P.; Seitsonen, A. P.; Iannuzzi, M.; Hutter, J. Chemical Reactions on Metal-Supported Hexagonal Boron Nitride Investigated With Density Functional Theory. *Chimia* **2014**, *68*, 596–601.

[197] Thompsett, D. *Fuel Cell Technology Handbook*; CRC Press: Boca Raton, 2003; Chapter 6.

[198] Man, I. C.; Su, H.-Y.; Calle-Vallejo, F.; Hansen, H. A.; Martinez, J.; Inoglu, N. G.; Kitchin, J.; Jaramillo, T. F.; Nørskov, J. K.; Rossmeisl, J. Universality in Oxygen Evolution Electrocatalysis on Oxide Surfaces. *ChemCatChem* **2011**, *3*, 1159–1165.

[199] Wintterlin, J.; Bocquet, M.-L. Graphene on Metal Surfaces. *Surf. Sci.* **2009**, *603*, 1841–1852.

[200] Edwards, R. S.; Coleman, K. S. Graphene Synthesis: Relationship to Applications. *Nanoscale* **2013**, *5*, 38–51.

[201] Henningsen, N.; Rurali, R.; Franke, K. J.; Fernández-Torrente, I.; Pascual, J. I. Trans to Cis Isomerization of an Azobenzene Derivative on a Cu(100) Surface. *Appl. Phys. A* **2008**, *93*, 241–246.

[202] Piantek, M.; Miguel, J.; Krüger, A.; Navio, C.; Bernien, M.; Ball, D. K.; Hermann, K.; Kuch, W. Temperature, Surface, and Coverage-Induced Conformational Changes of Azobenzene Derivatives on Cu(001). *J. Phys. Chem. C* **2009**, 20307–20315.

[203] Caldwell, J. D.; Anderson, T. J.; Culbertson, J. C.; Jernigan, G. G.; Hobart, K. D.; Kub, F. J.; Tadjer, M. J.; Tedesco, J. L.; Hite, J. K.; Mastro, M. A.; Myers-Ward, R. L.; Eddy, C. R.; Campbell, P. M.; Gaskill, D. K. Technique for the Dry Transfer of Epitaxial Graphene Onto Arbitrary Substrates. *ACS Nano* **2010**, *4*, 1108–1114.

[204] Schlüter, A. D.; Sakamoto, J. Putting Aromatic Compounds to Work: Rational Synthesis of Organic 2D Polymers. *Pure Appl. Chem.* **2012**, *84*, 861–867.

[205] Makiura, R.; Tsuchiyama, K.; Sakata, O. Self-Assembly of Highly Crystalline Two-Dimensional MOF Sheets on Liquid Surfaces. *CrystEngComm* **2011**, *13*, 5538–5541.

[206] Makiura, R.; Motoyama, S.; Umemura, Y.; Yamanaka, H.; Sakata, O.; Kitagawa, H. Surface Nano-Architecture of a Metal-Organic Framework. *Nature Materials* **2010**, *9*, 565–571.

[207] Zheng, Z.; Opilik, L.; Schiffmann, F.; Liu, W.; Bergamini, G.; Ceroni, P.; Lee, L.-T.; Schütz, A.; Sakamoto, J.; Zenobi, R.; Vandevondele, J.; Schlüter, A. D. Synthesis of Two-Dimensional Analogues of Copolymers by Site-To-Site Transmetalation of Organometallic Monolayer Sheets. *J. Am. Chem. Soc.* **2014**, *136*, 6103–6110.

[208] Payamyar, P.; Kaja, K.; Ruiz-Vargas, C.; Stemmer, A.; Murray, D. J.; Johnson, C. J.; King, B. T.; Schiffmann, F.; Vandevondele, J.; Renn, A.; Götzinger, S.; Ceroni, P.; Schütz, A.; Lee, L. T.; Zheng, Z.; Sakamoto, J.; Schlüter, A. D. Synthesis of a Covalent Monolayer Sheet by Photochemical Anthracene Dimerization at the Air/Water Interface and Its Mechanical Characterization by AFM Indentation. *Adv. Mater.* **2014**, *26*, 2052–2058.

[209] Chen, X.; Zhou, Q.; Cheng, Y.; Geng, Y.; Ma, D.; Xie, Z.; Wang, L. Synthesis, Structure and Luminescence Properties of Zinc(II) Complexes With Terpyridine Derivatives as Ligands. *Journal of Luminescence* **2007**, *126*, 81–90.

[210] Baker, A. T.; Craig, D. C.; Rae, A. D. The Crystal Structure of Bis(2,2':6',2"-Terpyridine)nickel(II) Perchlorate Hydrate. *Aust. J. Chem.* **1995**, *48*, 1373–1378.

[211] Baker, A. T.; Goodwin, H. A. Crystal Structure of Bis(2,2':6',2"-Terpyridine)iron(II) Bis(perchlorate) Hydrate. *Aust. J. Chem.* **1985**, *38*, 207–214.

[212] Pelascini, F.; Wesolek, M.; Peruch, F.; De Cian, A.; Kyritsakas, N.; Lutz, P. J.; Kress, J. Iron Complexes of Terdentate Nitrogen Ligands: Formation and X-Ray Structure of Three New Dicationic Complexes. *Polyhedron* **2004**, *23*, 3193–3199.

[213] Indumathy, R.; Radhika, S.; Kanthimathi, M.; Weyhermuller, T.; Unni Nair, B. Cobalt Complexes of Terpyridine Ligand: Crystal Structure and Photocleavage of DNA. *J. Inorg. Biochem.* **2007**, *101*, 434–443.

[214] Uma, V.; Kanthimathi, M.; Weyhermuller, T.; Nair, B. U. Oxidative DNA Cleavage Mediated by a New Copper (II) Terpyridine Complex: Crystal Structure and DNA Binding Studies. *J. Inorg. Biochem.* **2005**, *99*, 2299–2307.

[215] Hollis, L. S.; Lippard, S. J. Aqueous Chemistry of (2,2',2"-Terpyridine)gold(III). Preparation and Structures of [Au(terpy)Cl]Cl_2 3H_2O and the Mixed-Valence Au(I)-Au(III) Salt [Au(terpy)Cl]$_2$[$AuCl_2$]$_3$[$AuCl_4$]. *J. Am. Chem. Soc.* **1983**, *105*, 4293–4299.

[216] Bilic, A.; Reimers, J. R.; Hush, N. S. Adsorption of Pyridine on the Gold(111) Surface: Implications for "Alligator Clips" for Molecular Wires. *J Phys. Chem. B* **2002**, *106*, 6740–6747.

[217] Kühne, T. D.; Pascal, T. A.; Kaxiras, E.; Jung, Y. New Insights Into the Structure of the Vapor/Water Interface From Large-Scale First-Principles Simulations. *J. Phys. Chem. Lett.* **2011**, *2*, 105–113.

[218] Kuo, I.-F. W.; Mundy, C. J. An Ab Initio Molecular Dynamics Study of the Aqueous Liquid-Vapor Interface. *Science* **2004**, *303*, 658–660.

[219] Liu, X.; Lu, X.; Wang, R.; Meijer, E. J. Understanding Hydration of Zn^{2+} in Hydrothermal Fluids With Ab Initio Molecular Dynamics. *Phys. Chem. Chem. Phys.* **2011**, *13*, 13305–13309.

[220] Morchutt, C.; Björk, J.; Krotzky, S.; Gutzler, R.; Kern, K. Covalent Coupling via Dehalogenation on Ni(111) Supported Boron Nitride and Graphene. *Chem. Commun.* **2015**, *51*, 2440–2443.

[221] Smit, B. Screening Materials Relevant for Energy Technologies. *Chimia* **2015**, *69*, 248–252.